1986

Sampling strategies in space and time: effects on representation of mesoscale processes.

Heishman, John L.

NAVAL POSTGRADUATE SCHOOL
Monterey, California

THESIS

SAMPLING STRATEGIES IN SPACE AND TIME:
EFFECTS ON REPRESENTATION OF MESOSCALE PROCESSES

by

John Loren Heishman

September 1986

Thesis Advisor: Christopher N.K. Mooers
Co-advisor: Mary L. Batteen

Approved for public release; distribution is unlimited.

CURITY CLASSIFICATION OF THIS PAGE

REPORT DOCUMENTATION PAGE

a. REPORT SECURITY CLASSIFICATION UNCLASSIFIED	1b RESTRICTIVE MARKINGS
a. SECURITY CLASSIFICATION AUTHORITY	3 DISTRIBUTION / AVAILABILITY OF REPORT Approved for public release; distribution unlimited.
b. DECLASSIFICATION / DOWNGRADING SCHEDULE	
PERFORMING ORGANIZATION REPORT NUMBER(S)	5 MONITORING ORGANIZATION REPORT NUMBER(S)
a NAME OF PERFORMING ORGANIZATION aval Postgraduate School	6b. OFFICE SYMBOL (If applicable) 68
7a. NAME OF MONITORING ORGANIZATION Naval Postgraduate School	
. ADDRESS (City, State, and ZIP Code) onterey, California 93943-5000	7b. ADDRESS (City, State, and ZIP Code) Monterey, California 93943-5000
a. NAME OF FUNDING / SPONSORING ORGANIZATION	8b. OFFICE SYMBOL (If applicable)
9. PROCUREMENT INSTRUMENT IDENTIFICATION NUMBER	
. ADDRESS (City, State, and ZIP Code)	10. SOURCE OF FUNDING NUMBERS

PROGRAM ELEMENT NO.	PROJECT NO.	TASK NO	WORK UNIT ACCESSION NO.

. TITLE (Include Security Classification)
SAMPLING STRATEGIES IN SPACE AND TIME: EFFECTS ON REPRESENTATION OF MESOSCALE PROCESSES (UNCLASSIFIED)

. PERSONAL AUTHOR(S)
Heishman, John L.

3a. TYPE OF REPORT	13b. TIME COVERED	14. DATE OF REPORT (Year, Month, Day)	15 PAGE COUNT
Master's Thesis	FROM _____ TO _____	1986 September	173

. SUPPLEMENTARY NOTATION

COSATI CODES			18. SUBJECT TERMS (Continue on reverse if necessary and identify by block number)
FIELD	GROUP	SUB-GROUP	CCS, Primitive Equation Model, Objective Analysis, Spatial Sampling, Temporal Sampling

. ABSTRACT (Continue on reverse if necessary and identify by block number)

his study examines along-track spacing increments from model output to determine the largest eparation of data sampling permissible to achieve a reasonable representation of ocean esoscale features without serious aliasing. With this objective, three sampling strategies re tested and analyzed by conducting simulated aircraft and shipboard cruises. Due to the imited number of observations acquired during each cruise, analyses of the data fields tilize an objective analysis technique which assesses the spatial correlation and RMS error y comparing the sampled data sets to the assumed perfect PE output fields. Of the schemes ested, the sampling strategy of using finer sampling along the coast and random sampling ffshore with either aircraft of less than five-day hydrographic surveys results in the 'best' epresentation of mesoscale processes in a coastal region.

0 DISTRIBUTION / AVAILABILITY OF ABSTRACT ☒ UNCLASSIFIED/UNLIMITED ☐ SAME AS RPT ☐ DTIC USERS	21. ABSTRACT SECURITY CLASSIFICATION Unclassified
2a NAME OF RESPONSIBLE INDIVIDUAL hristopher N.K. Mooers	22b TELEPHONE (Include Area Code) 408-646-2552
	22c. OFFICE SYMBOL 68

D FORM 1473, 84 MAR 83 APR edition may be used until exhausted.
All other editions are obsolete

SECURITY CLASSIFICATION OF THIS PAGE

☆U.S. Government Printing Office: 1985—507-047

Approved for public release; distribution is unlimited.

Sampling Strategies in Space and Time: Effects on Representation of Mesoscale Processes

by

John L. Heishman
Lieutenant, United States Navy
B.S., University of Alabama, 1978

Submitted in partial fulfillment of the
requirements for the degree of

MASTER OF SCIENCE IN METEOROLOGY AND OCEANOGRAPHY

from the

NAVAL POSTGRADUATE SCHOOL
September 1986

ABSTRACT

This study examines along-track spacing increments from model output to determine the largest separation of data sampling permissible to achieve a reasonable representation of ocean mesoscale features without serious aliasing. With this objective, three sampling strategies are tested and analyzed by conducting simulated aircraft and shipboard cruises. Due to the limited number of observations acquired during each cruise, analyses of the data fields utilize an objective analysis technique which assesses the spatial correlation and RMS error by comparing the sampled data sets to the assumed perfect PE output fields. Of the schemes tested, the sampling strategy of using finer sampling along the coast and random sampling offshore with either aircraft or less than five-day hydrographic surveys results in the 'best' representation of mesoscale processes in a coastal region.

TABLE OF CONTENTS

LIST OF TABLES

LIST OF FIGURES

ACKNOWLEDGEMENTS

The guidance and support of my co-advisors, Dr. Christopher N.K. Mooers and Dr. Mary L. Batteen, have been important and essential in the preparation of this thesis. Dr. Mooers stimulated my interest in optimal sampling schemes through the introduction of the OPTOMA program and has shaped the progress of this study throughout. Special thanks are due Dr. Batteen who devoted many hours of her time, advice and suggestions on the interpretation of the results and many numerous other facets of this project. The opportunity to work with experts of the highest quality in the field of oceanography such as Dr. Mooers and Dr. Batteen has been a rewarding and enjoyable experience.

Thanks are also expressed to Dr. Robert L. Haney for the use of a variation of his primitive equation model which created the data field used in this study and to Dr. Michele M. Rienecker who developed the objective analysis programs and assisted in the explanation of the technique.

Finally, I would like to acknowledge my dear wife, Debbie, who has my deepest love for her patience and support. She contributed in many ways in seeing to the completion of this thesis.

I. INTRODUCTION

A. OBJECTIVES

There is an increasing demand for reliable and accurate models to represent and forecast ocean mesoscale features. Both dynamical and thermodynamical modeling are essential to extract the full information content for ocean monitoring and prediction. The efficient description and prediction of the flow field in the ocean is necessary because of the difficulty and cost of direct observations due both to the opacity and vastness of the sea and to the natural scales of the phenomena. Eastern boundary current flow regimes, such as the California Current System (CCS), are important for fisheries and climate-related processes; for search and rescue operations; for oil and gas recovery operations; for waste disposal; for biological, chemical, and geological experiments; and for physical oceanographic research. Due to the ocean's spatial and temporal scales of variability in which substantial changes in the flow system can occur within a week (Robinson *et al.*, 1984) or over several weeks (Kosro and Huyer, 1986), the establishment of a broad-based ocean observing and monitoring system which includes moored buoys, remotely sensed data, hydrographic data and aircraft deployed AXBT data is required.

The objectives of this research are first to examine along-track spacing increments from model output in order to determine the largest separation of data sampling permissible to achieve a reasonable representation of ocean mesoscale features without serious aliasing. Secondly, the degree of synopticity required of both shipboard hydrographic data and aircraft AXBT data for field representation will be evaluated. Lastly the above two objectives will be analyzed to determine a "best" sampling strategy from those tested for the study of mesoscale processes.

B. STUDY AREA

The "test block" of ocean investigated comprises a region extending from 36.5° to 39.3°N and 124° to 126.8°W, a 270 x 270 km horizontal domain. This area is located to the south of the Mendocino Escarpment in the California Current System (CCS) offshore of the continental slope. Average water depth is 4000 meters as depicted from the bathymetry, Fig. 1.1.

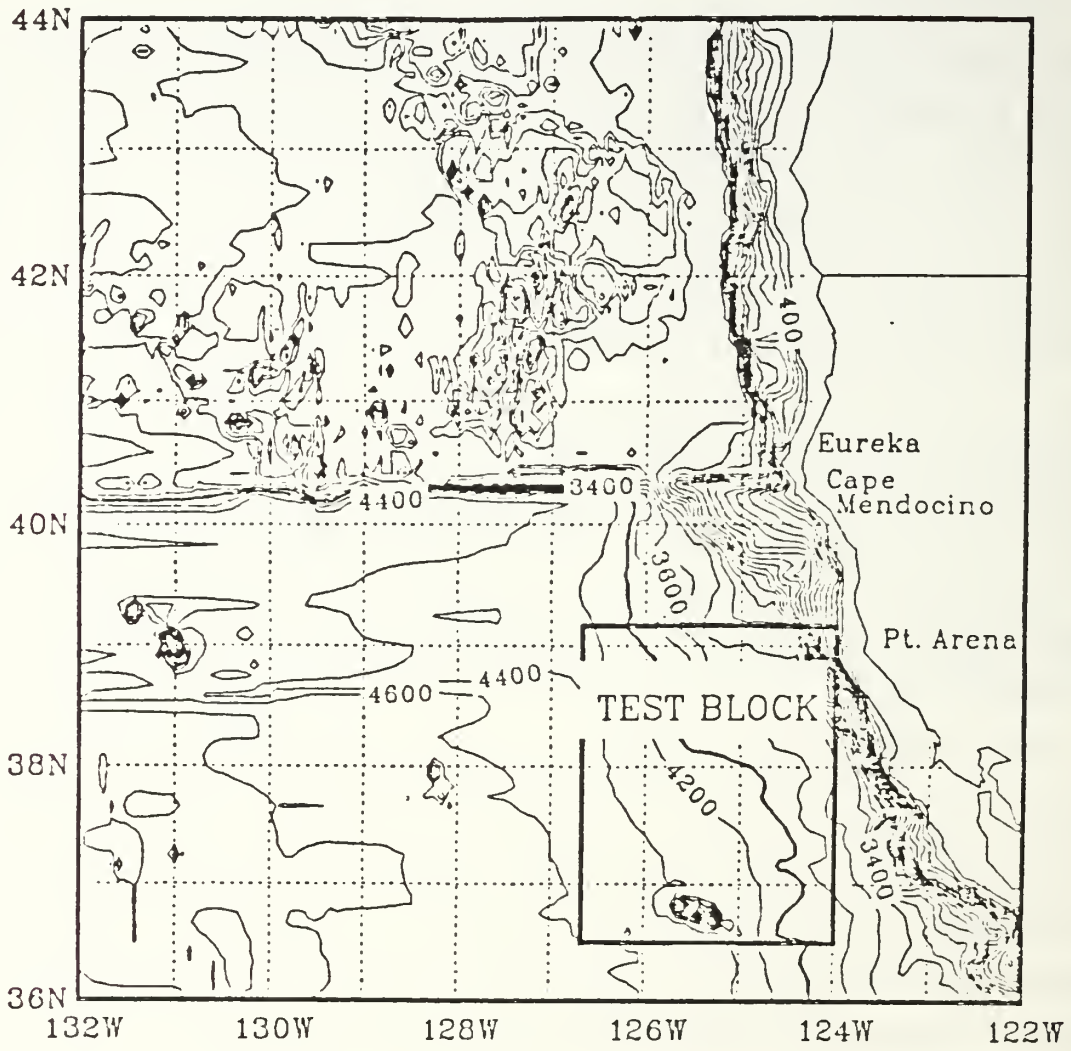

Figure 1.1 Bathymetry of Study Area.

Four currents constitute the CCS: the California Current, the California Undercurrent, the Davidson Current and the Southern California Countercurrent (Hickey, 1979). The average California Current is an eastern boundary current approximately 1000 km wide and less than 500 m deep with movement of the order 1 km/hr (Hickey, 1979). The higher latitudes from which the California Current flows is a region where precipitation exceeds evaporation so that the surface waters are relatively fresh. Evaporation and mixing downstream and the associated coastal upwelling tends to increase the surface salinity from 29.0 parts per thousand (ppt) to an average value of 33.0 to 34.0 ppt (Kosro and Huyer, 1986). Because of this equatorward flow from relatively high latitudes, its waters are also at lower temperatures than those at comparable latitudes in the central regions of the ocean. Seasonally, additional cold water is introduced along the California coast by upwelling which occurs from February to August in association with equatorward winds. As a general rule, surface isotherms are oriented more or less meridionally along the coast in contrast to their zonal orientation farther offshore. The vertical thermal gradient decreases close to the boundary, with the upper isotherms rising and the deeper isotherms sinking toward shore. Where higher temperatures are thus found at depth nearshore, the presence of a poleward undercurrent is indicated. This feature is the California Undercurrent (Wooster and Reid, 1960). The Davidson Current is a poleward, nearshore surface flow which occurs from October to February north of Point Conception (Chelton, 1984).The Southern California Countercurrent refers to the poleward flow found south of Point Conception inshore of the Channel Islands in the California Bight (Hickey, 1979).

The transient CCS differs markedly from the classical conceptual picture of a broad, slow climatological mean current. It is now known to consist of intense meandering current filaments (jets) interningled with synoptic-mesoscale eddies. These quasi-geostrophic jets, which at times extend for several hundred kilometers and may have sharp thermal and chemical fronts associated with them, entrain cold, upwelled coastal waters and rapidly advect them far offshore (Mooers and Robinson, 1984). They are on a scale of 100 to 300 kms with an intensity of 20 to 50 cm/sec (Bernstein *et al.*, 1977).

It has been postulated that the current meanders are triggered by topography close to the California coast and grow as a result of the baroclinic instability of the coastal equatorward surface jet in association with coastal upwelling and the poleward

California Undercurrent. Such unstable meanders sweep the cool water offshore and often lead to isolated eddies or vortex pairs (Rienecker *et al.*, 1984). Another possible explanation for the high variability of the CCS is that time-dependent winds parallel to the California coast, even if their curl is zero, create a source of vorticity in the surface layers of the ocean near the coast. The Rossby waves excited in this manner give rise to a complex system of mesoscale features and equatorward and poleward flowing currents near the coast (Philander and Yoon, 1982).

C. DATA ACQUISITION

The ocean is spatially and temporally inhomogenous and displays its inhomogeneity through a broad spectrum of space and time scales. To the degree that the ocean is inhomogenous, an increasingly large number of samples is required to be representative. Limited resources, that is, only one ship available for hydrographic sampling, require that samples over different parts of an area be taken sequentially rather than synoptically, whereas an areal sampling technique which satisfies the synopticity assumption must be rapid enough to sample the entire area of interest before any significant change occurs in the phenomenon.

The data acquired in this research is assumed to come from two sources, hydrographic ship XBT/CTD casts and P-3 aircraft deployed AXBTs. Several factors must be considered prior to conducting a hydrographic sampling operation. The vessel should be spacious enough to allow for the storage of the XBTs and CTDs required of the sampling plan. It should be stable and maneuverable at slow speeds for proper instrument deployment and station positioning. The range (fuel capacity) and working facilities of the ship should be compatible with the planned operational arrangements. Instruments which are required aboard the ship include a station positioning device such as LORAN C which is accurate to within 0.1 km with a resolution of 0.01 km and of course the XBT/CTDs to measure the temperature and pressure fields. The XBT provides temperature versus depth data. Temperature accuracy is generally within 0.2 C and depth accuracy is the greater of 4.6 m and 2% of depth. Measurements of pressure, temperature, and conductivity are acquired from CTD casts which on average give precisions of 0.1 dB and 0.001 C for pressure and temperature, respectively.

Factors which must be considered prior to the deployment of P-3 aircraft AXBTs include the cruising speeds and altitudes of the aircraft while on station, the number of AXBTs to be deployed, the minimum desired station spacing between deployments, the

depths and associated transmission times of the AXBTs, the number and frequencies of the AXBT transmission channels and the availability of a multichannel recording system (Colton and Mooers, 1985). The area of coverage by a P-3 flight is determined by its cruising speed and altitude. While on station the typical speed ranges from 160 to 210 knots. Due to the drop distance of the AXBTs from the aircraft to the ocean surface, the altitude maintained during an AXBT mission is lower than optimal for the P-3.

Two types of AXBTs are available for sampling: a shallow (305 m) AXBT which transmits for 200 seconds and a deep (760 m) AXBT with a 500 second transmission time. Their temperature and depth accuracies are identical to those of the XBT described earlier. Storage capacity onboard the aircraft is from 70 to 99 AXBTs.

The P-3 aircraft is equipped with four navigational systems in order to determine the geographic location of the AXBT deployment stations. These systems include the LITON-72 Inertial Navigation System (INS), Tactical Air Navigation (TACAN), Long-Range Navigation (LORAN) and Radar (Colton and Mooers, 1985). When all of the readings from the above instruments are considered the position accuracy is within 3.7 km of the true geographic location.

D. PRIMITIVE EQUATION MODEL DESCRIPTION

The output from Professor Haney's primitive equation (PE) numerical ocean model of the CCS is used here in the context of representing the "perfect measured" fields of temperature (T) and pressure (p). The model is based on the primitive equations of motion together with the Boussinesq approximations. The domain of the model is the rectangular region, extending from 124°W to 130°W and from 36.5°N to 42.5°N, covering an area of 6° longitude by 6° latitude. The region extends approximately 500 km offshore from the west coast of North America and it spans the California coastline from Point Sur in the south to Cape Blanco in the north (ca. 600 km). The major topographic feature in the area is the Mendocino Escarpment at 40.2°N. Figures 1.2 and 1.3 show the 3-dimensional aspects of the bottom topography of the region and that used in the model ocean, respectively.

The model has open boundary conditions except on the eastern coastal boundary. In the horizontal a space-staggered "B" scheme advocated by Arakawa and Lamb (1977) is used. There is uniform spacing in the horizontal plane with a grid spacing of 8 km in the east-west direction and 10 km in the north-south direction. The

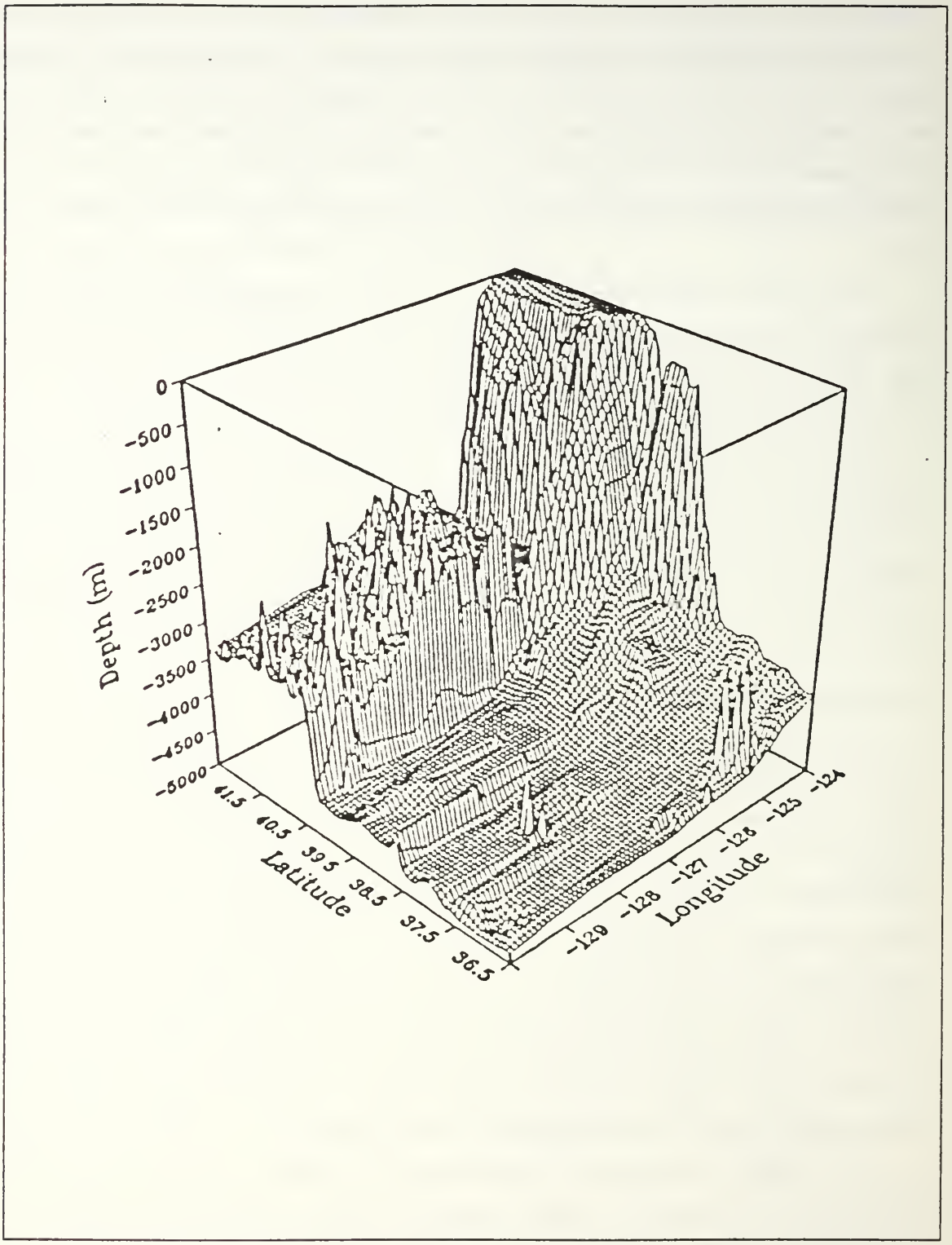

Figure 1.2 Actual bottom topography of study area.

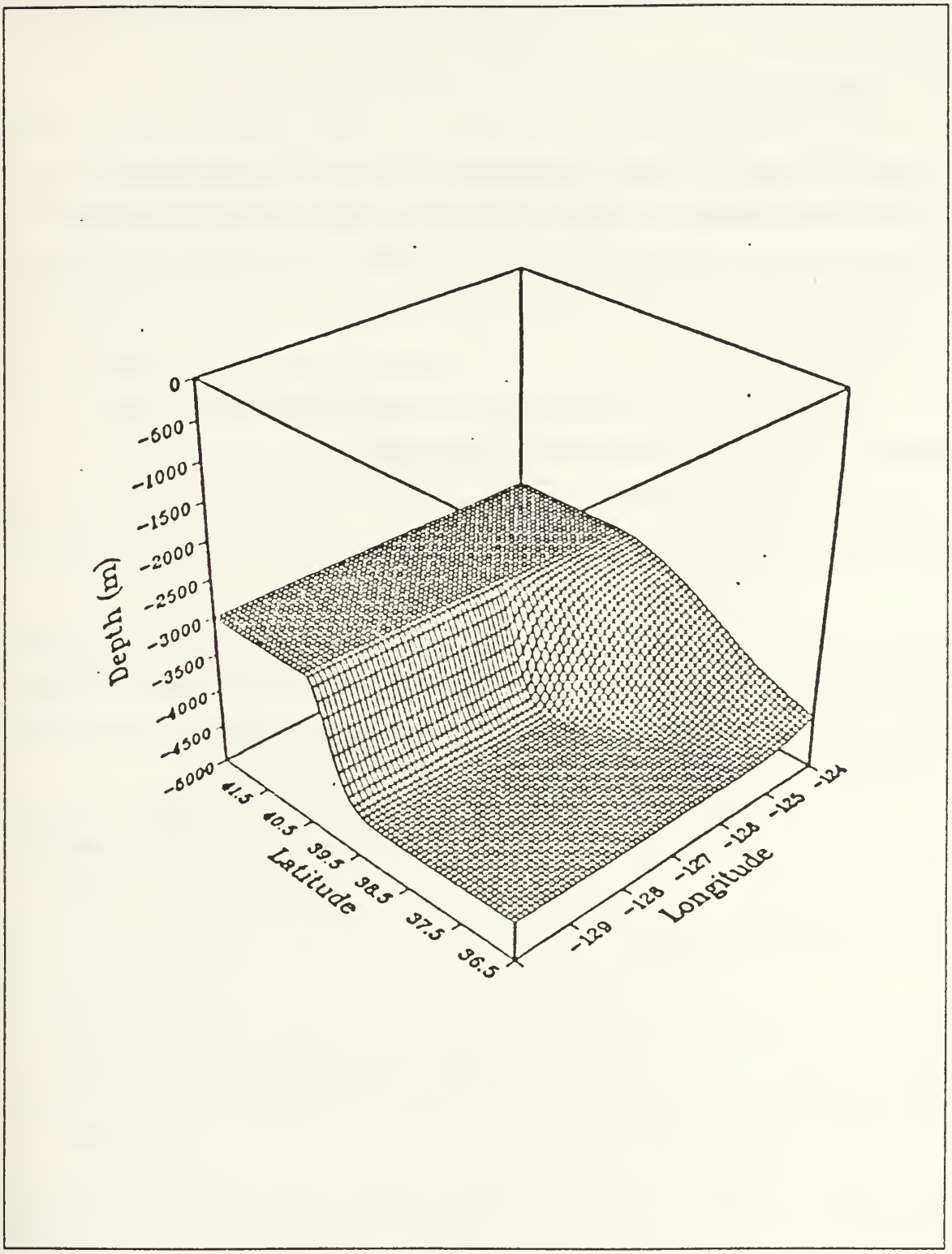

Figure 1.3 Bottom topography used in the PE model.

model incorporates 10 vertical levels and uses a sigma (non-dimensional depth) coordinate system.

E. OBJECTIVE ANALYSIS

Due to the limited number of observations, an efficient analysis technique must be employed to analyze the data field objectively. The technique used here is referred to as 'optimum interpolation'. Optimum interpolation was first applied in meteorology by Gandin (1963). It has been used successfully to analyze oceanic data by Bretherton *et al.* (1976), McWilliams (1976), Freeland and Gould (1976), White (1977) and White and Bernstein (1979).

1. Theory

Bretherton *et al.* (1976) describe the basic equations of the theory. First, consider a set of measured values of an oceanic variable

$$[\varphi_r,\ r = 1,...,N].$$

If φ_r represents the r^{th} observation of the field, then we can write

$$\varphi_r = \theta_r + \varepsilon_r$$

where θ_r is the true representative value of the field on the scale resolved by the grid and ε_r is the observational error, due to the effects of both instrumental and aliasing errors. In order to minimize the observational error due to aliasing, the grid spacing should be sufficiently fine to resolve all of the significant structure.

Next, we wish to find an estimate of θ_r, denoted by $[\theta_r]$, for model initialization. In some sense, this estimator should be the "best" that we can find. Therefore, restrict the estimator to be linear and estimate from neighboring measurements:

$$[\theta_r] = <\alpha_{rs}\varphi_s>,$$

where $<*>$ represents the summation from s = 1,...,k. If we further assume that $E(\varepsilon_r) = 0$ where $E(\varepsilon_r)$ is the normalized mean-square analysis error, then the generalized least squares estimates of α_r are those which minimize the quadratic form

$$([\theta_r] - \Phi\alpha_r)^T V^{-1}([\theta_r] - \Phi\alpha_r)$$

with respect to α_r and where $V = COV(\varepsilon_i,\varepsilon_j)$, that is, the covariance on the joint variability of ε_i and ε_j about their common mean which must be a non-negative definite form. The α_r are given by the solution to the linear equations

$$(\Phi^T V^{-1}\Phi)\alpha_r = \Phi^T V^{-1}[\theta_r].$$

The solutions are optimum in the sense that

- they are minimum mean square error estimates and
- they are maximum likelihood estimates if the errors are multivariate normal.

Let us further assume that

- the errors are uncorrelated and have the same variance such that $COV(\varepsilon_i,\varepsilon_j) = \delta_{ij}$ and $E(\varepsilon_i^2) = \sigma^2$. Therefore, $V = D(\sigma^2)$. That is, systematic errors are not allowed.
- $E(\theta_r) = 0$; and
- $E(\theta_r\varepsilon_s) = 0$.

Now, the solution to α_r can be written as

$$\alpha_r = (\Phi^T\Phi)^{-1}\Phi^T[\theta_r] \text{ so that}$$

$$[\theta_r] = \alpha_r{}^T\varphi = [\theta_r]^T\Phi(\Phi^T\Phi)^{-1}\varphi..$$

Since the means are assumed to be zero, the matrix $\Phi^T\Phi$ is the covariance matrix. Therefore, our best estimate is obtained by

$$[\theta_r] = (C_{rp}<A_{ps}{}^{-1}\varphi_s>)$$

where

$<*>$ is the summation from $s = 1,...,k$,

$(*)$ is the summation from $p = 1,...,k$ and

$$A_{ps} = E(\varphi_p\varphi_s) = F(X_p - X_s) + \sigma^2\delta_{rs} = C_{ps} + \sigma^2\delta_{rs}.$$

The minimum residual variance is

$$C_{xx}(1 - [\rho_{ix}\alpha_{xi}])$$

where $[*]$ is the summation from $i = 1,...,k$ so that the mean square interpolation error cannot exceed the variance of the function being interpolated.

2. **Research Use**

The dominant influences on an estimate at an interpolation point are the nearby data points. Thus, there is no advantage to using distant points. By introducing an influential radius in space and time we can restrict the observations used at an interpolation point (Carter and Robinson, 1981). If numerous observations exist within the influential radius, only those observations which have the highest correlations are kept to estimate the measurement at the interpolation position. Further, this number may be varied by a sorting technique.

An isotropic correlation function was estimated and applied to determine the best data points to be used for a particular interpolation point. It is of the form

$$C(r) = (1 - \alpha r^2)e^{-br^2}$$

where α is determined from the zero-crossing distance of the autocorrelation function, r is the distance from the interpolation point to a particular data point within the influential radius and b is the factor which determines the shape of the correlation function.

Due to the possibilities of spurious growth of short waves it is usually desirable to eliminate very high wavenumber components. This can be accomplished with the use of a filter. The type which was examined here was a Shapiro filter. A detailed description and explanation of this filter can be found in Shapiro (1971).

The Shapiro filter is a low-pass filter which is highly wavenumber selective. Depending upon the order of the filter, varying amounts of the higher wavelength components are removed. The response function of the filter, denoted by R, is given by

$$R = 1 - S(1 - \cos k\Delta x) = 1 - 2S\sin^2 \pi\Delta x/L,$$

where L is the wavelength, Δx the grid length and S a numerical filtering element. Note that when $R > 1$ the wave is amplified while $R < 1$ results in damping. For any order n the values of the smoothing elements S which are required are obtained from solutions of

$$(2S_p)^{n/2} = -1,$$

where p takes on all integer values (1,2,...,n) in sequence. The order n is equivalent to 2^j where j takes on all integer values in sequence (0,1,2,...). Thus, for $n = 2$ (a second order filter was applied here), S takes on the values of 1/2 and -1/2. For $L = 2\Delta x$, $R = 0$, hence two-grid length waves will be eliminated by the filter. Wavelengths greater than $2\Delta x$ but less than $14\Delta x$ will be damped by various amounts. Wavelengths greater than $14\Delta x$ will not be affected by the filter. This is shown in Figure 1.4, the response function of the second order Shapiro filter.

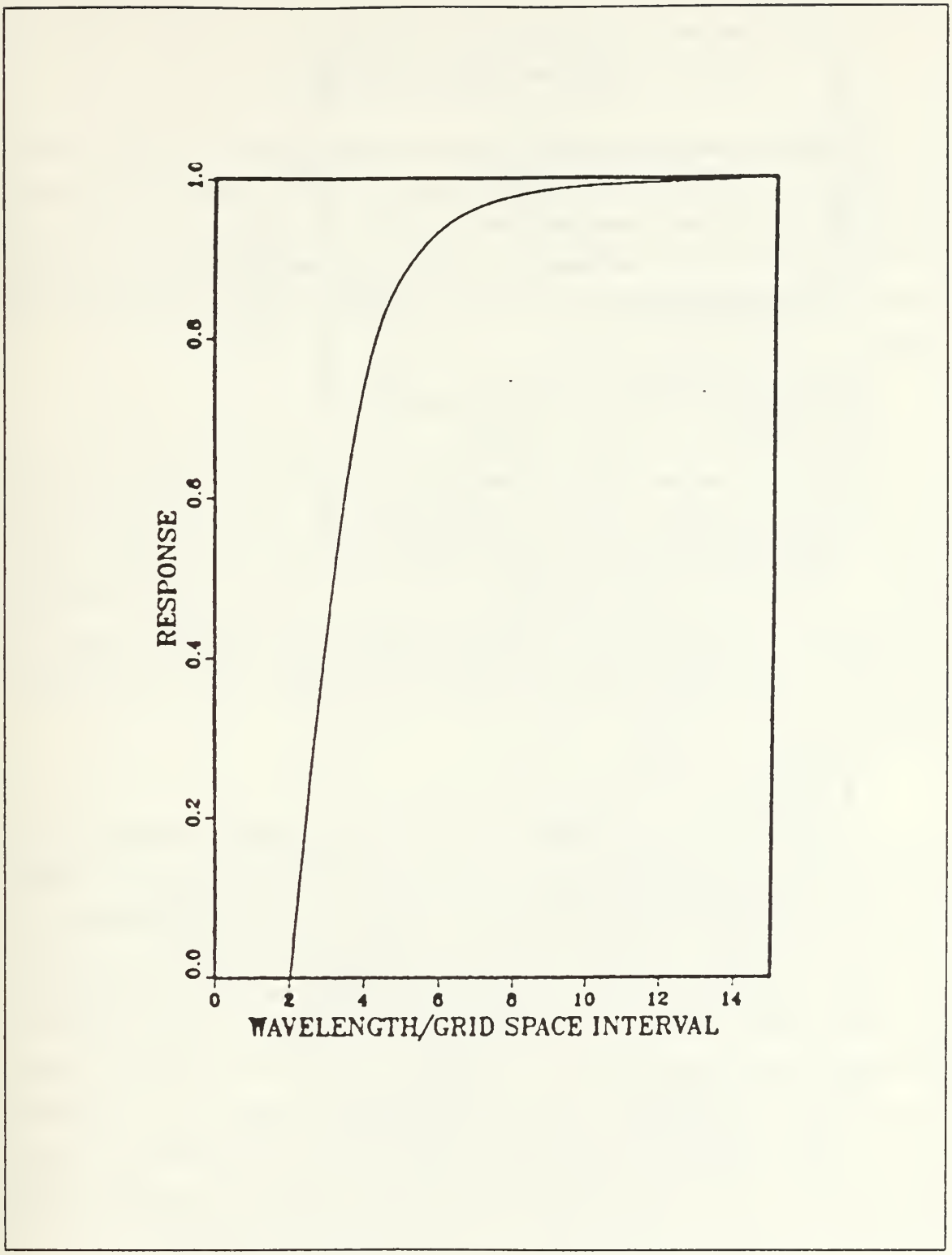

Figure 1.4 Response function of a second order Shapiro filter.

II. PE MODEL OUTPUT

The "perfect measured" fields of temperature and pressure were created from a PE numerical ocean model. Uniform grid spacing in the horizontal plane of 9 km in both the north-south and east-west directions (rather than 10 km in the north-south and 8 km in the east-west directions) was used to prevent possible feature resolution biases. The investigated area of coverage was comprised of a 31 x 31 horizontal grid domain.

A. TEMPERATURE AND PRESSURE FIELDS

The temperature field was interpolated from the model sigma levels to the particular depth of interest with the requirement that the depths chosen fall between the same two sigma levels at all points within the domain. This same requirement was used in computing the pressure field which was calculated relative to 2400 m depth. Days 38 through 42 of the model output run were examined. This 5-day period corresponded to the time frame in which the shipboard hydrographic cruises were conducted. Day 40 was chosen as the central interpolation time for the objective analysis.

1. Day 38

a. Surface

The coolest temperatures (15.5°C) in the sea surface temperature field (SST), Figure 2.1a, are found adjacent to the shoreline indicating coastal upwelling. There is a well defined temperature front of 1 C range oriented north-south along the coast. In the southeast quadrant, where the temperature front meanders, there exists two cold-core eddies approximately 30 km in diameter separated by a warm-core eddy. The corresponding surface pressure field, Figure 2.1b, depicts a strong, broad and meandering current flowing southward parallel to the temperature front with cyclonic eddies present in the region of the cool temperature anomalies. Two anticyclonic eddies, 70 km in diameter, are located on the offshore side of the current. A circular, closed isotherm of 14.5°C in the west, central region correlates to an intense cyclonic eddy. The overall pressure range observed in this mapping is 40 dyn/cm^2.

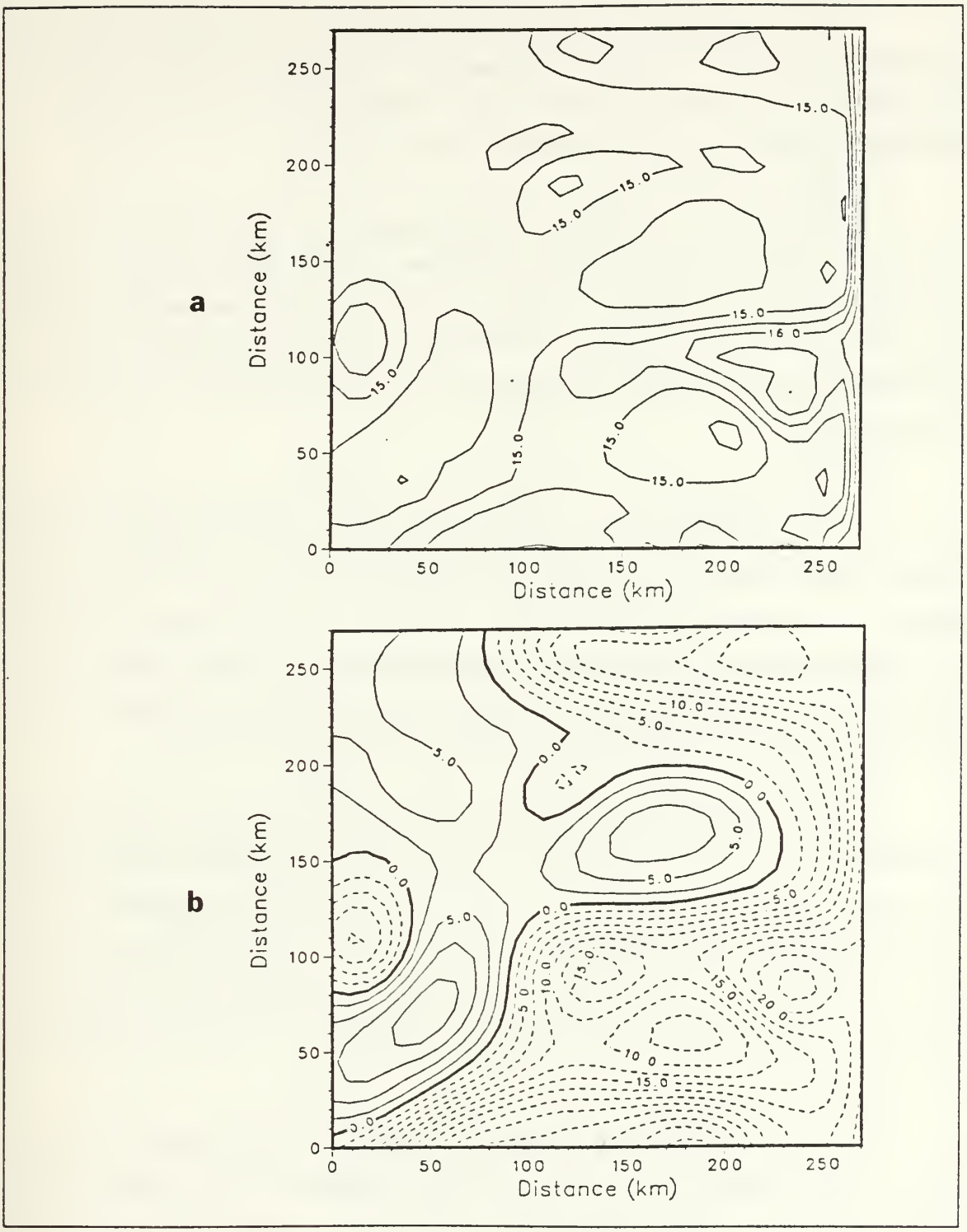

Figure 2.1 PE model SST(a) and pressure(b) fields on day 38, contour intervals of 0.5 C and 2.5 dyn/cm^2, respectively.

b. 25 m

The temperature field at 25 m, Figure 2.2a, shows no indication of a strong temperature gradient. Coastal upwelling remained evident as the coolest temperatures were observed near or adjacent to the shore. Compared with the surface pattern, no significant changes were seen in the pressure field (Fig. 2.2b).

c. 50 m

From the 50 m temperature map, Figure 2.3a, cool anomalies (less than 11°C) extend offshore in the northern and southern portions of the domain. A strong temperature front of 2 C range exists along the coastline. In the pressure field, Figure 2.3b, cyclonic eddies were present in the region of the cool anomalies. Again, two anticyclonic, warm-core eddies with diameters of 70 km dominated the central and offshore areas.

d. 100 m

The temperature field at 100 m, Figure 2.4a, exhibited the same basic pattern as was observed at 50 m. The cool anomaly in the northeast quadrant is now closed. A warm intrusion in the north and southwest portions and a large warm anomaly in the central part of the domain are clearly evident. Located between the two warm intrusions is a well defined cold-core eddy approximately 40 km in diameter. The pressure map, Figure 2.4b, supports the warm and cool temperature anomalies. Both the warm and cold-core eddies continue unchanged in position and intensity.

e. 200 m

From the 200 m temperature map, Figure 2.5a, a dramatic change in the temperature front is evident. What was a well defined, tight gradient feature in the upper layers, appears as a broad, less packed feature. The cool filament in the southeast quadrant is less pronounced. A near pinching off of an 8.5°C warm pool of water is evident in the central portion of the domain. The pressure field, Figure 2.5b, displays the corresponding anticyclonic eddy in association with the new temperature pattern.

f. 350 m

The dominant features in the 350 m temperature map, Figure 2.6a, is the absence of the temperature front and the more pronounced cool filament in the southeast quadrant. Cold upwelling alongshore lingers. Figure 2.6b shows the enhancement of the warm-core eddy in the central domain and a change in the directional flow pattern to an onshore (offshore) regime in the north (south) regions.

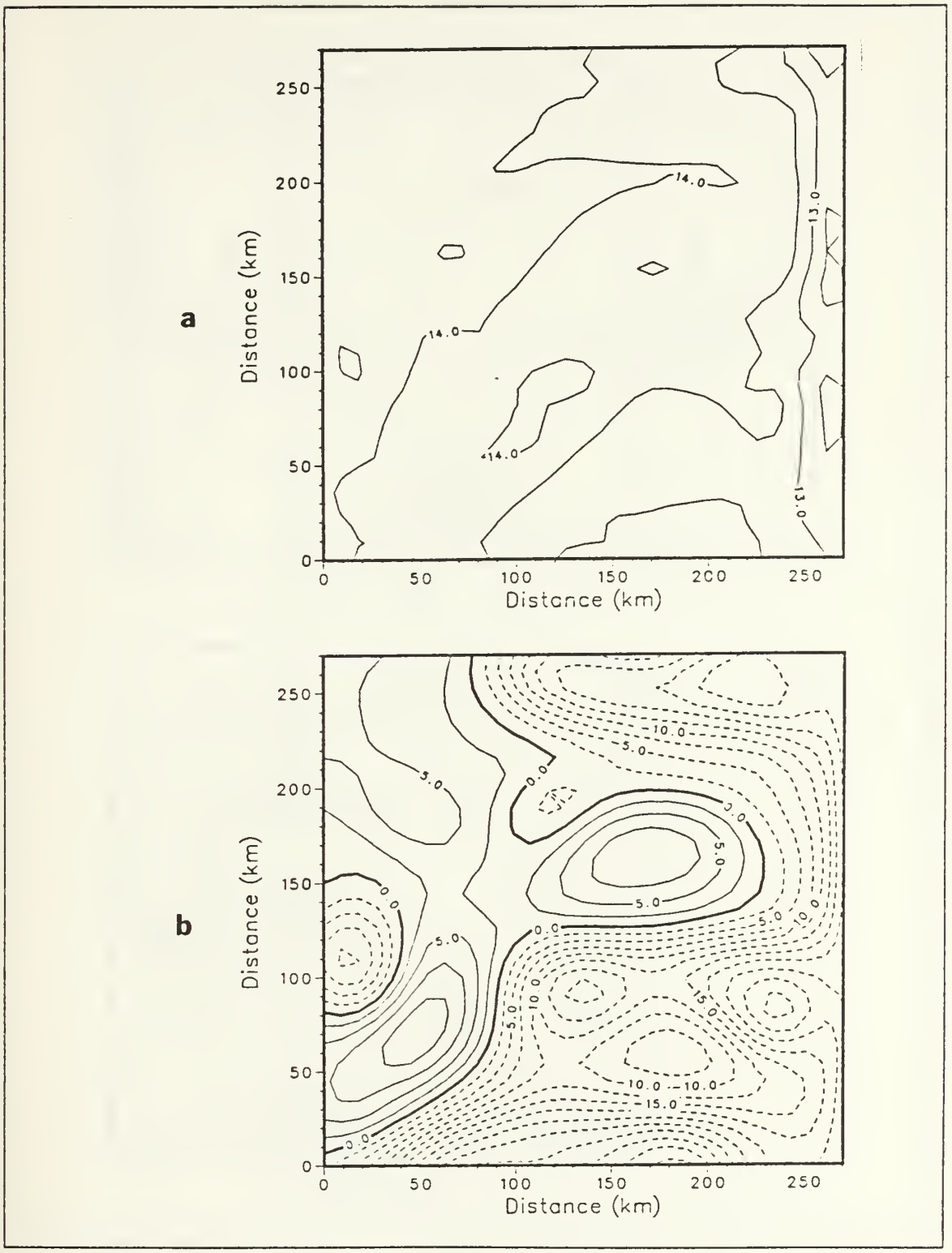

Figure 2.2 Same as Fig. 2.1 but at 25 m.

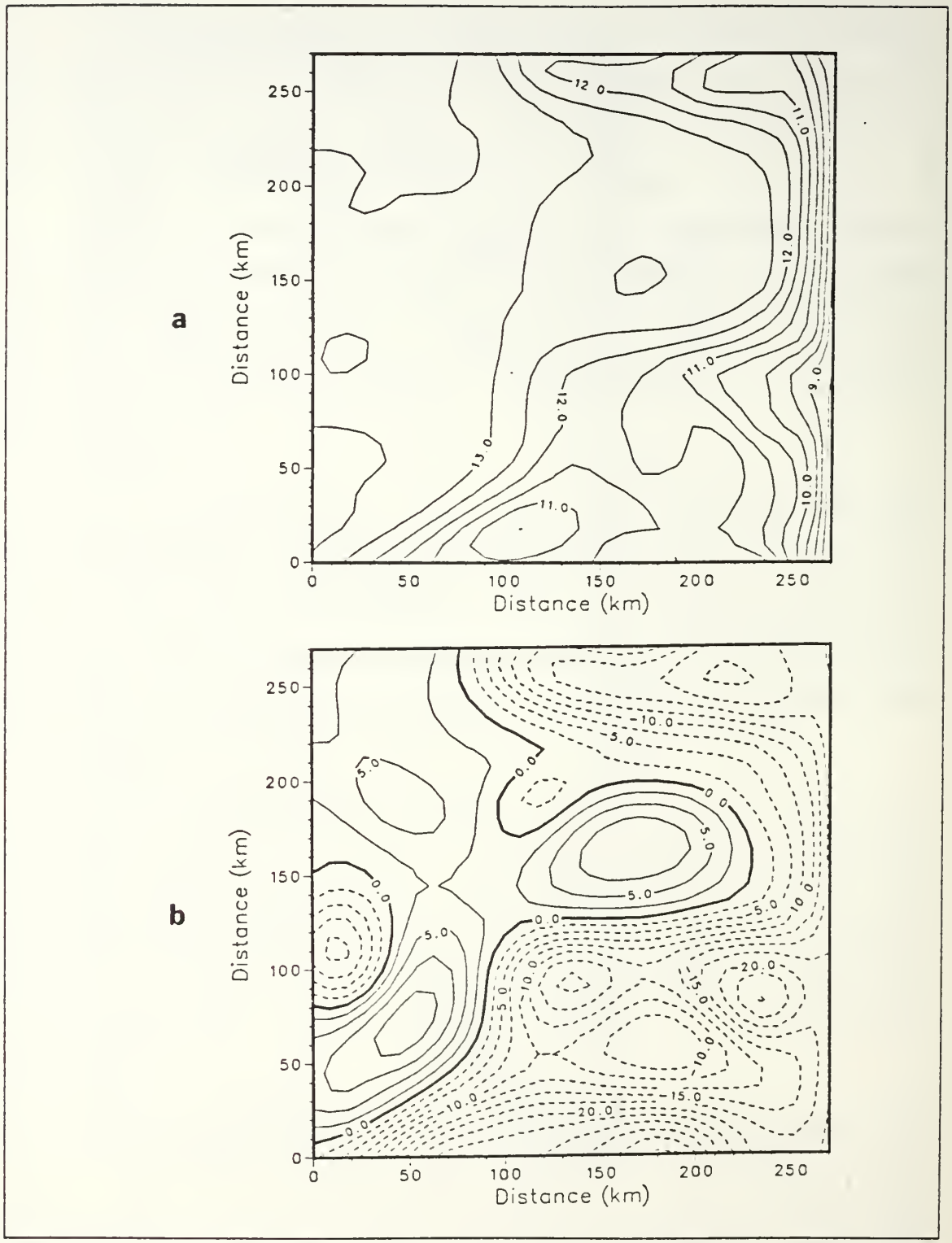

Figure 2.3 Same as Fig. 2.1 but at 50 m.

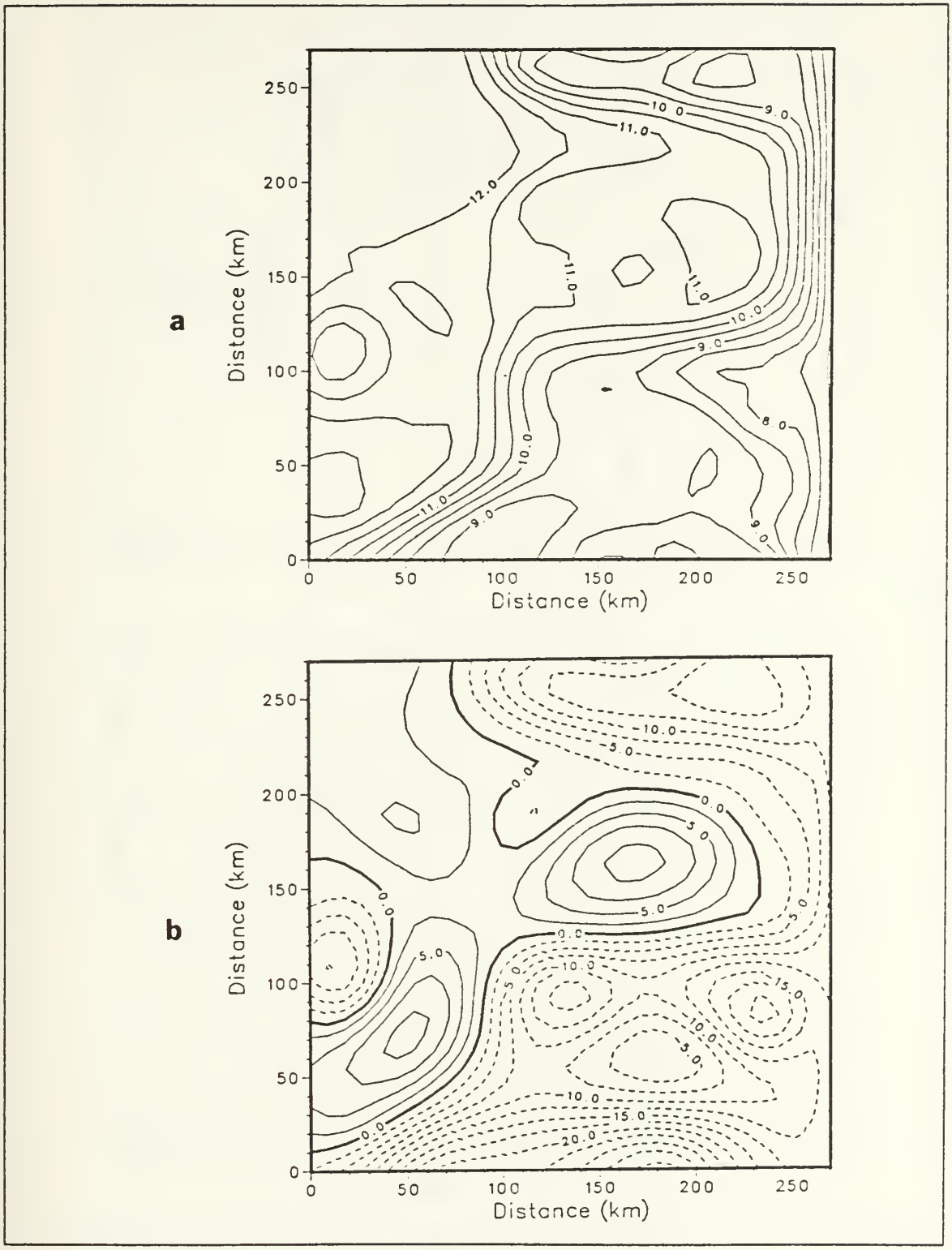

Figure 2.4 Same as Fig. 2.1 but at 100 m.

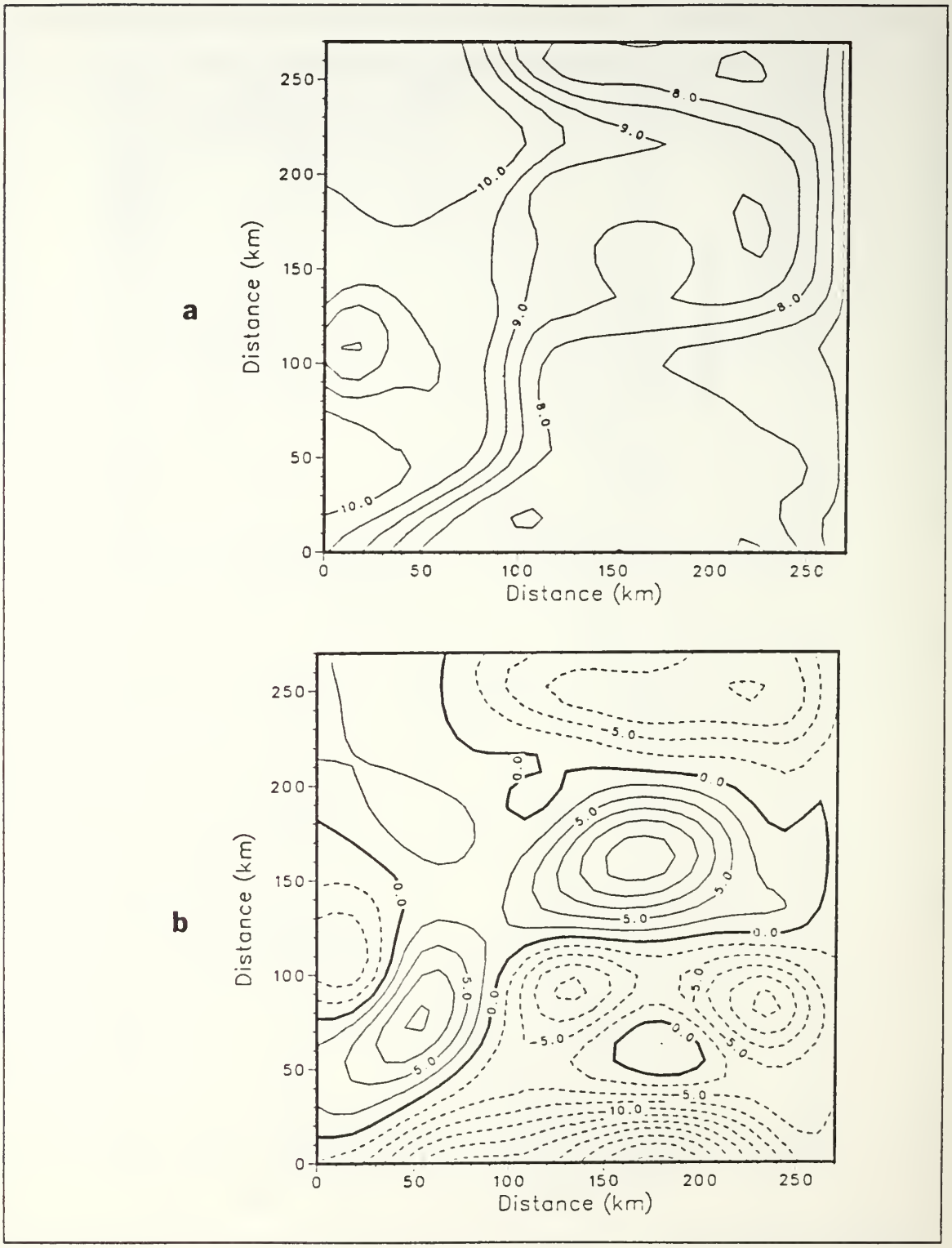

Figure 2.5 Same as Fig. 2.1 but at 200 m.

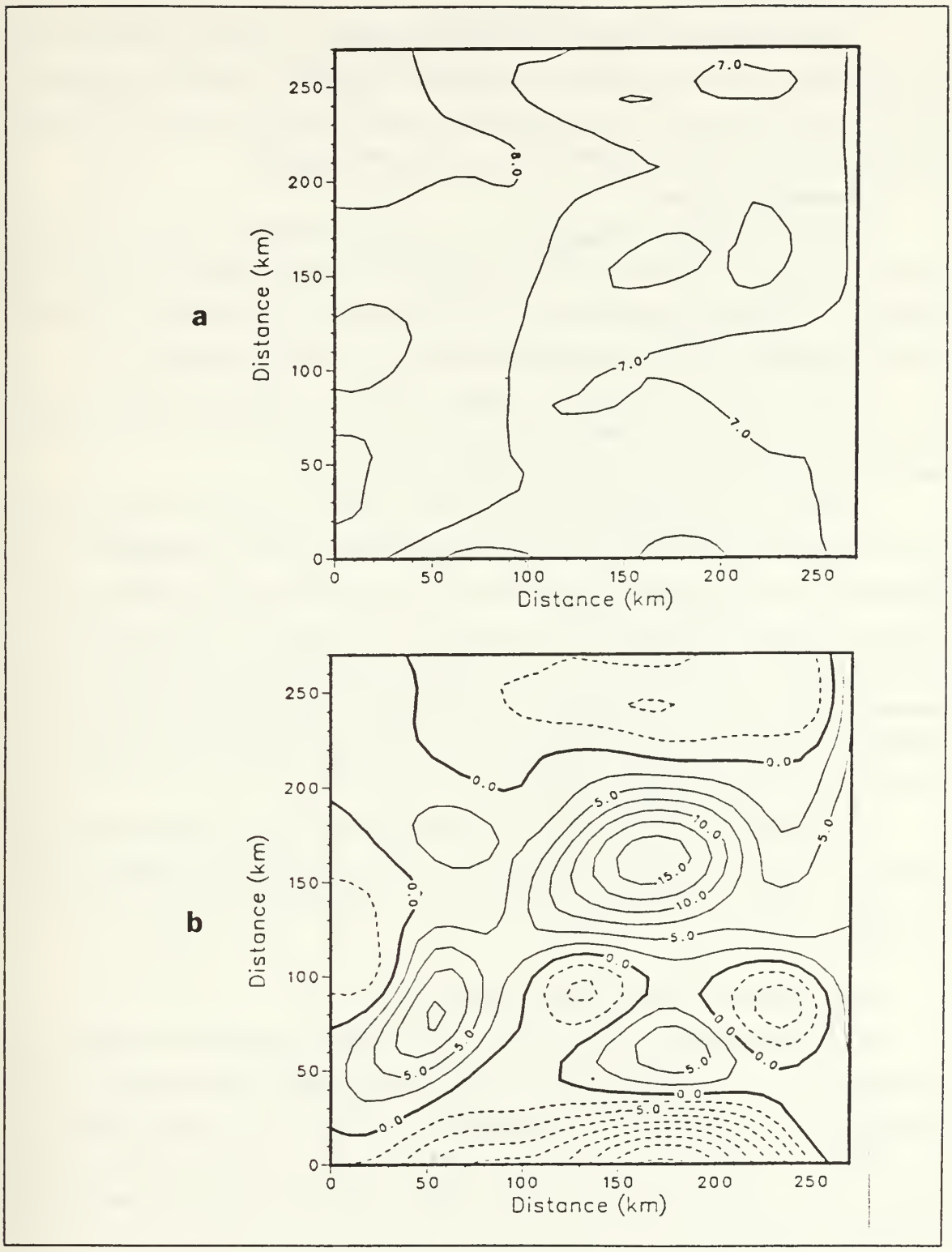

Figure 2.6 Same as Fig. 2.1 but at 350 m.

g. Below 500 m

The temperature fields at depth tend toward isothermal conditions with cool and warm water cells located in conjunction with their associated eddies (Figs. 2.7-2.9). With the exception of the persistence of the anticyclonic eddy in the central domain, no evidence of eddy activity survives below 900 m depth.

2. **Temporal Variation**

The same sequence of temperature and pressure fields for days 40 and 42 are shown in Figures 2.10 through 2.27. An analysis of the temporal variation was conducted for the entire period, i.e., days 38 through 42, to evaluate the degree of synopticity required of shipboard hydrographic data for field representation.

At each respective depth the pattern exhibited is highly correlated to past days. The meandering, southward flowing current and temperature front remained nearly stationary throughout the 5-day period as expected.

Eddies on both the eastern and western side of the current usually moved west, southwest, particularly those in the southern region which propagated in the same direction as the mean flow. This movement was characterized by a mean speed of 5 km/day, although variations about this did exist. For example, the large anticyclonic eddy which dominated the central portion of the domain throughout the water column remained stationary. The movement of the eddies is apparently controlled by a combination of advection by the large scale flows and the tendency for propagation to the west as a packet of Rossby modes.

The warm and cool temperature anomalies and pools of water tended to propagate at the same speed and direction as their associated eddies above 1500 m depth. Below 2000 m depth little variation in the temperature pattern and movement was evident.

B. OA INTERPOLATED TEMPERATURE FIELD

To evaluate the performance of the objective analysis technique, OA interpolated temperature maps were obtained for five typical depths from observations at each of the grid points, a total of 961. The interpolated values, which were neither filtered nor detrended (see Appendix A), were computed from the two closest and highest correlated values within a 25 km radius of influence which was based on temperature correlation calculations.

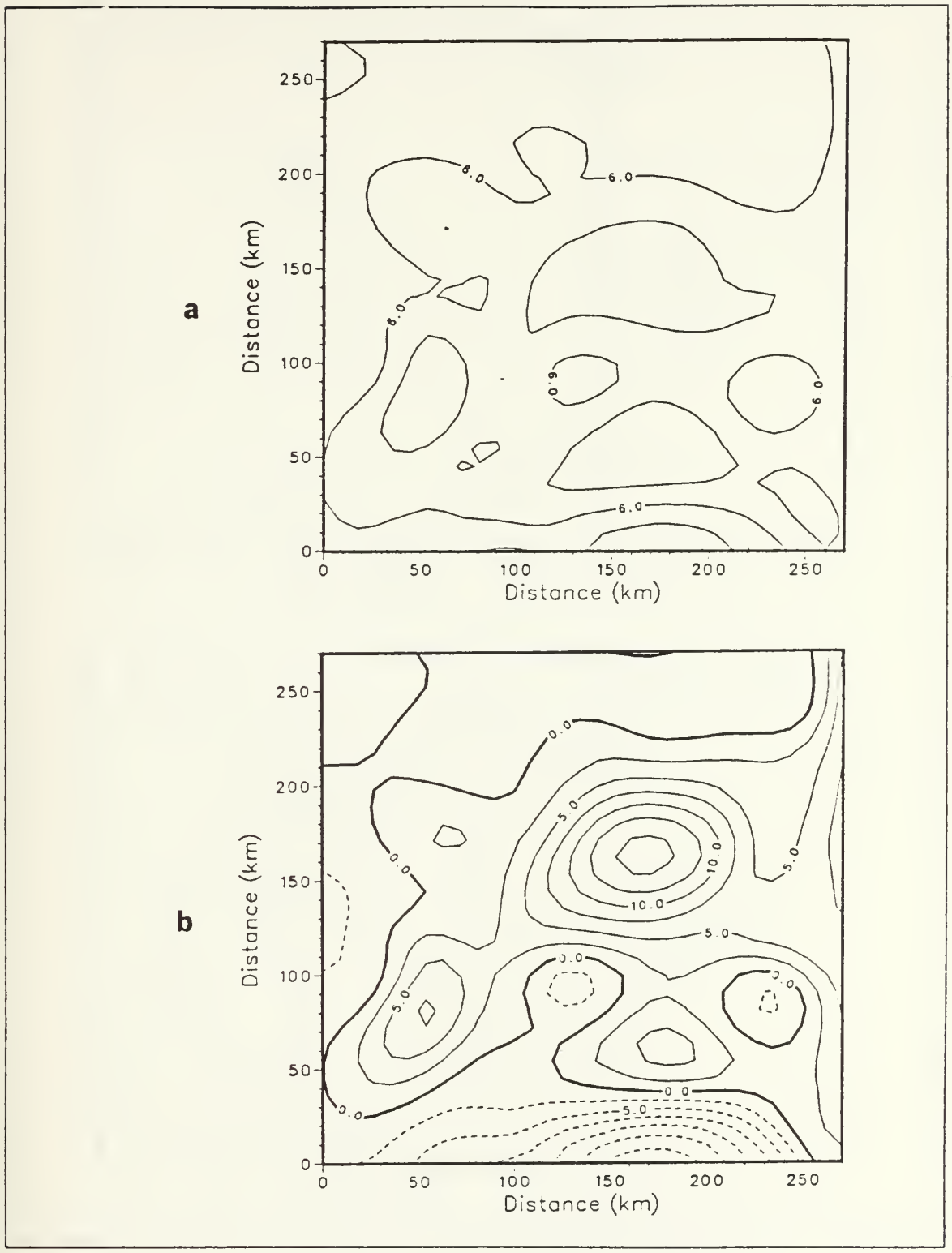

Figure 2.7 Same as Fig. 2.1 but at 550 m.

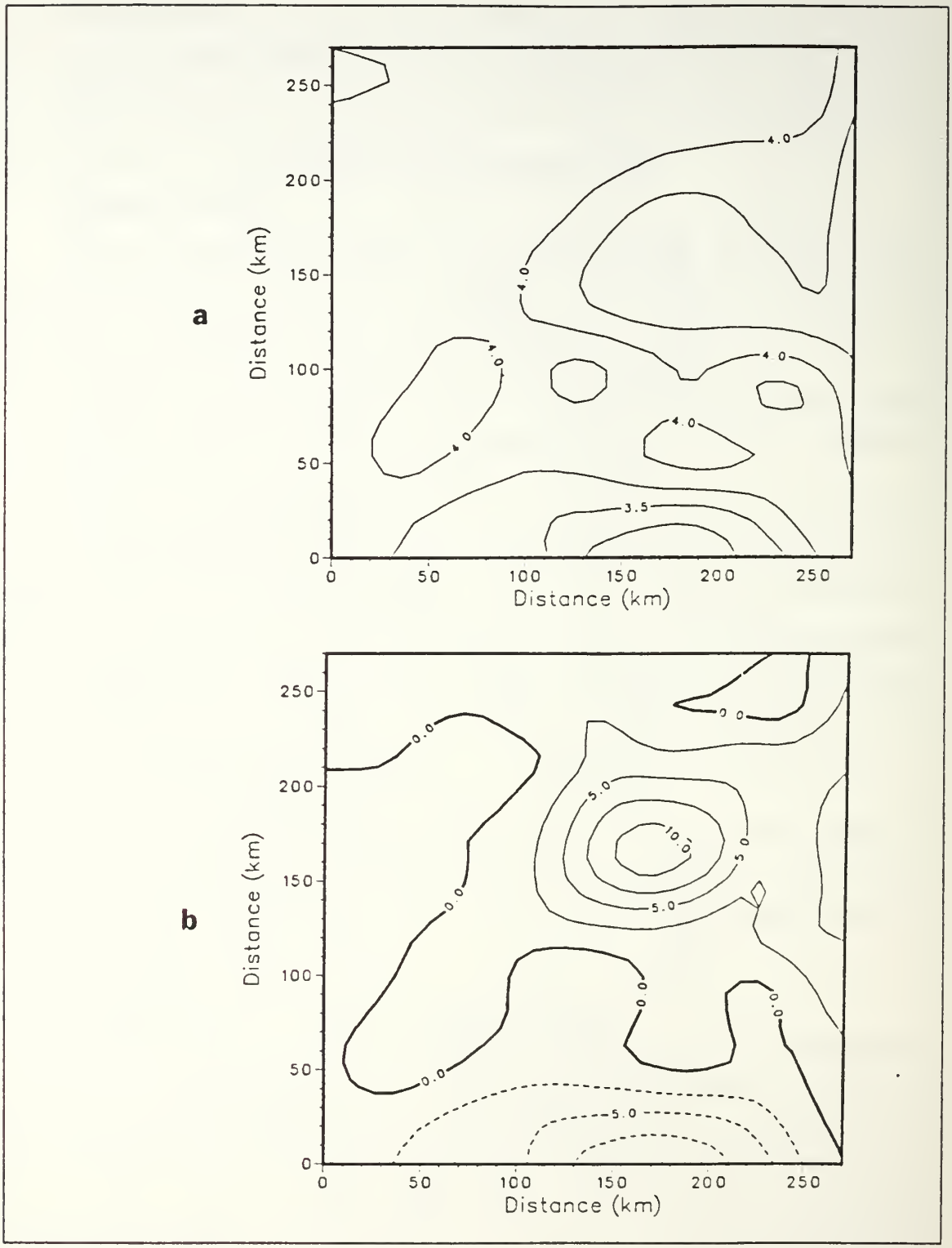

Figure 2.8 Same as Fig. 2.1 but at 900 m.

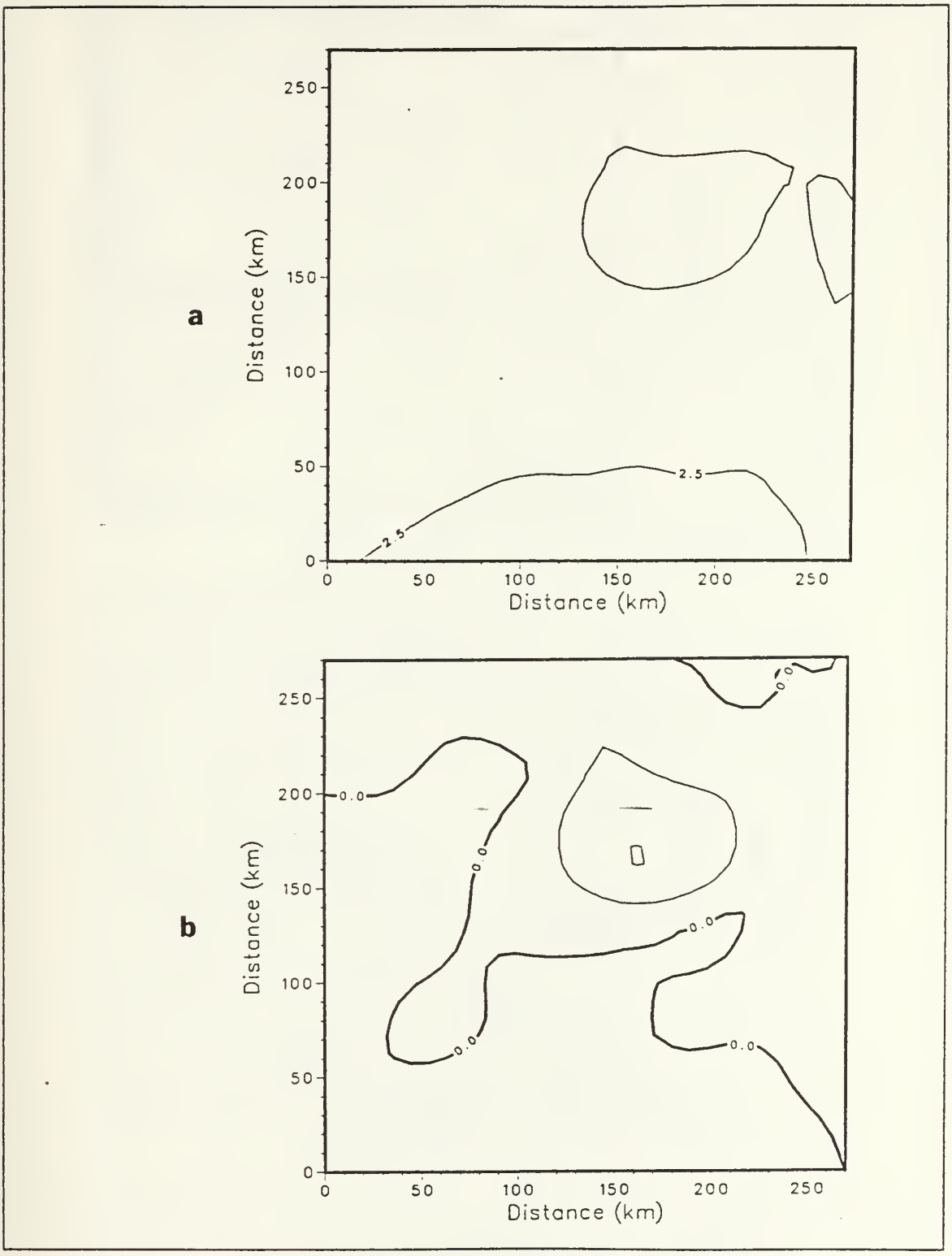

Figure 2.9 Same as Fig. 2.1 but at 1500 m.

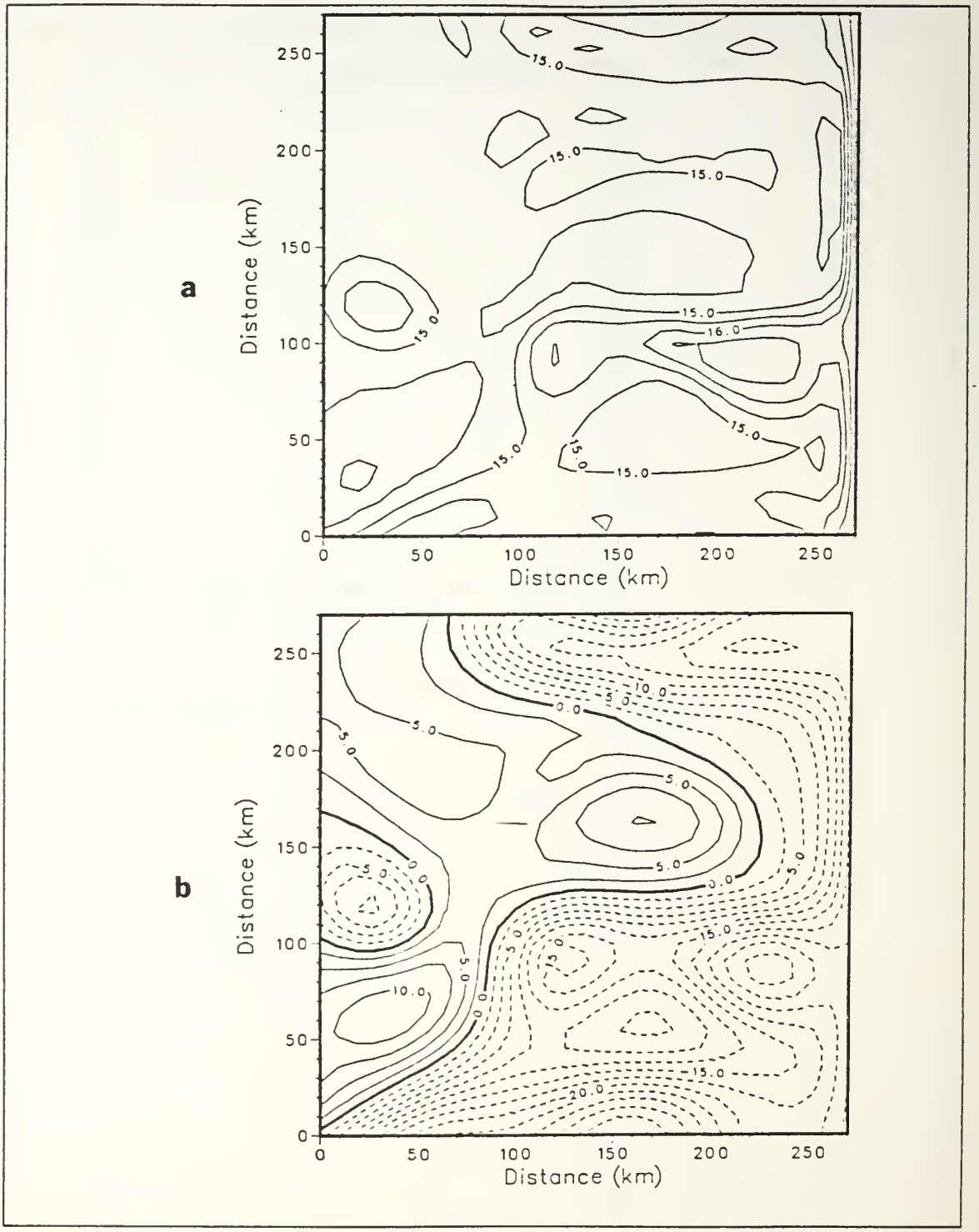

Figure 2.10 PE model SST(a) and pressure(b) fields on day 40, contour intervals of 0.5 C and 2.5 dyn/cm^2, respectively.

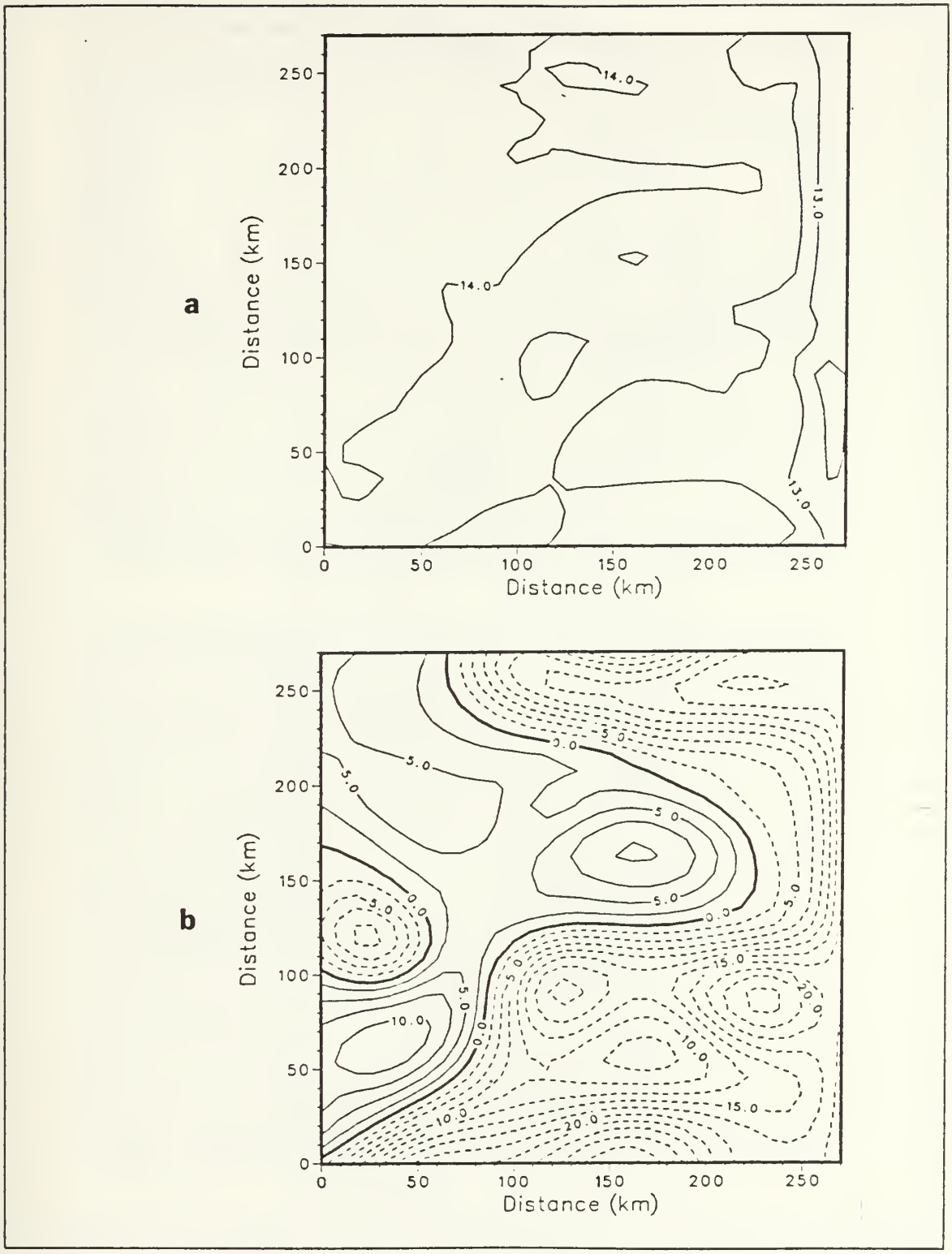

Figure 2.11 Same as Fig. 2.10 but at 25 m.

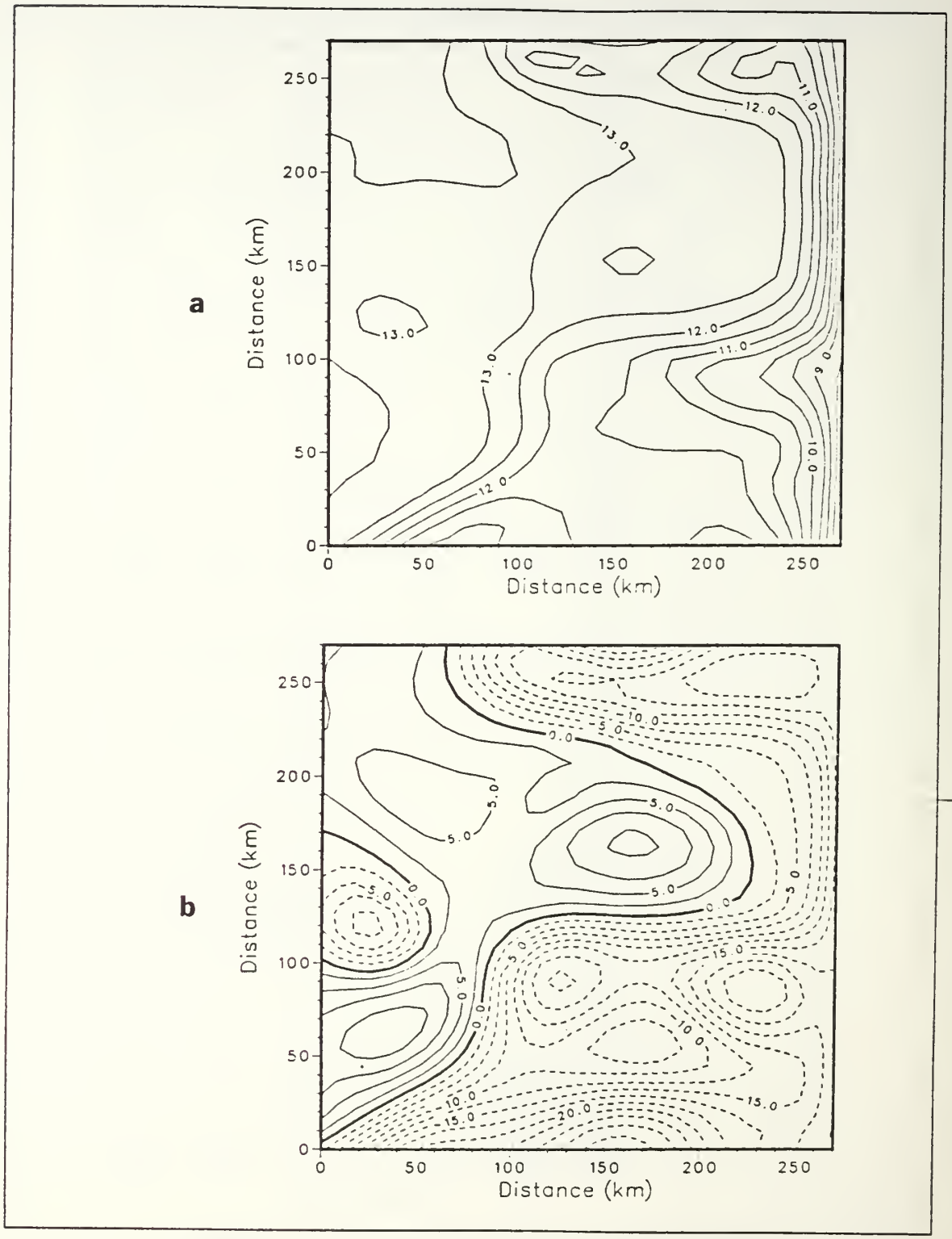

Figure 2.12 Same as Fig. 2.10 but at 50 m.

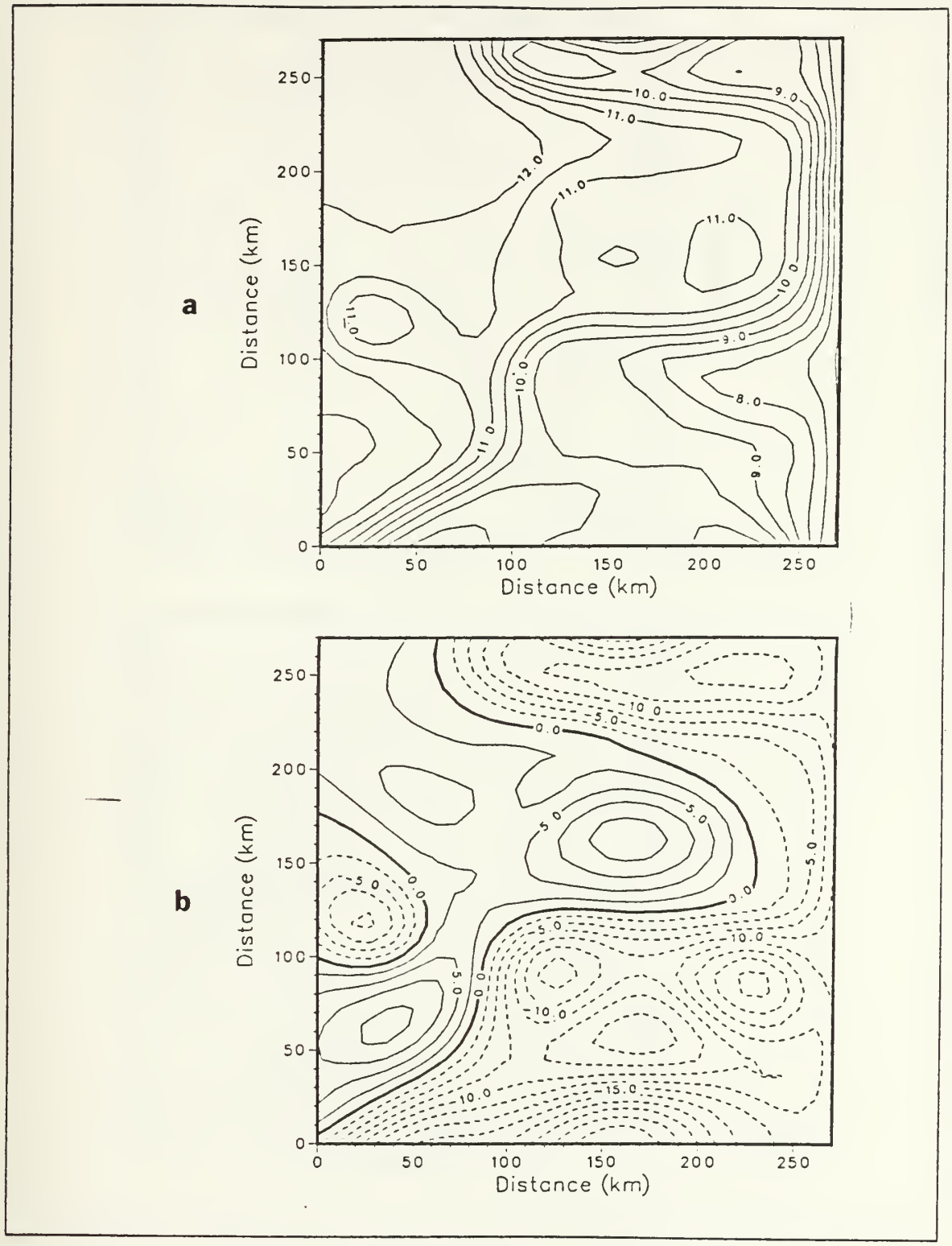

Figure 2.13 Same as Fig. 2.10 but at 100 m.

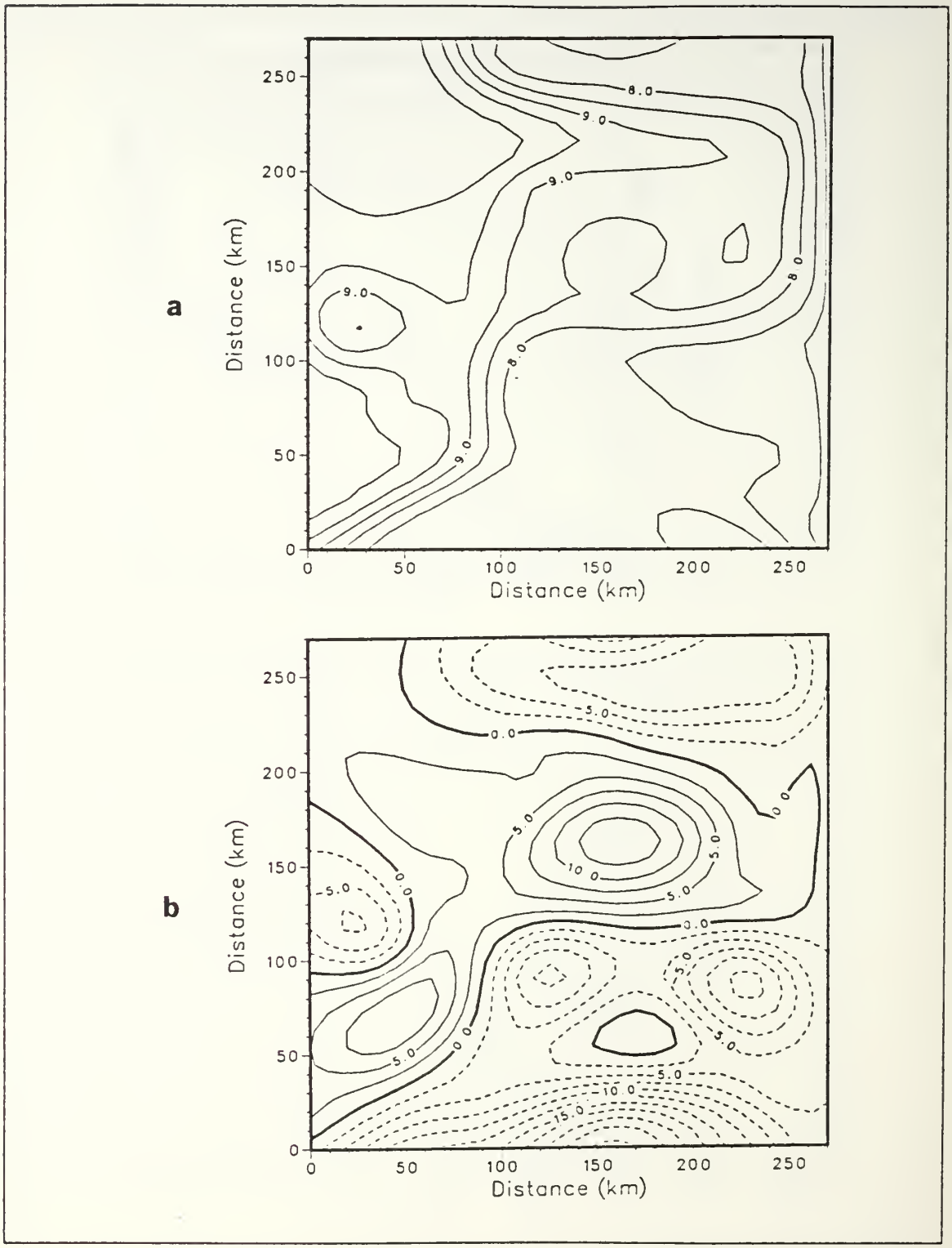

Figure 2.14 Same as Fig. 2.10 but at 200 m.

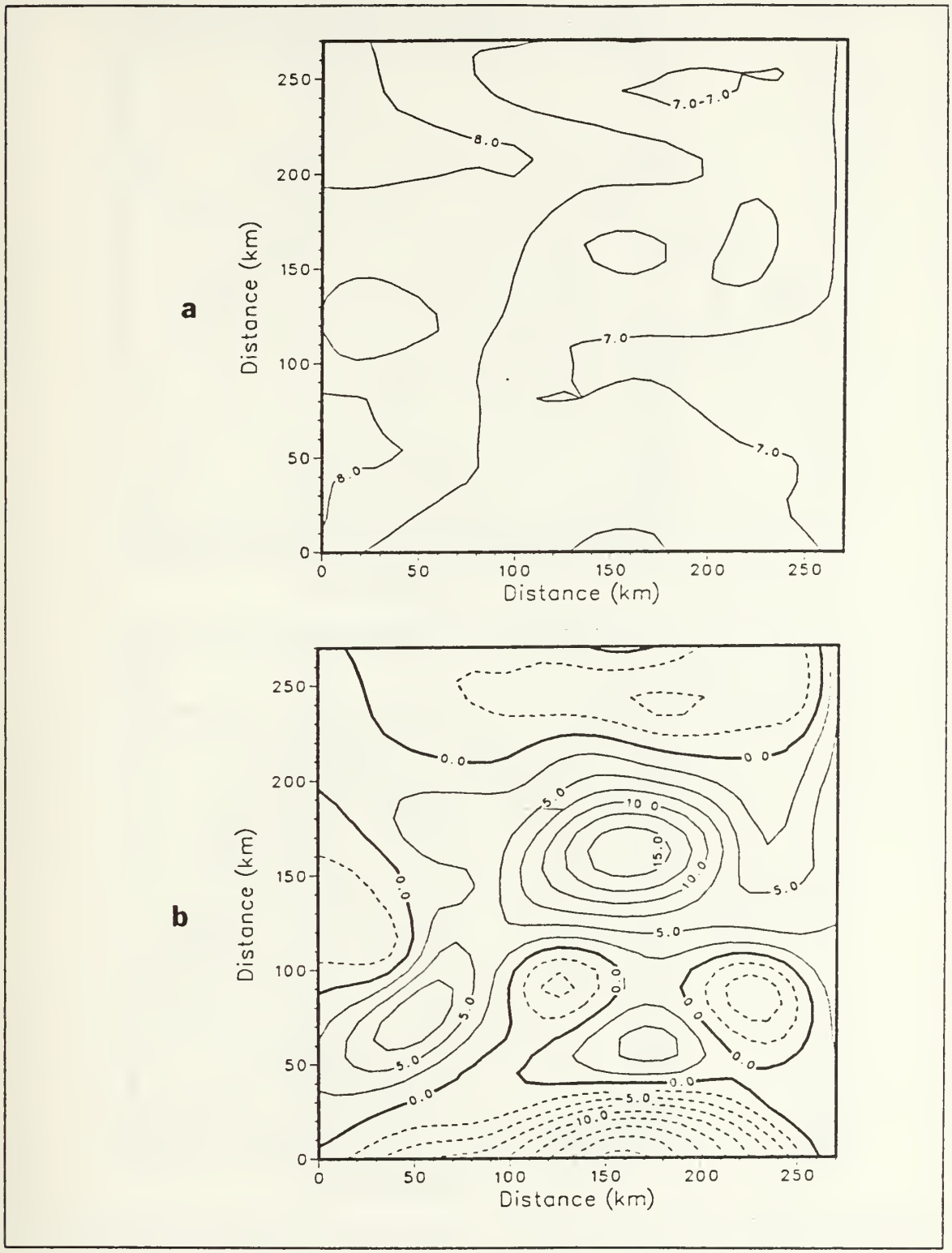

Figure 2.15 Same as Fig. 2.10 but at 350 m.

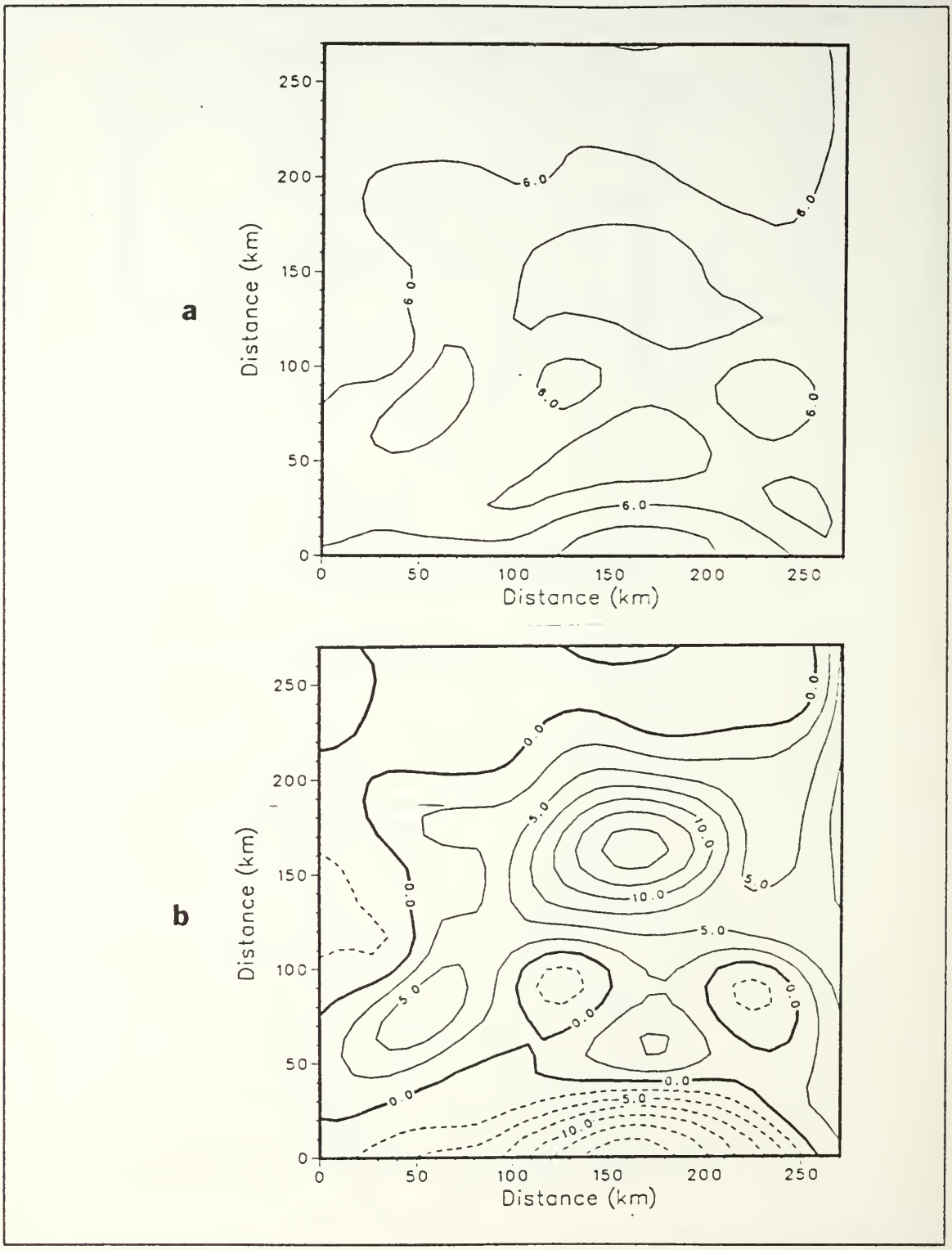

Figure 2.16 Same as Fig. 2.10 but at 550 m.

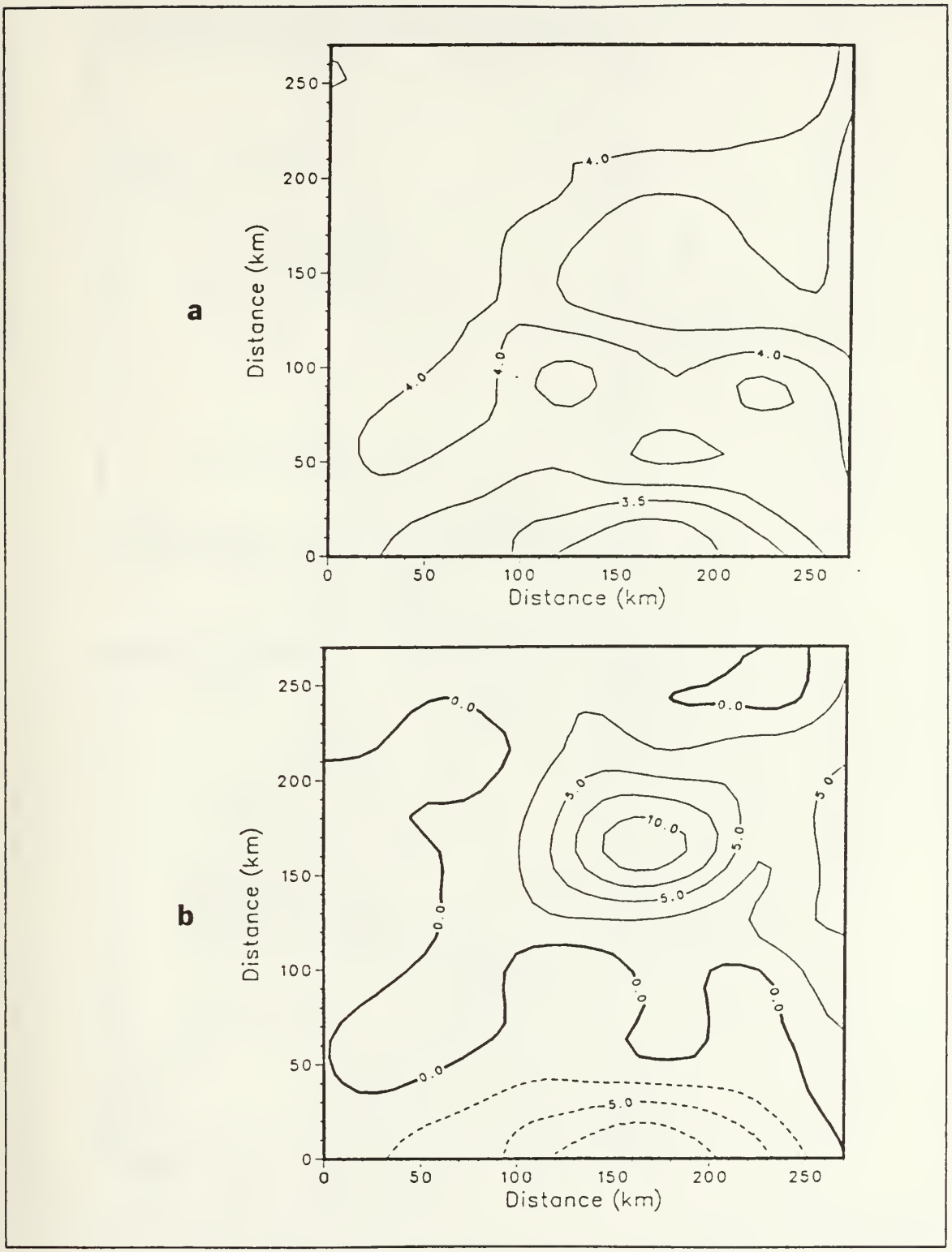

Figure 2.17 Same as Fig. 2.10 but at 900 m.

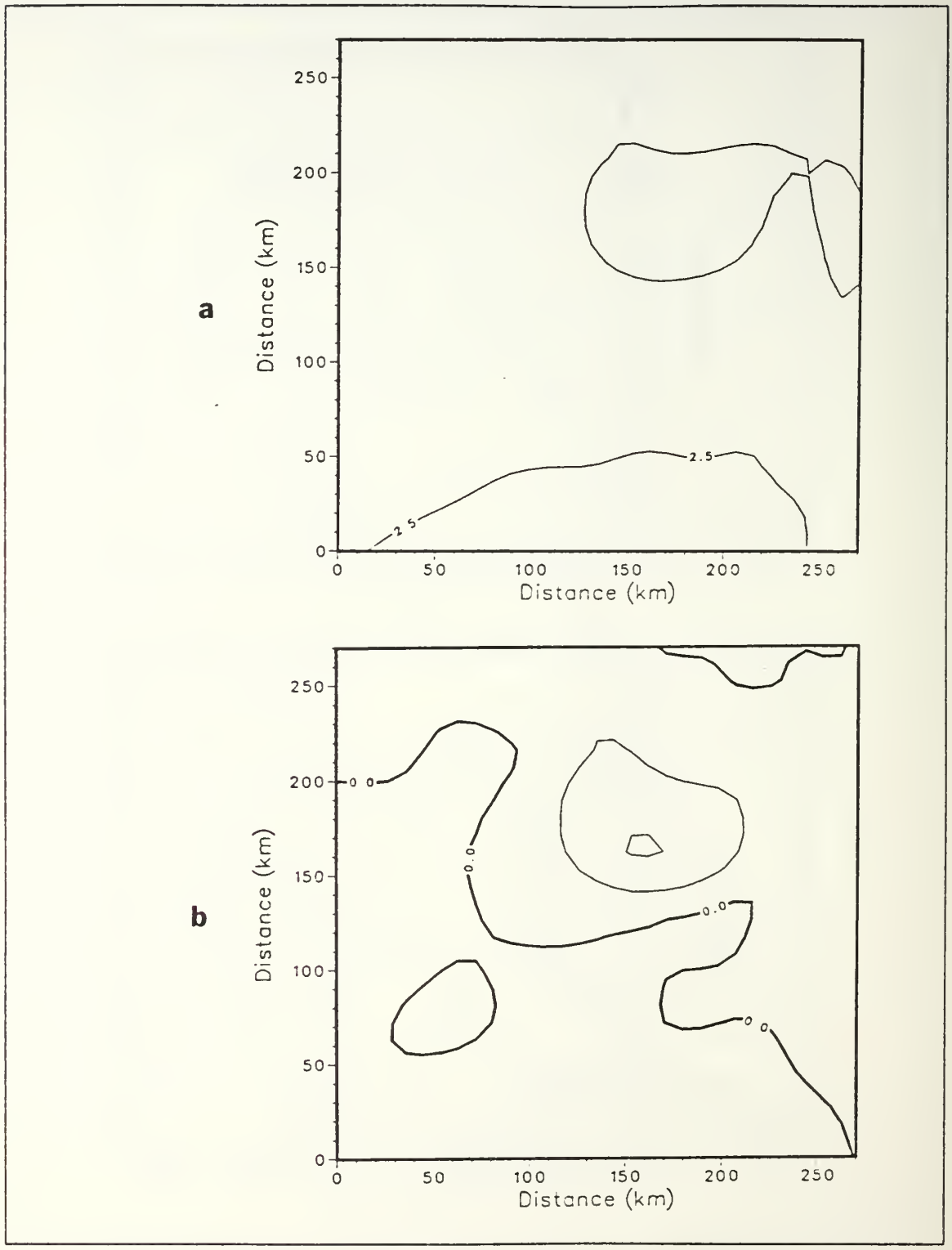

Figure 2.18 Same as Fig. 2.10 but at 1500 m.

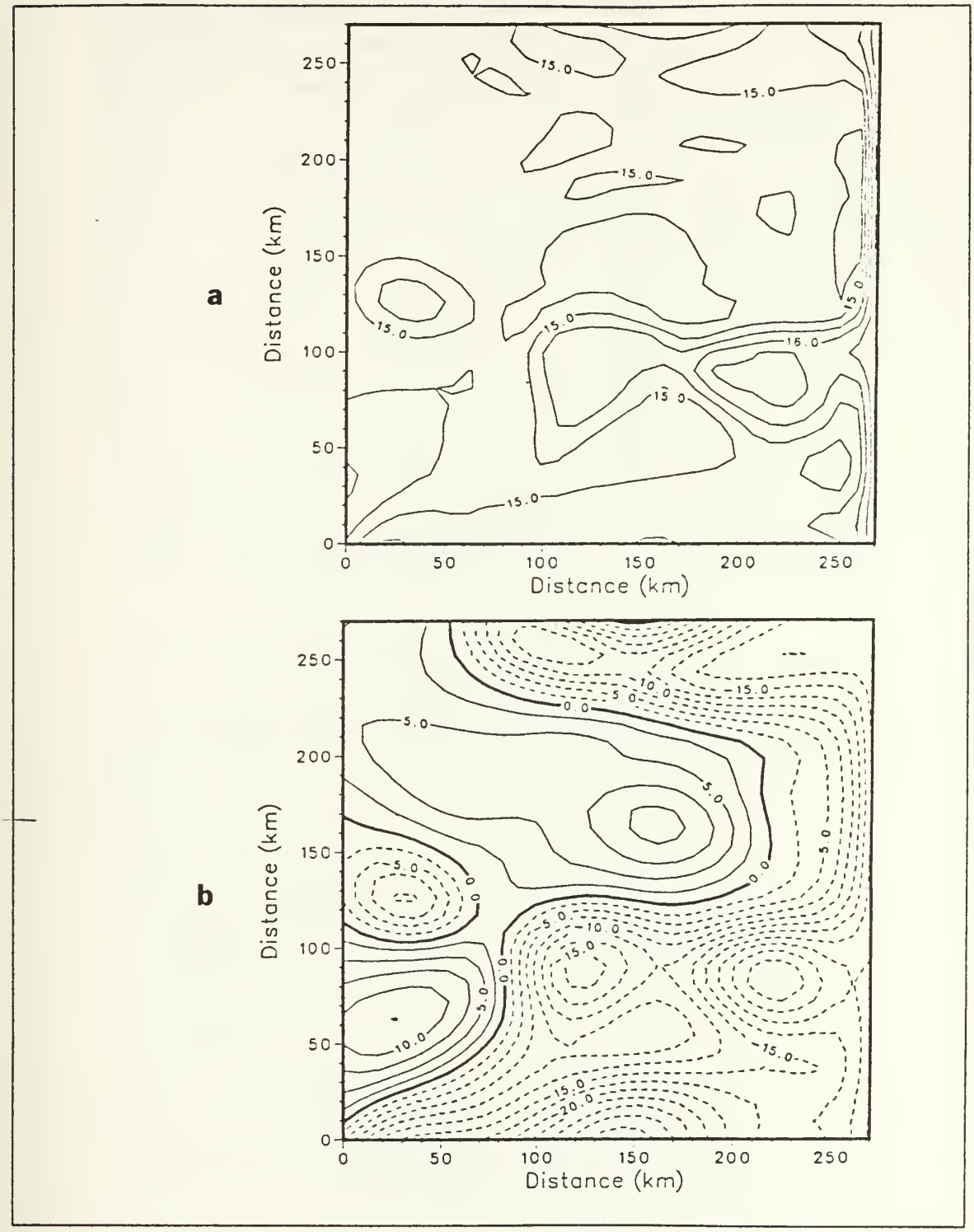

Figure 2.19 PE model SST(a) and pressure(b) fields on day 42, contour intervals of 0.5 C and 2.5 dyn/cm^2, respectively.

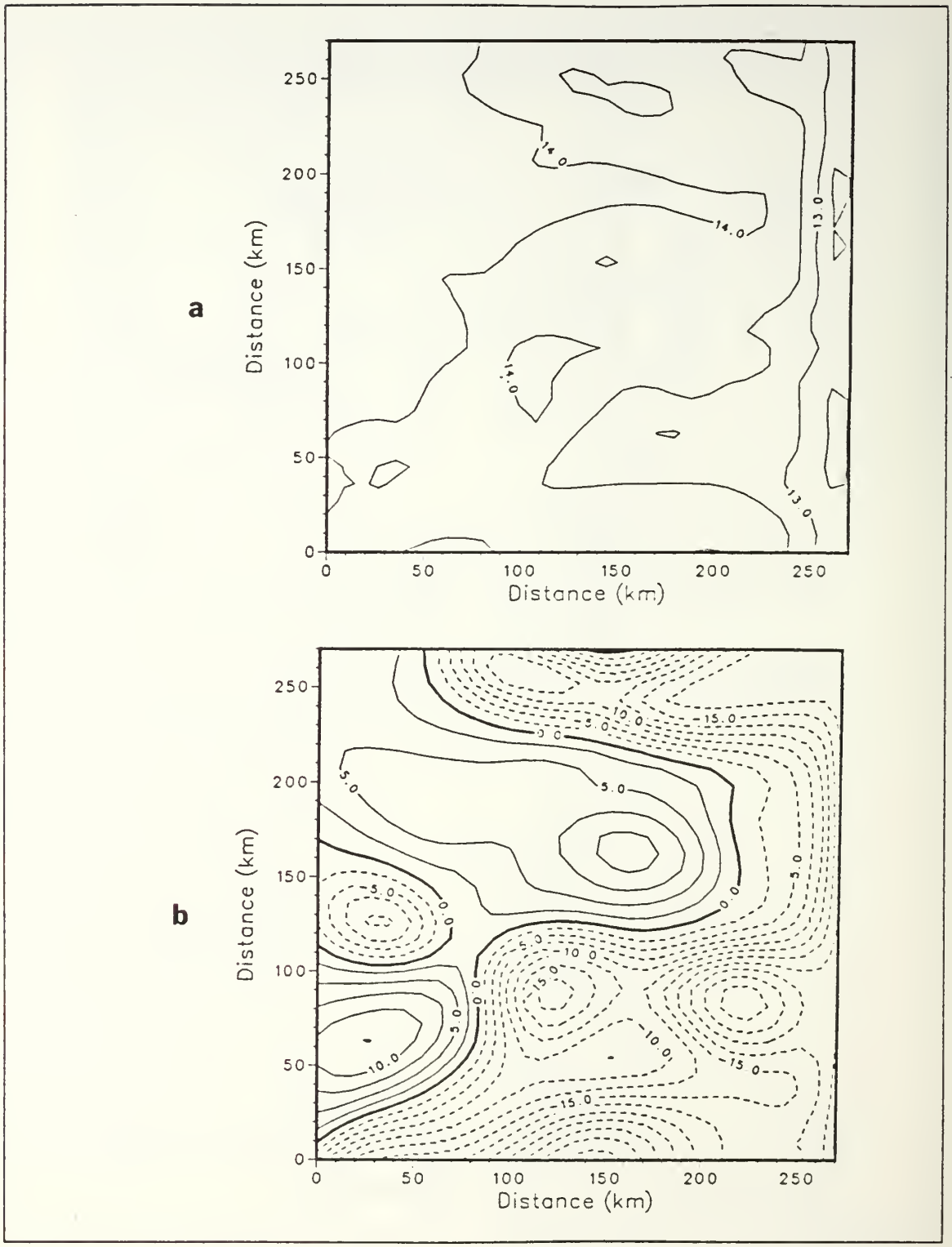

Figure 2.20 Same as Fig. 2.19 but at 25 m.

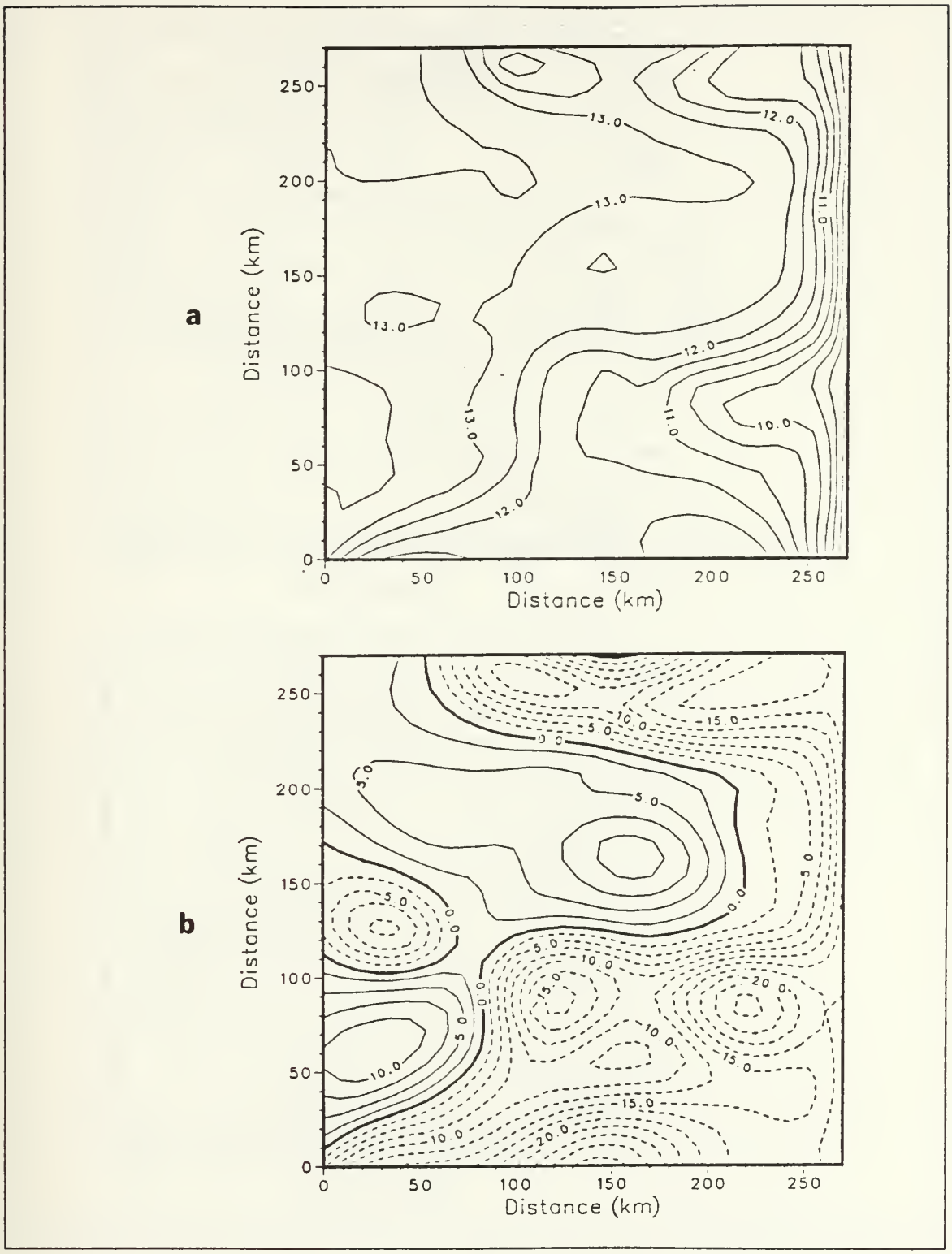

Figure 2.21 Same as Fig. 2.19 but at 50 m.

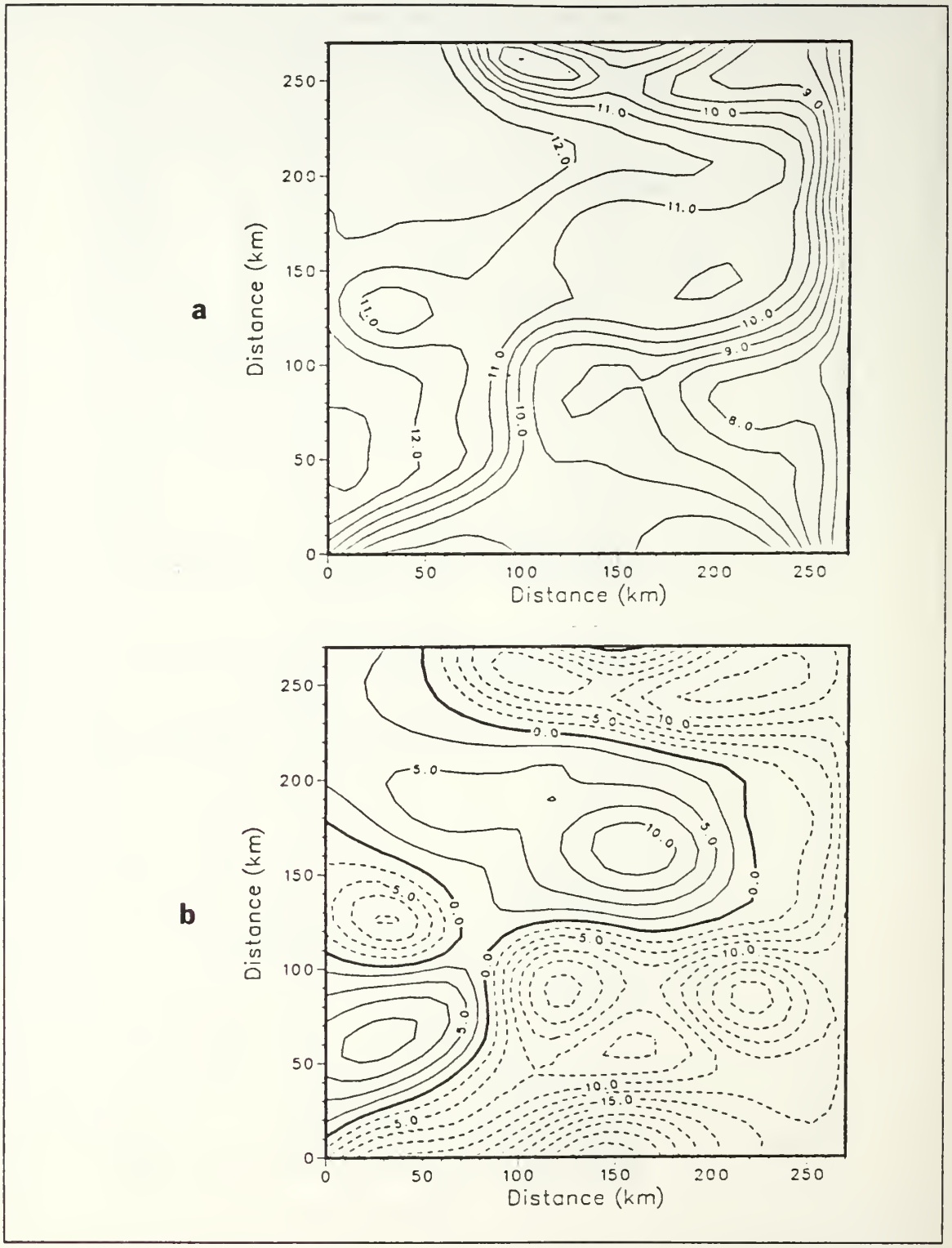

Figure 2.22 Same as Fig. 2.19 but at 100 m.

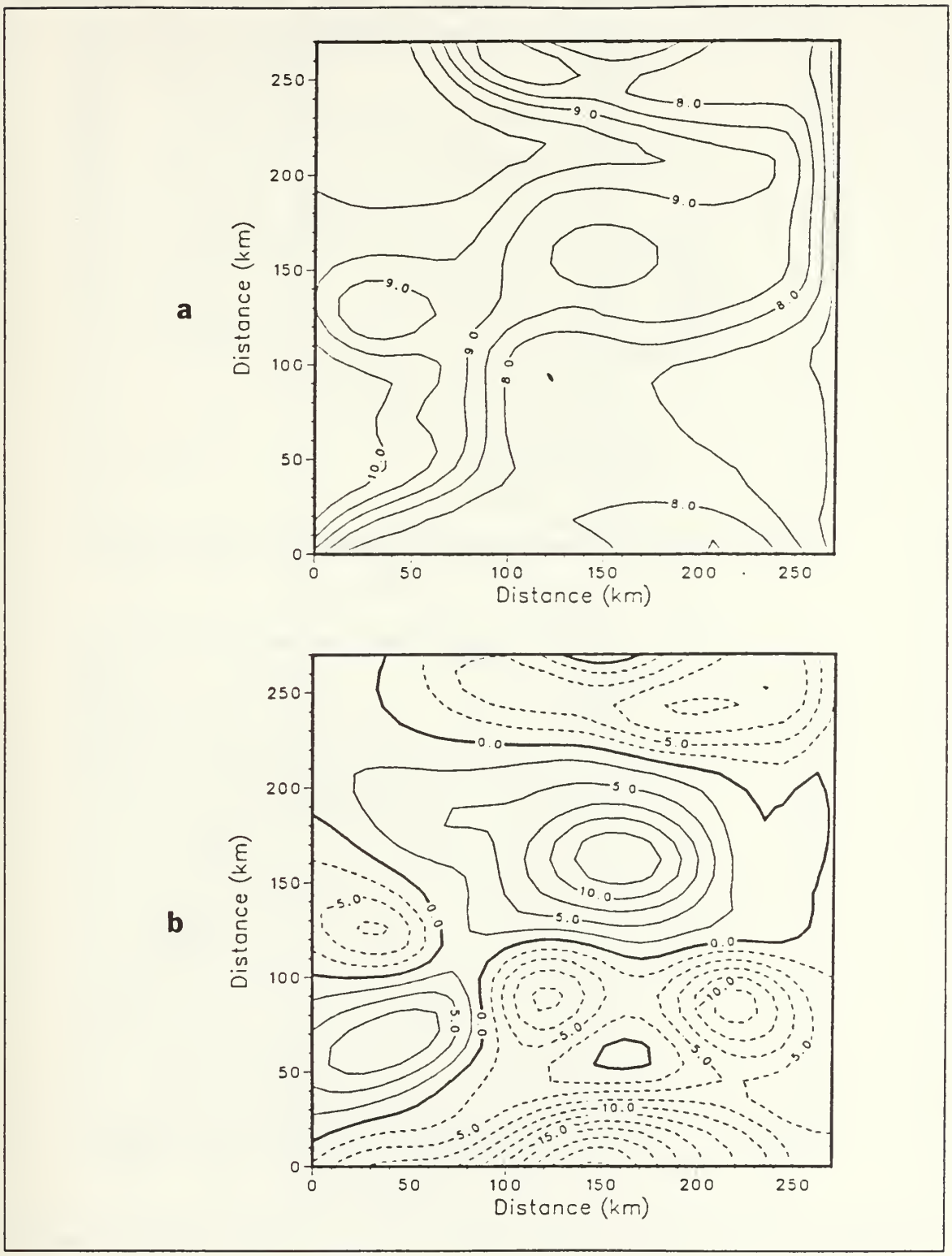

Figure 2.23 Same as Fig. 2.19 but at 200 m.

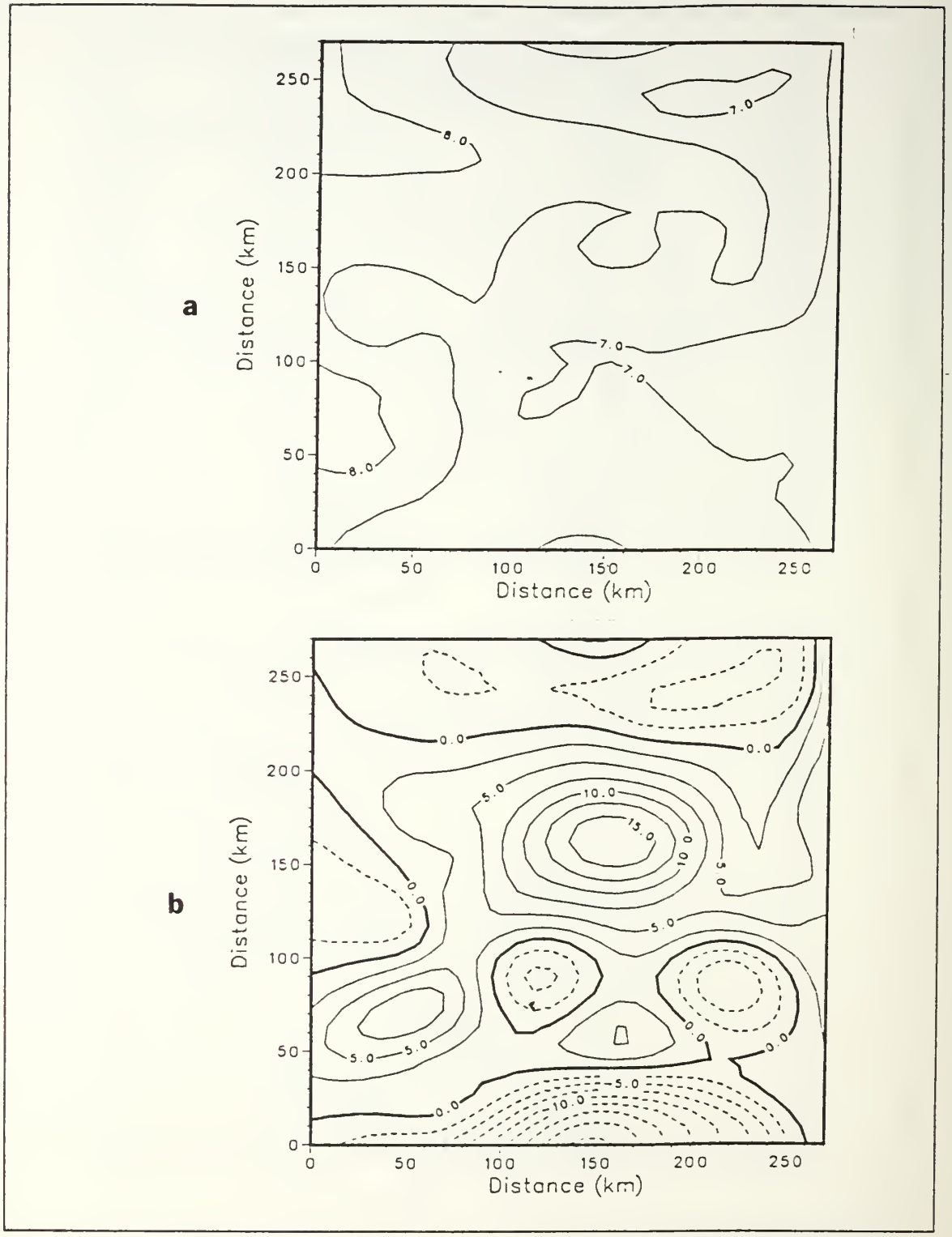

Figure 2.24 Same as Fig. 2.19 but at 350 m.

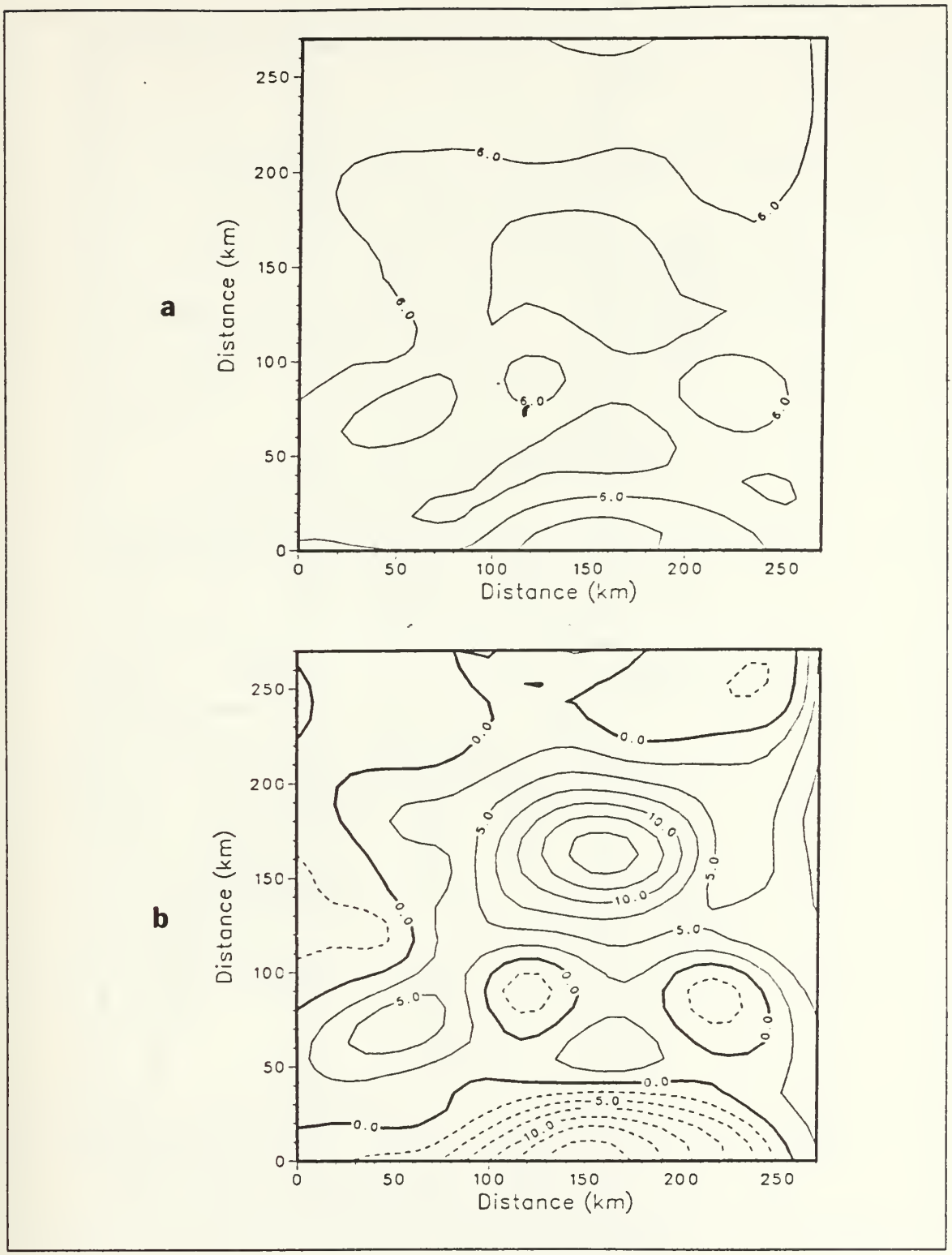

Figure 2.25 Same as Fig. 2.19 but at 550 m.

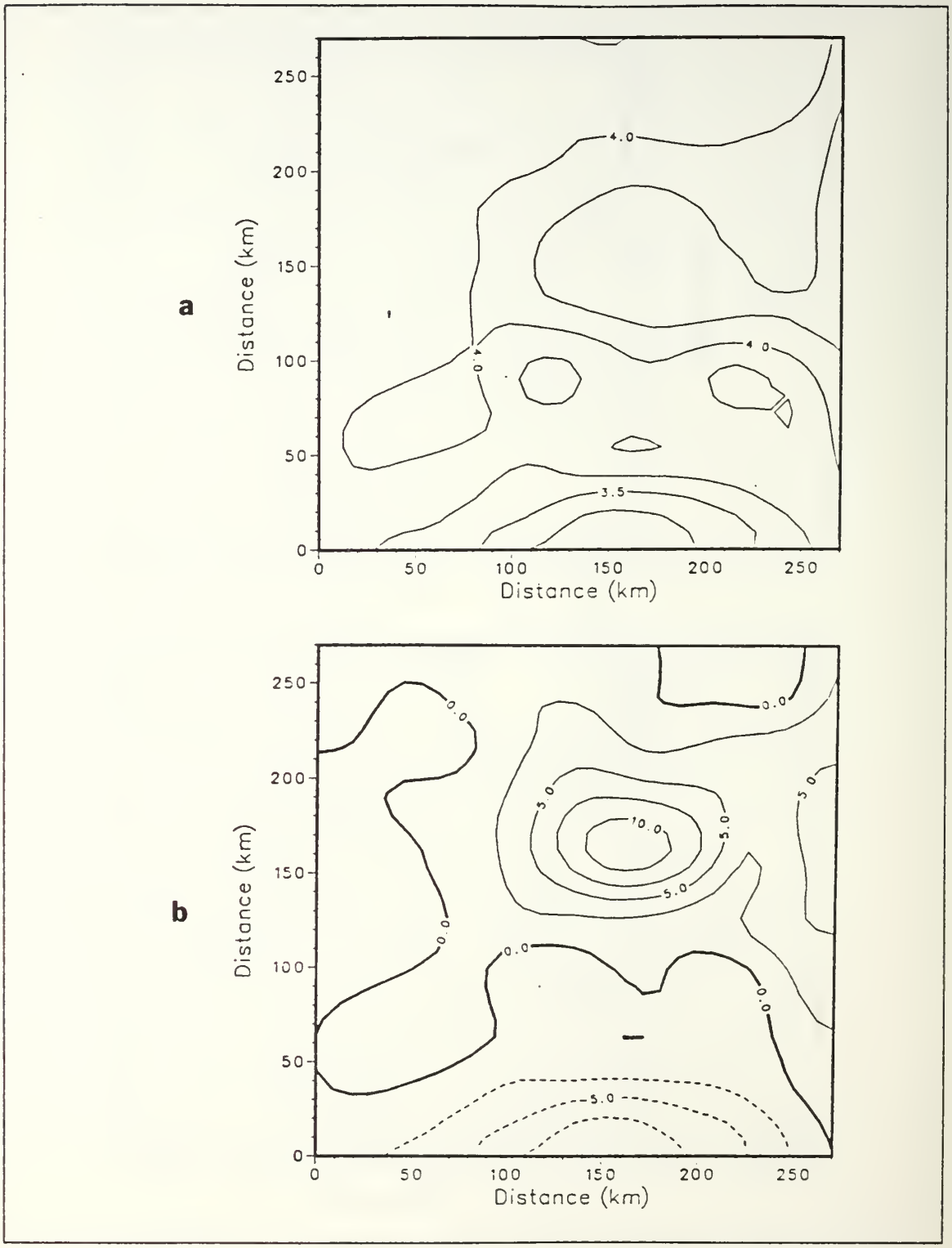

Figure 2.26 Same as Fig. 2.19 but at 900 m.

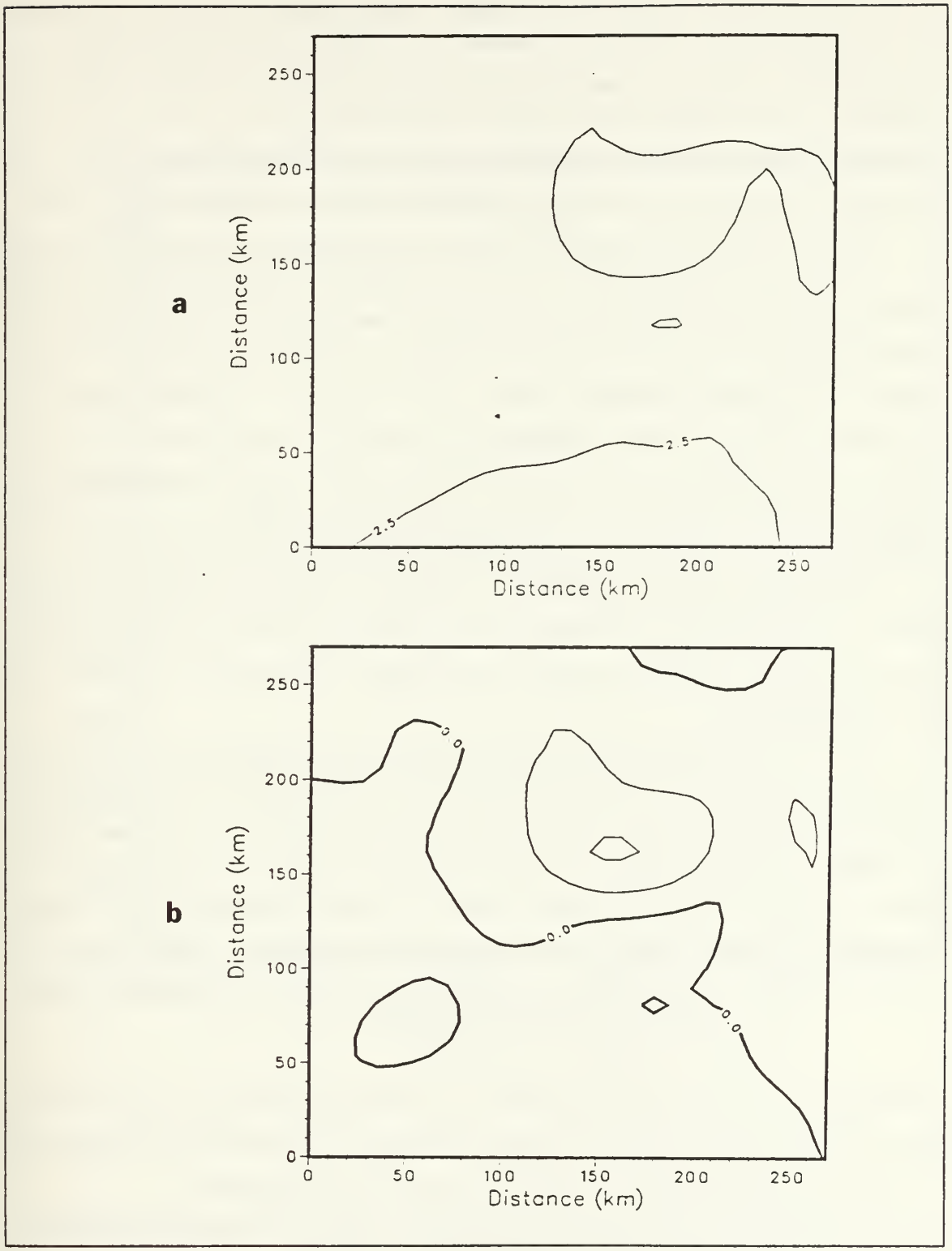

Figure 2.27 Same as Fig. 2.19 but at 1500 m.

At each depth, temperature correlation versus spatial separation calculations were computed (Figs. 2.28-2.32). Maximum correlation values, occurring at the zero-separation distance, ranging from 0.8 at the surface to 0.98 at 550 m depth, were supplied to the OA routine. Each of the correlation curves drop off steadily in a near exponential fashion from their maximum value to a zero-crossing distance which tends to increase with depth due to the more isothermal conditions experienced with depth.

The OA interpolated temperature maps are presented in Figures 2.33 through 2.37. To evaluate the performance of the OA technique a comparison was conducted between each of the OA interpolated temperature maps and each of the respective PE 'perfect' maps (Figs. 2.10a, 2.11a, 2.12a, 2.14a and 2.16a). The simplest way to obtain a measure of the overall similarity between the two maps is to compute the pattern correlation coefficient which is defined as the zero-lag spatial correlation. The more closely the two surfaces correspond, the higher the pattern correlation between them. With the exception of a pattern correlation of 0.99 at 550 m depth, the correlation was perfect.

Another often used comparison is the difference between the perfect and sampled fields. It is constructed by substracting the two matrices of grid values from each other. Due to the perfect correlation pattern, the difference field behaved as expected with very small differences.

A set of difference measures which describe the difference field include the root-mean-square error (RMSE), the systematic root-mean-square error ($RMSE_s$), the unsystematic root-mean-square error ($RMSE_u$) and the mean absolute error (MAE). The RMSE is always positive and is not constrained to values less than 1.0 as is the pattern correlation coefficient. Identical fields give RMSE equivalent to zero whereas increasingly dissimilar maps have increasingly greater error between them. The RMSE can be decomposed into its $RMSE_s$ and $RMSE_u$ components through the relationship

$$RMSE^2 = RMSE_s^2 + RMSE_u^2.$$

Linear bias produced by the OA technique is described by $RMSE_s$, whereas $RMSE_u$ may be interpreted as a measure of precision (Wilmott *et al.*, 1985). In all cases RMSE > MAE which makes RMSE a conservative measure of average error.

A summary of the statistical measures of the PE and OA temperature comparison at each depth is presented in Table 1 for this experimental case. Both average errors, MAE and RMSE, are very small at each depth. This is reasonable due

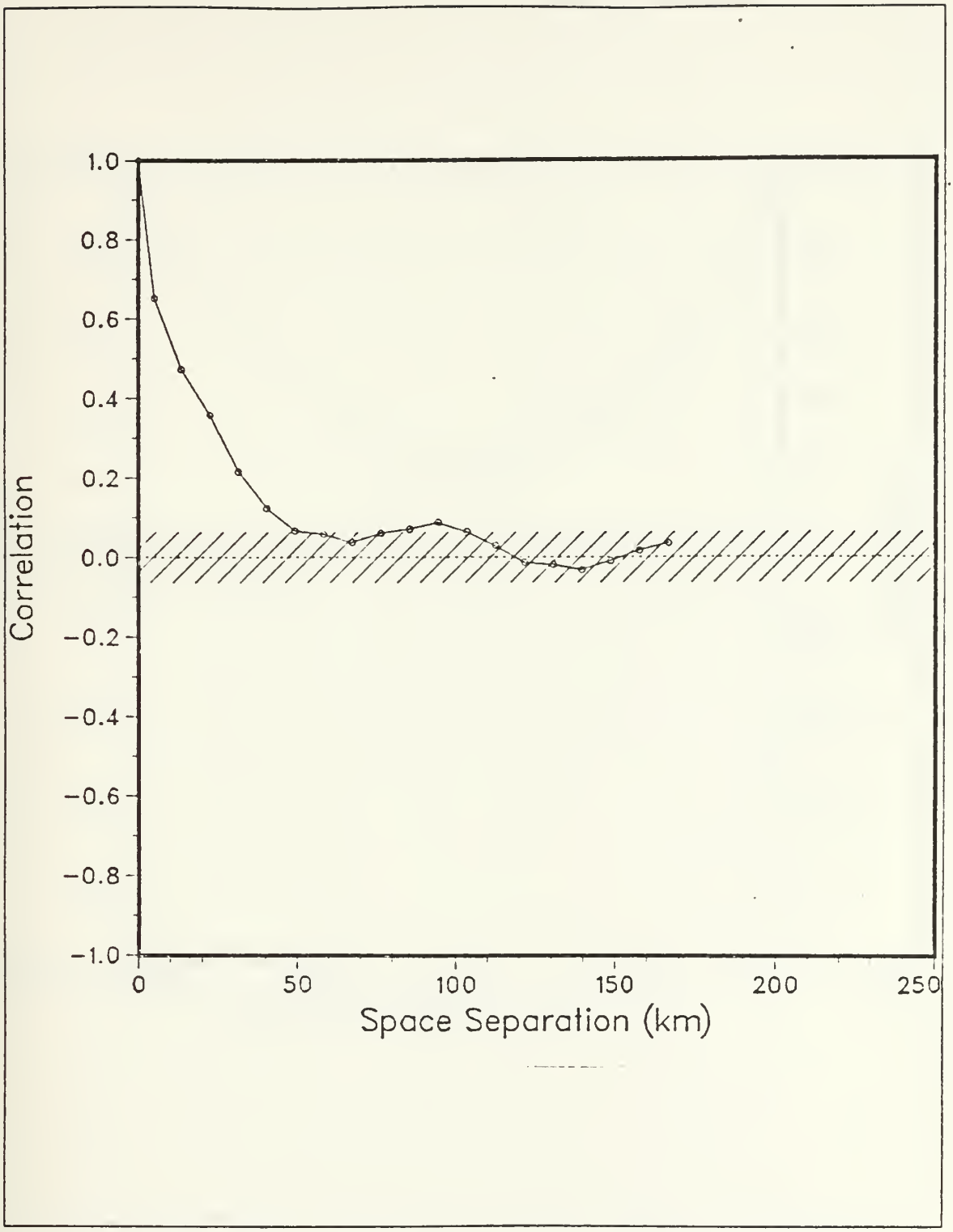

Figure 2.28 Correlation of the surface temperature, zero-crossing distance of 118 km.

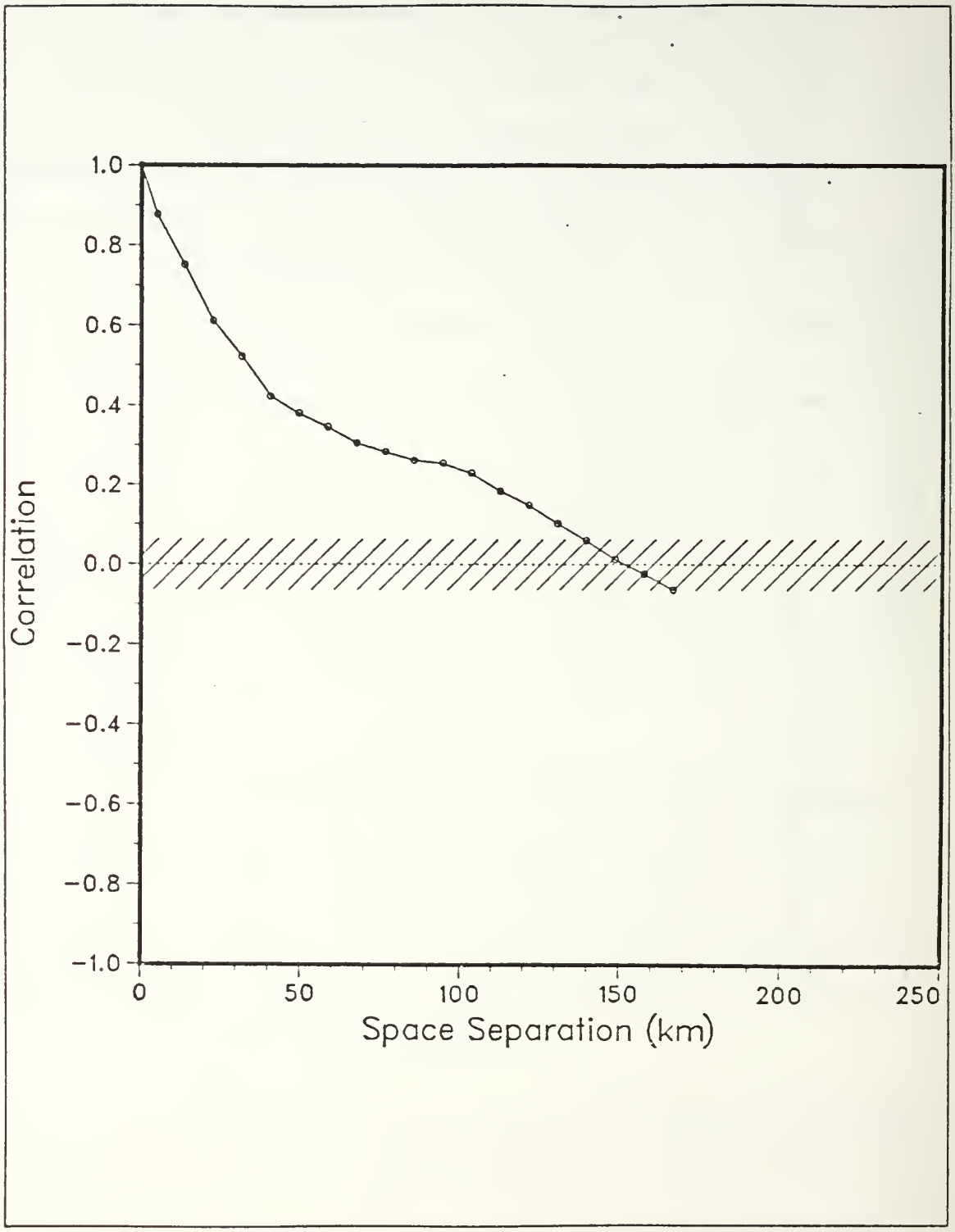

Figure 2.29 Same as Fig. 2.28 but at 25 m, zero-crossing distance of 150 km.

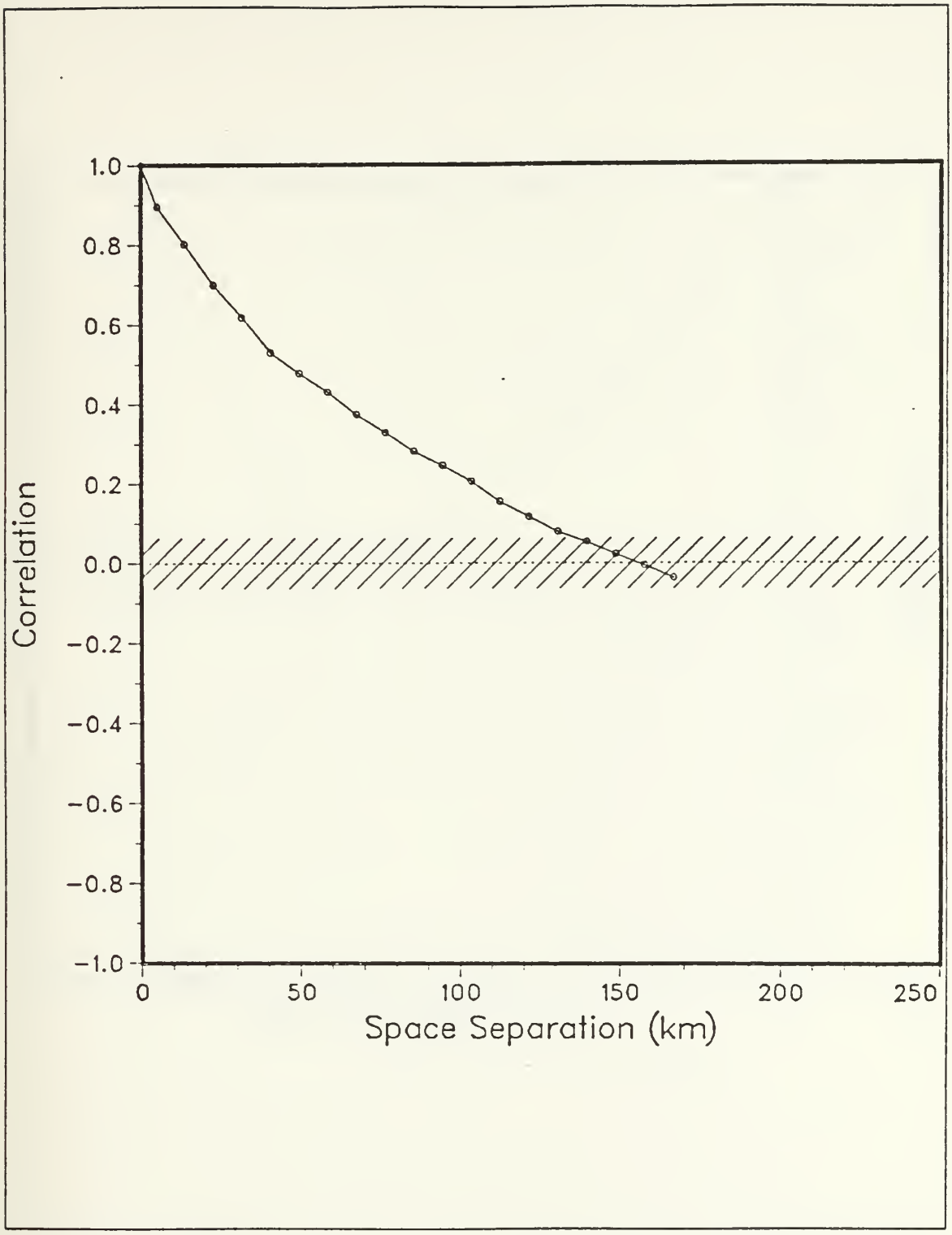

Figure 2.30 Same as Fig. 2.28 but at 50 m, zero-crossing distance of 155 km.

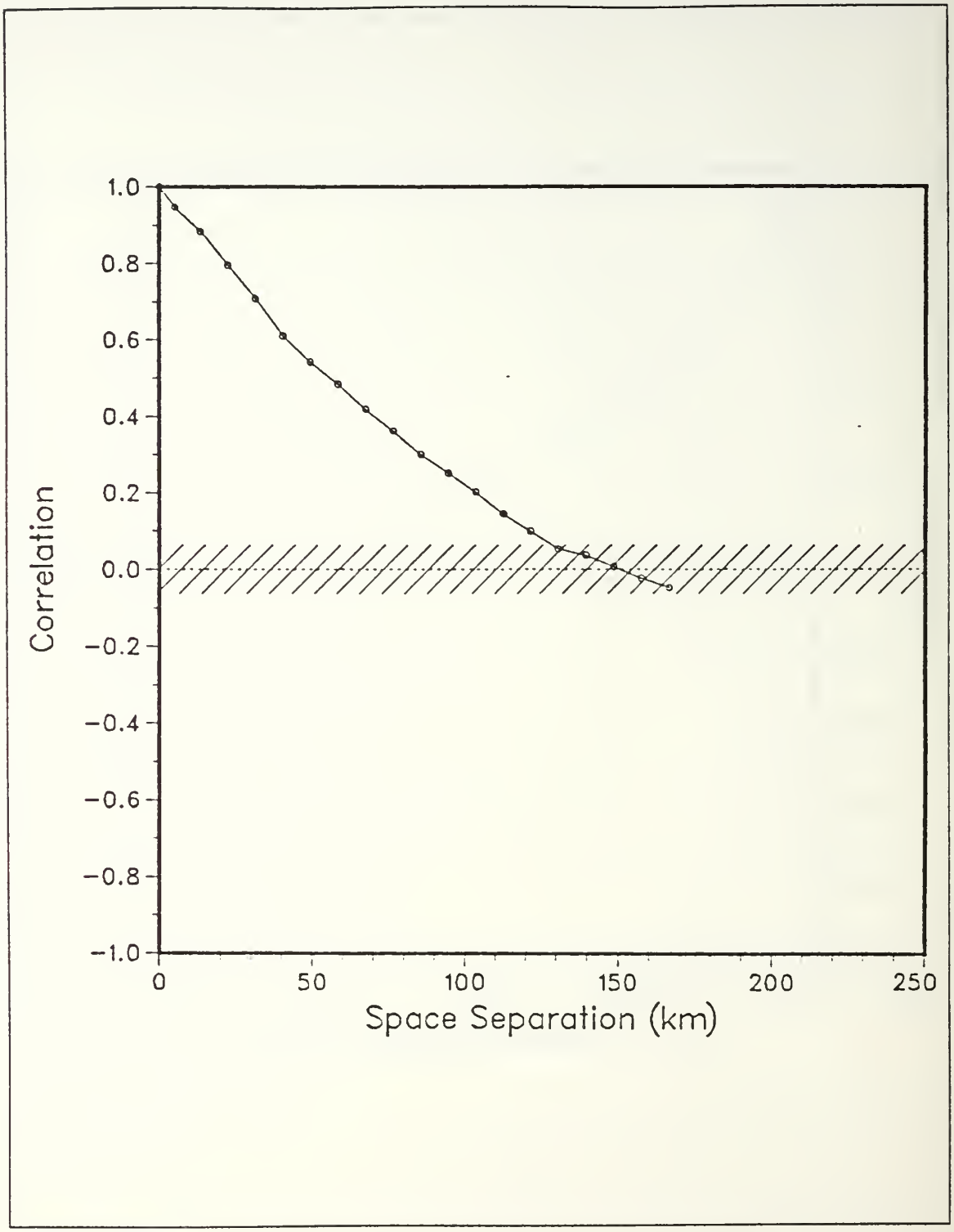

Figure 2.31 Same as Fig. 2.28 but at 200 m, zero-crossing distance of 150 km.

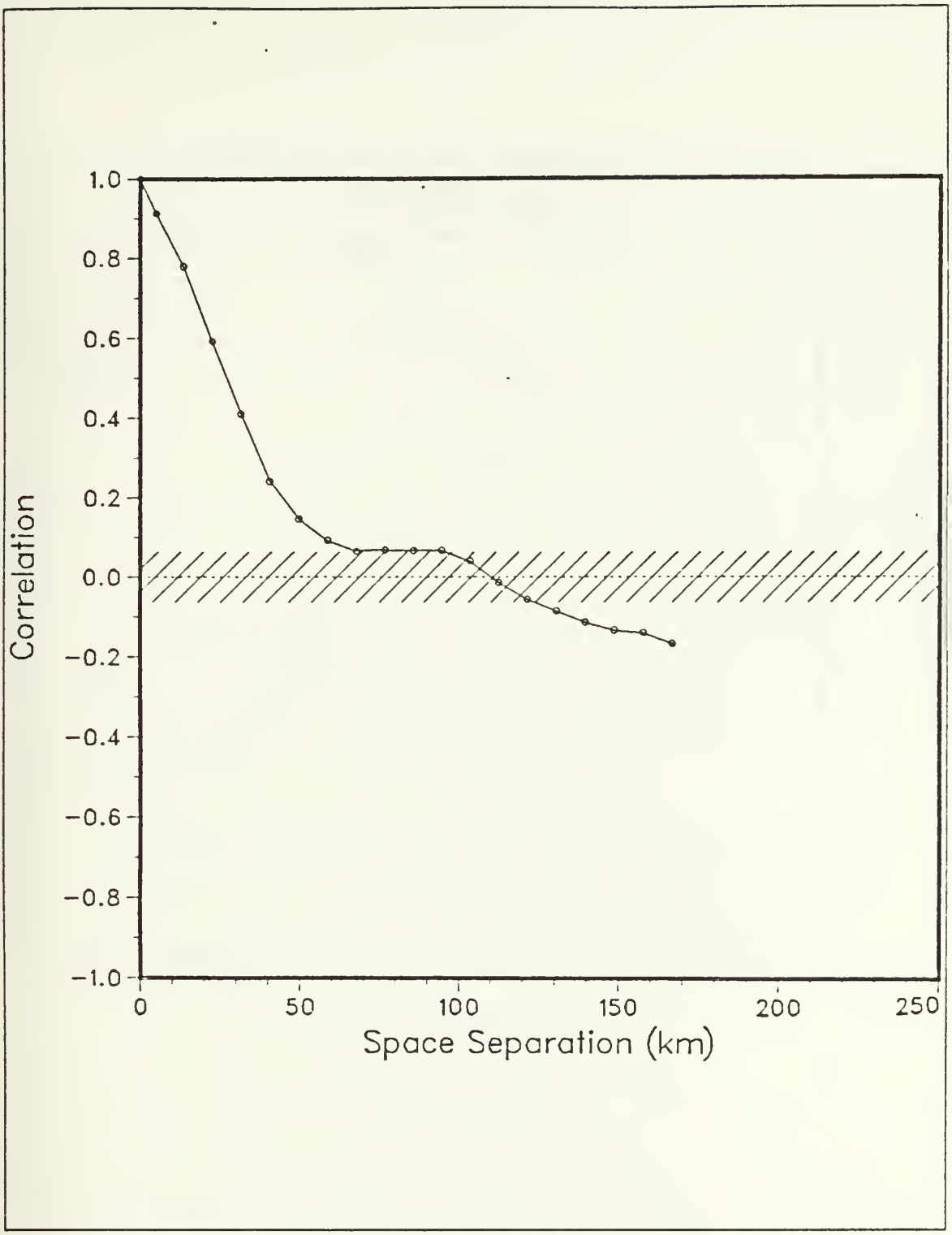

Figure 2.32 Same as Fig. 2.28 but at 550 m, zero-crossing distance of 110 km.

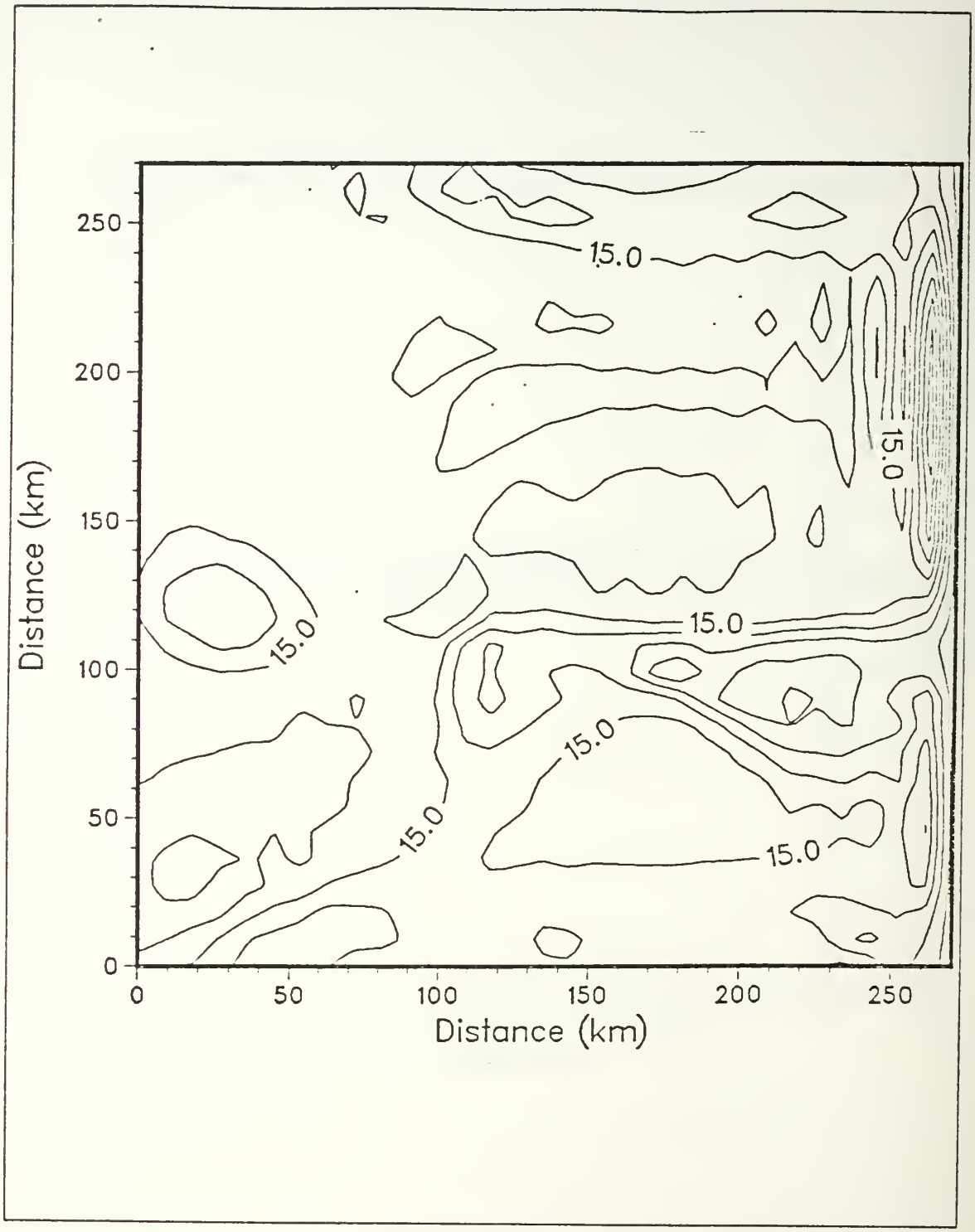

Figure 2.33 OA interpolated surface temperature field on day 40, contour interval 0.5 C, pattern correlation 1.00.

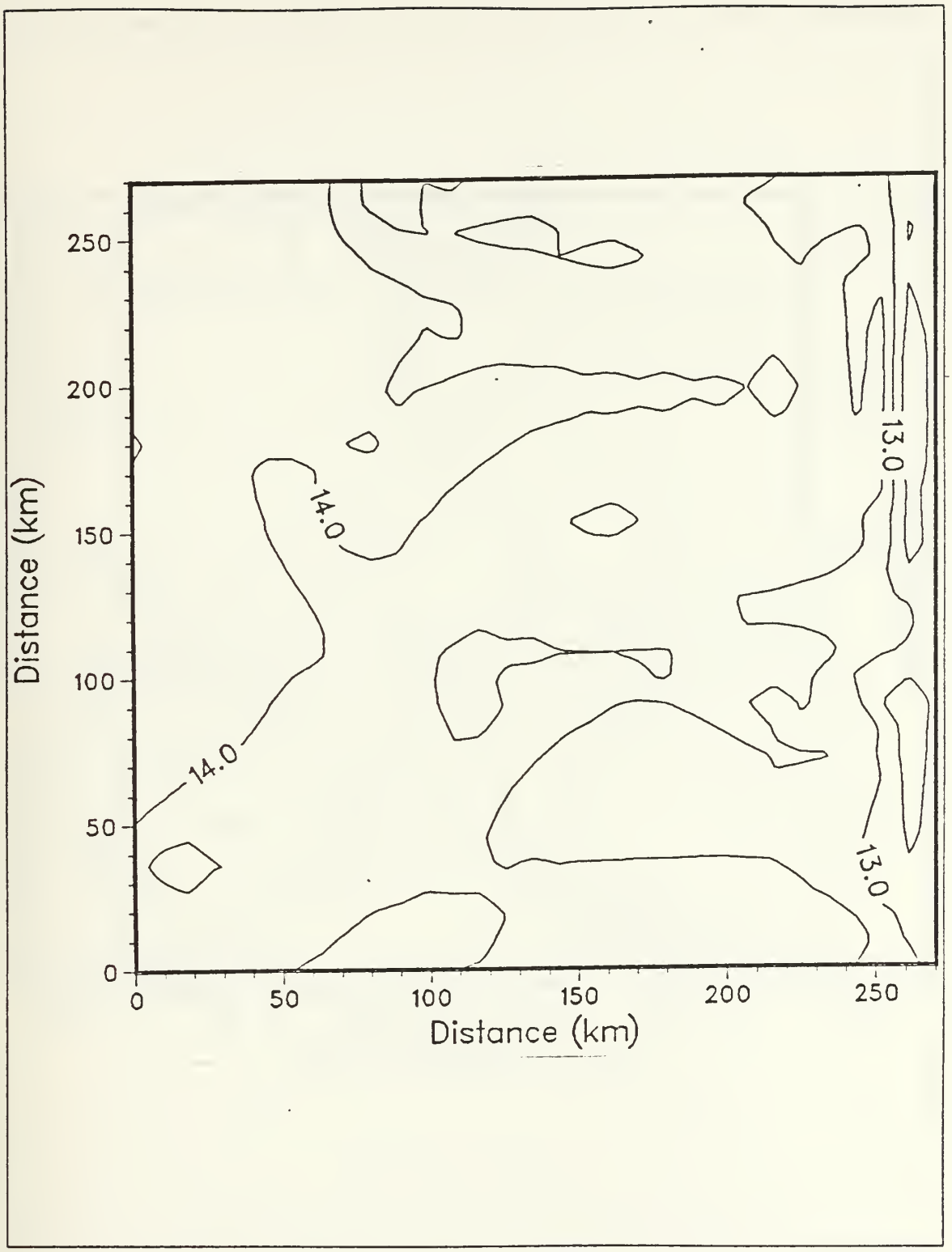

Figure 2.34 Same as Fig. 2.33 but at 25 m.

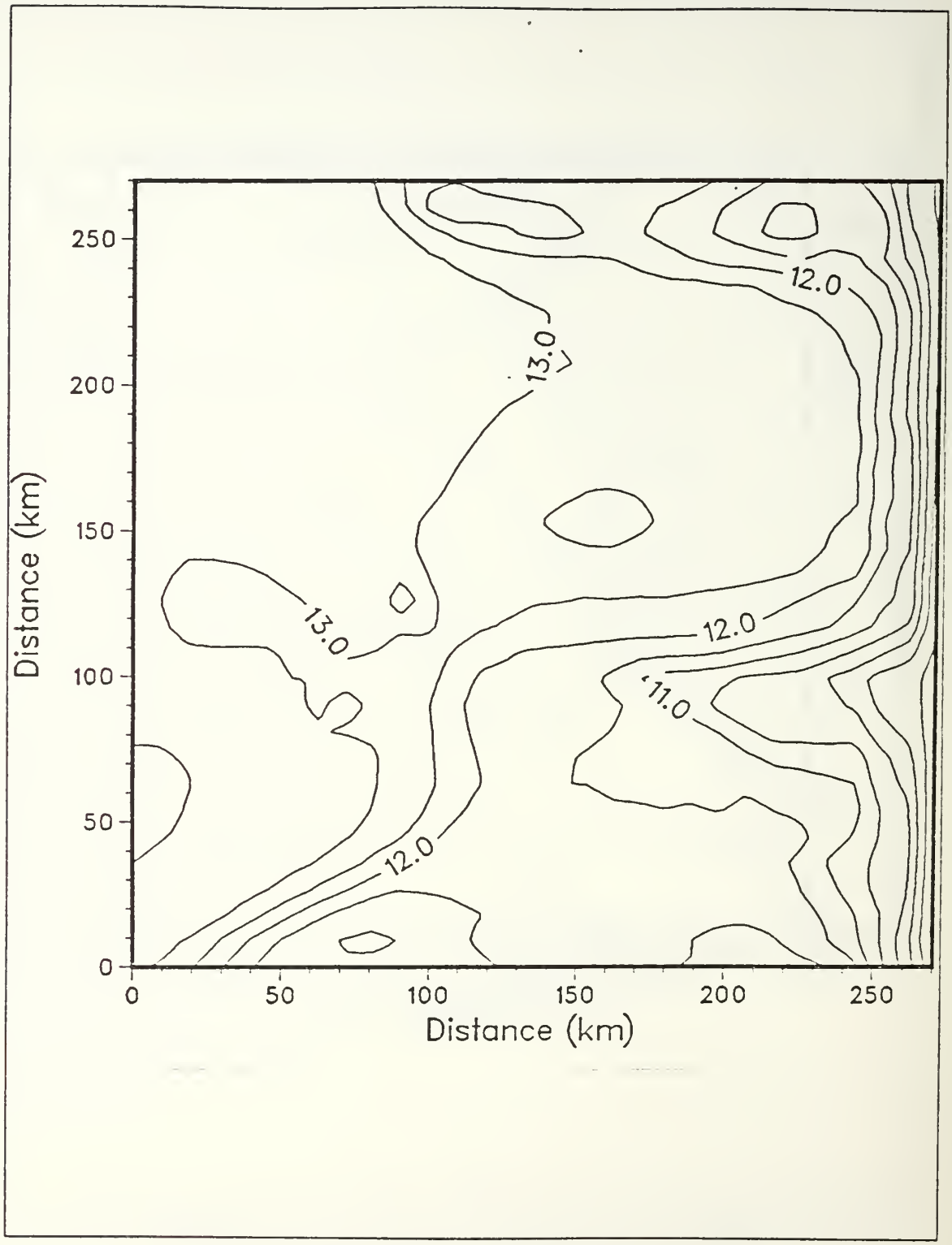

Figure 2.35 Same as Fig. 2.33 but at 50 m.

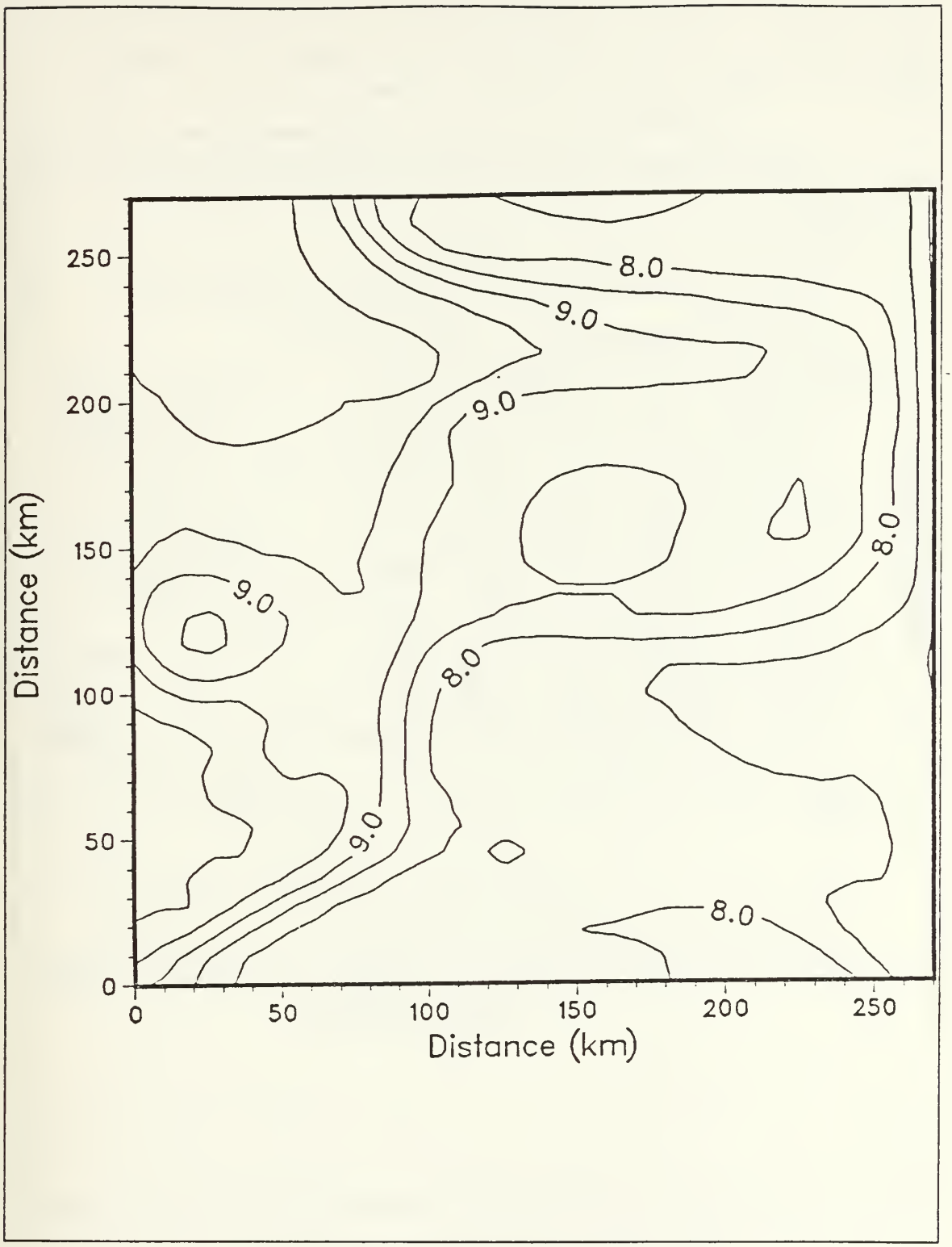

Figure 2.36 Same as Fig. 2.33 but at 200 m.

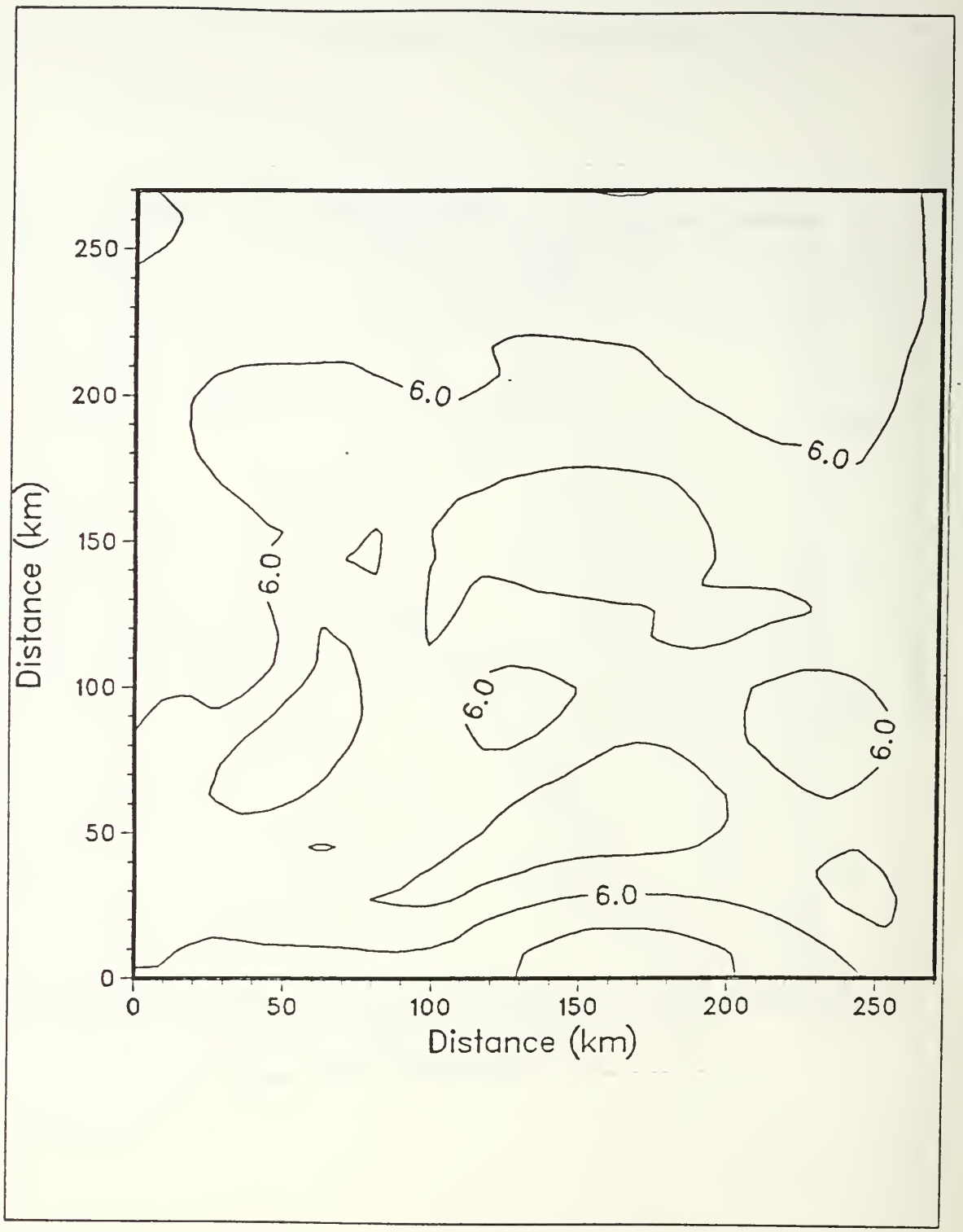

Figure 2.37 Same as Fig. 2.33 but at 550 m, pattern correlation 0.99.

to the high pattern correlation. The absolute and relative magnitudes of the systematic and unsystematic errors indicate that the OA technique produces a relatively small error. Although these errors are small, a majority of the mean-square error is likely attributable to linear systematic causes residing in the OA technique.

TABLE 1
STATISTICAL MEASURES OF EXPERIMENTAL CASE

	Surface	25 m	50 m	200 m	550 m
PE Mean Temp	14.98	13.72	12.27	8.61	6.11
OA Mean Temp	14.98	13.72	12.27	8.60	6.11
PE Variance	0.50	0.22	1.50	1.06	0.12
OA Variance	0.50	0.18	1.20	0.84	0.09
Zero-Crossing	118.0	150.0	155.0	150.0	110.0
Pattern Corr	1.00	1.00	1.00	1.00	1.00
MAE	0.09	0.05	0.12	0.11	0.04
RMSE	0.11	0.06	0.14	0.12	0.05
$RMSE_s$	0.09	0.05	0.13	0.11	0.04
$RMSE_u$	0.04	0.03	0.07	0.06	0.03

III. SPATIAL SAMPLING

An areal sampling technique satisfying the synopticity assumption was simulated using three different sampling strategies. The goal in areal sampling is to cover the X, Y plane with a sufficient number of observations to provide a representative sample in as small a time frame as possible. To provide the representative time constraints, a P-3 aircraft was tasked to perform the sampling because of its rapidity and convenience. The distribution of the temperature field from the PE model output was found to be unsmooth and displayed no preferred pattern in any direction. However, when observations were distributed quasi-uniformly over the test area, as for the first sampling strategy, it was found that a coastal bias toward smaller scales was required to capture the tight gradient features of the temperature front. Thus, previous experience and knowledge of the temperature field was found to be useful in selecting the stratified sampling schemes. By using this *a priori* knowledge, heavier sampling was conducted for the latter two cruises in the areas where more internal variability existed.

Each of the three P-3 cruises was conducted on day 40 of the PE model output run. The AXBT temperature data were interpolated to the grid using an inverse distance weighting to compute a grid point value from the two closest and highest correlated values within a 50 km radius of influence. The temperature field at five depths were mapped by applying the OA routine with the following supplied parameters:

- data were neither filtered nor detrended but the mean was removed (see Appendix A);
- data were assumed to be sampled in real time; and
- non-constant, depth-dependent correlation and zero-crossing values were used.

A. P-3 CRUISE I

All three P-3 flights consisted of ninety-nine AXBT stations which is about the maximum number of stations presently used. Cruise I consisted of AXBT stations with a fixed north-south sampling interval of 27 km. East-west station intervals of 27 km were planned near shore out to 180 km offshore with the remaining 90 km of the test block being equally spaced at 45 km. The actual observational positions are illustrated in Figure 3.1.

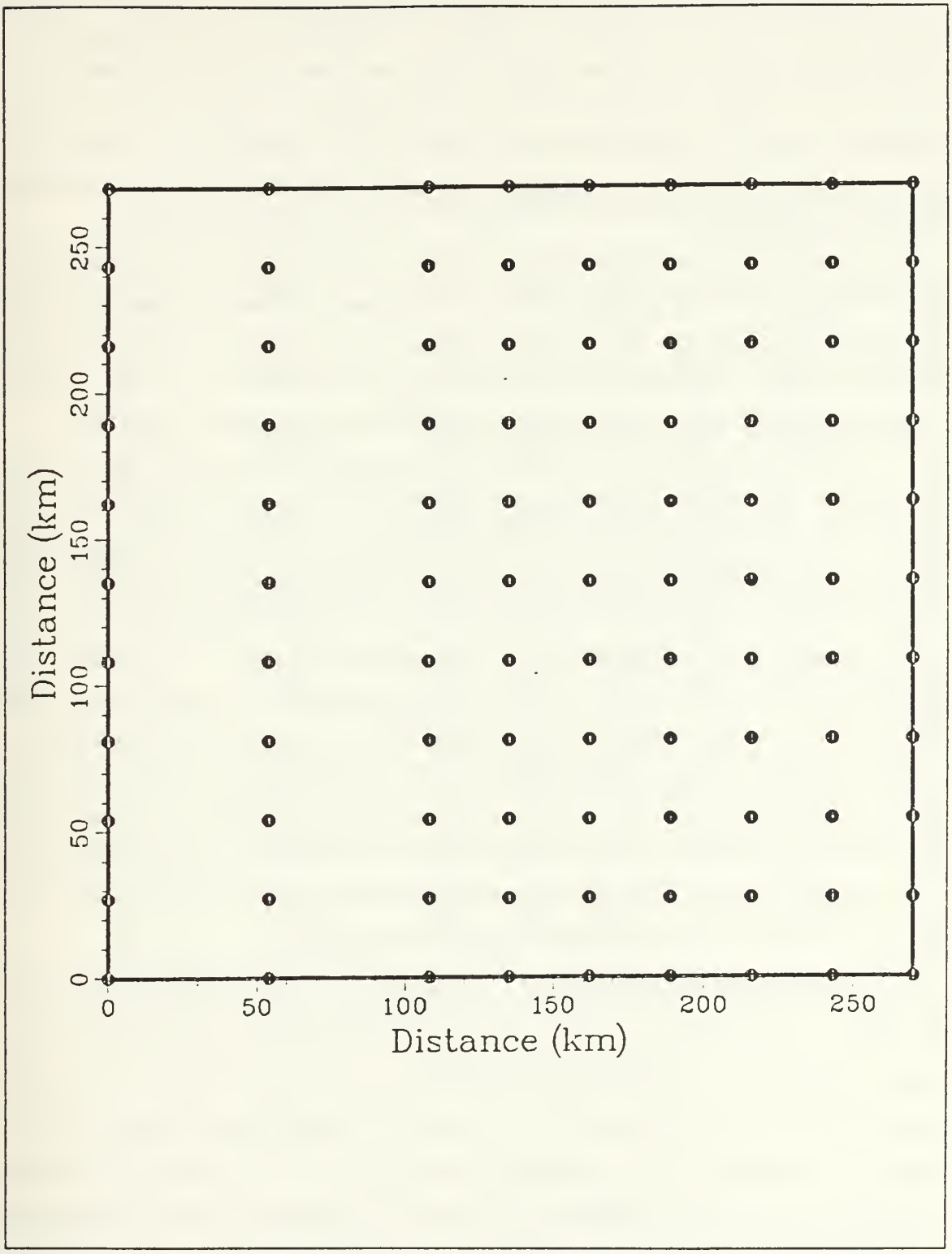

Figure 3.1 Cruise I station positions.

The error field was calculated as a percentage of the variance in the data at each interpolated position and is shown in Figure 3.2. This field behaves as expected for a near uniform distribution of observations. Minimum errors (12%) were experienced at the AXBT stations themselves while errors increased outward away from each observation position uniformly. Errors as great as 37% occurred in the area furthest from the eastern boundary, coinciding as expected with the largest space intervals between observations.

Autocorrelation versus depth curves of the temperature field were calculated and plotted (Figs. 3.3-3.7). A typical pattern of a maximum correlation at zero lag with an exponential falloff to the zero-crossing distance was exhibited at each of the five examined depths. Tendencies toward greater zero-crossing distances at deeper depths occurred, probably due to the weakening of the temperature structure with depth.

Statistical measurements of the PE model temperature fields at five depths versus the respective OA interpolated temperature fields from P-3 Cruise I were calculated to obtain an overall measure of the resemblance between the two fields. These statistical values are presented in Table 2. The poorest OA analysis occurred at the surface where only a 63% pattern correlation existed. PE (Fig. 3.8) and OA (Fig. 3.9) maps of the surface temperature field, along with the corresponding (PE - OA) temperature difference map (Fig. 3.10), show that this poor correlation was largely due to strong gradients, in association with the temperature front and the cool filament along the eastern boundary being improperly displayed in the OA field as weaker in strength. The negative temperature differences in these areas discernable in Figure 3.10 show that the OA technique overestimates the temperatures of these features. Absence of the closed 15°C isotherm (Fig. 3.9) along the central western boundary as seen in Figure 3.8 was largely due to the coarse 45 km spatial sampling in this area.

Pattern correlations greater than the 90% level were found for depths between 25 and 200 m (Table 2). At 25 m depth the most significant difference in the temperature structure was the lack of detail in the depiction of a warm tongue of water in the central domain (compare Figs. 3.11, 3.12 and 3.13). This tongue, only 15 km in width, appears in a region where the 27 km north-south observational spacing gaps the feature on both sides. The interpolated temperature field at 50 m depth illustrates an example of an excellent correlation to the true field as seen not only in the pattern correlation (Table 2) but also in the PE, OA and difference maps (Figs. 3.14-3.16). One major drawback of the OA field is its weakness in the portrayal of the strong,

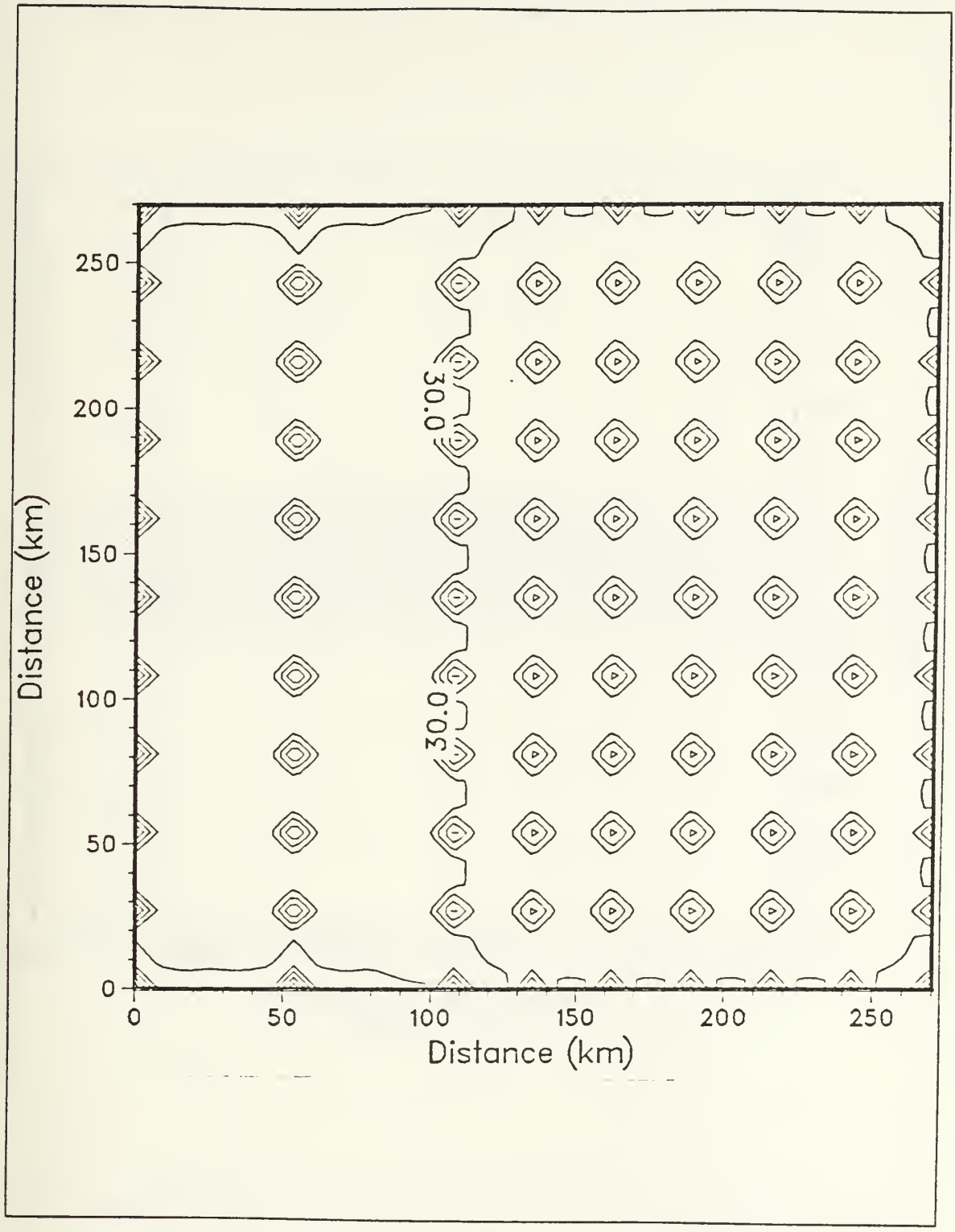

Figure 3.2 Cruise I temperature error field with error range from 12 to 37%.

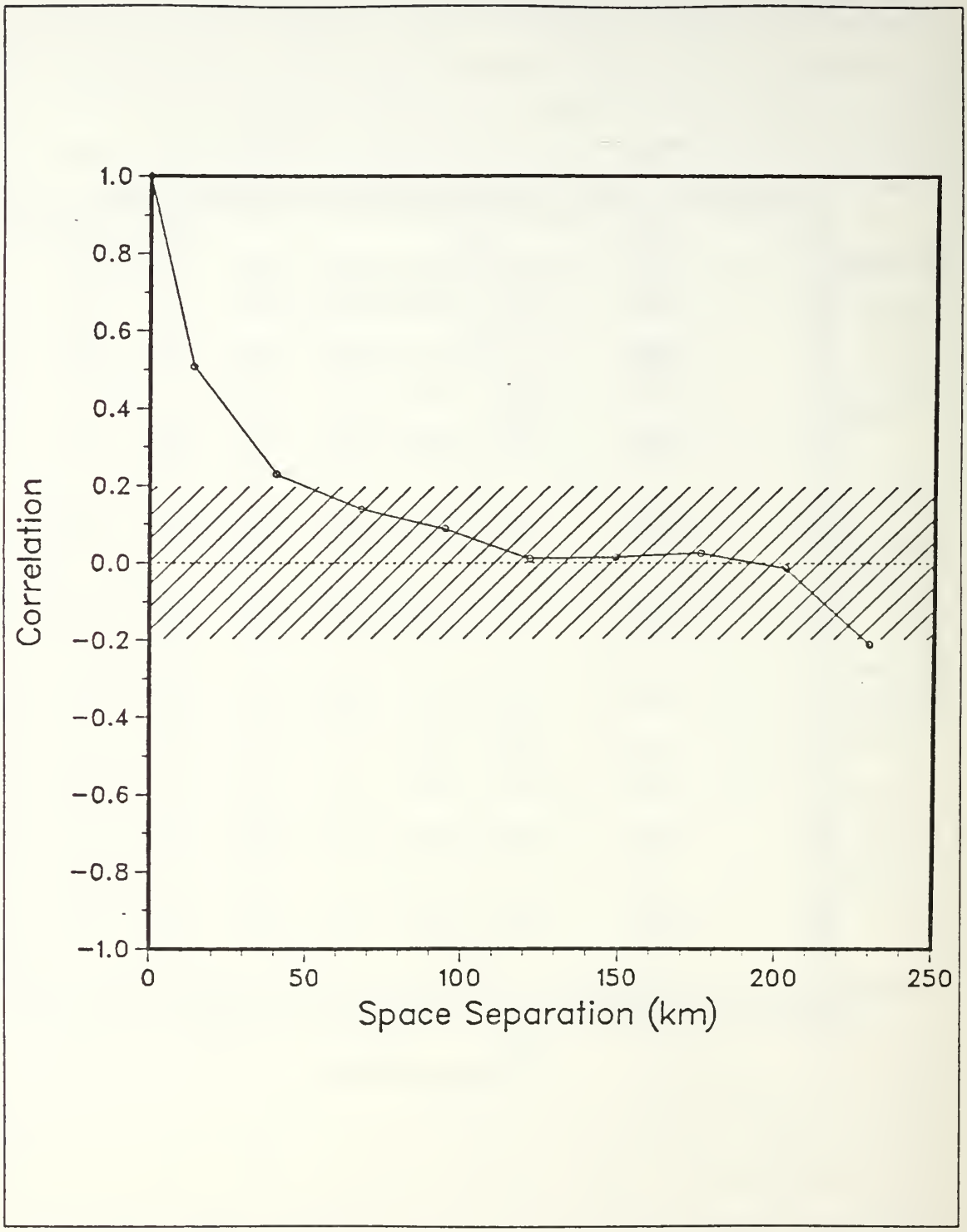

Figure 3.3 Correlation of temperature at sea surface on day 40, Cruise I, zero-crossing distance of 121.5 km.

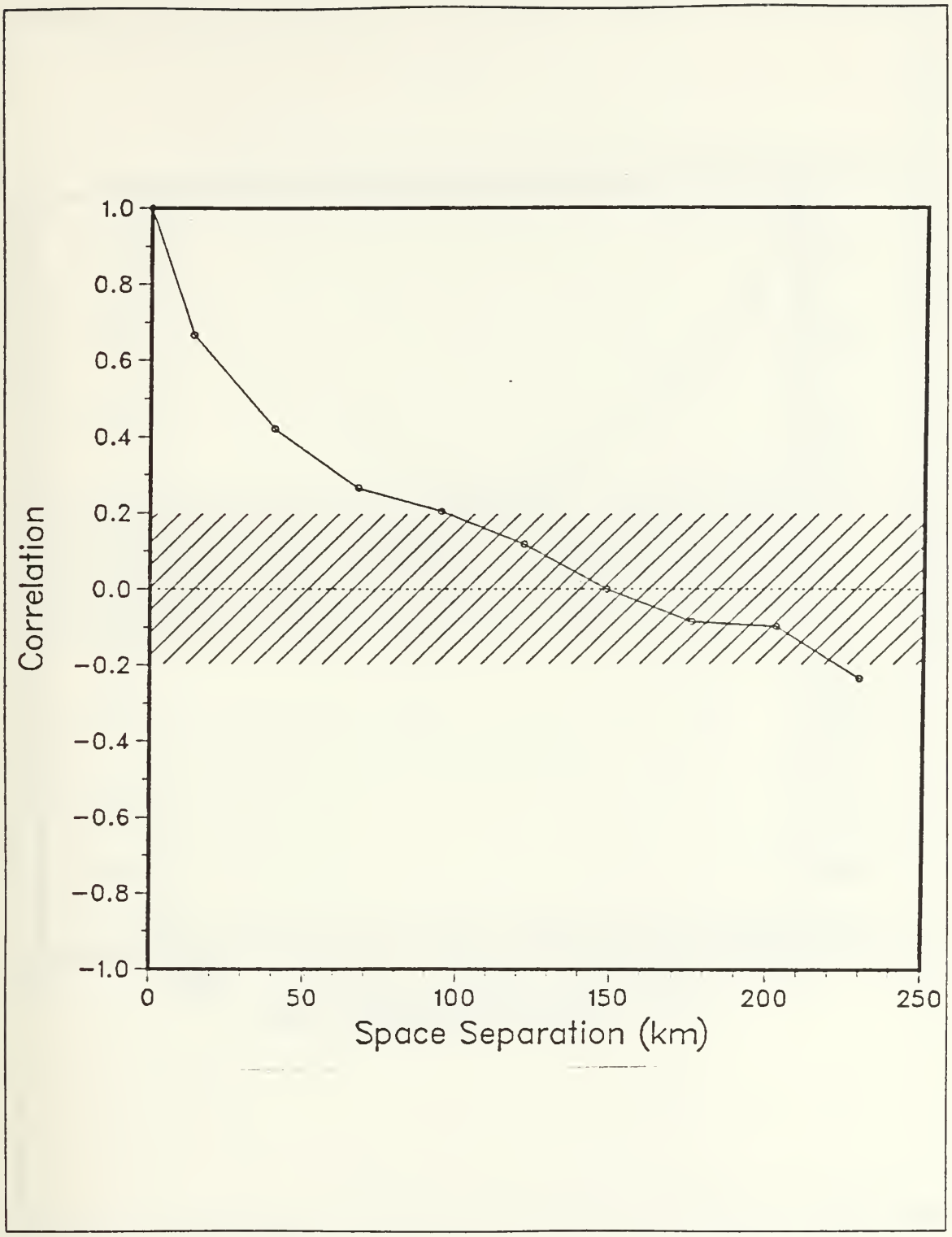

Figure 3.4 Same as Fig. 3.3 but at 25 m, zero-crossing distance of 148.5 km.

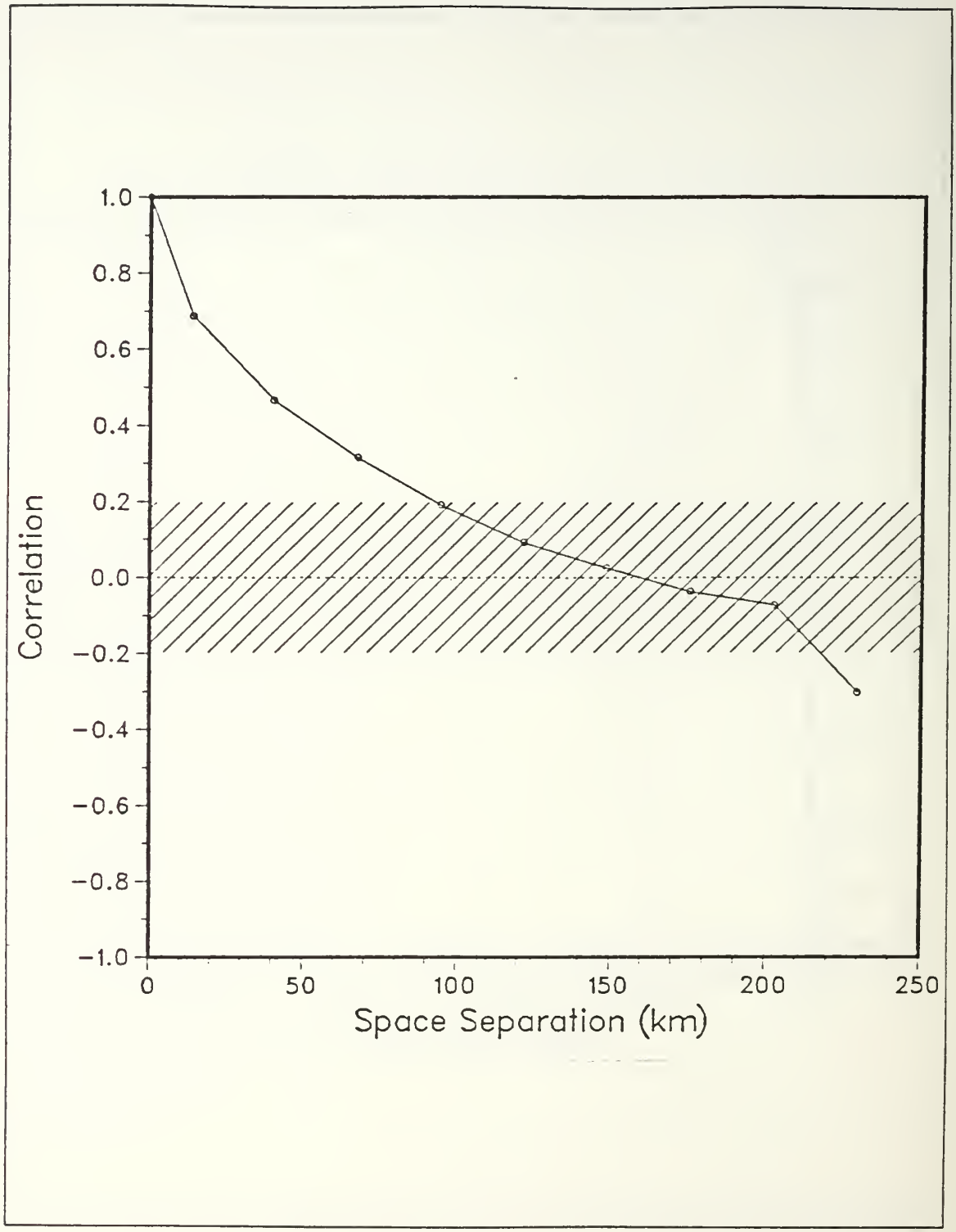

Figure 3.5 Same as Fig. 3.3 but at 50 m, zero-crossing distance of 162.5 km.

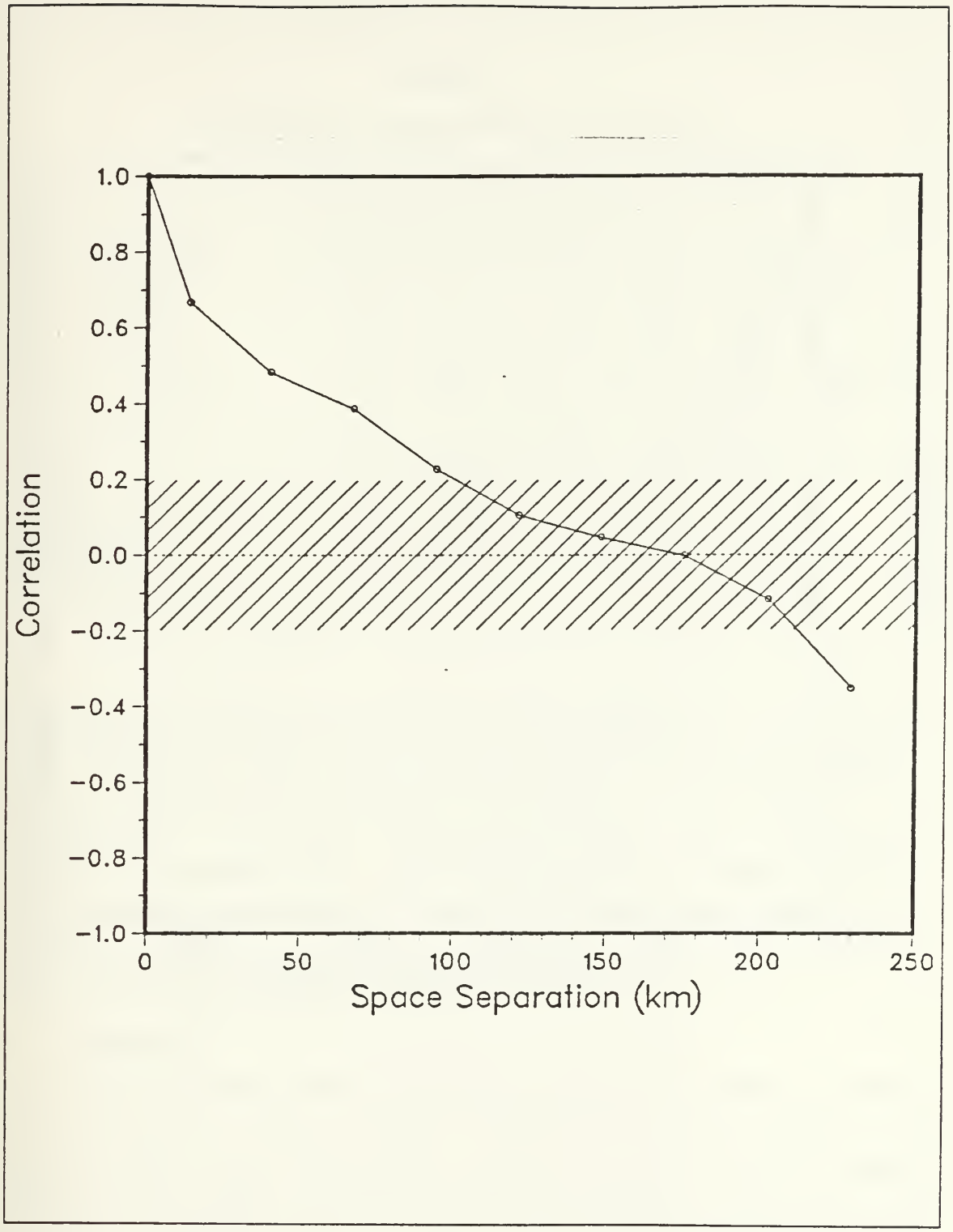

Figure 3.6 Same as Fig. 3.3 but at 200 m, zero-crossing distance of 175.5 km.

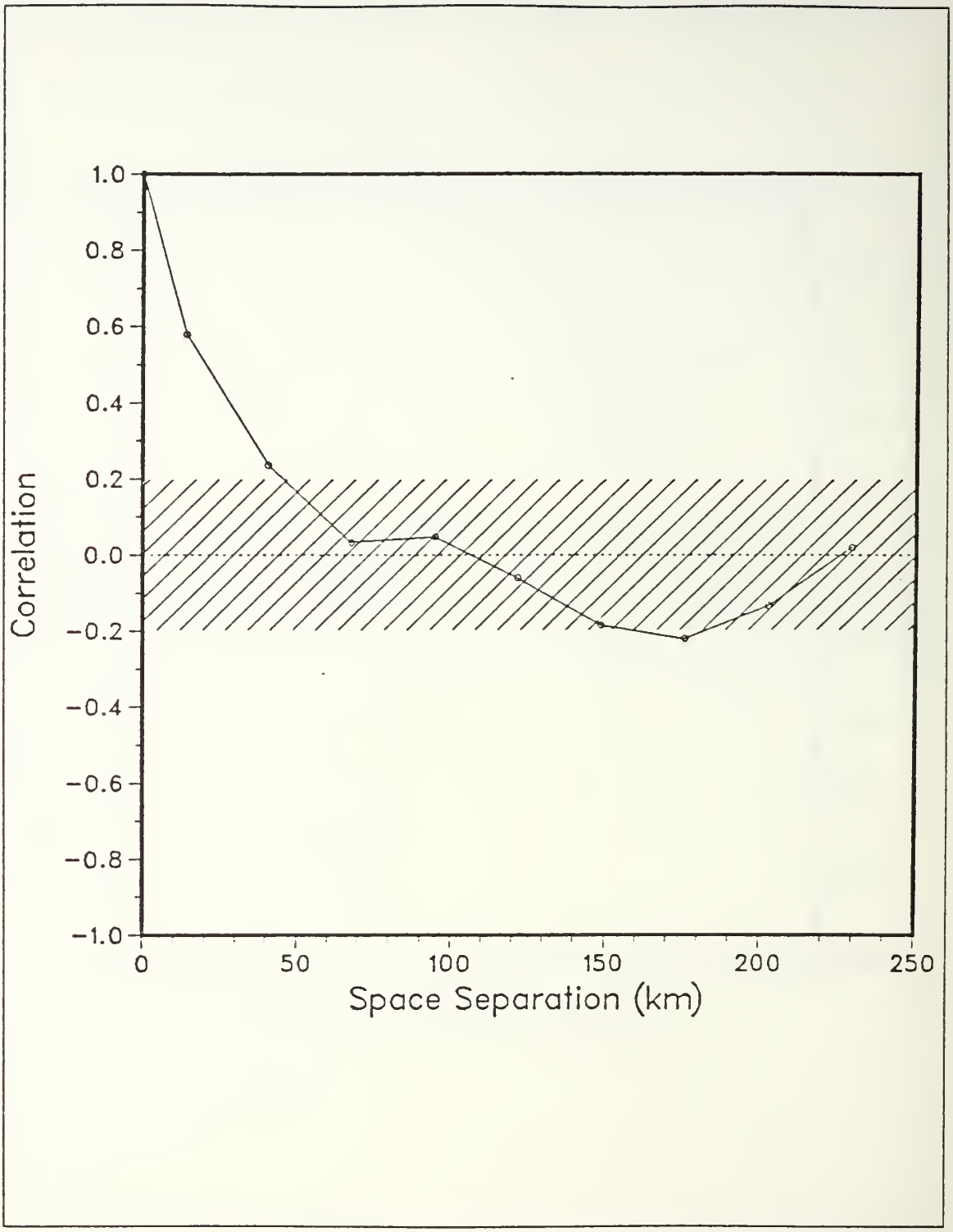

Figure 3.7 Same as Fig. 3.3 but at 550 m, zero-crossing distance of 107.5 km.

TABLE 2
STATISTICAL MEASURES OF P-3 CRUISE I

	Surface	25 m	50 m	200 m	550 m
PE Mean Temp	14.98	13.72	12.27	8.61	6.11
OA Mean Temp	15.07	13.74	12.25	8.61	6.14
PE Variance	0.50	0.22	1.50	1.06	0.12
OA Variance	0.30	0.16	1.44	0.94	0.06
Zero-Crossing	121.5	148.5	162.5	175.5	107.5
Pattern Corr	0.63	0.91	0.95	0.94	0.86
MAE	0.36	0.14	0.26	0.26	0.13
RMSE	0.57	0.20	0.37	0.35	0.18
$RMSE_s$	0.13	0.04	0.03	0.04	0.05
$RMSE_u$	0.55	0.19	0.37	0.35	0.17

tight gradient temperature front. Comparison at 200 m depth (Figs. 3.17-3.19) again indicates the problem of detatil in the depiction of smaller scale temperature features which are less than the station spacing distance. Along the western boundary and in the central region of the domain both a cool pool and a warm cell of water, respectively, are non-existent due to this problem. The effect of differences in station spacing and feature scales is dramatically portrayed at 550 m depth (Figs. 3.20-3.22). Not one of the small pools of water is depicted well. The warm cells are overestimated whereas opposite temperature differences exist in the cooler pools.

B. P-3 CRUISE II

A stratified sampling scheme employing ninety-nine AXBT stations was chosen for Cruise II with more sampling along the coast then offshore, that is, spacing in the east-west direction varied from a minimum of 9 km near the coast with steadily increasing distances offshore to a maximum of 81 km. The same north-south spacing of 27 km as employed in Cruise I was used. The actual observation positions are illustrated in Figure 3.23. Figure 3.24 shows the error field of the sampling scheme. As expected the smallest errors (12%) occur at the AXBT observation stations while a

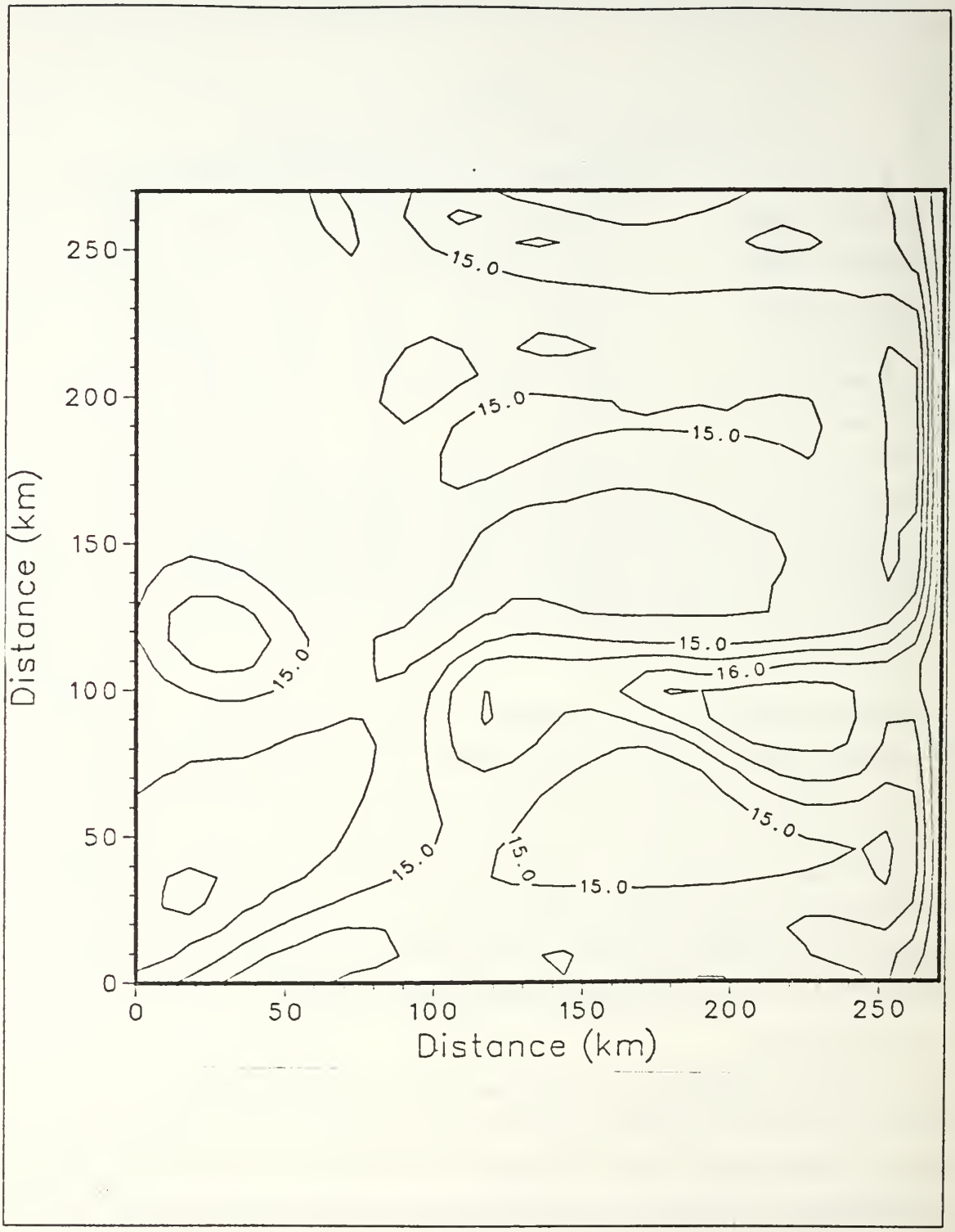

Figure 3.8 PE model SST field on day 40, contour interval of 0.5 C.

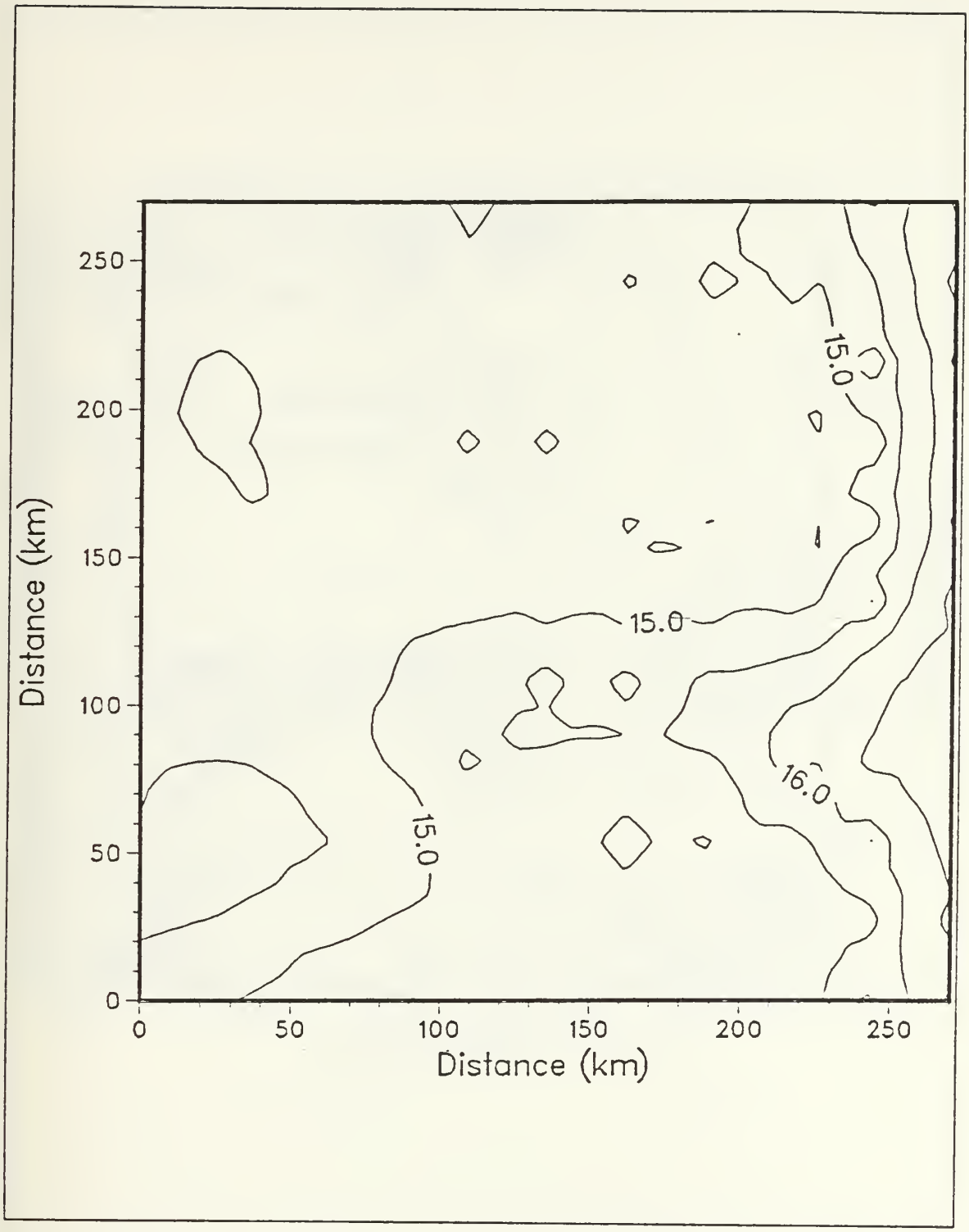

Figure 3.9. OA interpolated SST field on day 40,
Cruise I, pattern correlation of 0.63,
T range of 13.89 to 16.95 C.

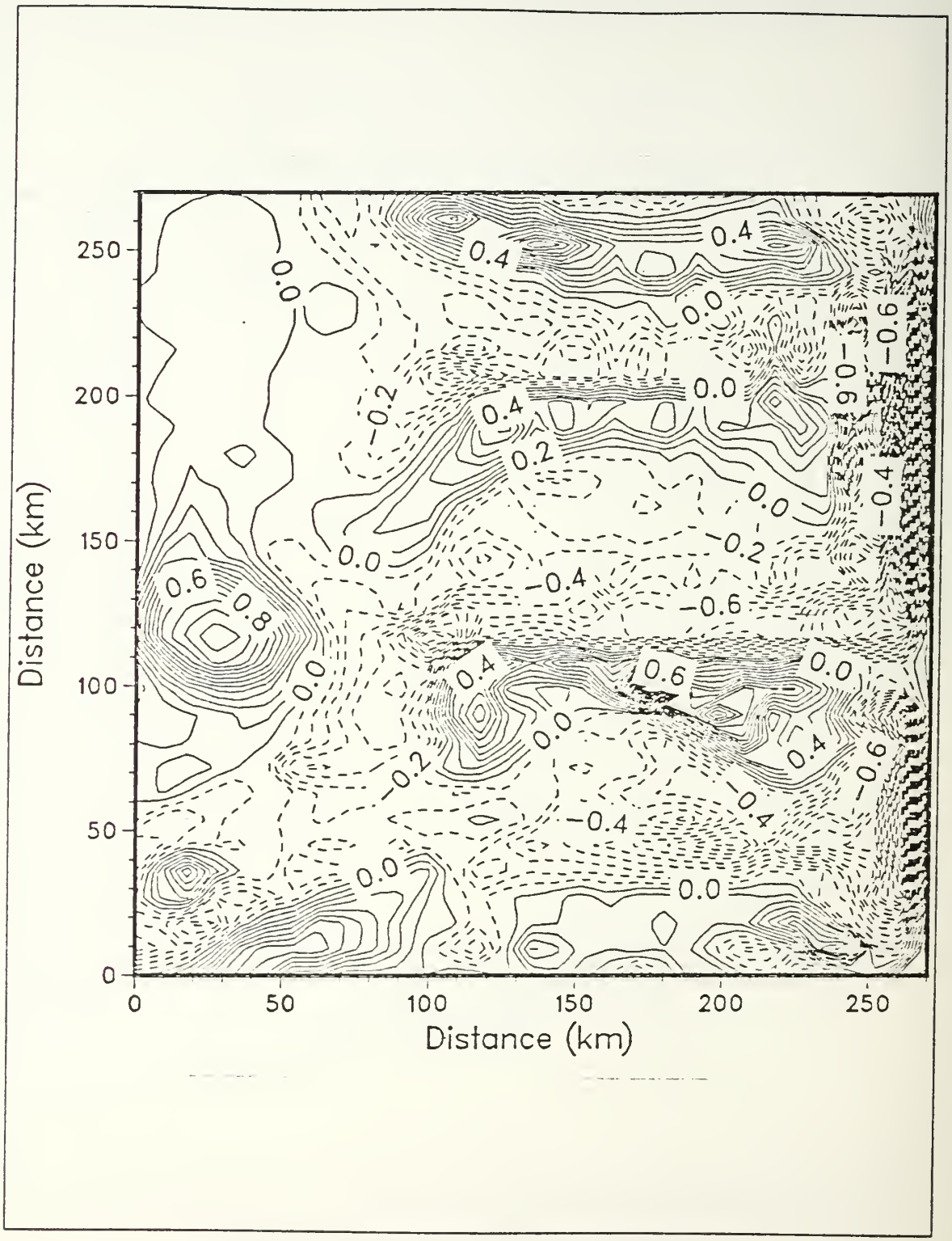

Figure 3.10 SST difference field on day 40, Cruise I.

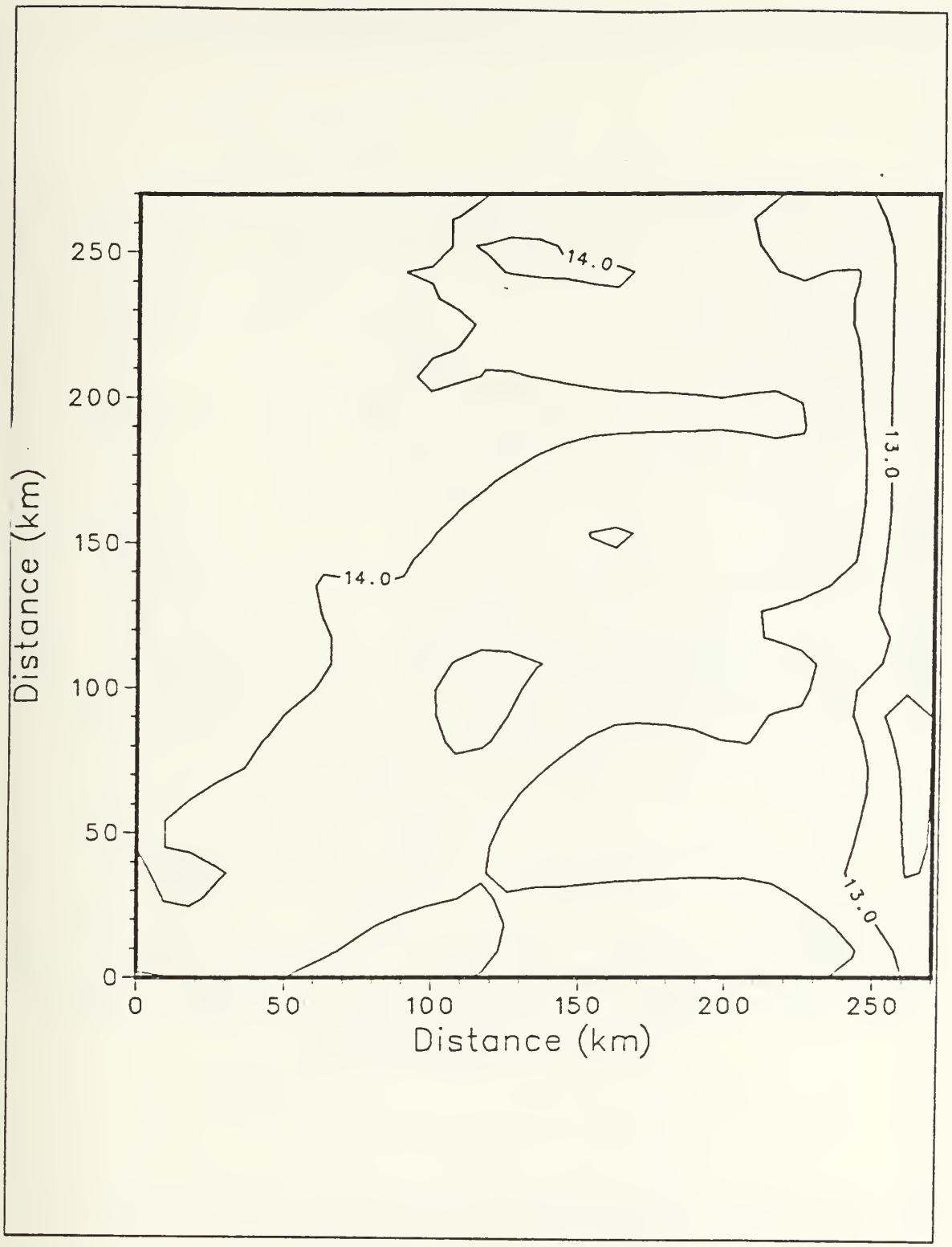

Figure 3.11 Same as Fig. 3.8 but at 25 m.

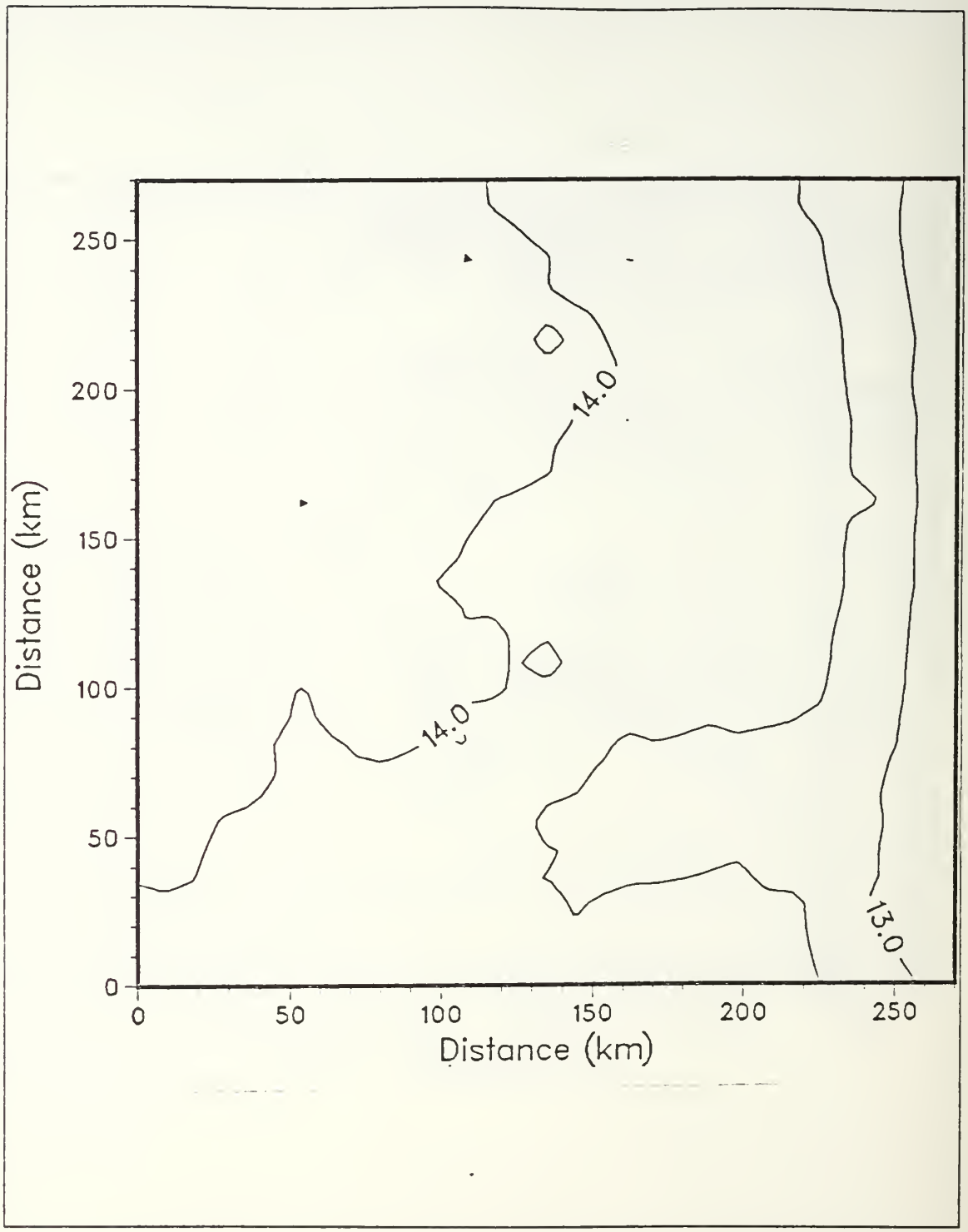

Figure 3.12 Same as Fig. 3.9 but at 25 m,
pattern correlation 0.91,
T range of 12.51 to 14.42 °C.

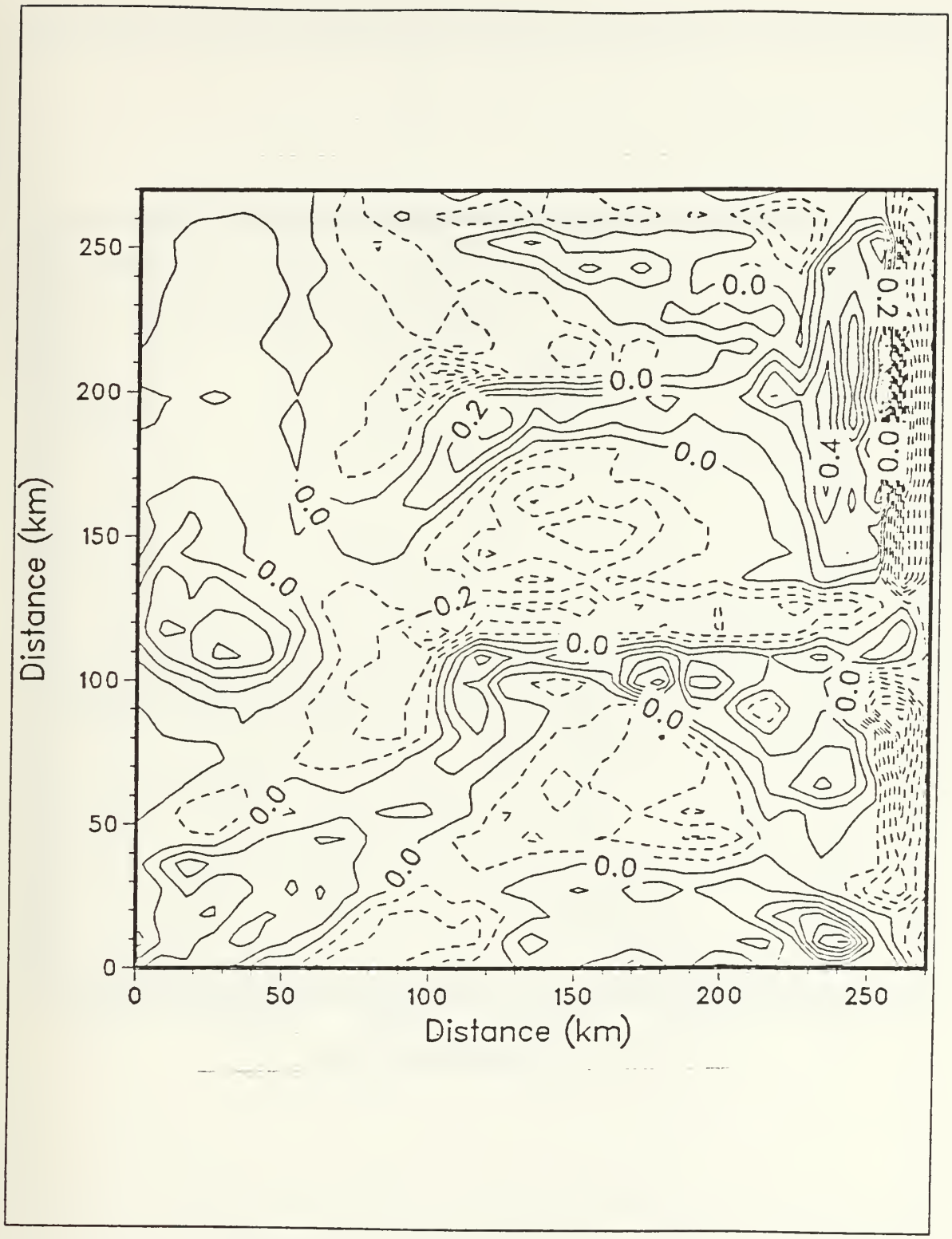

Figure 3.13 Same as Fig. 3.10 but at 25 m.

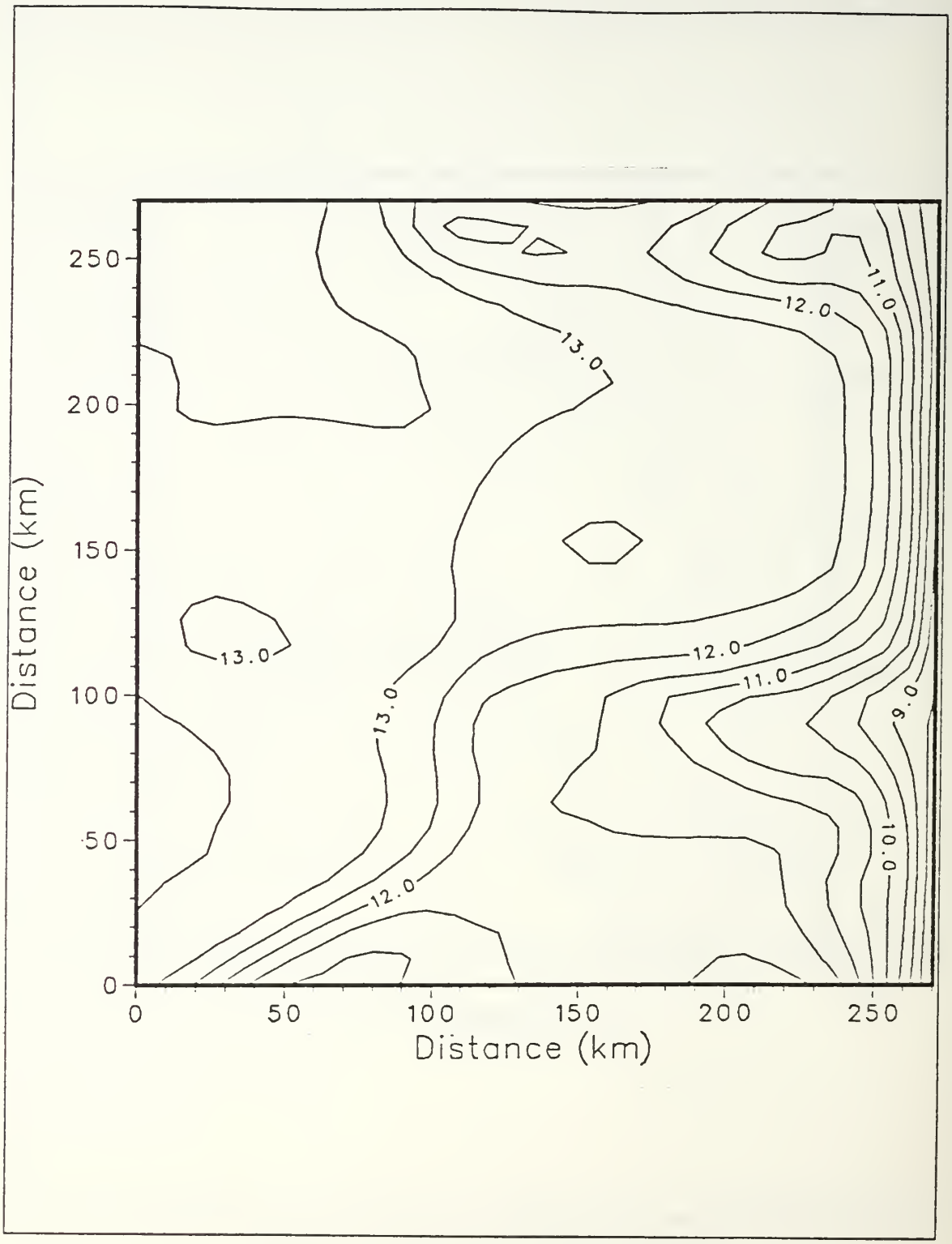

Figure 3.14 Same as Fig. 3.8 but at 50 m.

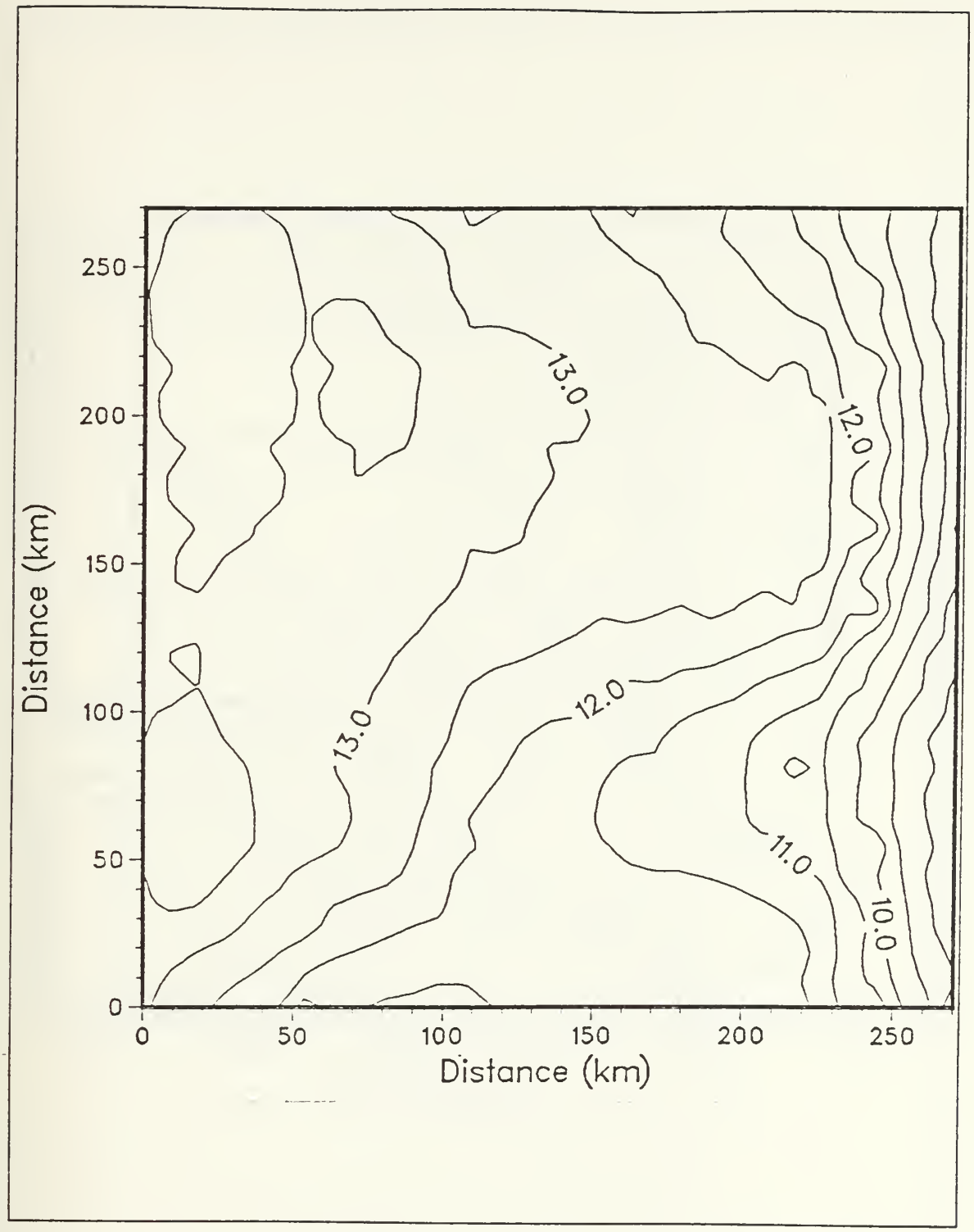

Figure 3.15 Same as Fig. 3.9 but at 50 m, pattern correlation 0.95, T range of 7.94 to 13.75 C.

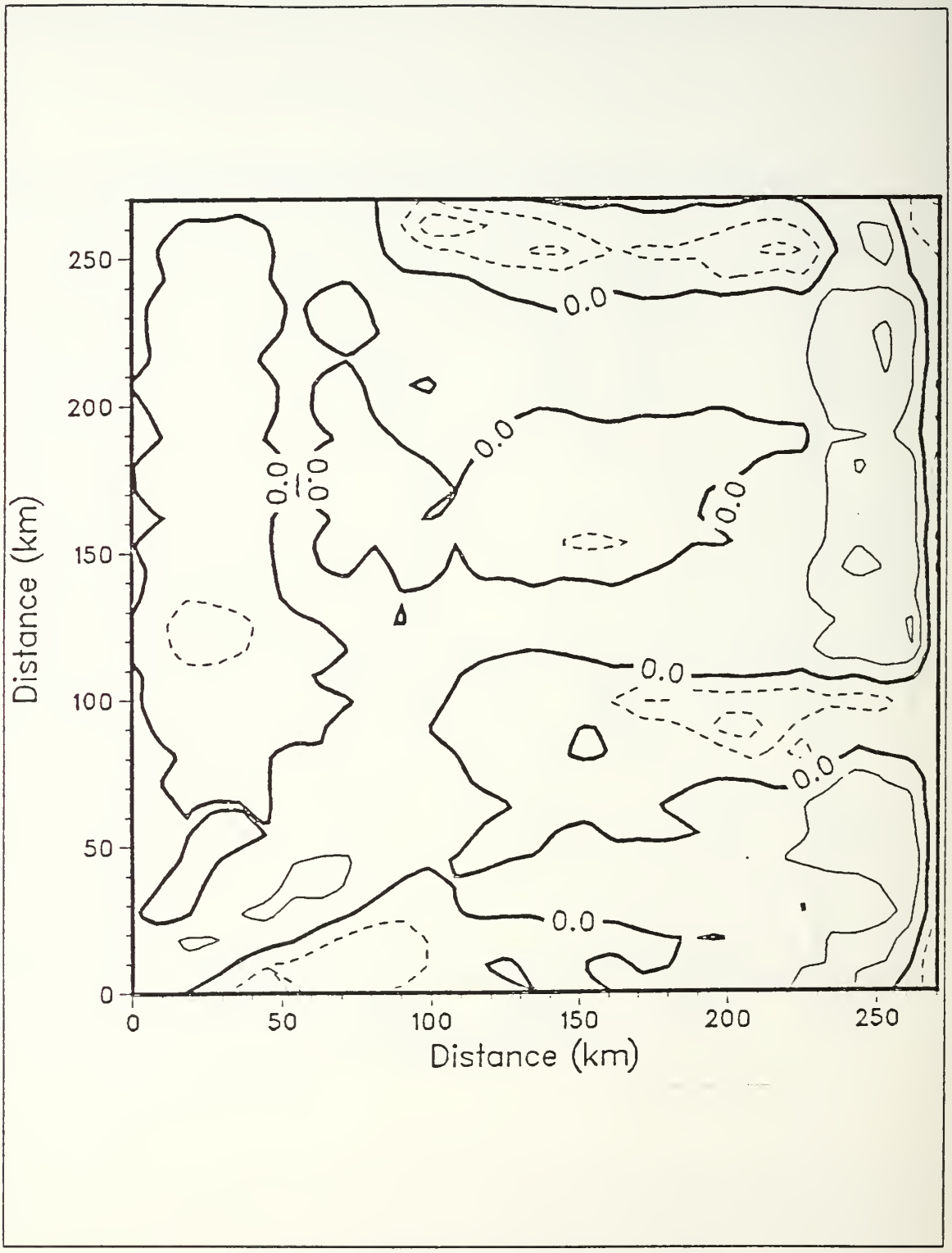

Figure 3.16 Same as Fig. 3.10 but at 50 m.

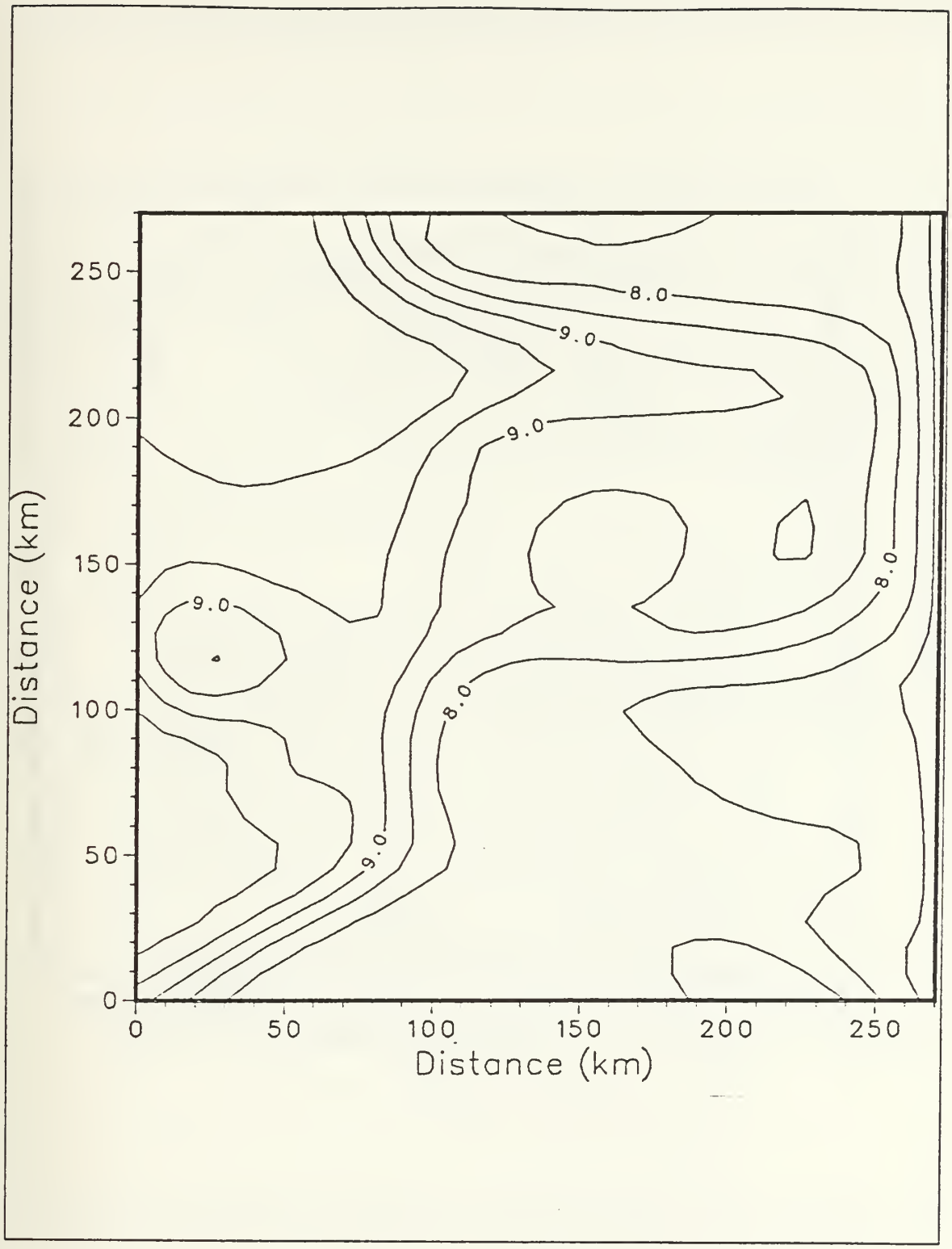

Figure 3.17 Same as Fig. 3.8 but at 200 m.

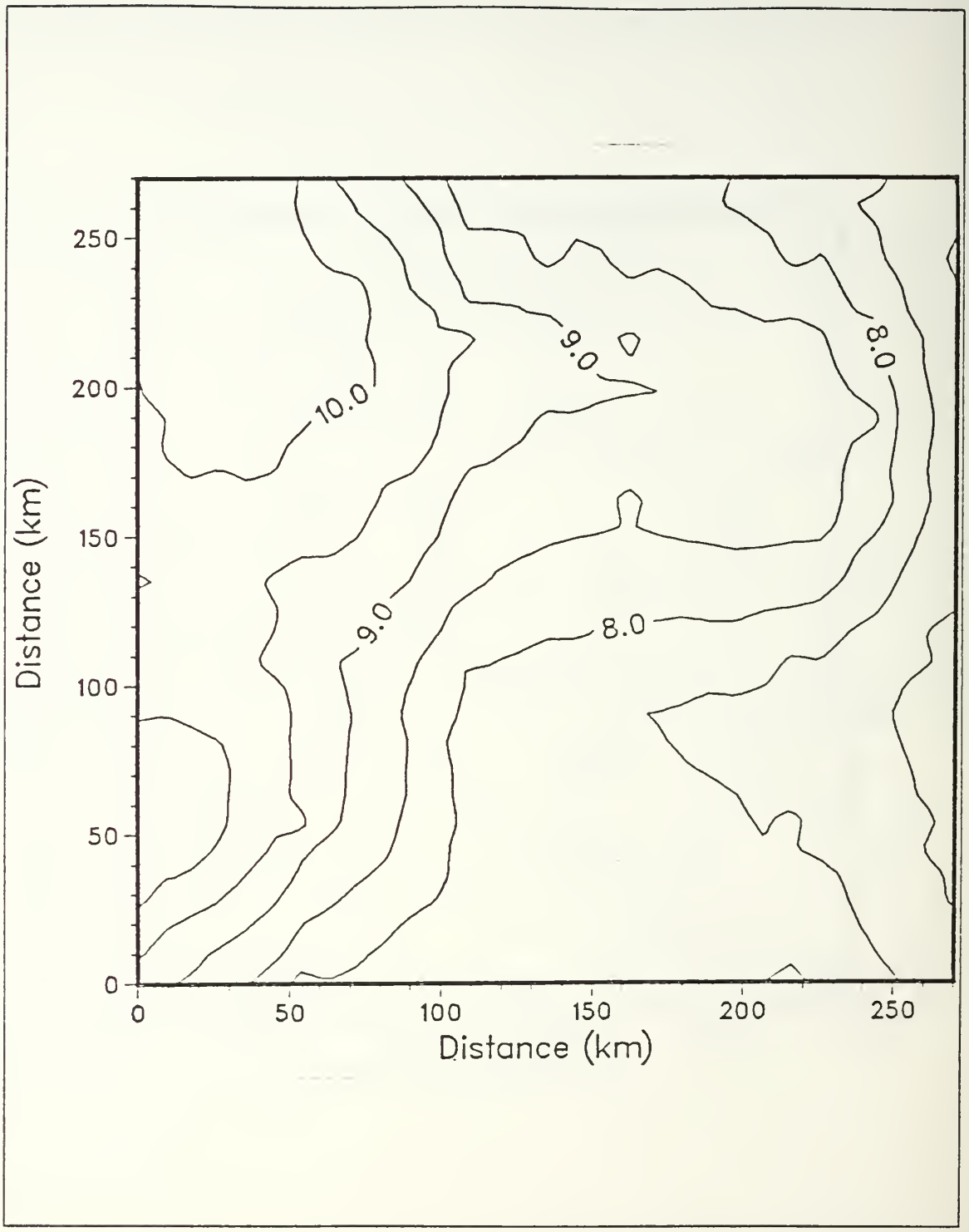

Figure 3.18 Same as Fig. 3.9 but at 200 m, pattern correlation 0.94, T range of 6.68 to 10.42 C.

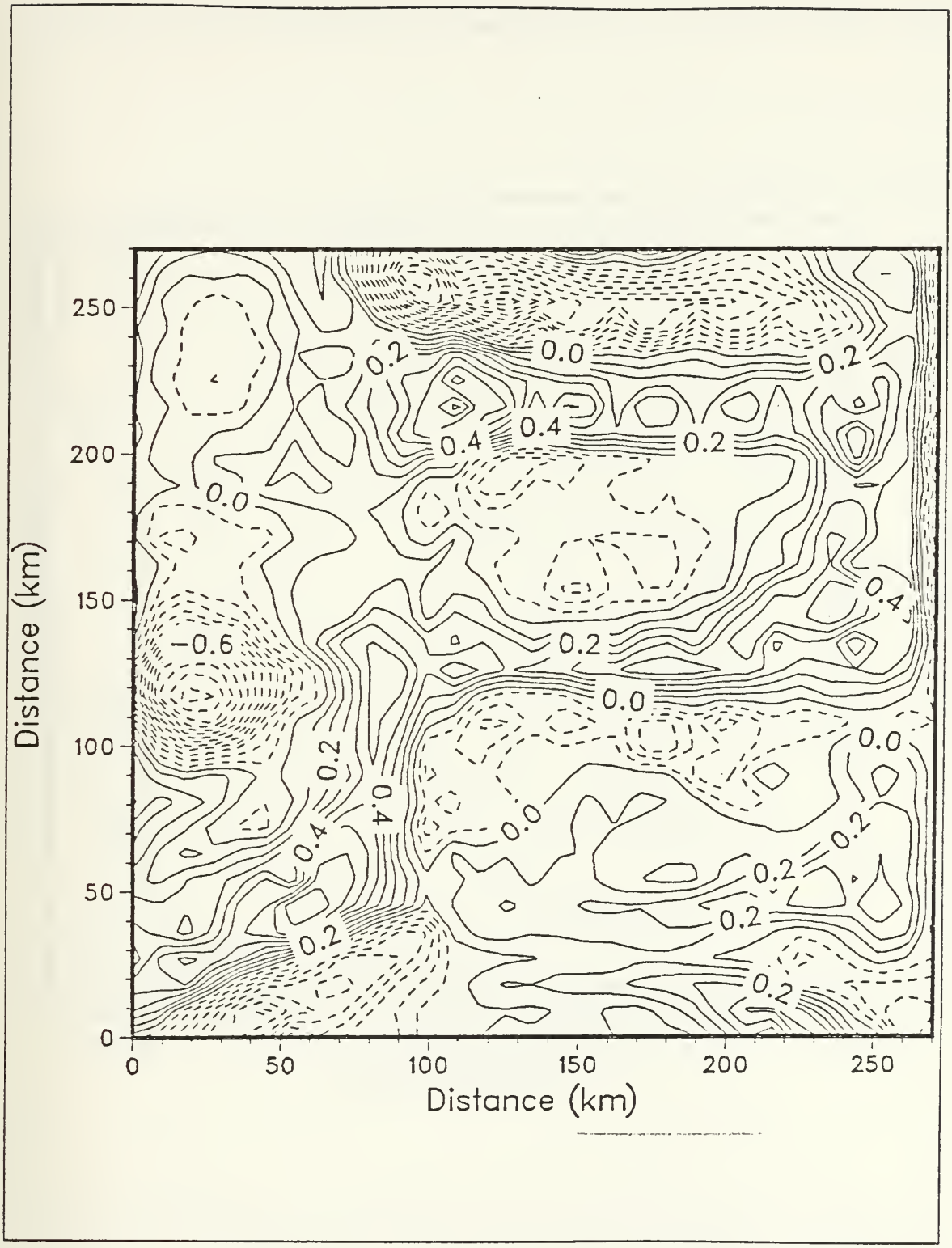

Figure 3.19 Same as Fig. 3.10 but at 200 m.

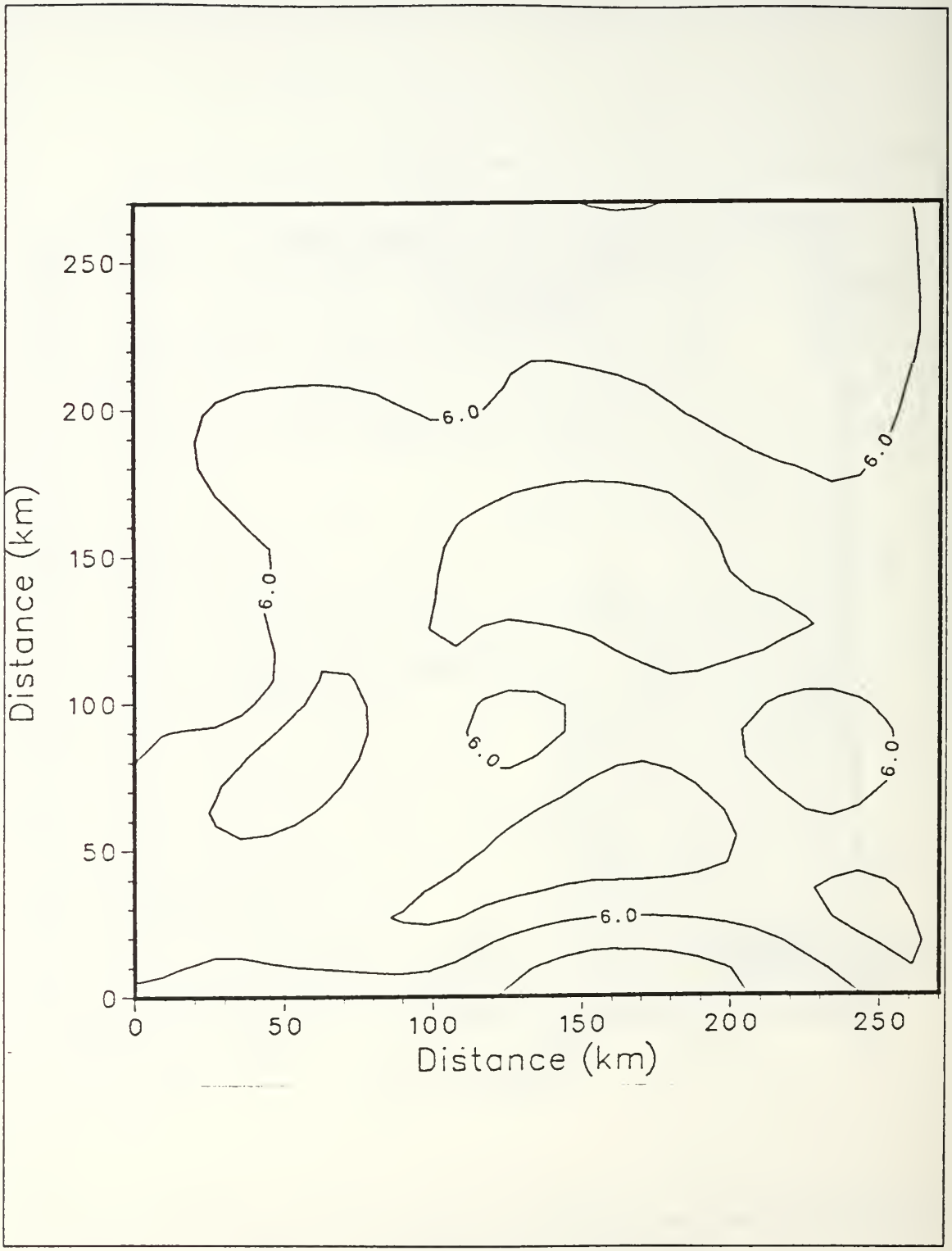

Figure 3.20 Same as Fig. 3.8 but at 550 m.

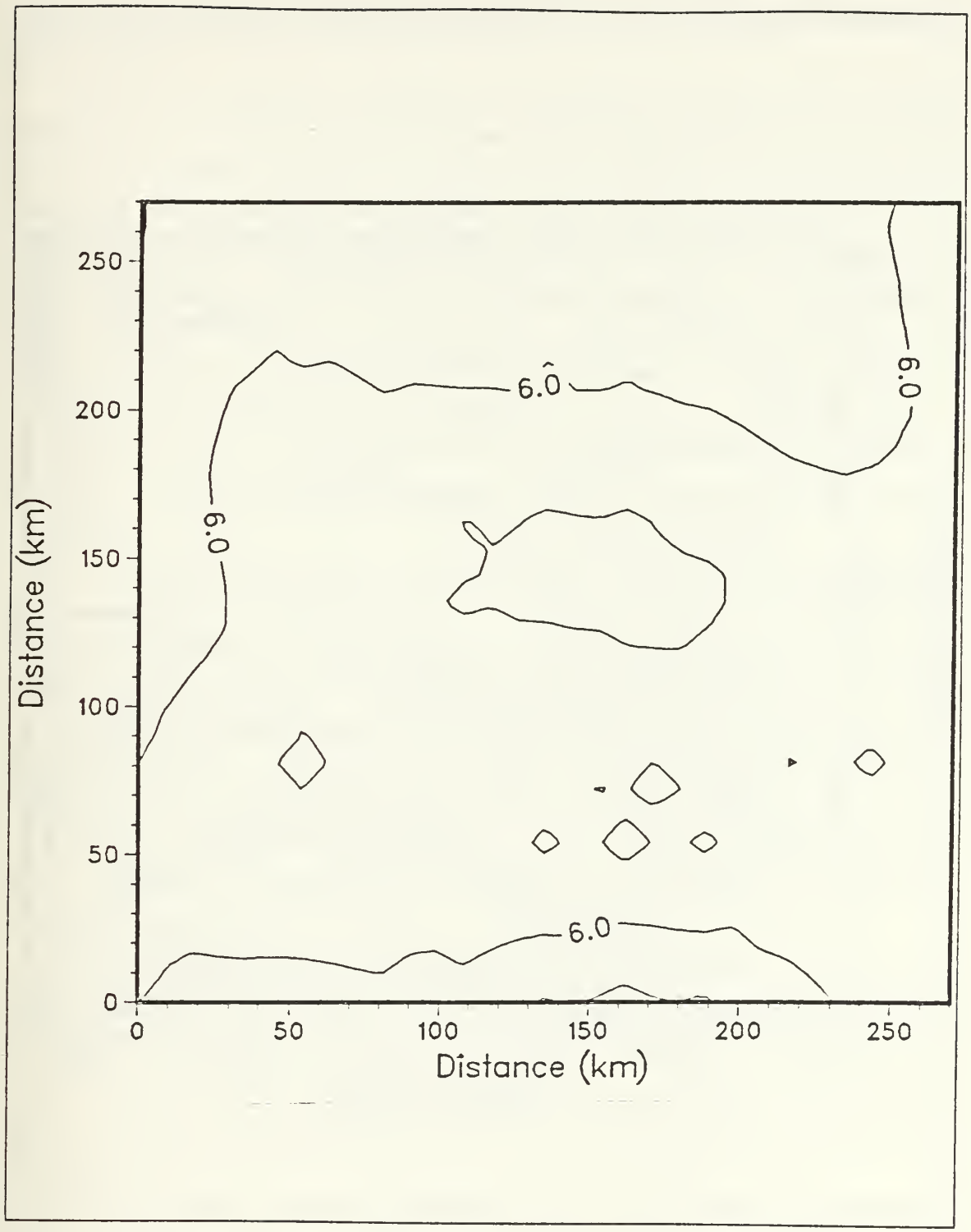

Figure 3.21 Same as Fig. 3.9 but at 550 m,
pattern correlation 0.86,
T range of 6.12 to 6.99 C.

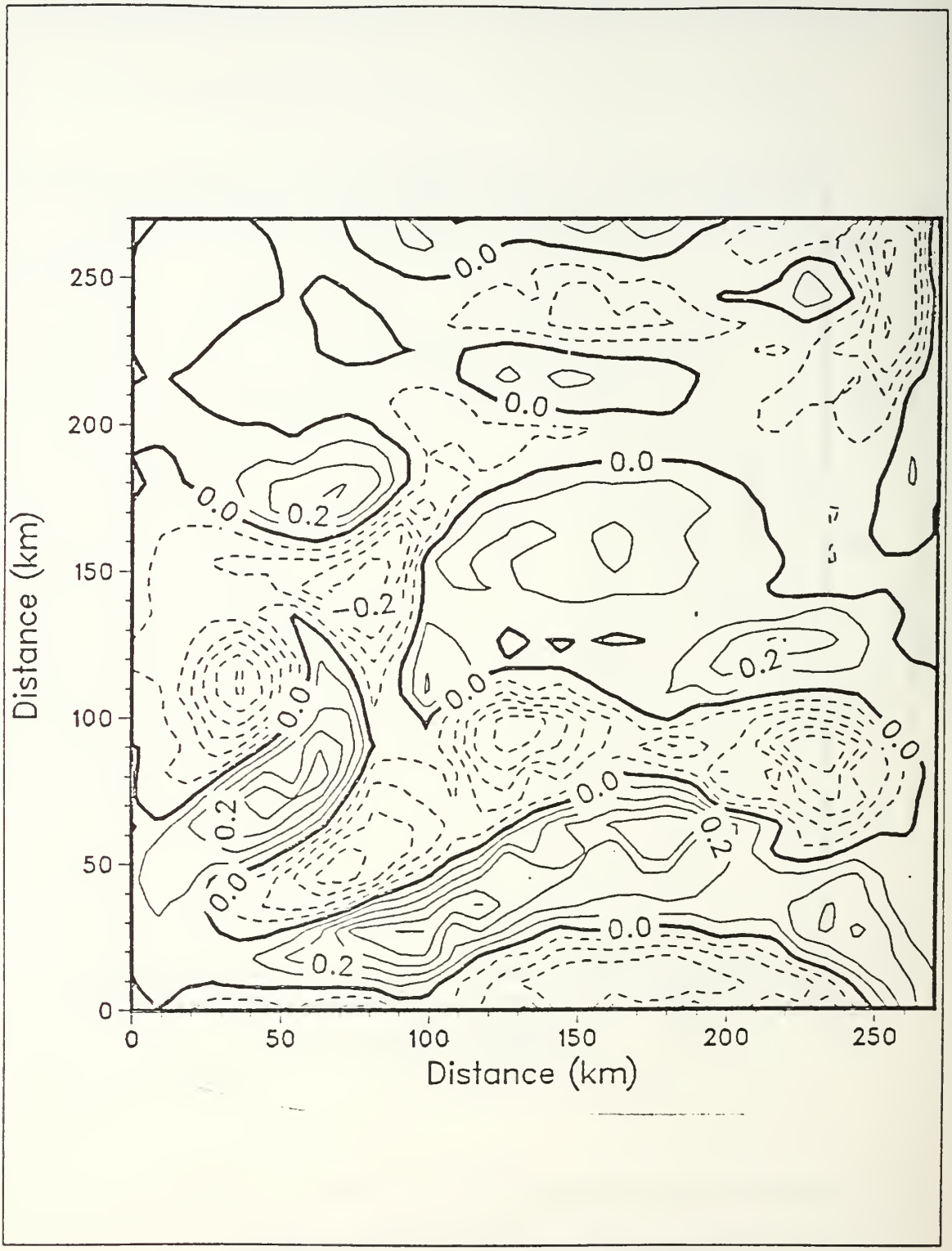

Figure 3.22 Same as Fig. 3.10 but at 550 m.

maximum in the error field of 48% occupies the area between the largest AXBT station spacing offshore.

Based on the temperature correlation at 50 m (Fig. 3.26), there was a maximum correlation of 1.00 at zero-separation distance and a zero-crossing of approximately 150 km. The correlation patterns at the other depths exhibited a similar pattern of a rapid falloff from zero lag with an exponential decay to the zero-crossing distance with no intermittant peaks of high autocorrelation. Zero-crossing distances tended to be somewhat less, approximately 130 km, in the upper layers of the ocean (Fig. 3.25) due to higher mesoscale variability. Half-correlation points varied from a minimum at the surface of 15 km to a maximum at 550 m depth of 35 km. No repetition is evident in each of the correlograms, giving an impression that the pattern of observations is non-periodic. Little, if any, importance should be attached to the autocorrelations at lags greater than the zero-crossing distances because they fall within the level of small confidence.

The statistics calculated for the comparison of the PE 'perfect' data fields and the OA interpolated fields are presented in Table 3. Again, the OA surface temperature field shows a poor resemblance to the true field (Figs. 3.27-3.28) with a pattern correlation of 71% indicating a dissimilar match. Depiction of the major features of the PE field along the eastern boundary were best represented. Entire features in the western and central domain are absent as a result of the sampling pattern employed. The difference map, Figure 3.29, indicates that the OA technique overestimated the warm temperatures and underestimated the cooler ones in this area. Maximum negative differences occurred along the eastern boundary in conjunction with the strong temperature front.

The temperature analysis at 25 m depth (Figs. 3.30-3.31) was favorable. Overall pattern correlation of 91% indicates a very similar match. The difference field, Figure 3.32, shows a clear underestimate of the temperatures throughout the majority of the domain with the weakest interpretation of temperatures occurring in the southwest region. This can be explained by the variation of the sampling distance in the east-west direction.

The high pattern correlation coefficient of 0.95 at 50 m depth is very reasonable when one notices the strong resemblance of the flow field between the PE and OA maps (Figs. 3.33-3.34). However, degradation of the temperature field still occurs along the western boundary where station spacing was a maximum. The difference field,

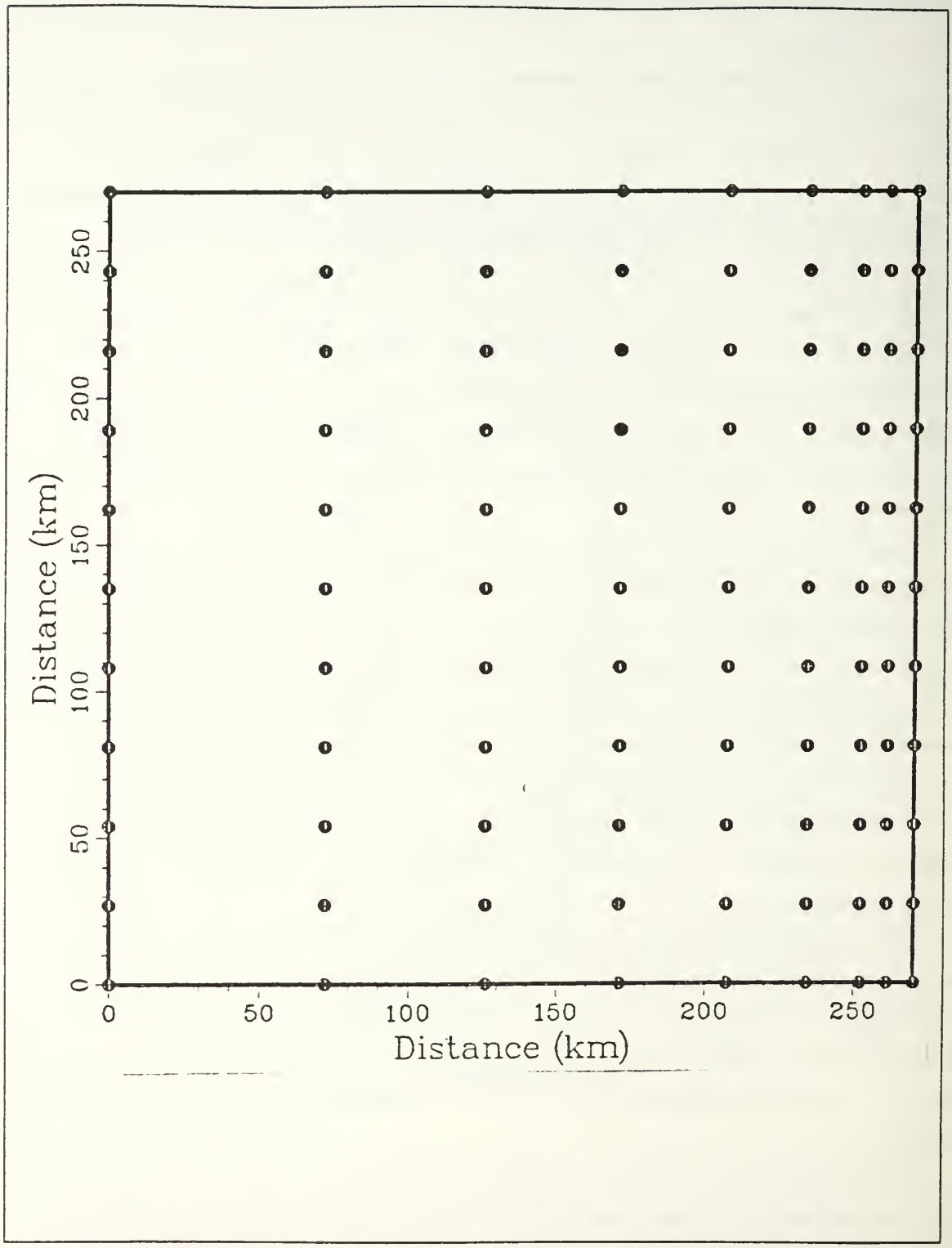

Figure 3.23 Cruise II station positions.

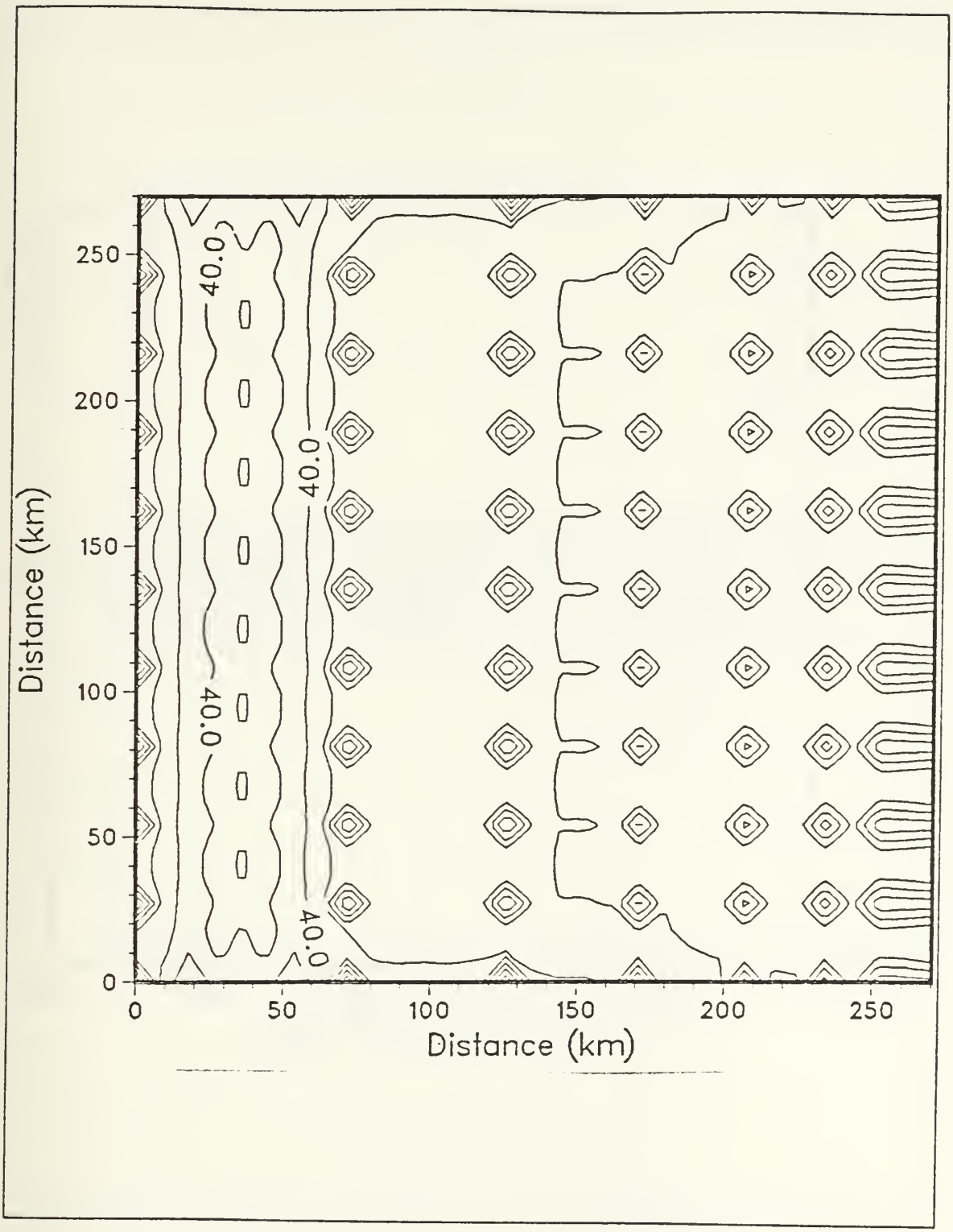

Figure 3.24 Cruise II temperature error field with error range from 12 to 48%.

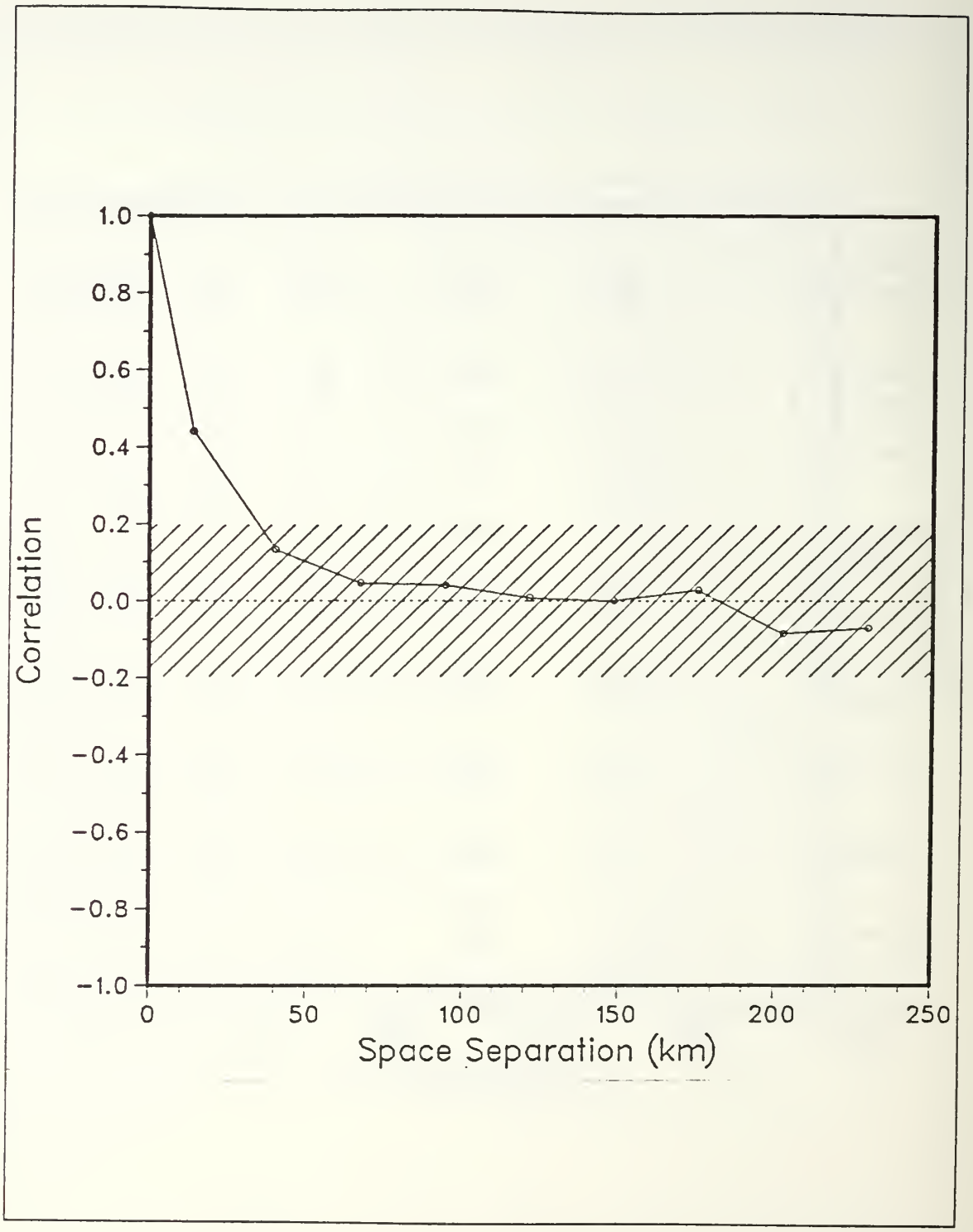

Figure 3.25 Correlation of temperature at sea surface on day 40, Cruise II, zero-crossing distance of 121.5 km.

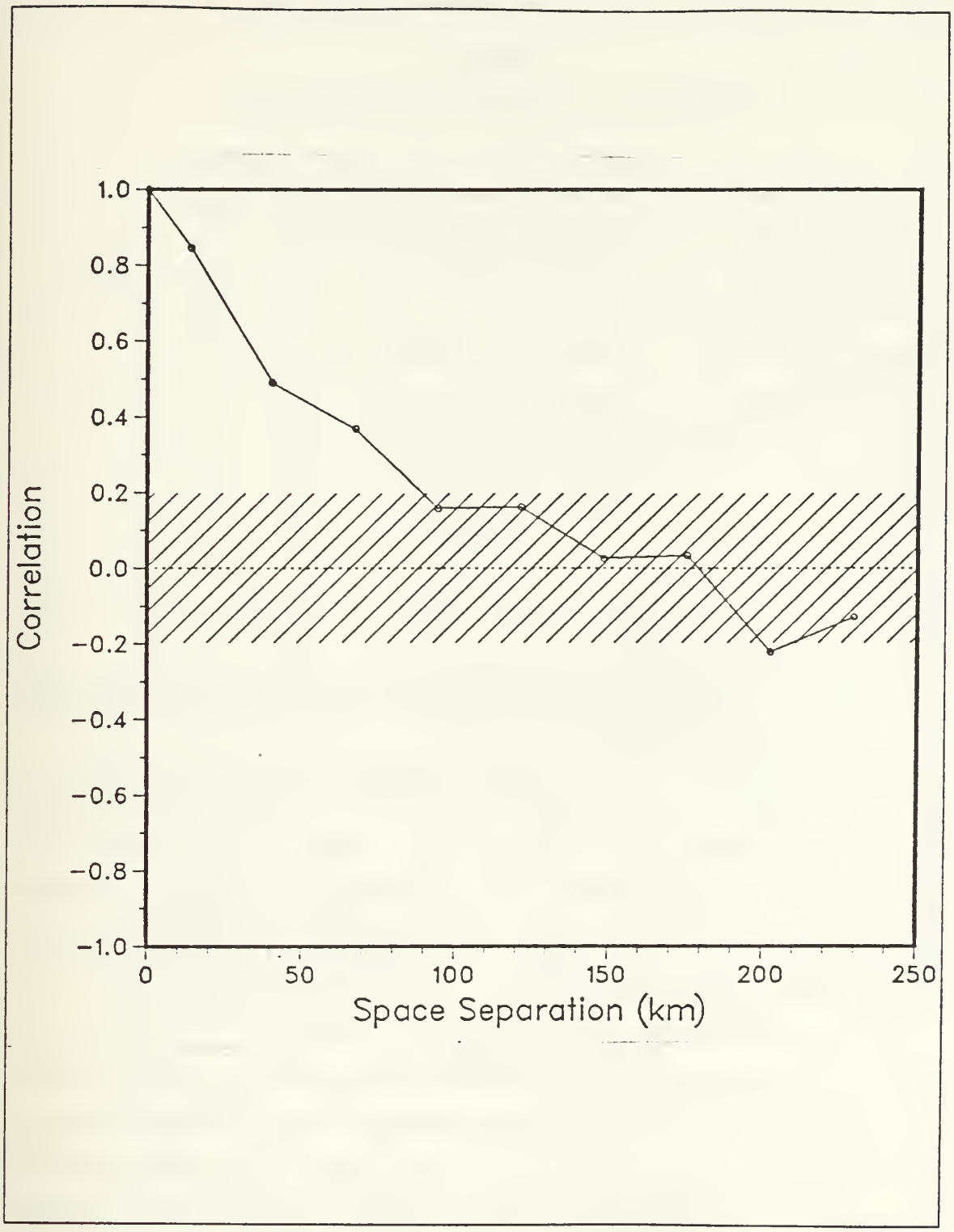

Figure 3.26 Same as Fig. 3.25 but at 50 m, zero-crossing distance of 148.5 km.

TABLE 3
STATISTICAL MEASURES OF P-3 CRUISE II

	Surface	25 m	50 m	200 m	550 m
PE Mean Temp	14.98	13.72	12.27	8.61	6.11
OA Mean Temp	15.00	13.71	12.25	8.59	6.12
PE Variance	0.50	0.22	1.50	1.06	0.12
OA Variance	0.21	0.17	1.30	0.87	0.05
Zero-Crossing	121.5	121.5	148.5	105.5	142.5
Pattern Corr	0.71	0.91	0.95	0.94	0.85
MAE	0.35	0.15	0.27	0.26	0.14
RMSE	0.50	0.19	0.37	0.35	0.19
$RMSE_s$	0.05	0.02	0.03	0.04	0.06
$RMSE_u$	0.49	0.47	0.37	0.35	0.18

Figure 3.35, shows negative values indicating an overestimate of the temperature field by the OA technique in this region.

At first examination, the 200 m analyzed temperature field (Fig. 3.37) appears to be an inferior depiction of the true field (Fig. 3.36), but the basic pattern is still quite representative as is indicative of the 94% correlation. Major features such as the cool filament in the southeast, the warm temperature intrusion in the northwest and the north-south temperature front, although weak, remain evident. The absence of the cool pool of water in the central western region in the interpolated temperature field is due to the lack of observations within that area.

The OA analysis at 550 m depth exhibited an 86% pattern correlation value. Differences in temperature between the PE (Fig. 3.39) and OA (Fig. 3.40) fields were greatest in the areas where mesoscale features existed (Fig. 3.41). In large part, this can be explained by the near isothermal structure at depth along with a sampling scheme which concentrated acquiring data along the coast. A more equally spaced observational pattern in both the east-west and north-south directions could improve the representation of mesoscale features in the interpolated field.

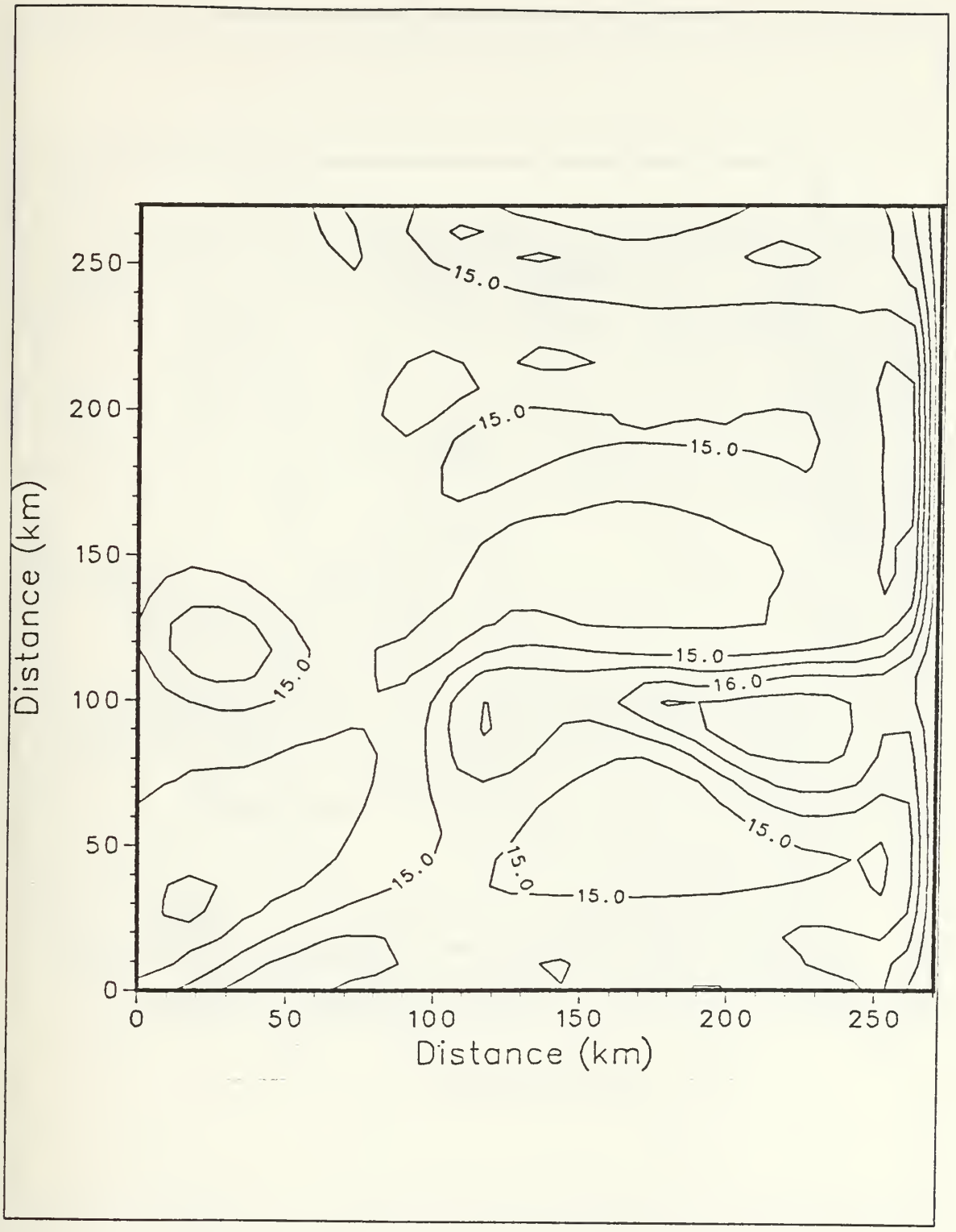

Figure 3.27 PE model SST field on day 40, contour interval of 0.5 C.

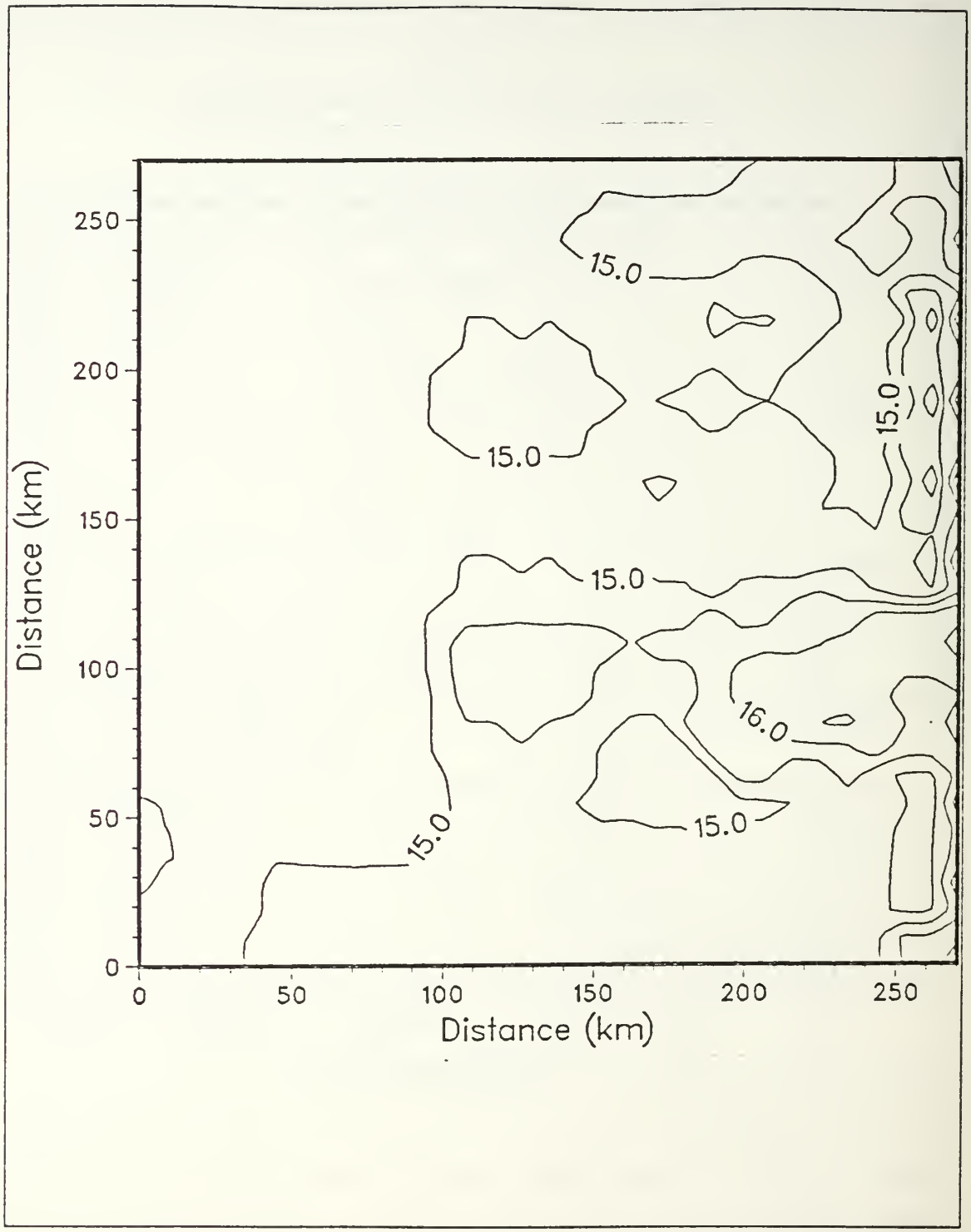

Figure 3.28 OA interpolated SST field on day 40,
Cruise II, pattern correlation 0.71,
T range of 12.54 to 16.95 C.

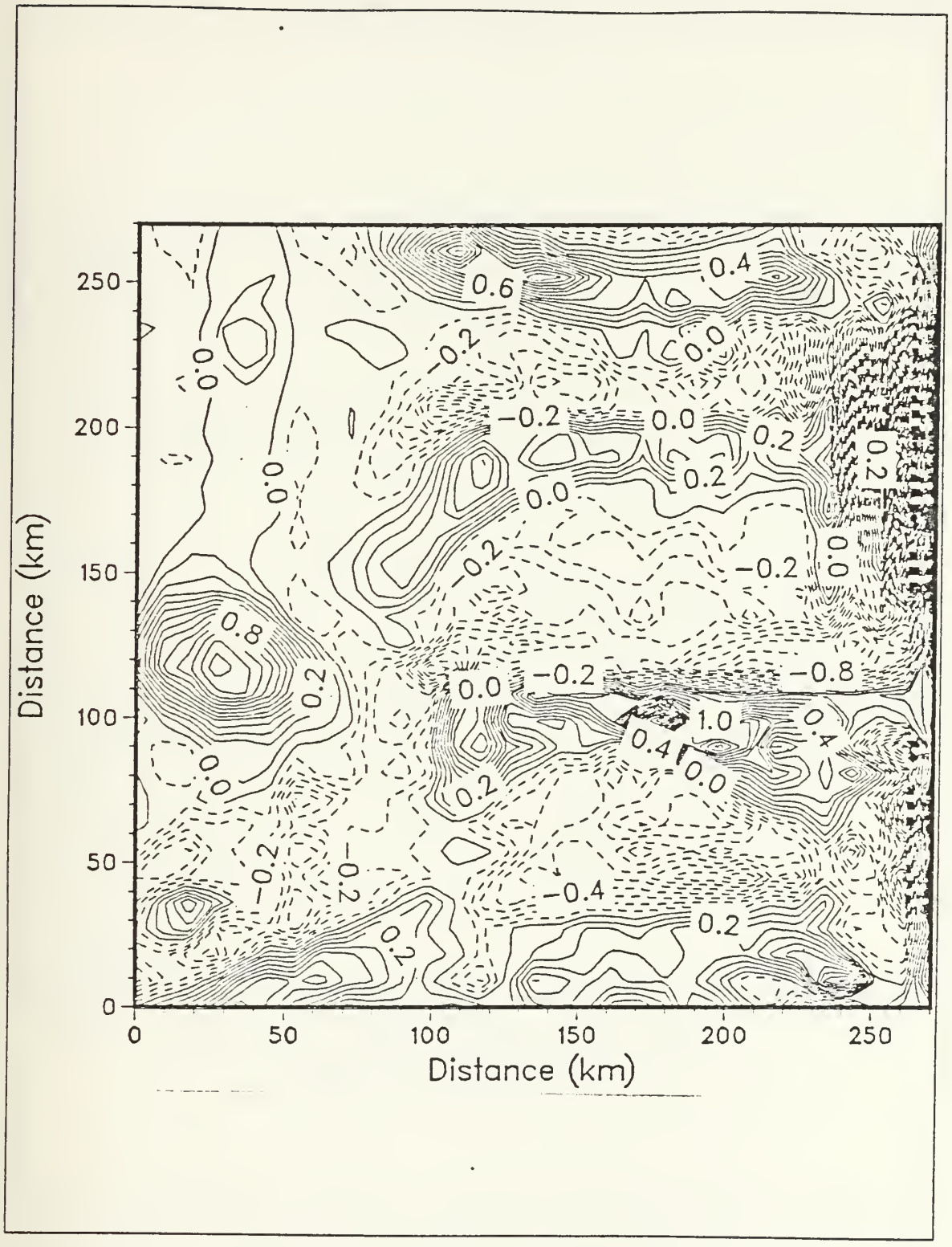

Figure 3.29 SST difference field on day 40, Cruise II.

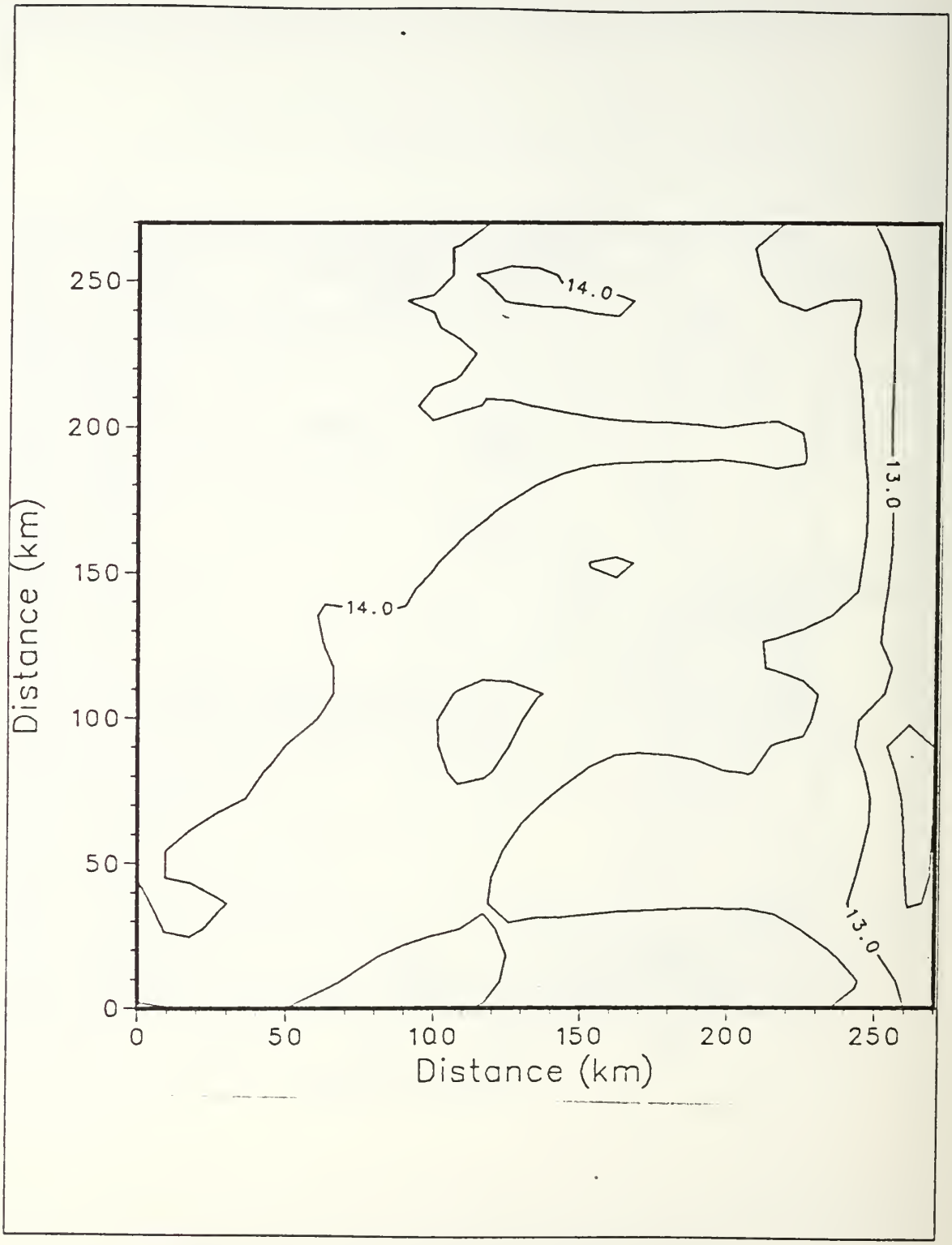

Figure 3.30 Same as Fig. 3.27 but at 25 m.

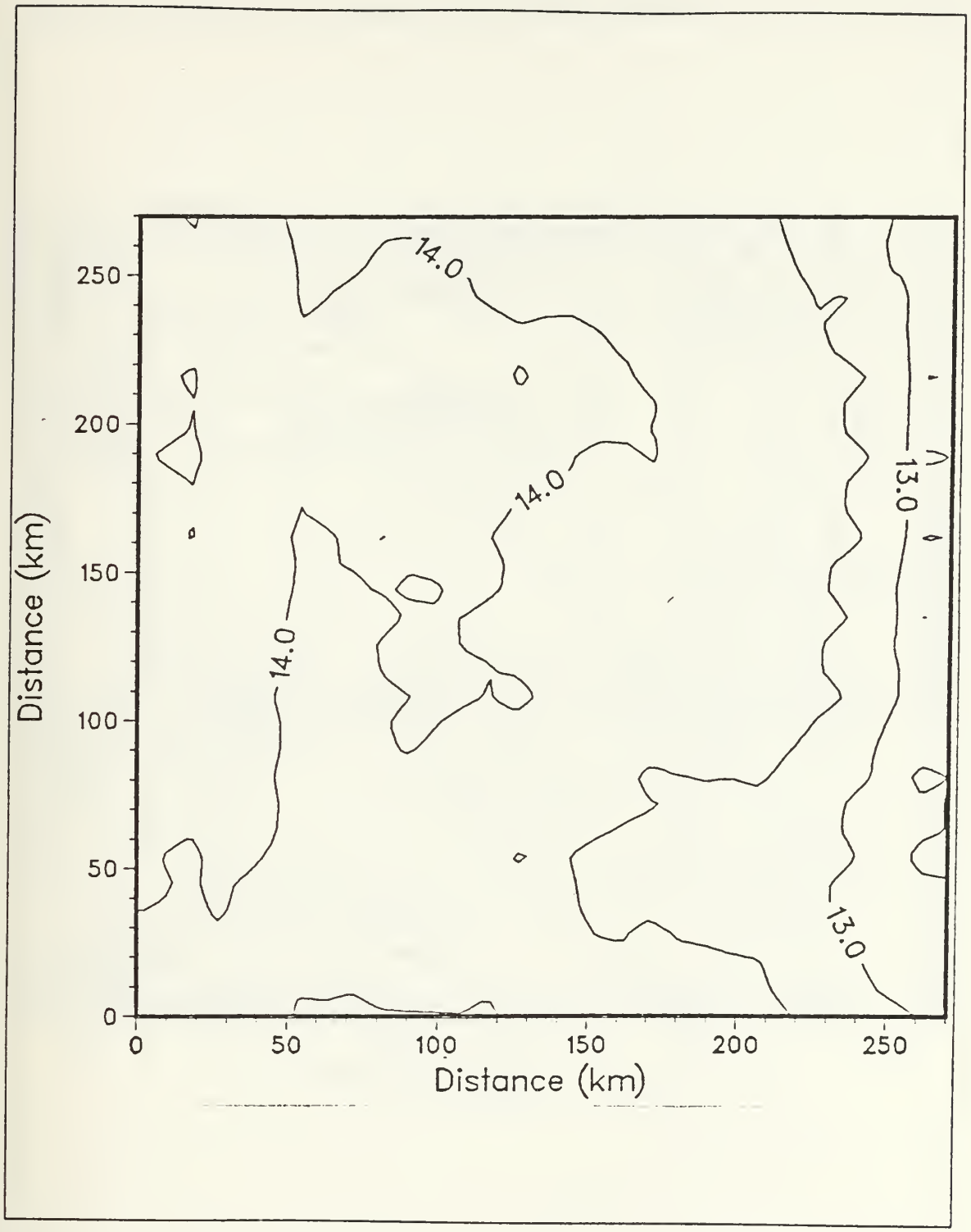

Figure 3.31 Same as Fig. 3.28 but at 25 m,
pattern correlation 0.91,
T range of 12.01 to 14.43 C.

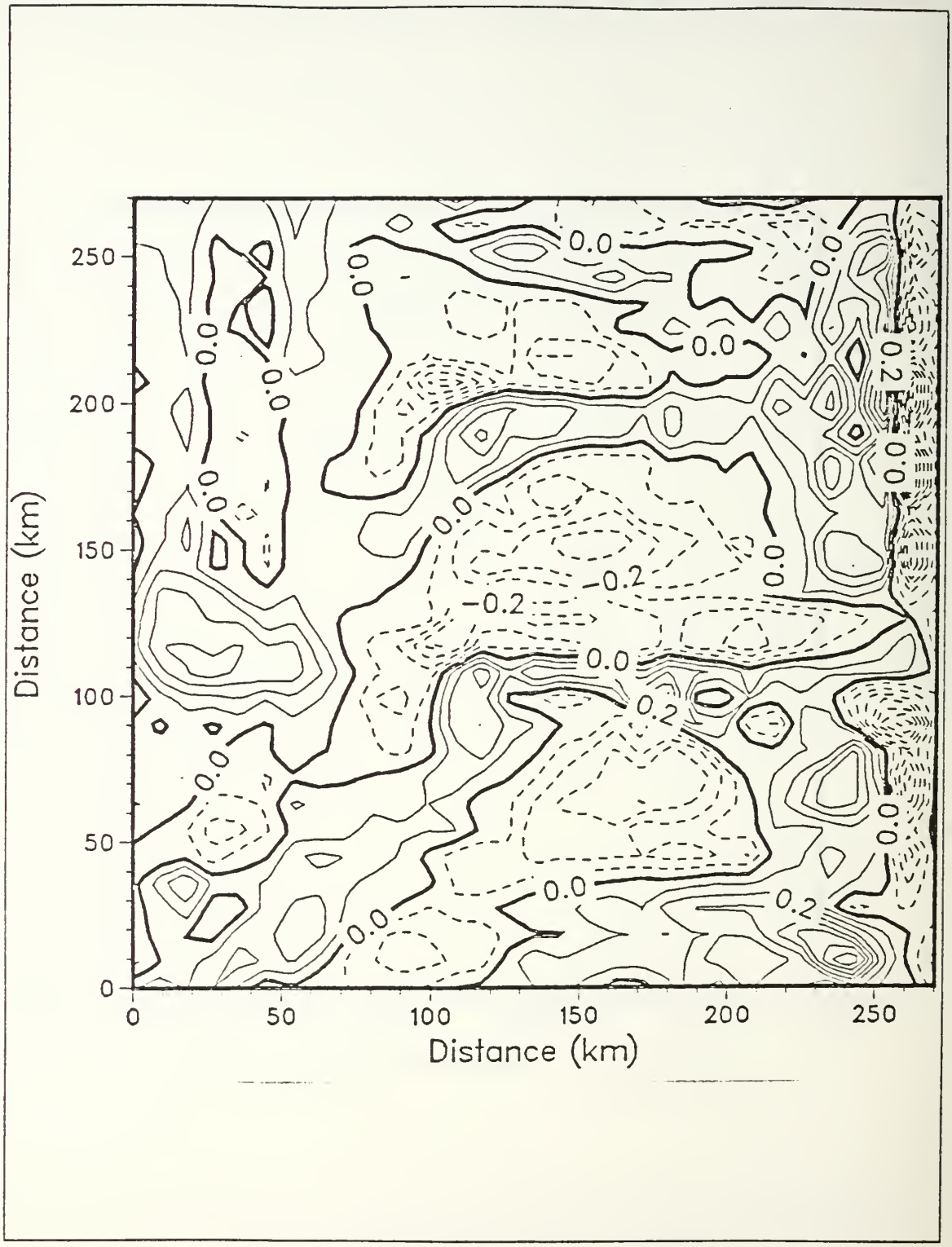

Figure 3.32 Same as Fig. 3.29 but at 25 m.

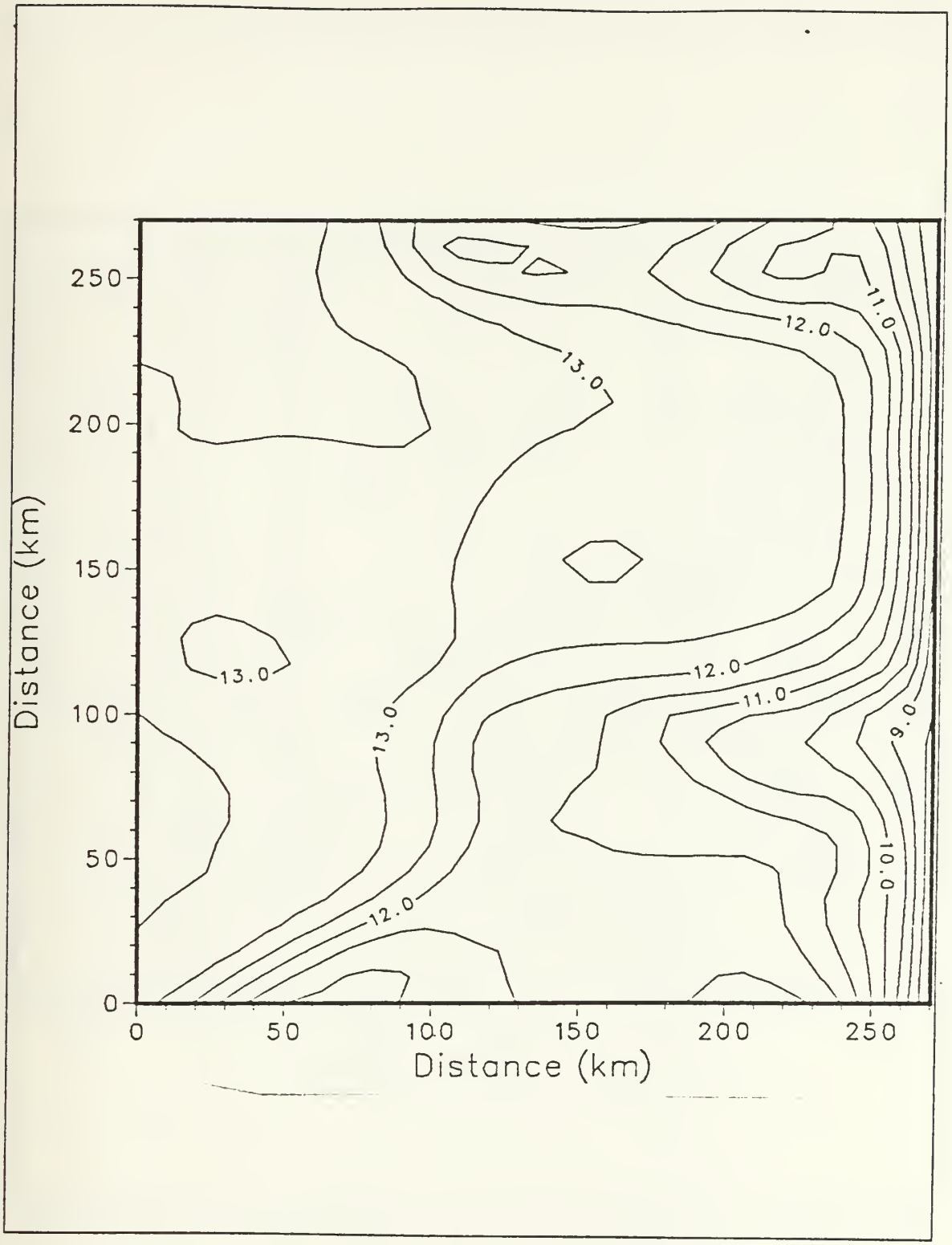

Figure 3.33 Same as Fig. 3.27 but at 50 m.

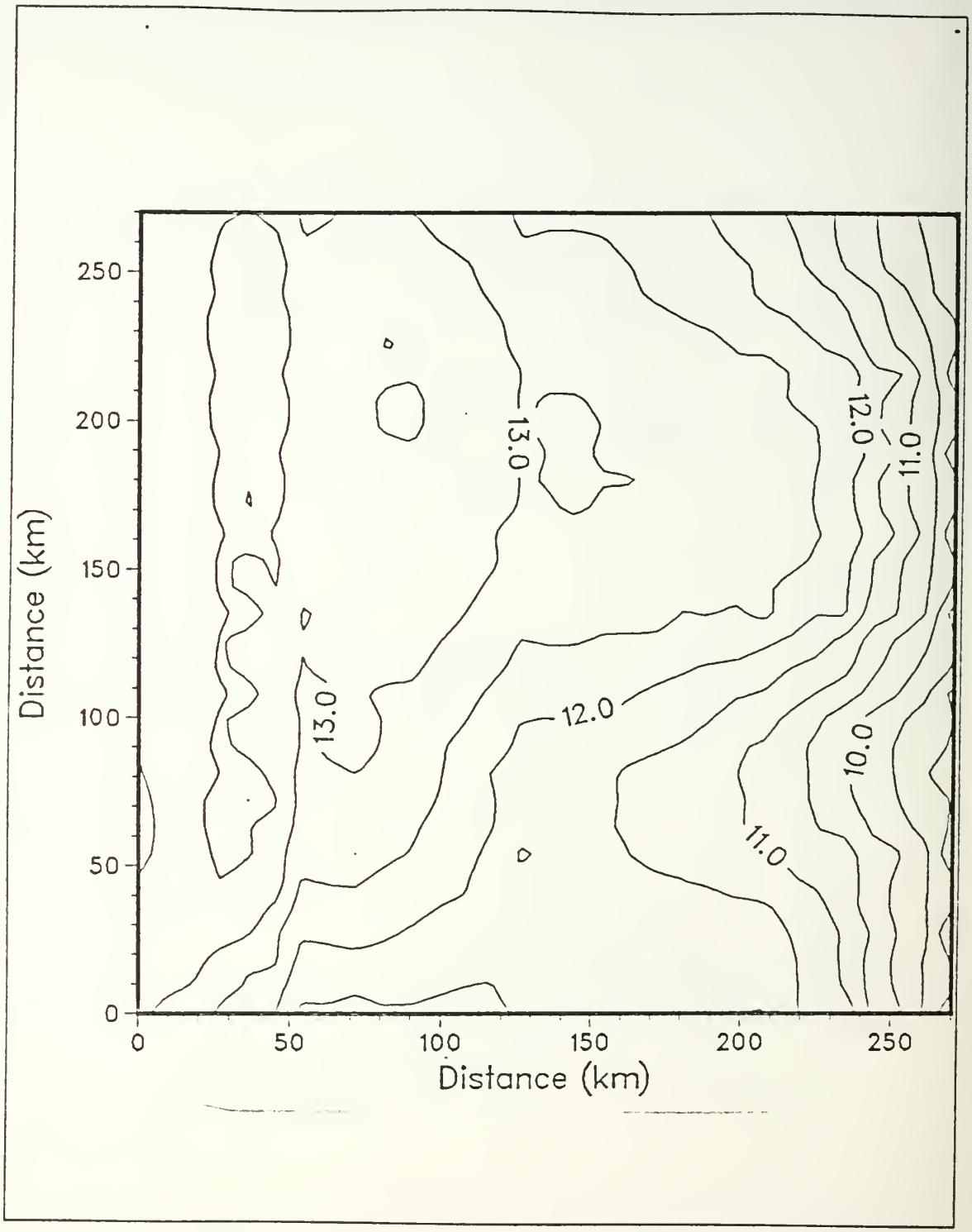

Figure 3.34 Same as Fig. 3.28 but at 50 m, pattern correlation 0.95, T range of 7.94 to 13.75 C.

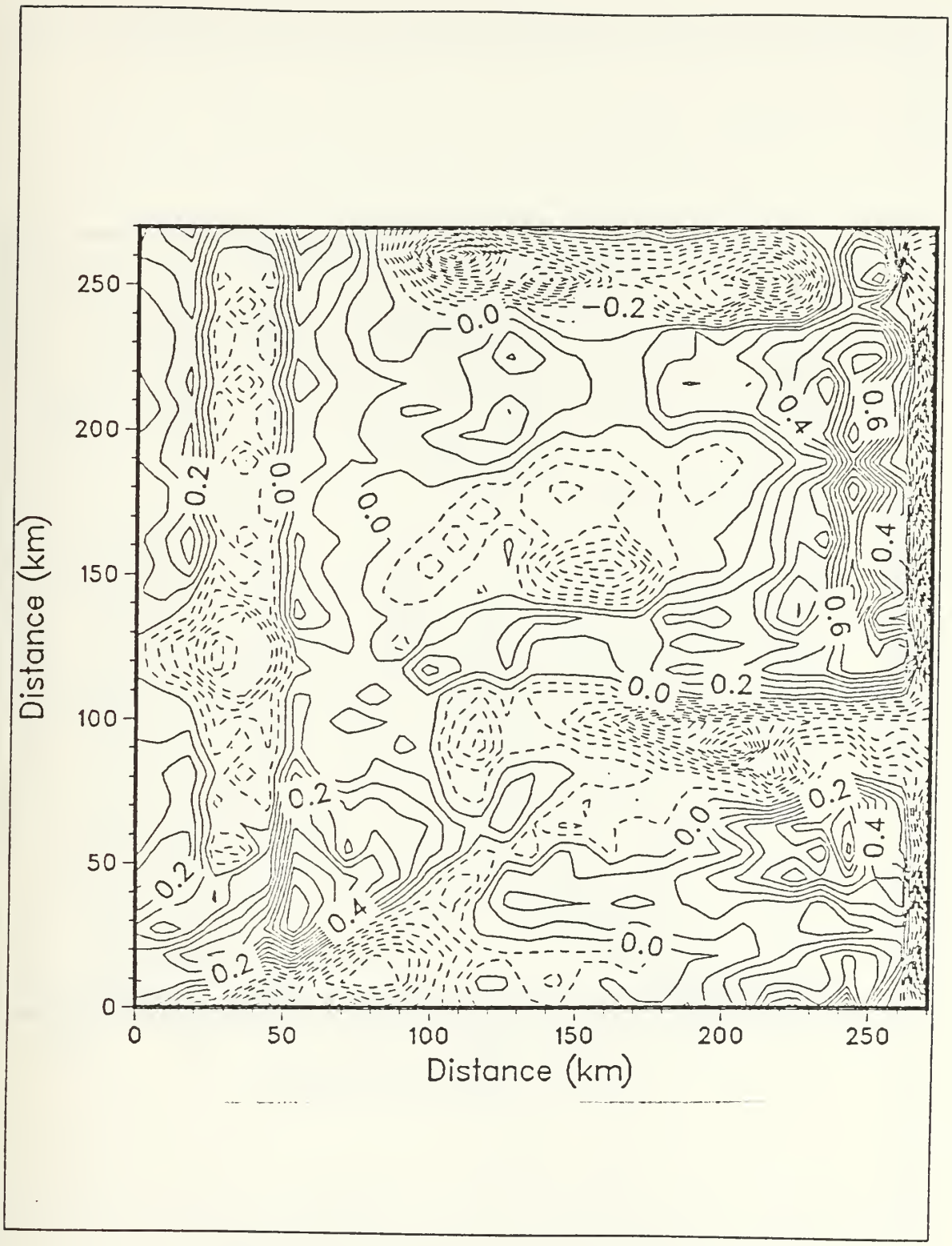

Figure 3.35 Same as Fig. 3.29 but at 50 m.

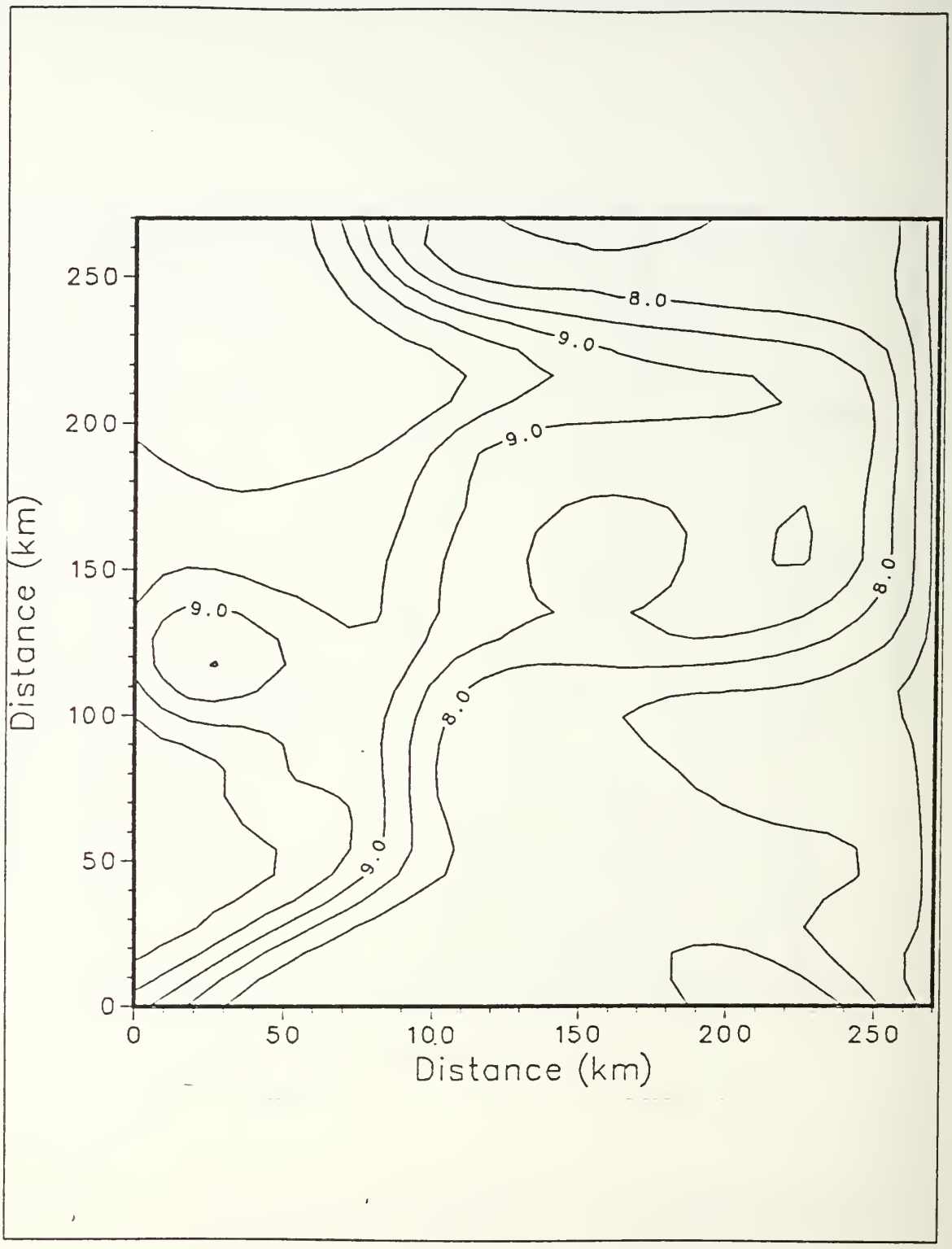

Figure 3.36 Same as Fig. 3.27 but at 200 m.

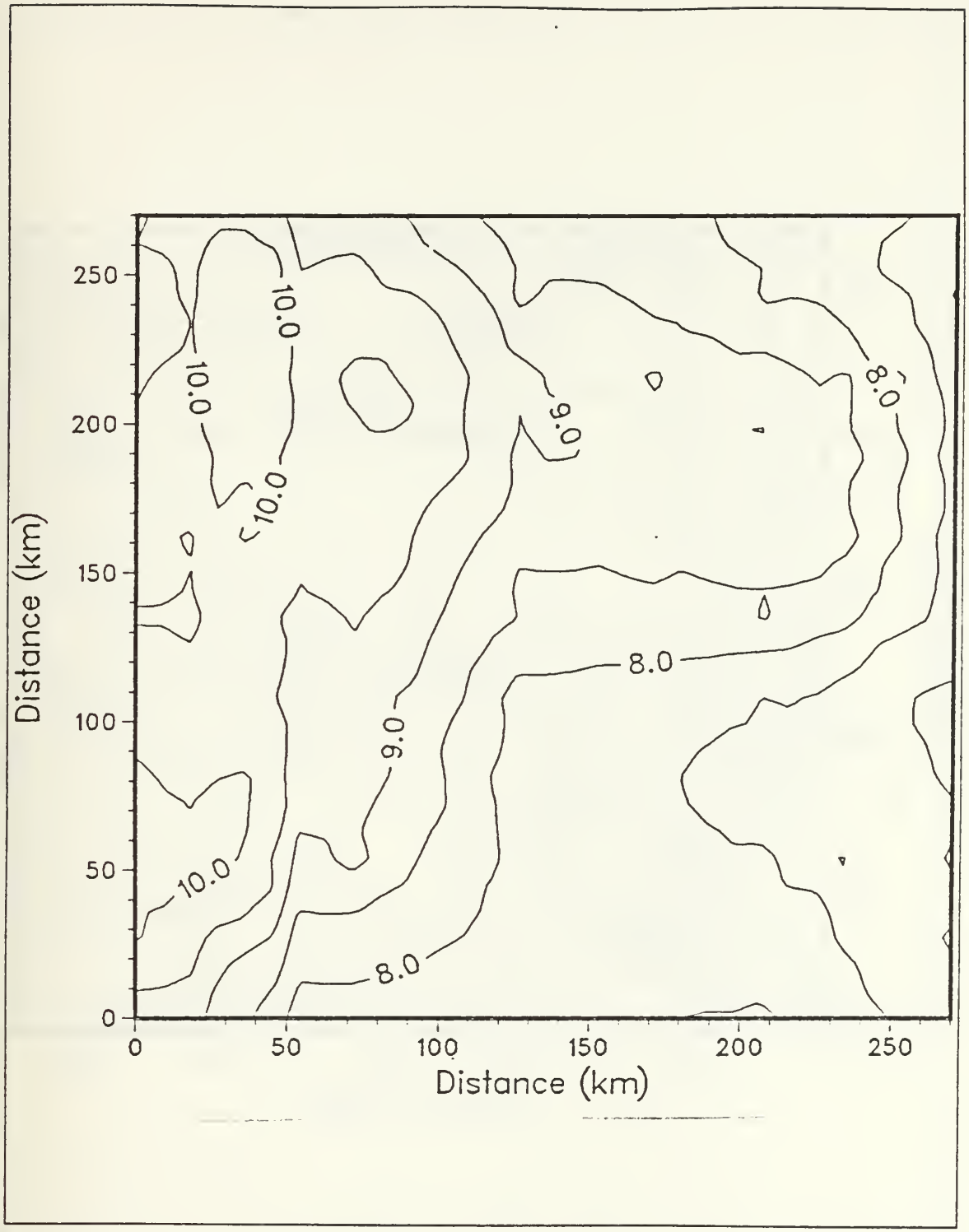

Figure 3.37 Same as Fig. 3.28 but at 200 m, pattern correlation 0.94, T range of 6.68 to 10.42 C.

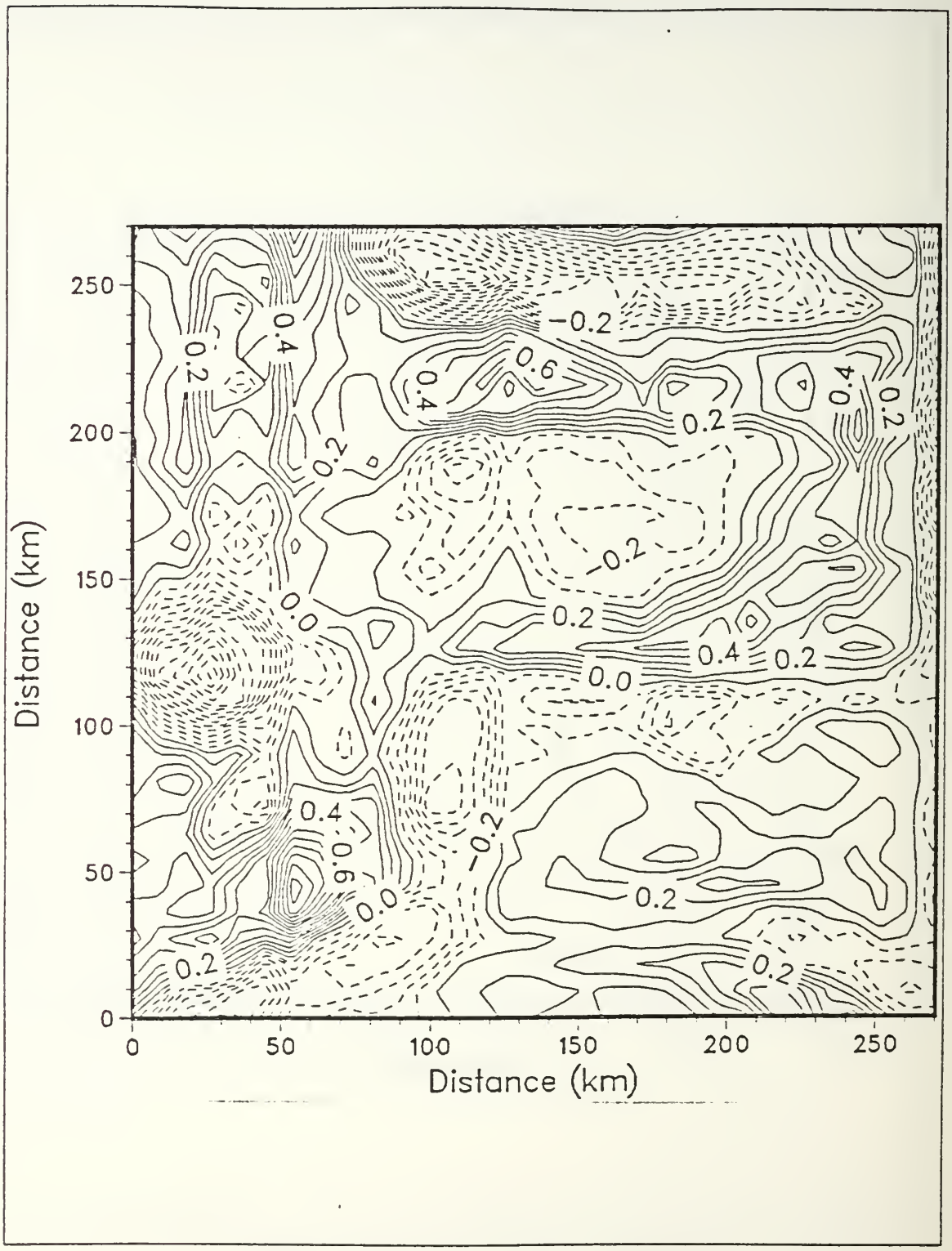

Figure 3.38 Same as Fig. 3.29 but at 200 m.

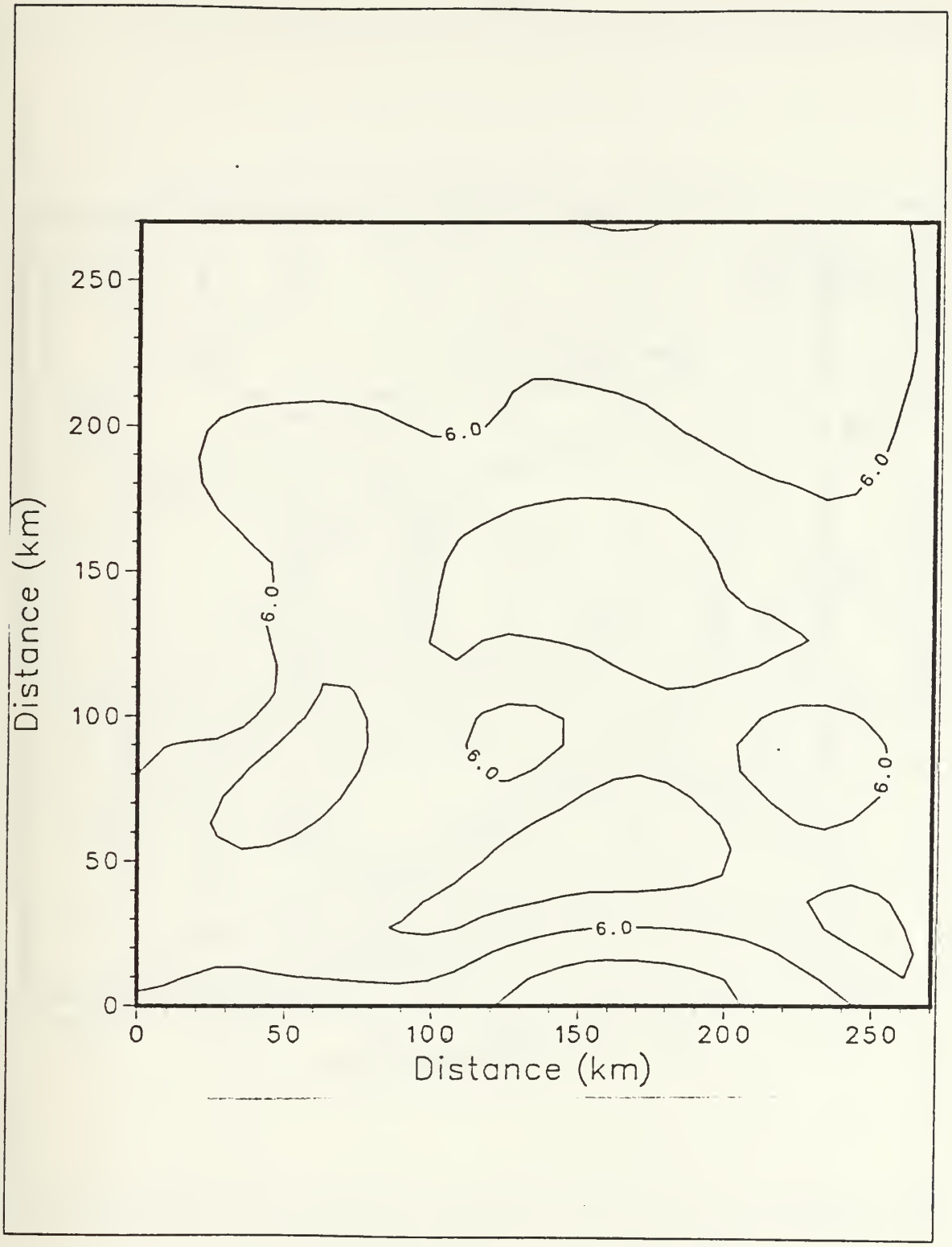

Figure 3.39 Same as Fig. 3.27 but at 550 m.

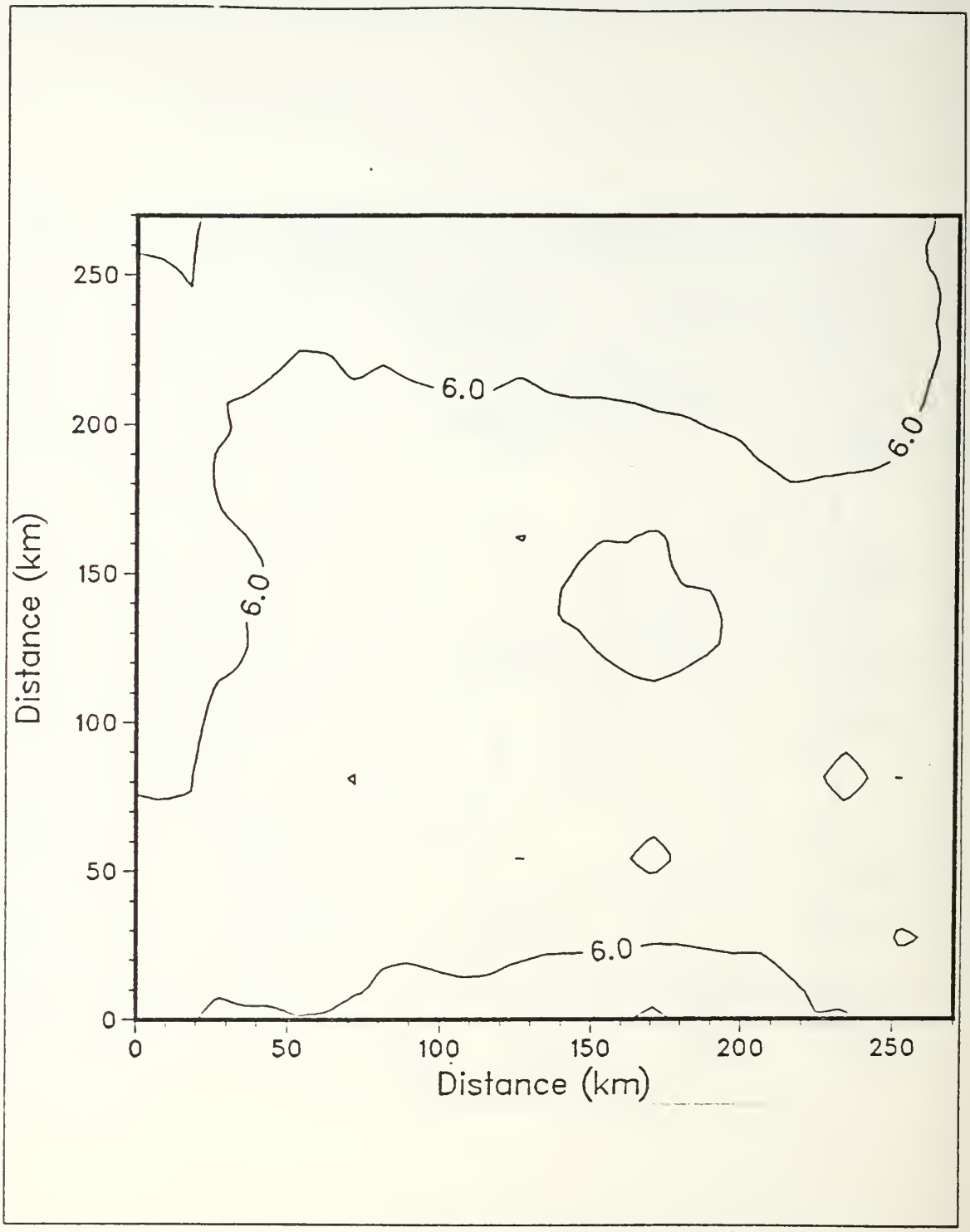

Figure 3.40 Same as Fig. 3.28 but at 550 m,
pattern correlation 0.85,
T range of 5.20 to 6.91 C.

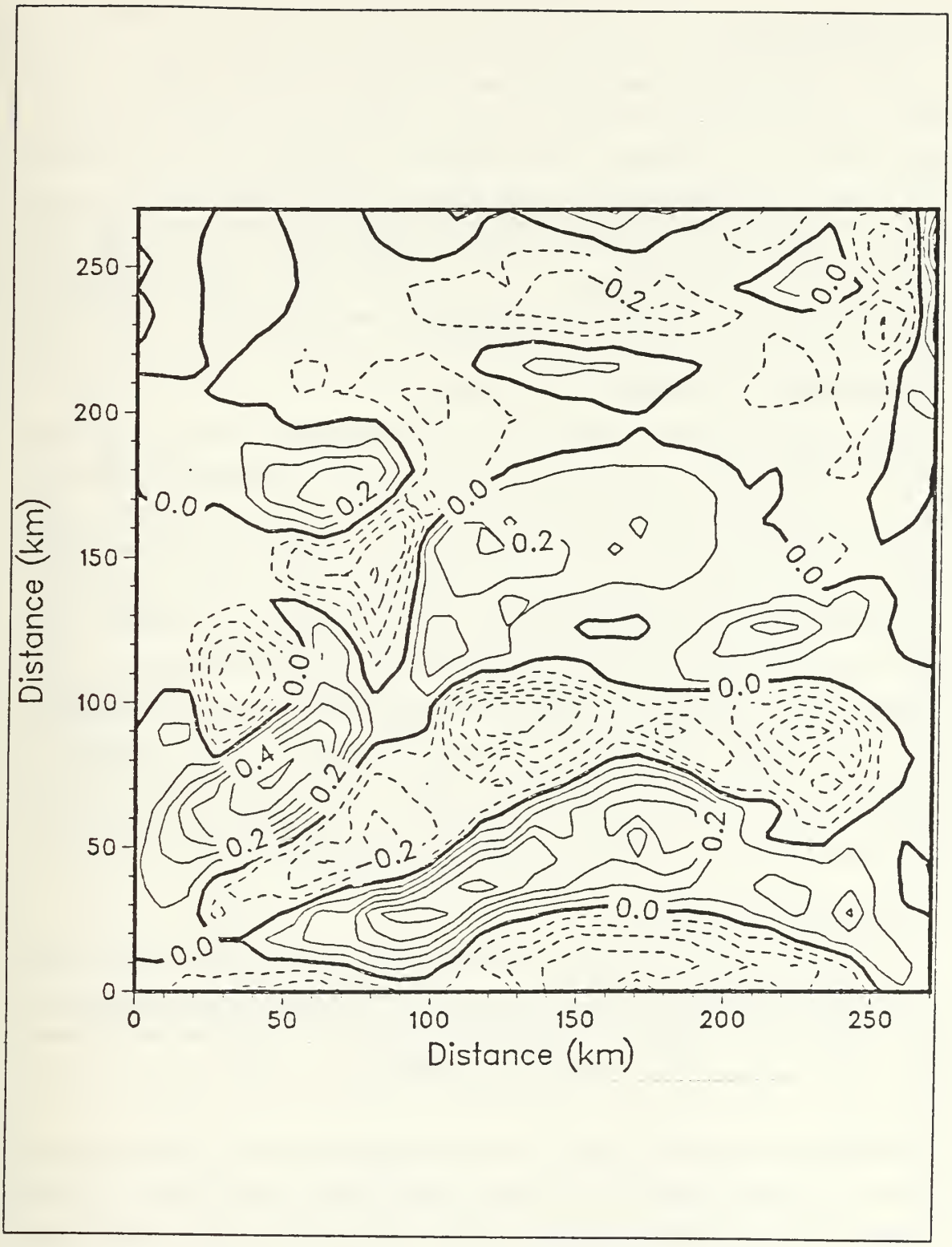

Figure 3.41 Same as Fig. 3.29 but at 550 m.

C. P-3 CRUISE III

The sampling pattern employed for the third cruise closely resembles, in many aspects, the scheme used in Cruise II. Heavier sampling was conducted along the eastern boundary in an attempt to better resolve the temperature structure exhibited there. A more random sampling scheme was stressed outside of 50 km from the eastern boundary. The AXBT observational stations are illustrated in Figure 3.42. The interpolation of the error field, Figure 3.43, acts as before in that minimum errors are located at the sampled positions with maximum errors occurring in areas furthest from AXBT stations. Autocorrelation plots of the temperature reveal no noticable differences as those exhibited for the second cruise.

The pattern correlation values unveil no salient departures from the previous sampling schemes. However, close examination of the OA interpolated temperature fields at the surface, 50 m and 200 m depths (Figs. 3.44, 3.46 and 3.48) point out the interesting concept of a more random sampling pattern. Within 50 km of the eastern boundary, differences are non-existent due to the same sampling pattern. Outside of this area disparities in the accurate depiction of the temperature field between the cruises becomes evident. At each of the three depths previously mentioned, a much better and a higher quality depiction of the mesoscale temperature features are depicted in the western region of the domain. Cool and warm pools of water undetected or poorly represented by Cruises I and II are resolved to a greater extent with the random sampling scheme. This is supported by each of the respective difference maps (Figs. 3.45-3.47) which show less temperature departures in the western domain.

D. CRUISE COMPARISONS

As mentioned earlier, the pattern correlations for each of the three cruises versus the true field at the different depths show no large deviations. When comparing the correlations computed between each of the cruises, similar statistical results were obtained. On average, a 95% pattern similarity was shown to exist in the 25 to 200 m depth range.

Differences in the mean absolute errors are negligible, less than 0.02, in all cases. The MAEs are approximately twice as large when comparing the OA fields with the true field as they are between the cruises. This is due to the fact that MAE values depend on the magnitudes of the difference field so that larger mean absolute errors are indicative of larger differences between the compared fields.

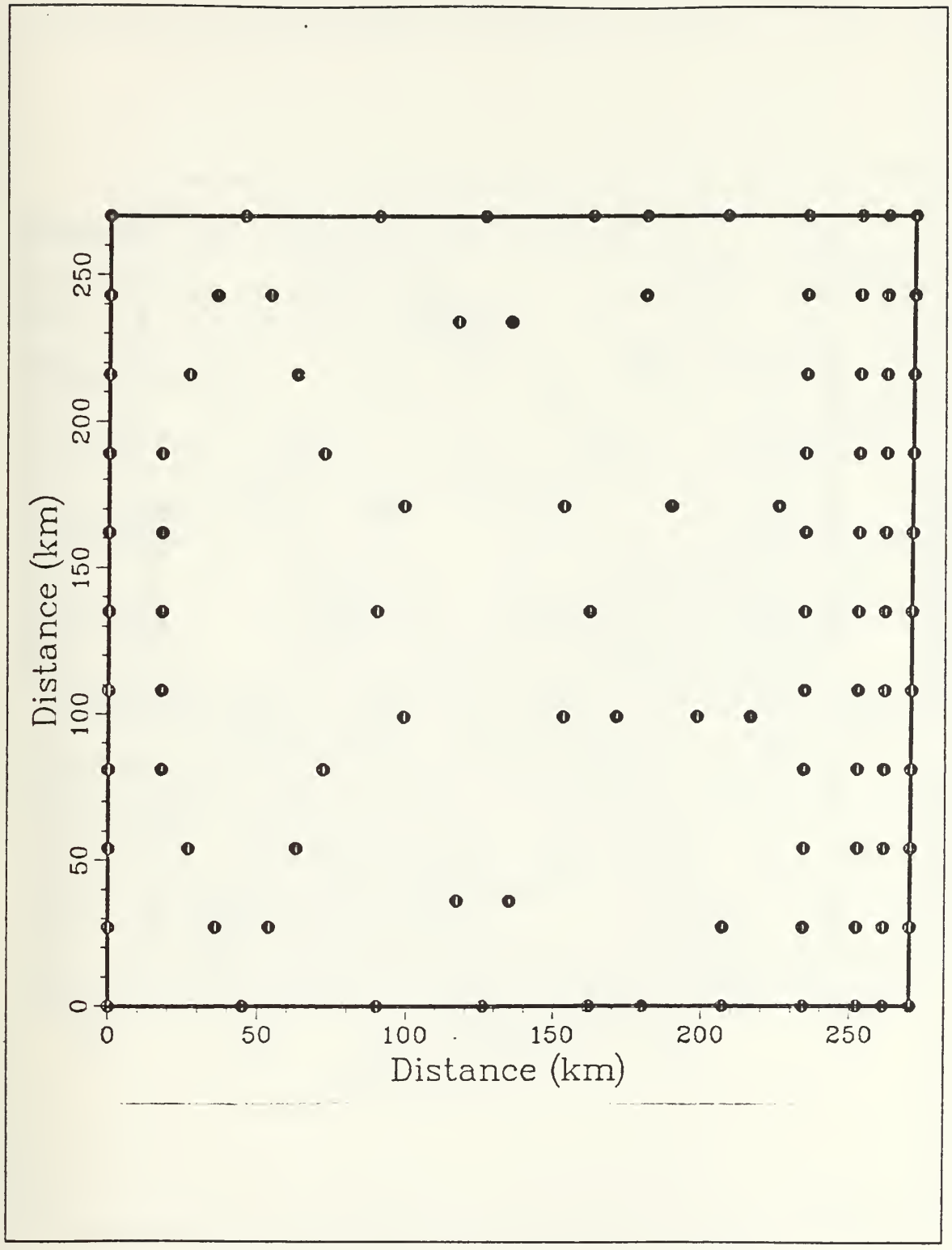

Figure 3.42 Cruise III station positions.

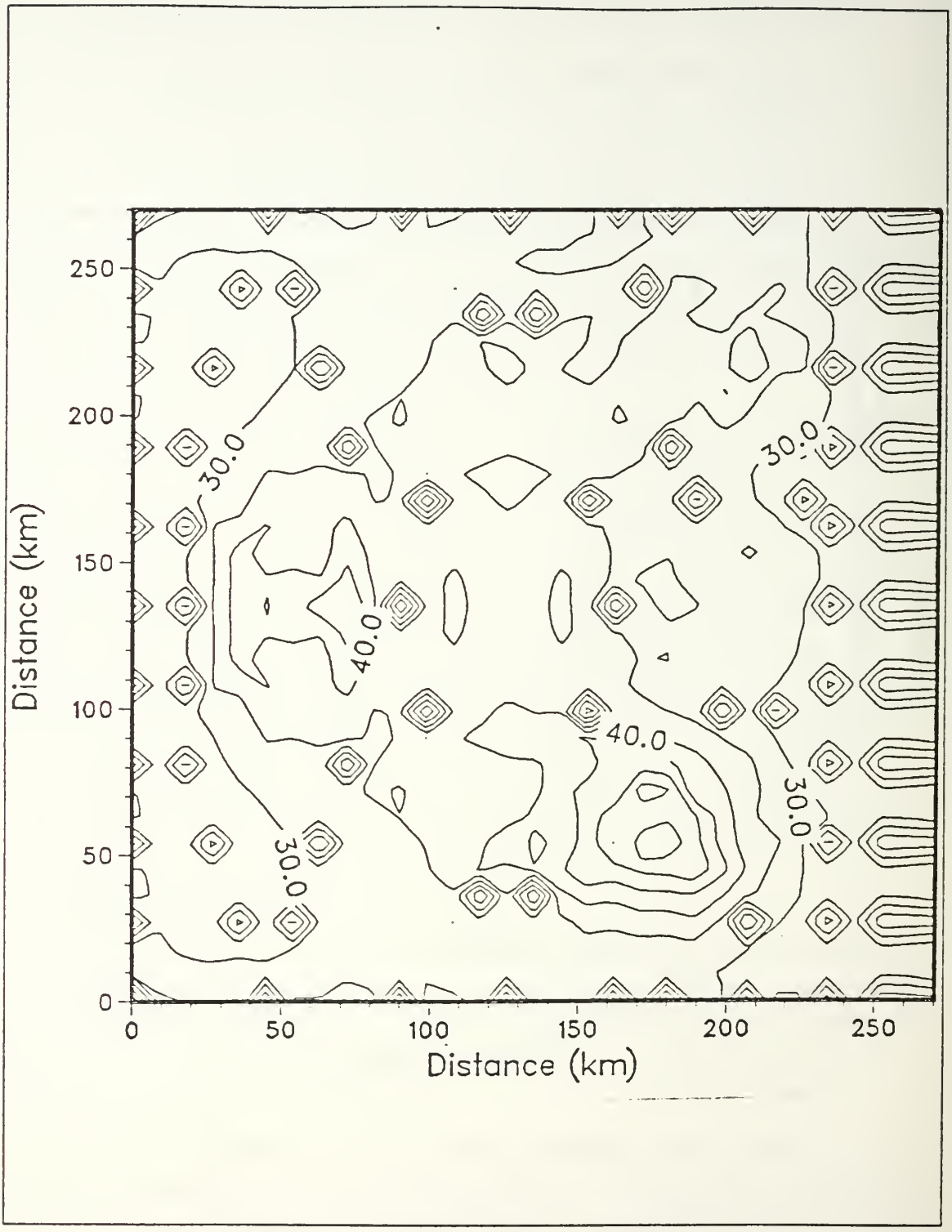

Figure 3.43 Cruise III temperature error field with error range from 14 to 60%.

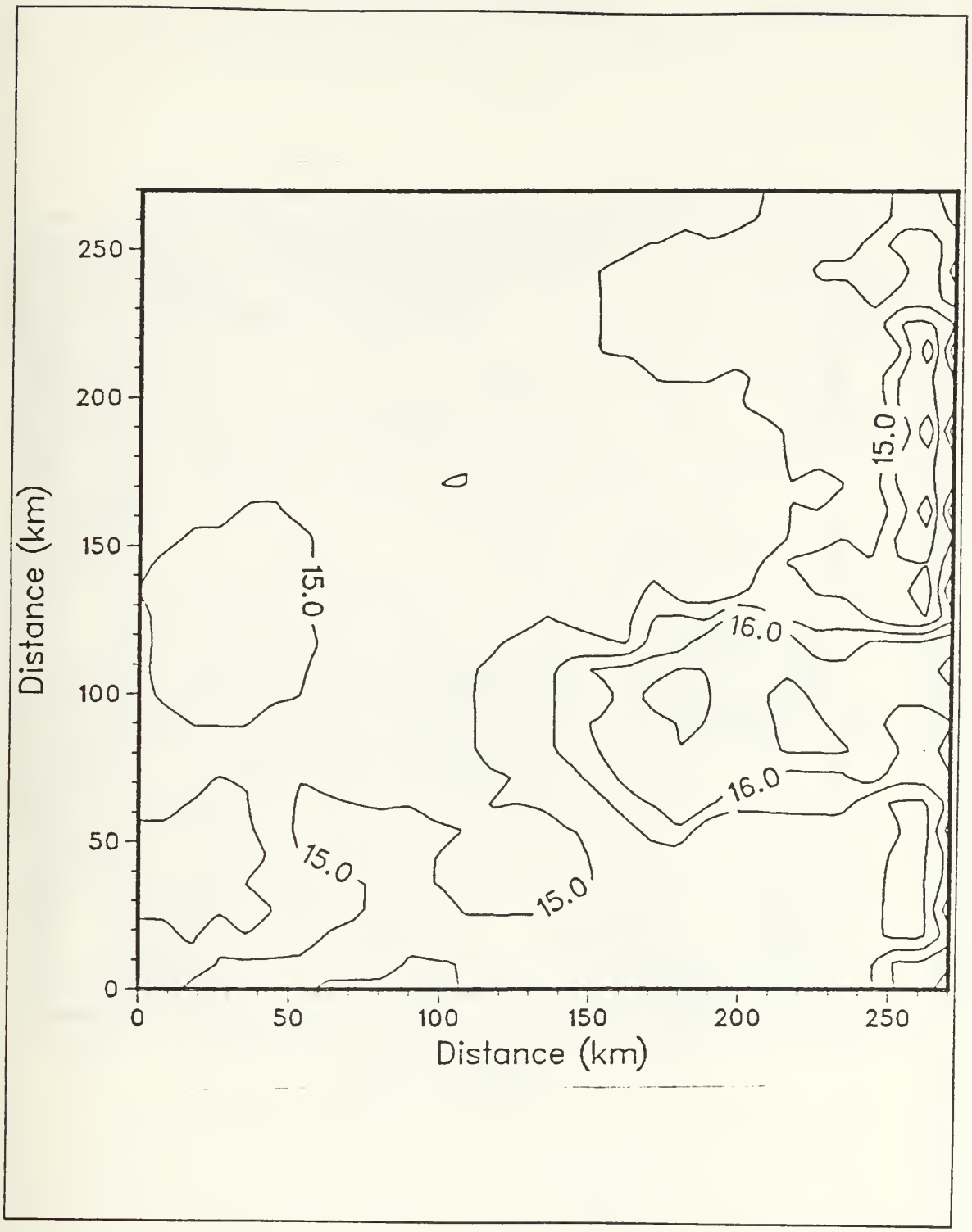

Figure 3.44 OA interpolated SST field on day 40,
Cruise III, pattern correlation 0.66,
T range of 12.53 to 16.87 C.

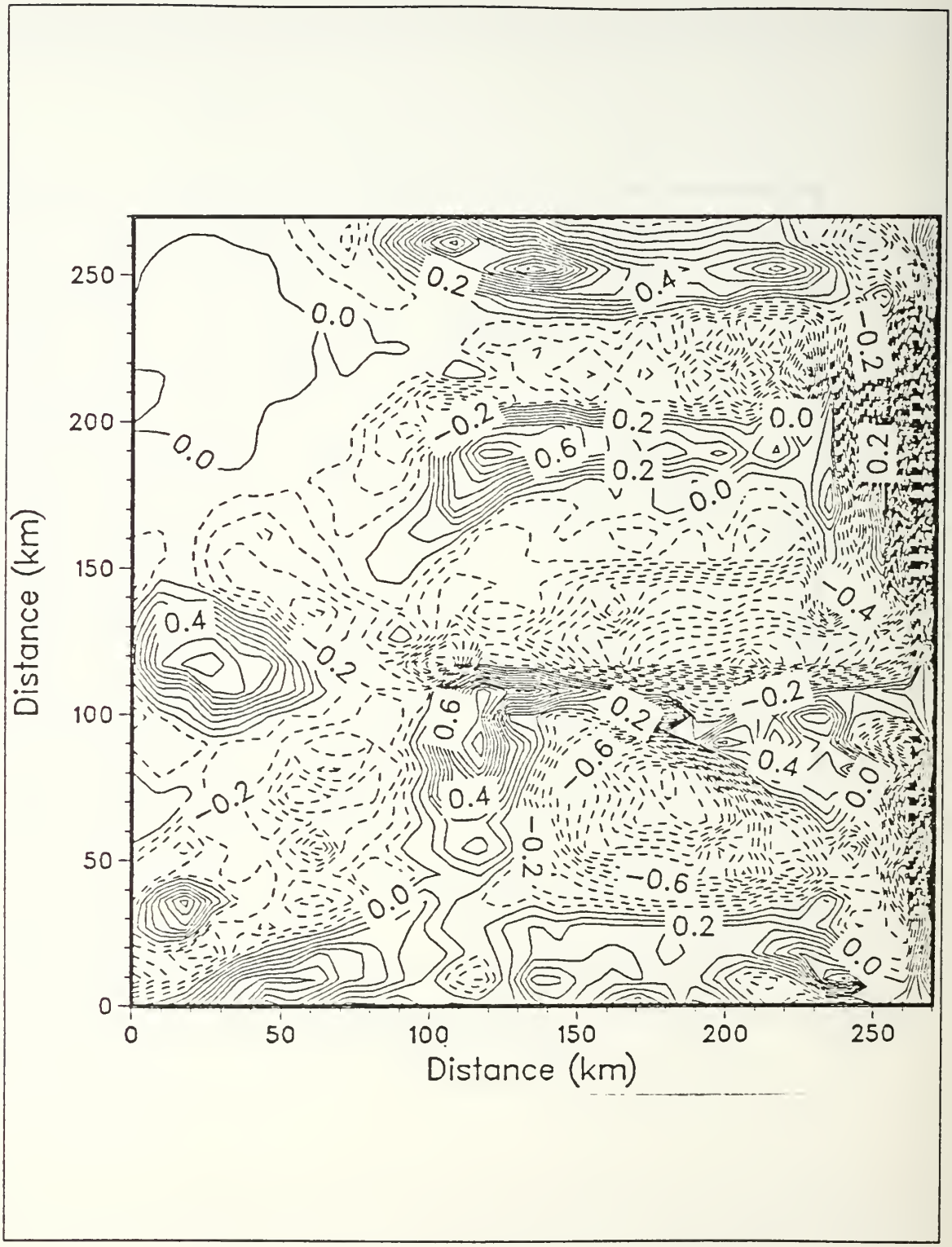

Figure 3.45 SST difference field on day 40, Cruise III.

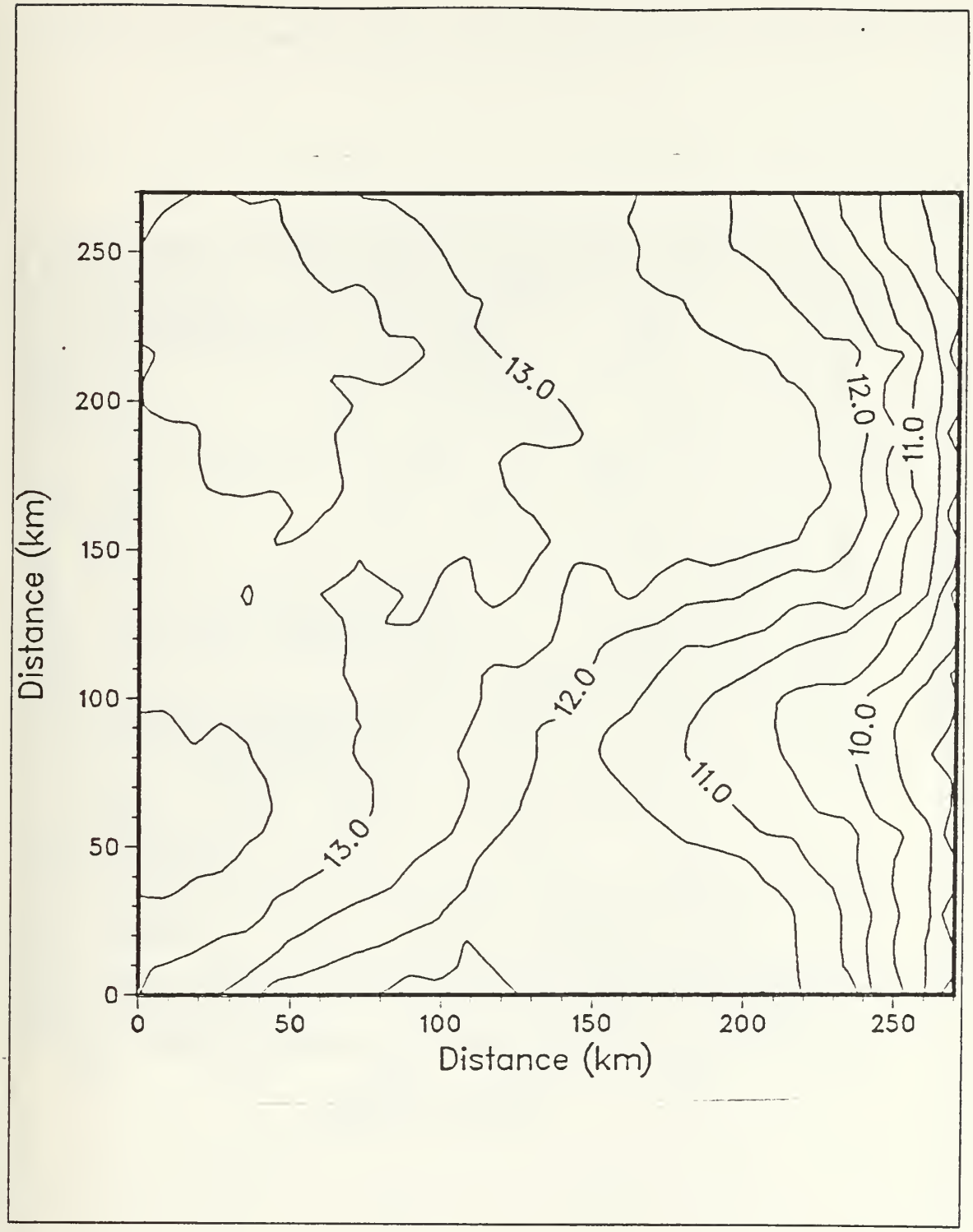

Figure 3.46 Same as Fig. 3.44 but at 50 m, pattern correlation 0.95, T range of 7.94 to 13.75 C.

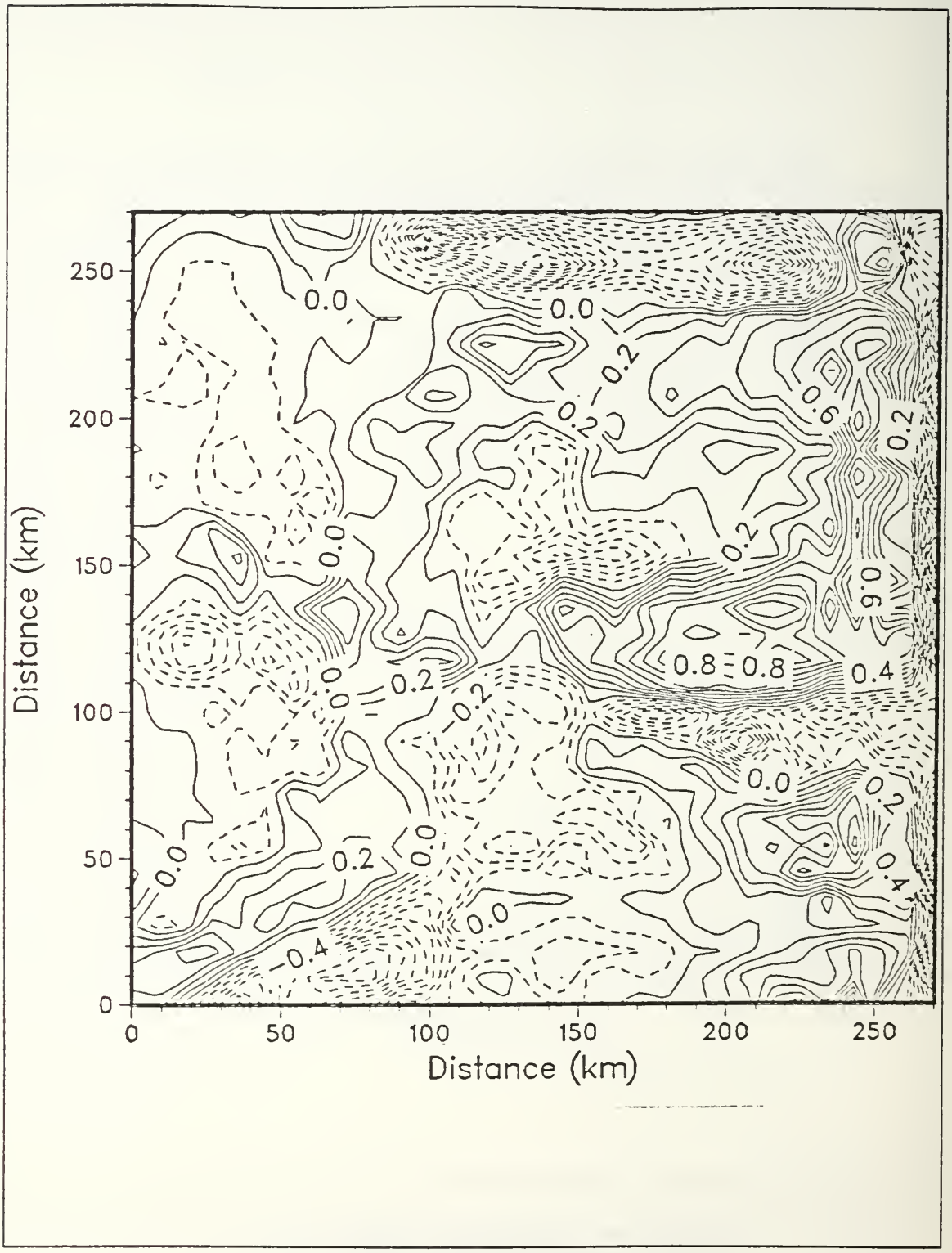

Figure 3.47 Same as Fig. 3.45 but at 50 m.

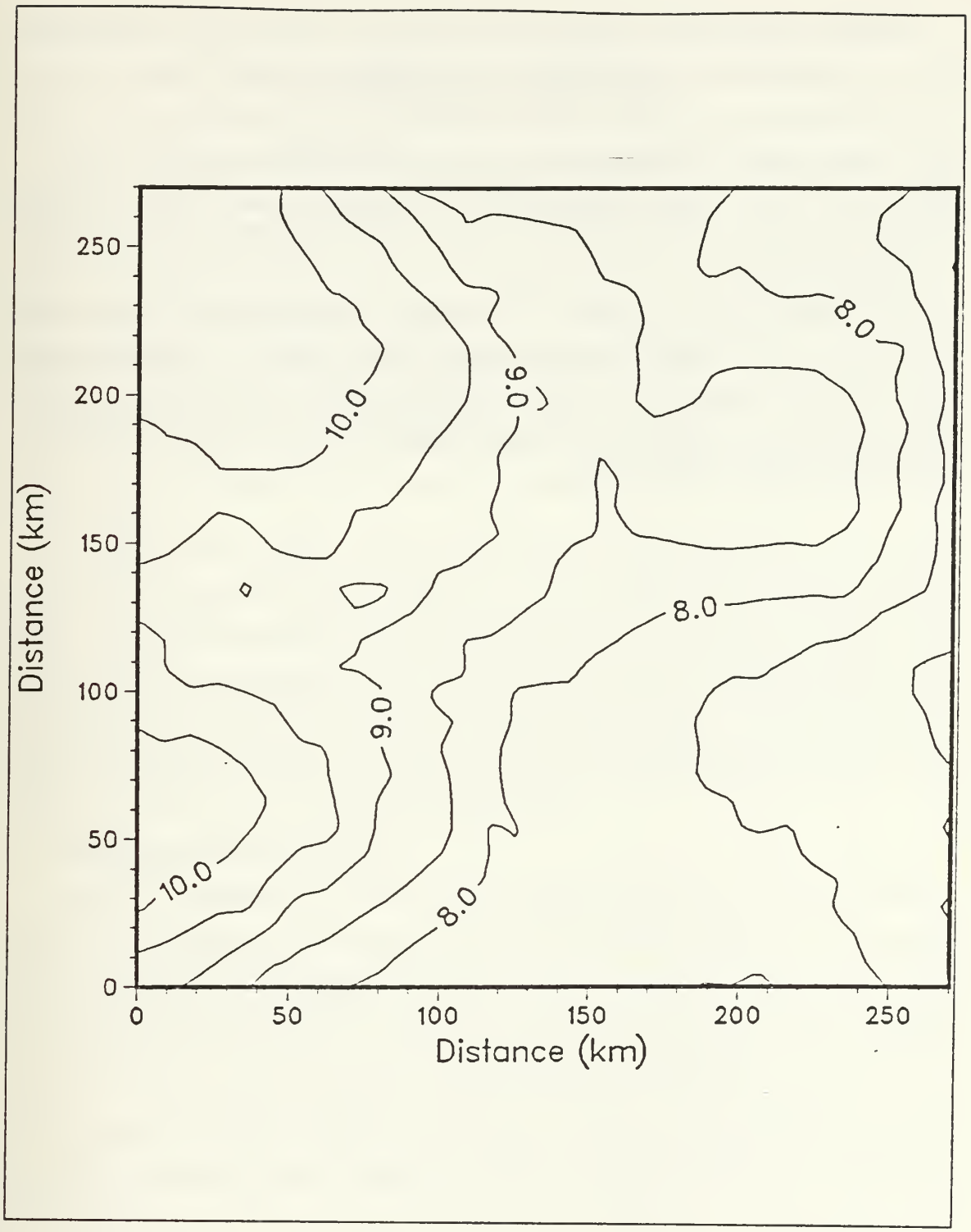

Figure 3.48 Same as Fig. 3.44 but at 200 m, pattern correlation 0.95, T range of 6.68 to 10.44 C.

A similar analysis was conducted in conjunction with the root mean-square errors. The magnitudes of the systematic and unsystematic RMSEs indicate that the OA technique produces a relatively small systematic error at all depths for each of the cruises. The majority of the mean-square error is attributable to unsystematic errors (greater than 95% of the error). This suggests the imprecision of the OA interpolated fields as compared to each other and to the PE fields which was evident in certain areas of the domain.

Based upon the error measures, no confident conclusions can be drawn in determining the best sampling strategy in space. Only through visual comparison can one confidently conclude that Cruise III is the best sampling scheme among the three which were tested. An ensemble of space sampling strategies are probably necessary to determine an optimal sampling array.

IV. TEMPORAL SAMPLING

Due to limited resources and capabilities, the majority of today's oceanic data acquisition arises from samples taken sequentially rather than synoptically. Traditionally, oceanographers go to sea on a single ship for periods of weeks to conduct a sampling cruise. The data thus acquired tend to be viewed synoptically in such a manner that the data are analyzed as a set, ignoring the fact that they are separated in time. In so doing, the assumption that the variable is constant in time during the duration of the entire sampling period must be postulated. This theory may be reasonable for certain oceanic variables under set conditions but the temperature field in the area of interest in this study does not exhibit a pattern of consistency in the time domain.

As with the P-3 cruises, *a priori* knowledge of the temperature field was employed in selecting the stratified sampling schemes for the shipboard hydrographic surveys. Each survey was conducted on day 38 through day 42 of the PE model output run. The non-filtered, non-detrended XBT temperature data were then interpolated to the grid using the two closest and highest correlated values within a 50 km radius of influence. Temperature maps at five depths were plotted by applying the OA technique. Day 40 was chosen as the central interpolation time.

A. HYDROGRAPHIC SURVEY I

Survey I paralleled the near uniform sampling distribution of P-3 Cruise I. Ninety-nine XBT stations were planned at a fixed north-south spacing of 27 km and an east-west spacing of 27 km near shore out to 180 km offshore with the remaining 90 km of the domain equally spaced at 45 km. An average of twenty XBTs were dropped daily during the five-day cruise. The actual observational positions are illustrated in Figure 4.1. The error field, Figure 4.2, behaves as expected with a minimum error of 12% occurring at the XBT observational stations. Error percentages increase outward from each of the stations with maximums of 38% coinciding in the areas with 45 km space intervals.

Autocorrelation versus depth curves of the temperature field displayed no noticable change as those observed for P-3 Cruise I. The correlation at the various depths exhibited similar characteristics showing zero crossings at approximately 150 km

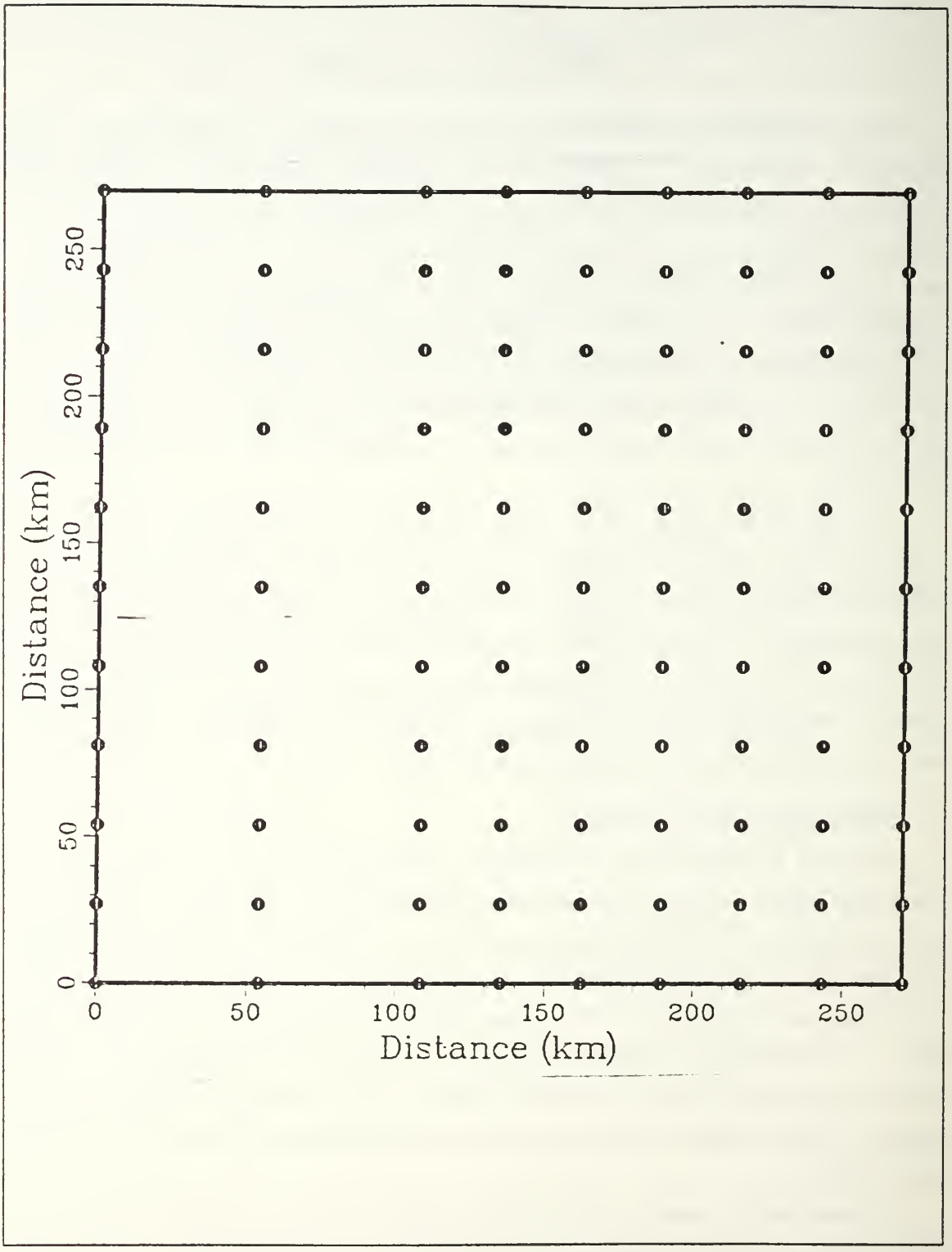

Figure 4.1 Survey I station positions.

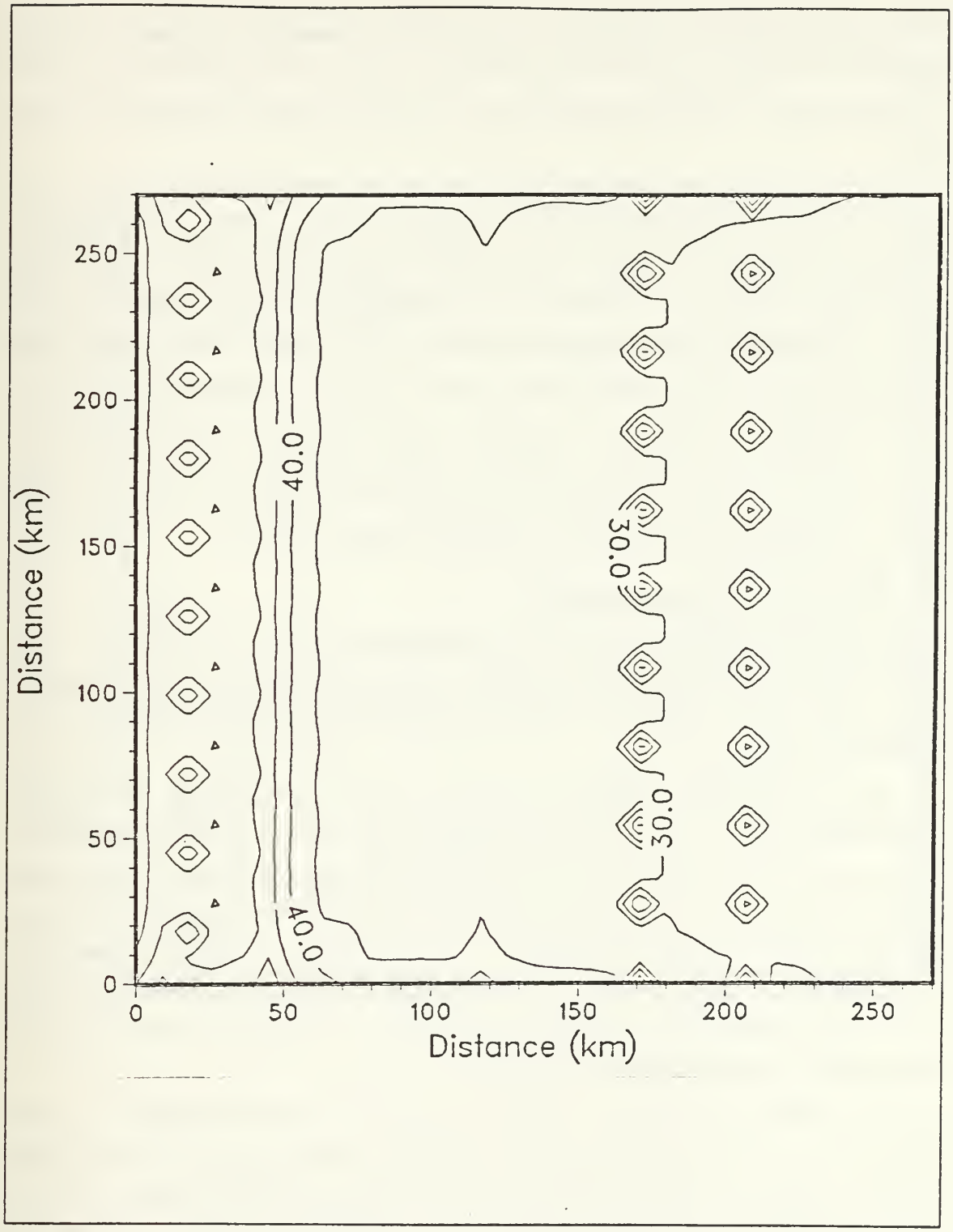

Figure 4.2 Survey I temperature error field with error range from 12 to 38%.

with a 0.5 correlation at 25 km. It was therefore reasonable to assume that the temperature variations at points within 25 km of a given position within the domain were related, that is, all points within 25 km could be expected to influence a given point.

The temperature structure throughout the water column as produced by the OA technique strongly resembled the PE temperature fields. The poorest pattern correlation occurred at the surface (63%) where strong gradients in the temperature pattern were poorly represented (Fig. 4.3). Correlations at the other depths were well above 0.80 indicating a good comparison between the two fields. The most significant differences in the temperature structure occurred in the portrayal of fine scale temperature features which were too small to resolve due to the uniform sampling scheme employed. Temperature difference fields exhibited a typical trend of overestimations in warm anomalous areas and underestimations in cool anomalous regions as exemplified by the difference plot at the surface (Fig. 4.4).

B. HYDROGRAPHIC SURVEY II

Survey II used the same stratified sampling pattern as that of P-3 Cruise II. This plan consisted of ninety-nine XBT stations with a north-south spacing of 27 km and varied spacing in the east-west direction. The actual observational positions are illustrated in Figure 4.5.

The temperature correlation at 50 m (Fig. 4.6) illustrates the typical autocorrelation pattern found during Hydrographic Survey II. A maximum correlation of 1.0 exists at the zero-separation distance. From zero lag a rapid falloff occurs in an exponential fashion in which the half-correlation point drops to a distance of 40 km. The zero-crossing distance occurs at 162.5 km. Little significance should be placed on the autocorrelation values beyond the zero-crossing distance. The layers above 50 m (not shown) experienced a similar autocorrelation pattern but with decreased zero-crossings and half-correlation distances.

Two variations of Survey II were conducted. The first case assumed that the temperature was constant in time during the five-day sampling period. The associated error field, Figure 4.7, shows minimum errors of 15% at the XBT station positions which were sampled on day-40. Maximum errors of 67% are located in the western domain due to large spatial and temporal variations of the sampling scheme. Statistical values for this case are presented in Table 4 of the comparison between the

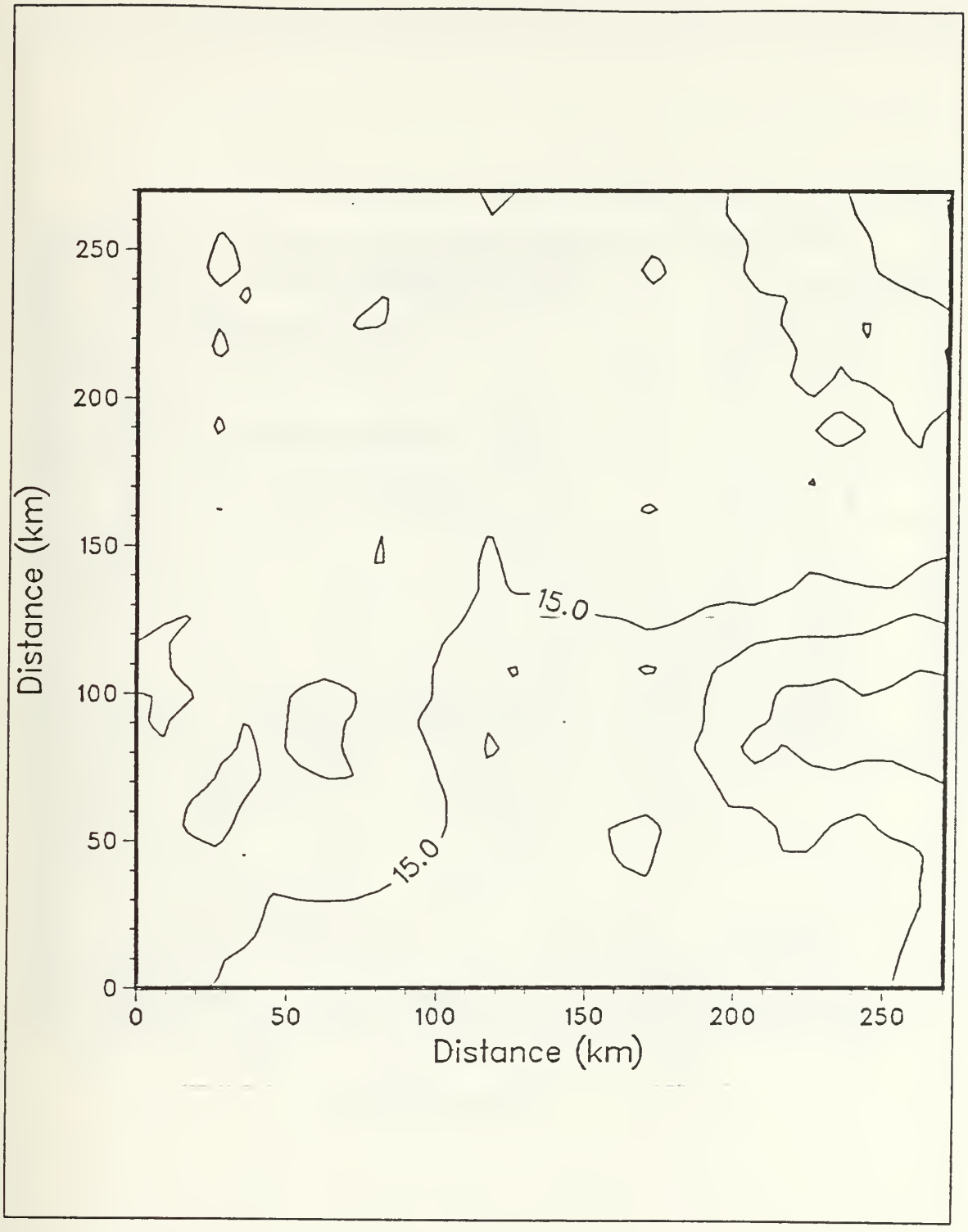

Figure 4.3 OA interpolated SST field on day 40,
Survey I, pattern correlation 0.63,
T range of 13.75 to 16.95 C.

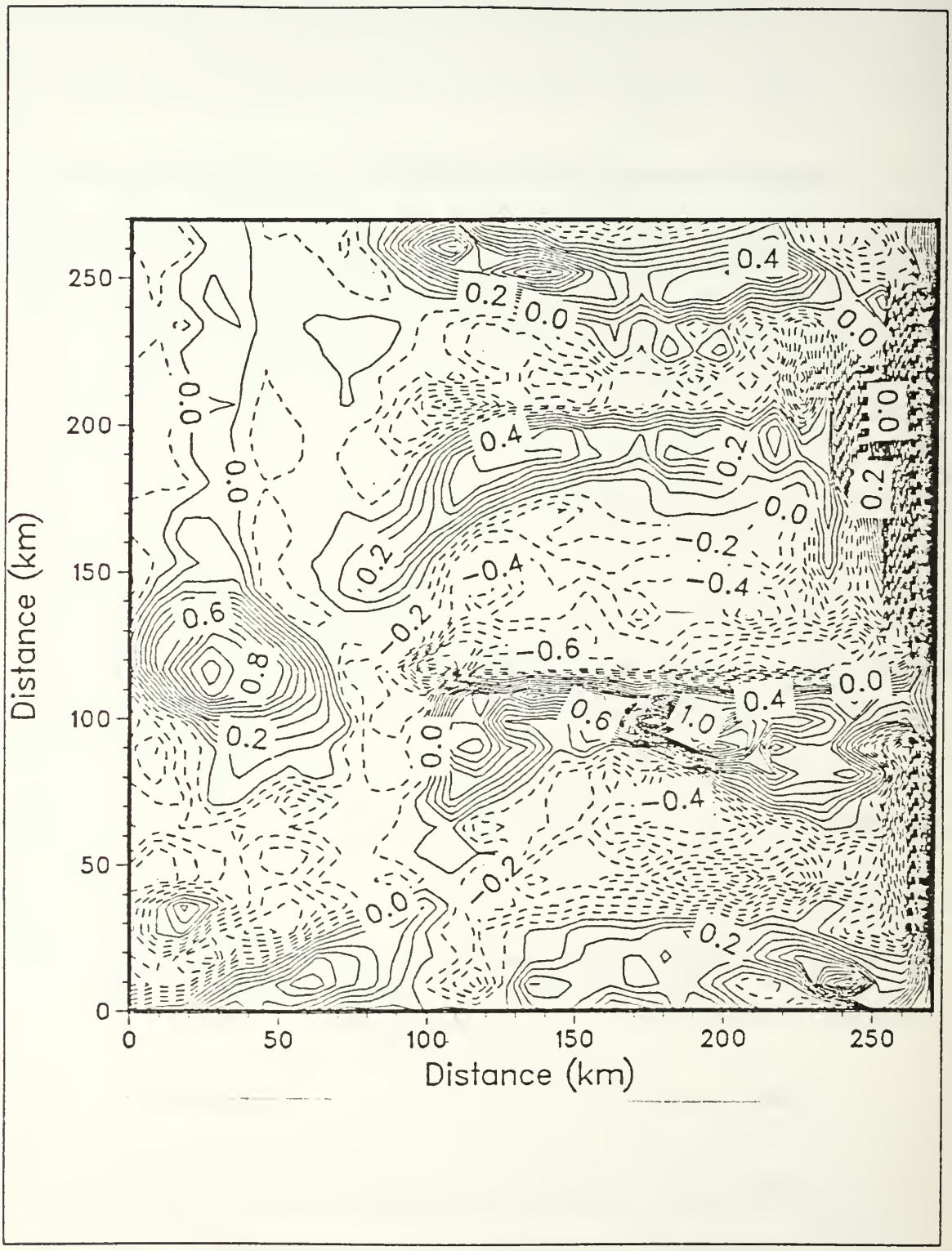

Figure 4.4 SST difference field on day 40, Survey I.

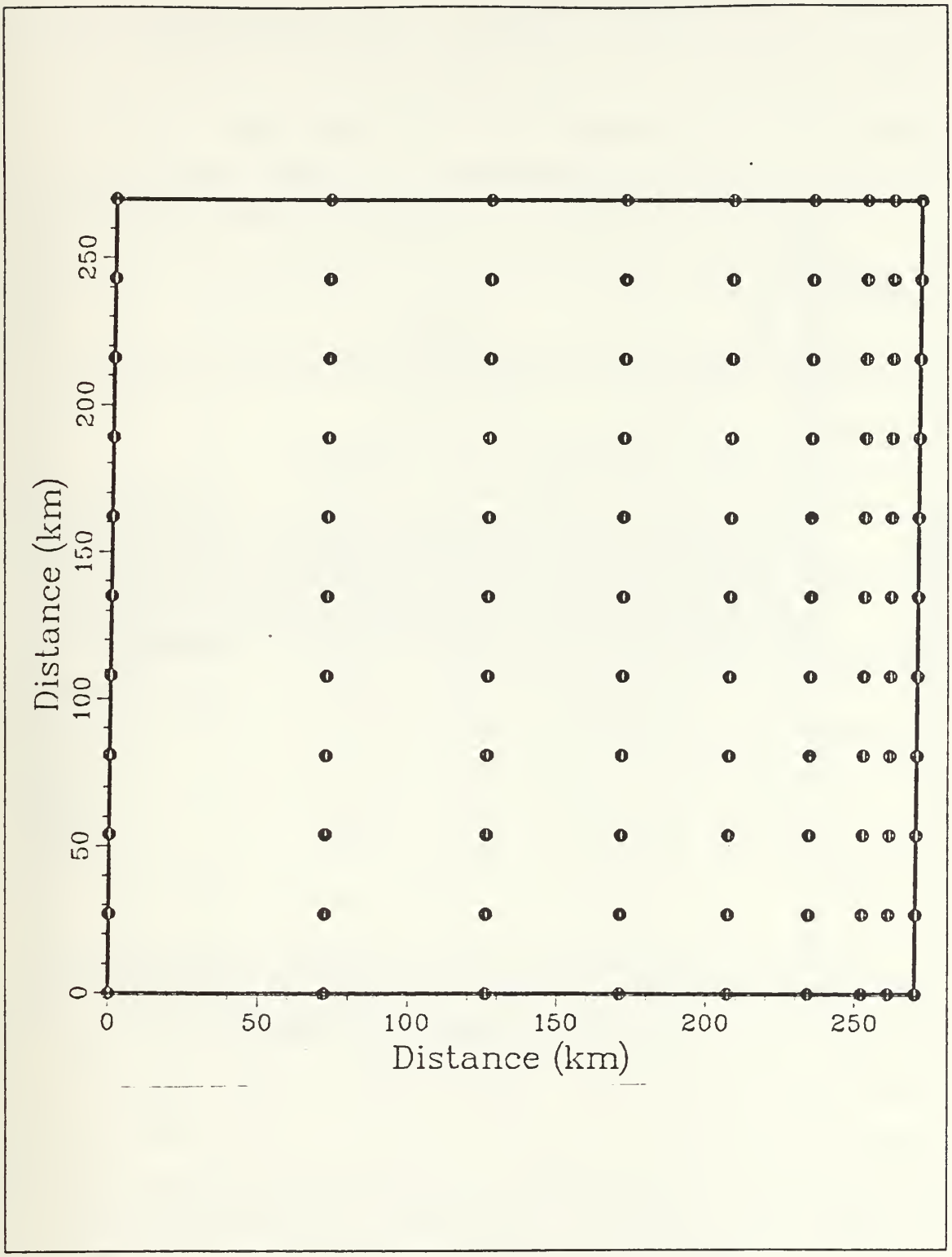

Figure 4.5 Survey II station positions.

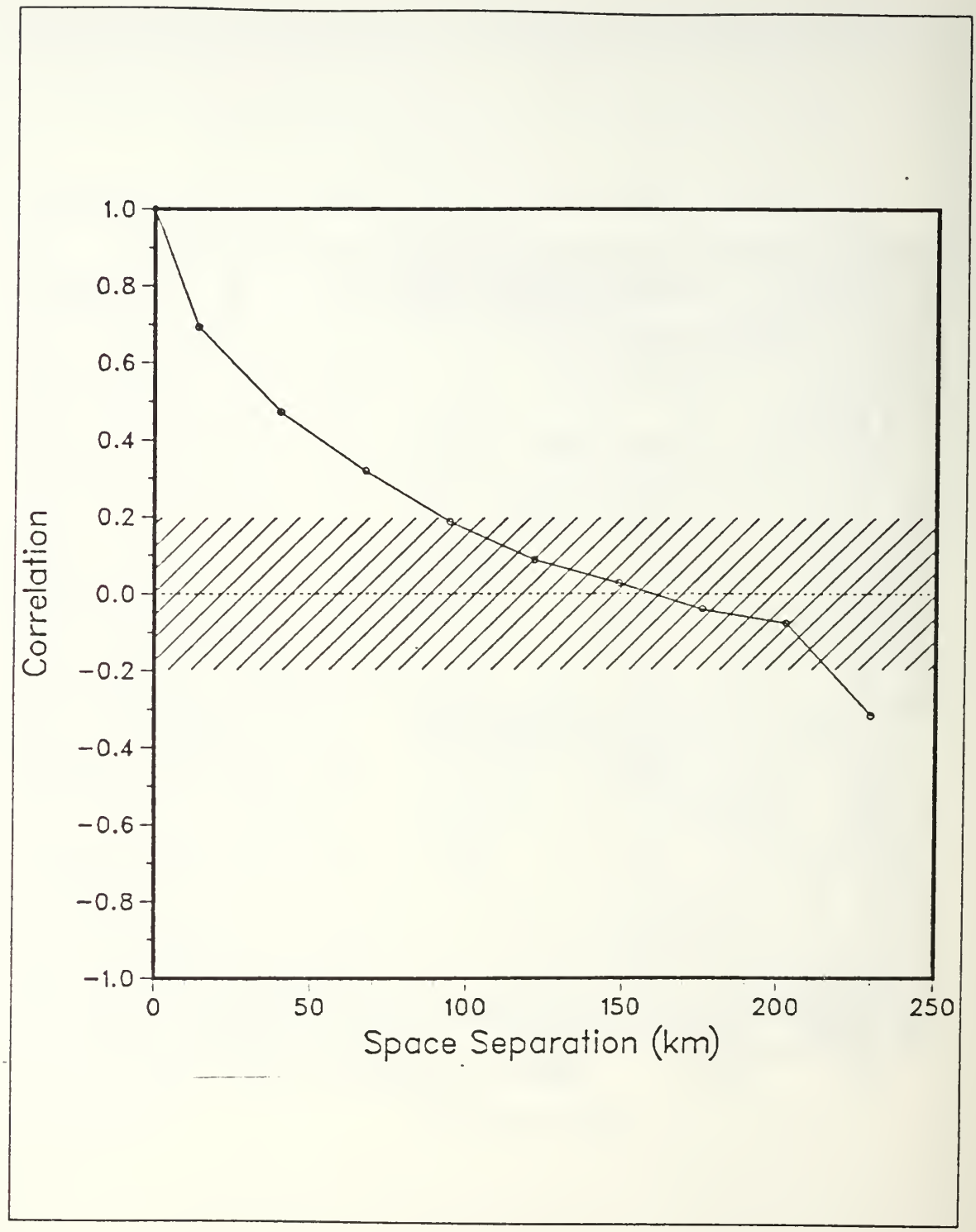

Figure 4.6 Correlation of temperature at 50 m on day 40, Survey II, zero-crossing distance of 162.5 km.

PE model temperature fields and the OA interpolated temperature fields. The OA surface field represents a 72% pattern correlation with the true field (Fig. 4.8). Major differences, Figure 4.9, occur along the eastern boundary as the OA technique fails to perfectly represent the tight gradient of the existing temperature front. Large positive temperature differences, indicating OA underestimations, are located in the cool filament extending offshore from the coast in the southern portion of the domain.

TABLE 4

STATISTICAL MEASURES OF HYDROGRAPHIC SURVEY II-NO ADVECTION

	Surface	25 m	50 m	200 m	550 m
PE Mean Temp	14.98	13.72	12.27	8.61	6.11
OA Mean Temp	15.00	13.72	12.26	8.62	6.11
PE Variance	0.50	0.22	1.50	1.06	0.12
OA Variance	0.20	0.17	1.29	0.88	0.52
Zero-Crossing	121.5	148.5	162.5	175.5	134.5
Pattern Corr	0.72	0.91	0.95	1.00	0.84
MAE	0.35	0.15	0.27	0.06	0.14
RMSE	0.50	0.19	0.37	0.09	0.20
$RMSE_s$	0.07	0.01	0.03	0.02	0.06
$RMSE_u$	0.49	0.19	0.36	0.09	0.19

The overall pattern correlations at 25, 50 and 200 m depths were all above 90% indicative of closely related mappings. Throughout the domain positive differences were evident (Figs. 4.11, 4.13 & 4.15). The 25 m depth field exhibited the same qualities as found at the surface, notably the misrepresentation of the cool filament offshore from the eastern boundary (Fig. 4.10). At 50 m, in which the OA interpolated temperature field showed a pattern correlation of 95%, a near perfect flow pattern was created (Fig. 4.12). However, misrepresentation of the portrayal of the warm intrusion of water in the northwest region of the domain due to the lack of observations in this area is evident. Even though the 200 m depth OA interpolated temperature field showed a

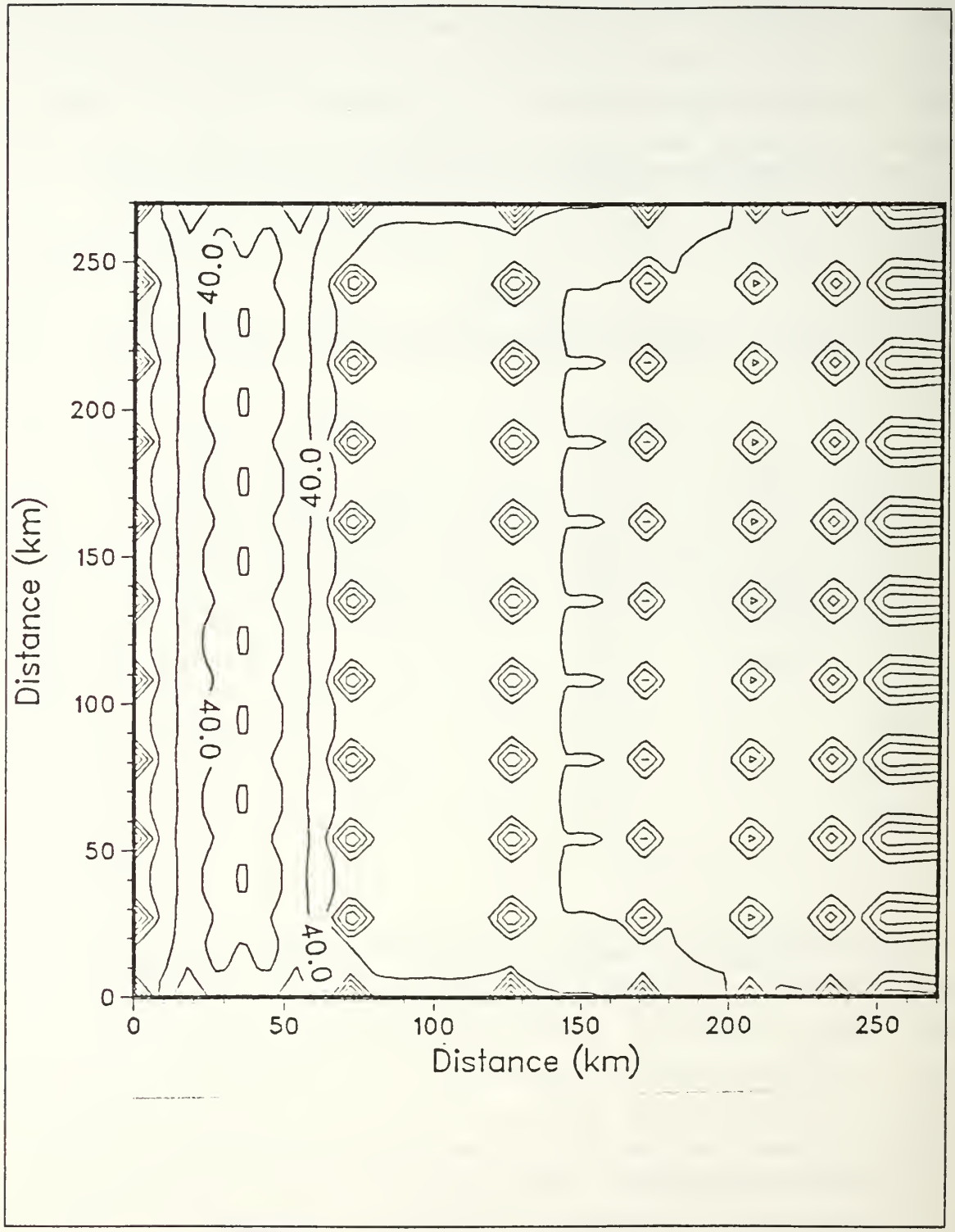

Figure 4.7 Survey II temperature error field with error range from 12 to 67%.

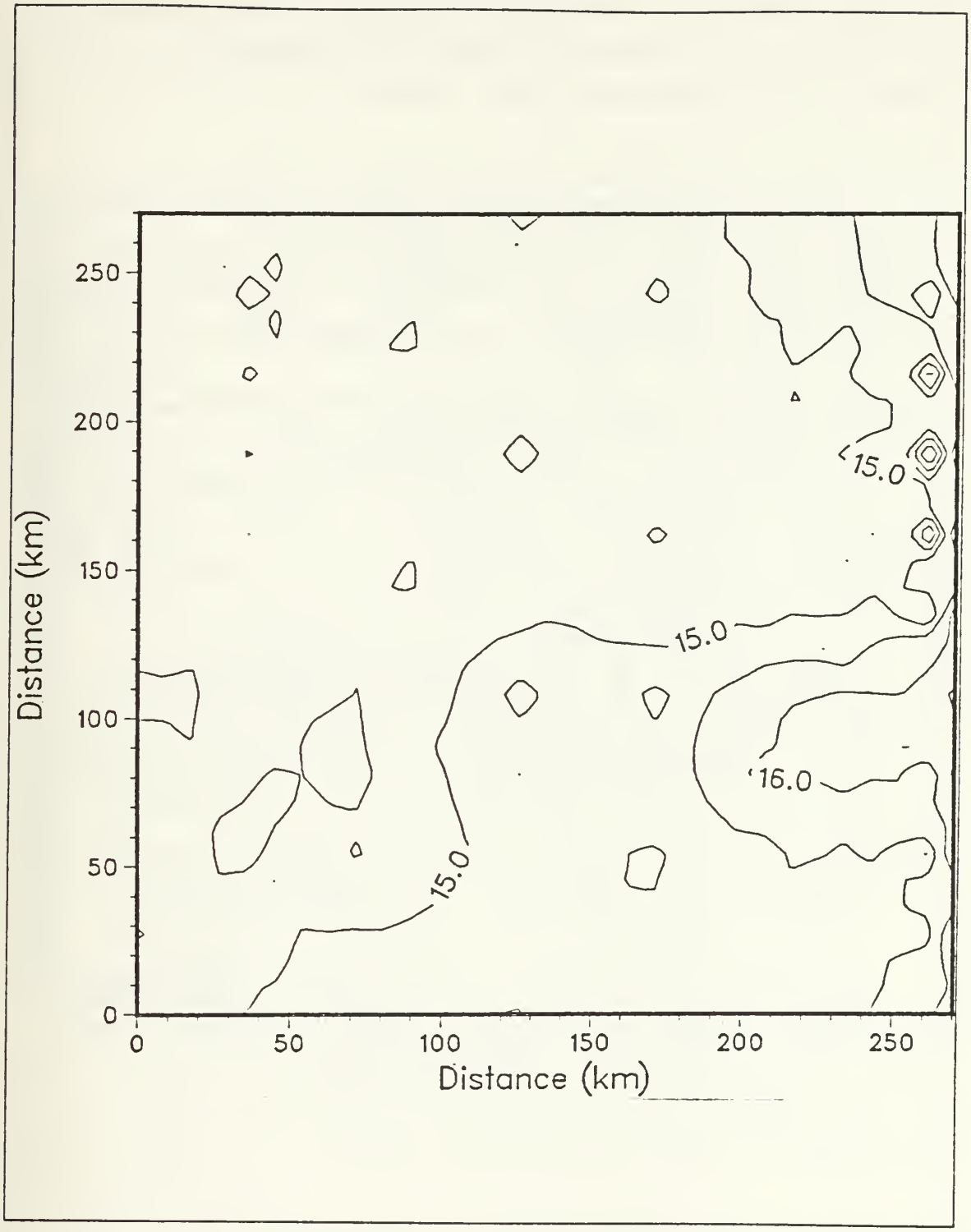

Figure 4.8 OA interpolated SST field on day 40,
Survey II, pattern correlation 0.72,
T range of 13.72 to 16.91 C.

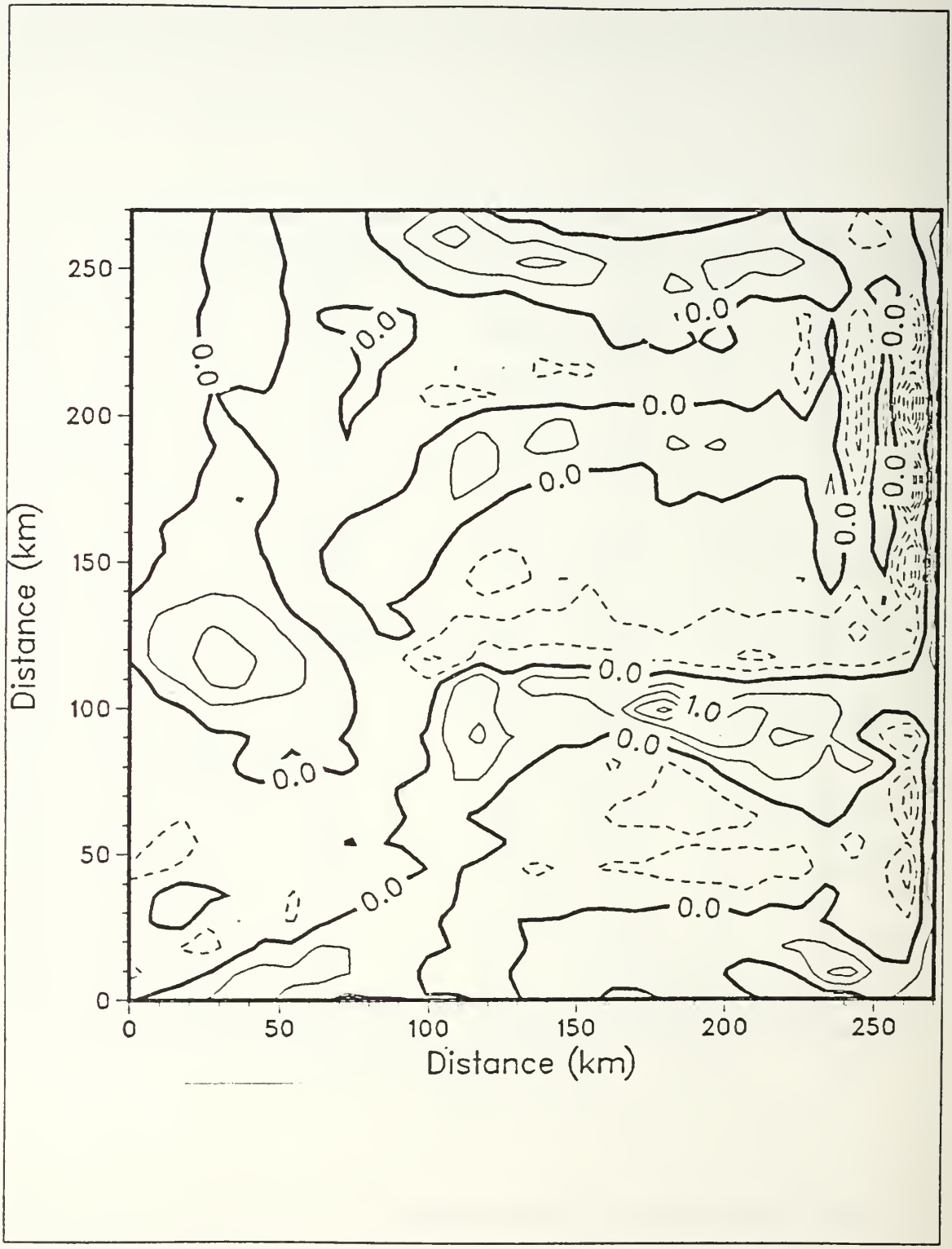

Figure 4.9 SST difference field on day 40, Survey II.

pattern correlation of 100%, it appears to be a poor visual representation of the true field (Fig. 4.14). Deficiencies in the depiction of the meandering temperature front and the cool cell of water can be attributable to larger space sampling within the respective areas.

A poor OA analysis of the temperature field occurred at 550 m depth (Fig. 4.16) in which a pattern correlation of 84% was obtained. This low pattern correlation may be explained by a combination of circumstances, including the existence of near isothermal conditions and the application of a non-equal X, Y directional spacing pattern which led to large temperature differences in the areas where mesoscale features existed (Fig. 4.17).

The second case of Survey II assumed that the temperature fields were advected during the five-day sampling period instead of remaining constant. Since propagation of the mesoscale features was characterized by a mean speed of 5 km/day to the southwest, this movement was supplied directly to the OA routine as an advection speed of the temperature field. The error field shown in Figure 4.18, behaves as expected with the minimum error of 15% coinciding with the XBT observational stations on day 40. Errors increase outward from the day-40 observations to a maximum error of 67% in the western domain due to both space and time scales. There were no dramatic departures in the pattern correlation values between the two cases. The largest difference occurred at the surface along the eastern boundary (Fig. 4.19). Due to the advection of the temperature field throughout the area of interest at a propagation speed of 5 km/day, evidence of the coastal temperature front is missing. This effect of a false appearance occurs to a much lesser degree at depth as the temperature front becomes weaker.

C. HYDROGRAPHIC SURVEY III

A mirror image of the sampling strategy employed during P-3 Cruise III was used for the third survey in which a more random sampling pattern beyond 50 km of the eastern boundary was stressed. The ninety-nine XBT observational stations are displayed in Figure 4.20. Temperature autocorrelation values were comparable to those observed in Survey II.

Again, two cases were analyzed, one which assumed the data acquired over a five-day period to be real-time and the other which considered the effects of advection of the temperature field at a propagation speed of 5 km/day. Interpretation of the

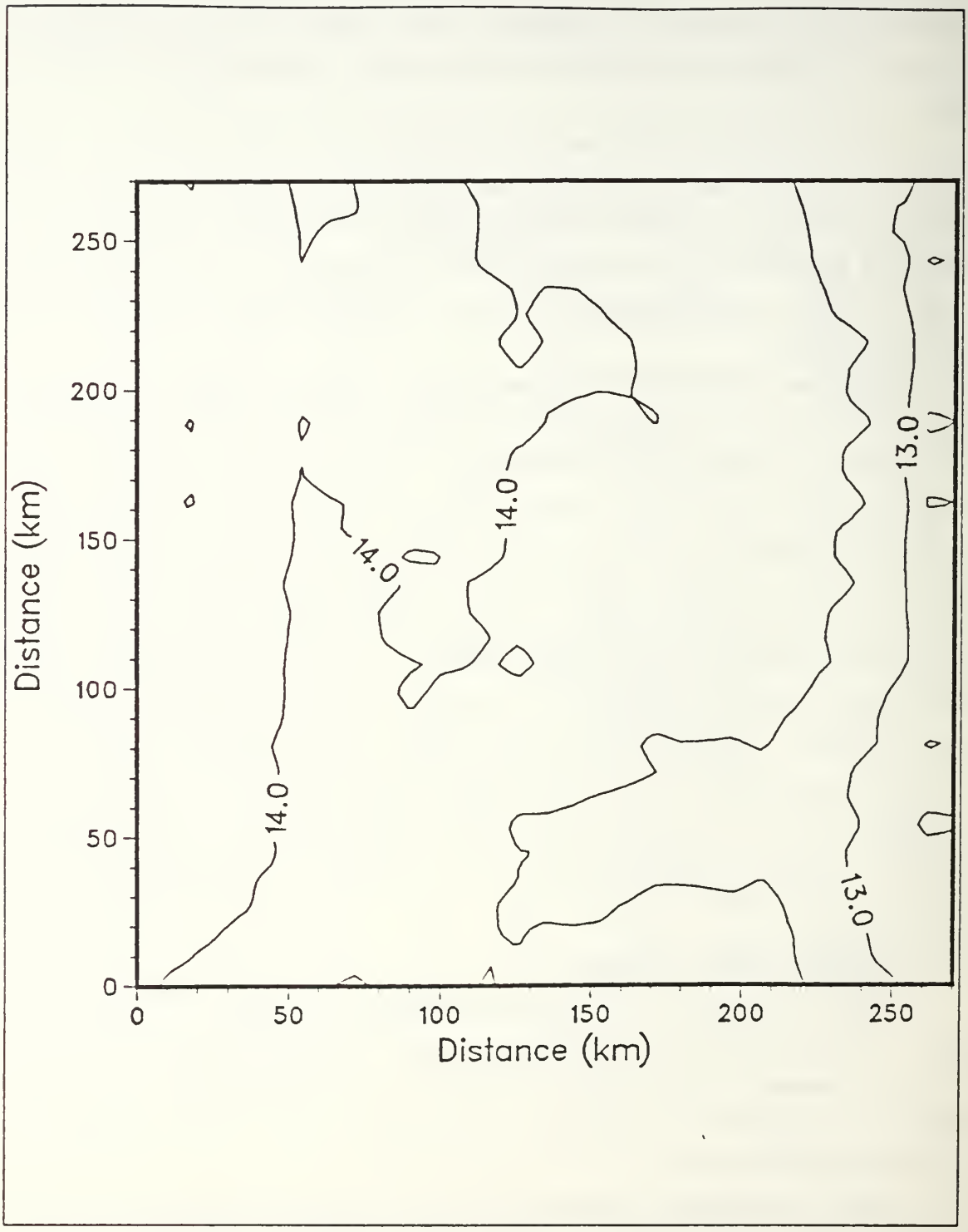

Figure 4.10 Same as Fig. 4.8 but at 25 m,
pattern correlation 0.91,
T range of 12.50 to 14.48 °C.

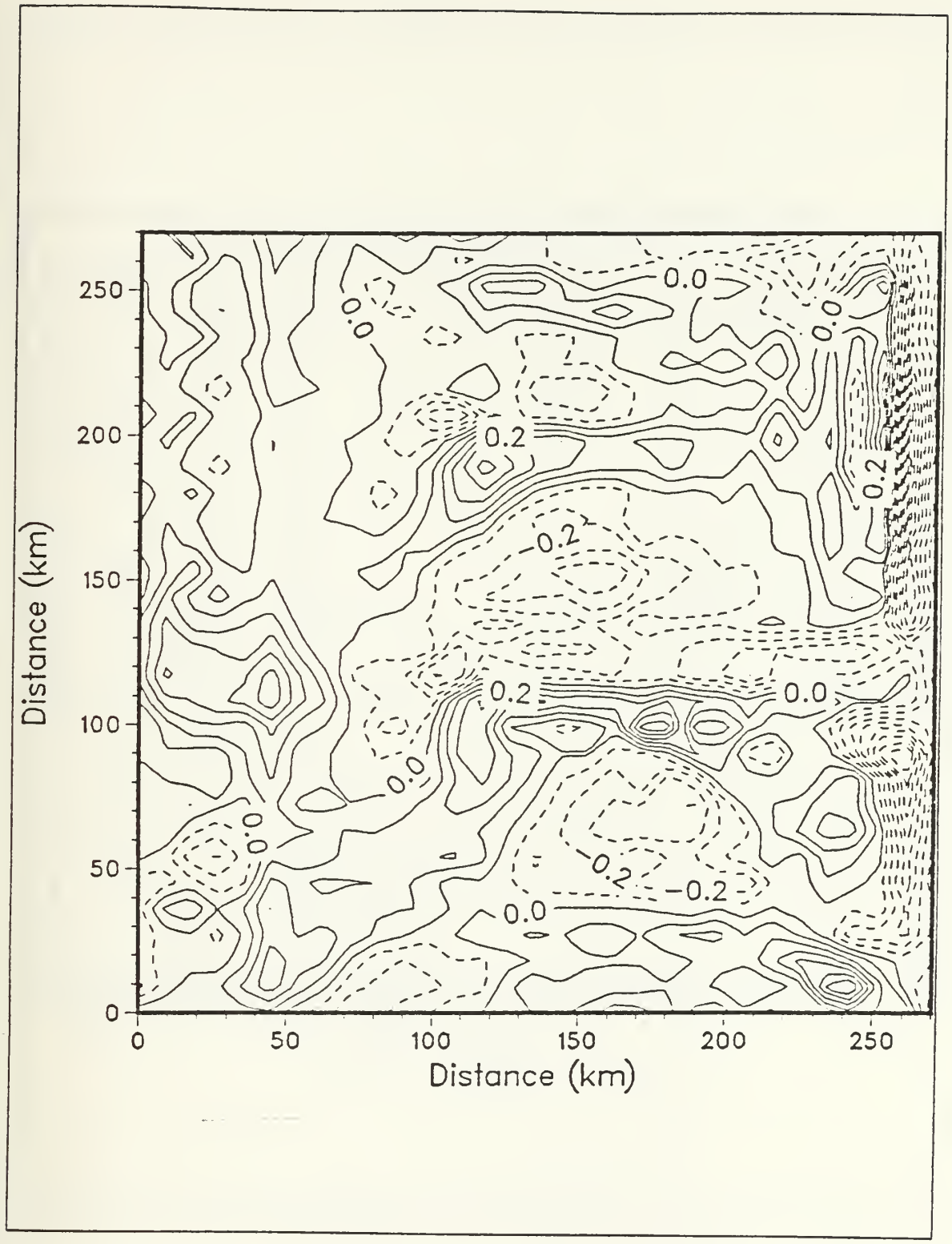

Figure 4.11 Same as Fig. 4.9 but at 25 m.

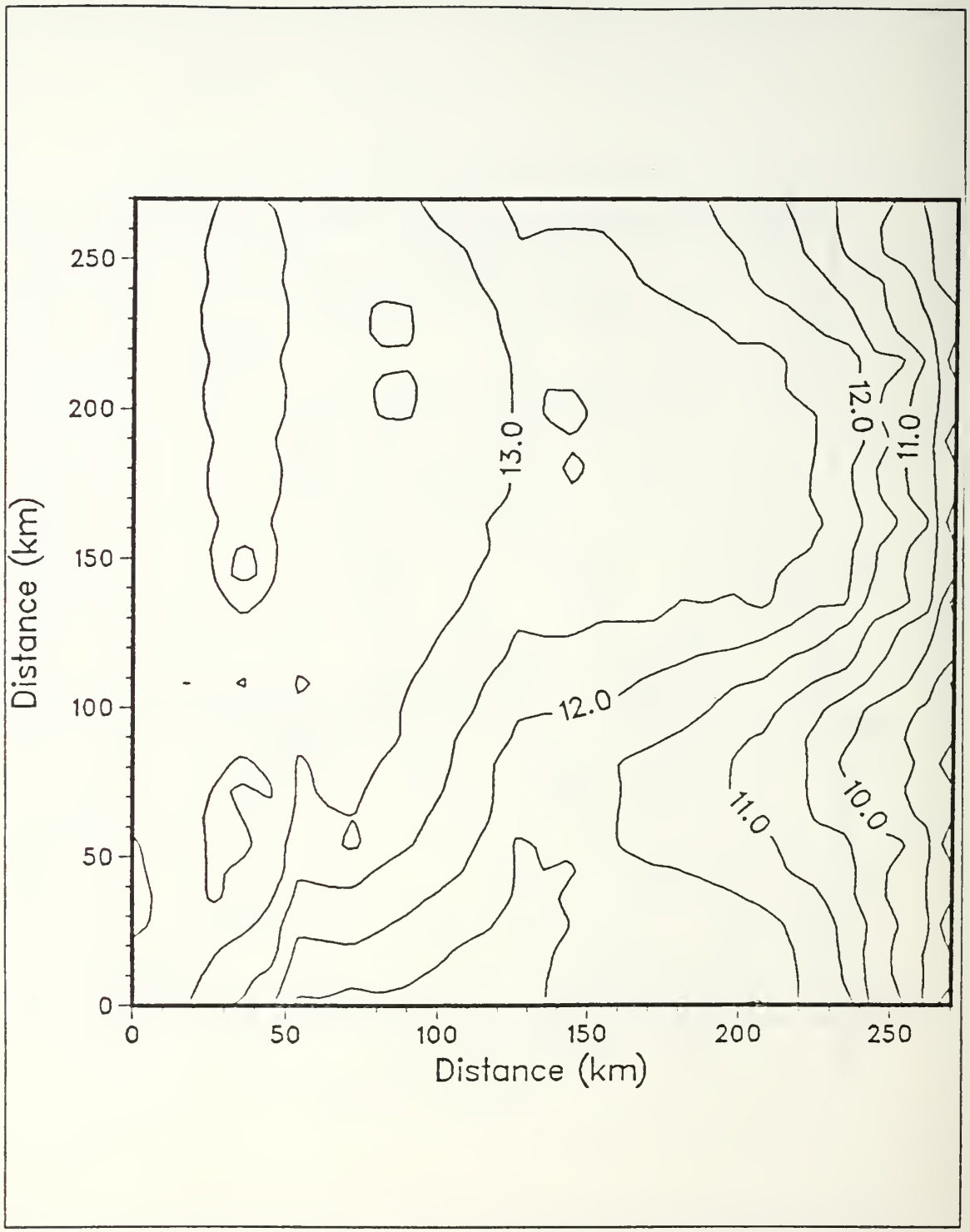

Figure 4.12 Same as Fig. 4.8 but at 50 m,
pattern correlation 0.95,
T range of 7.96 to 13.73 C.

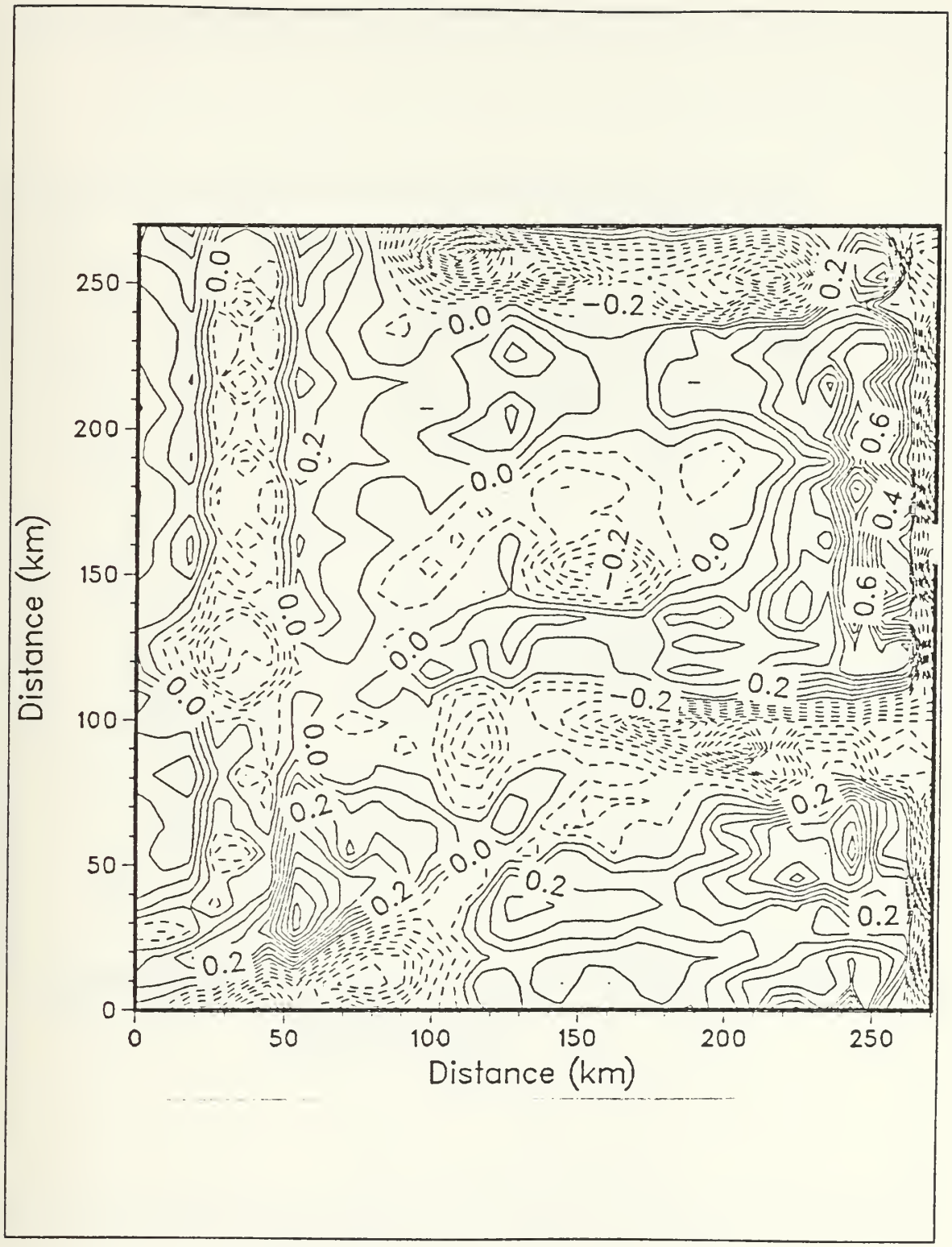

Figure 4.13 Same as Fig. 4.9 but at 50 m.

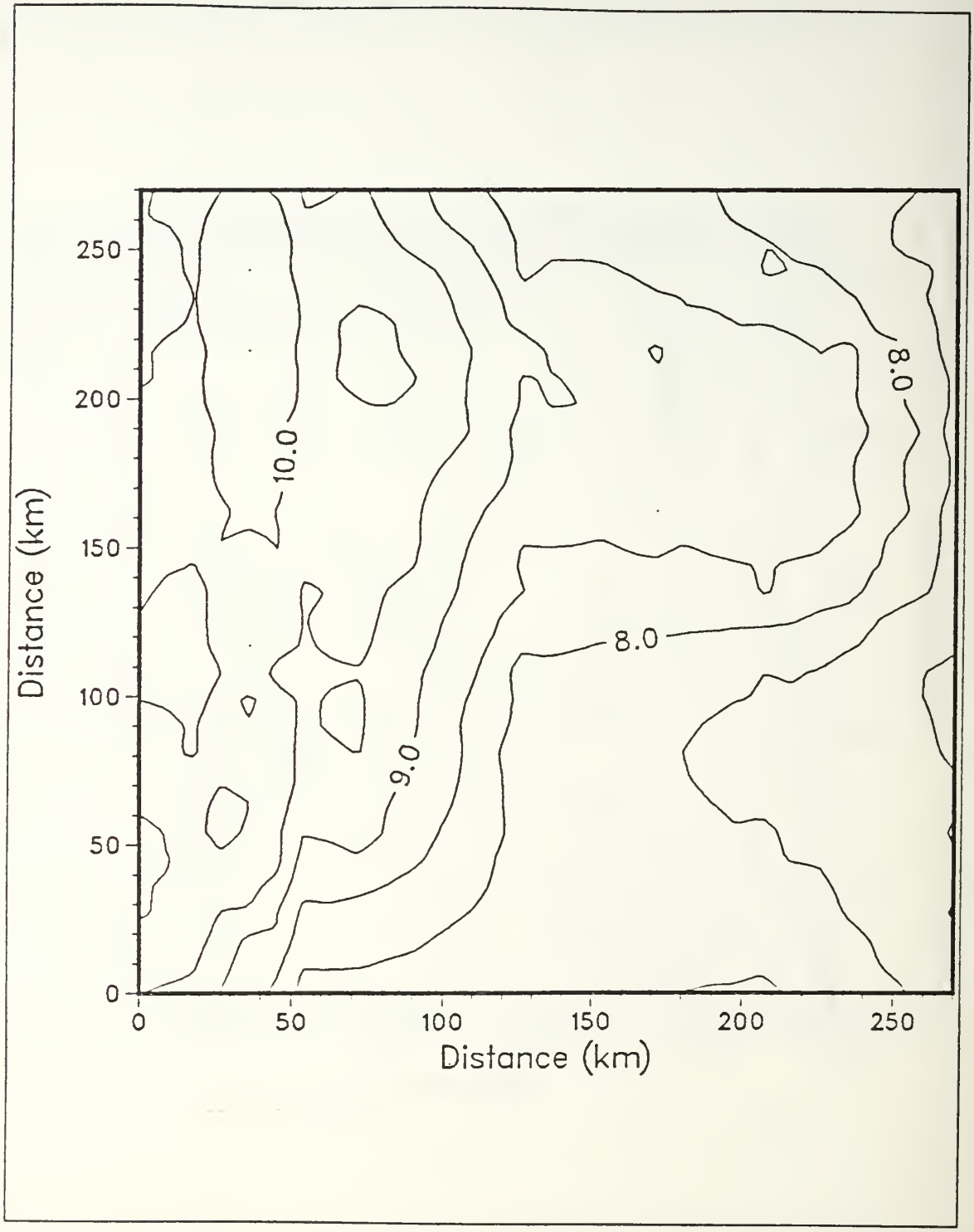

Figure 4.14 Same as Fig. 4.8 but at 200 m, pattern correlation 1.00, T range of 6.72 to 10.37 C.

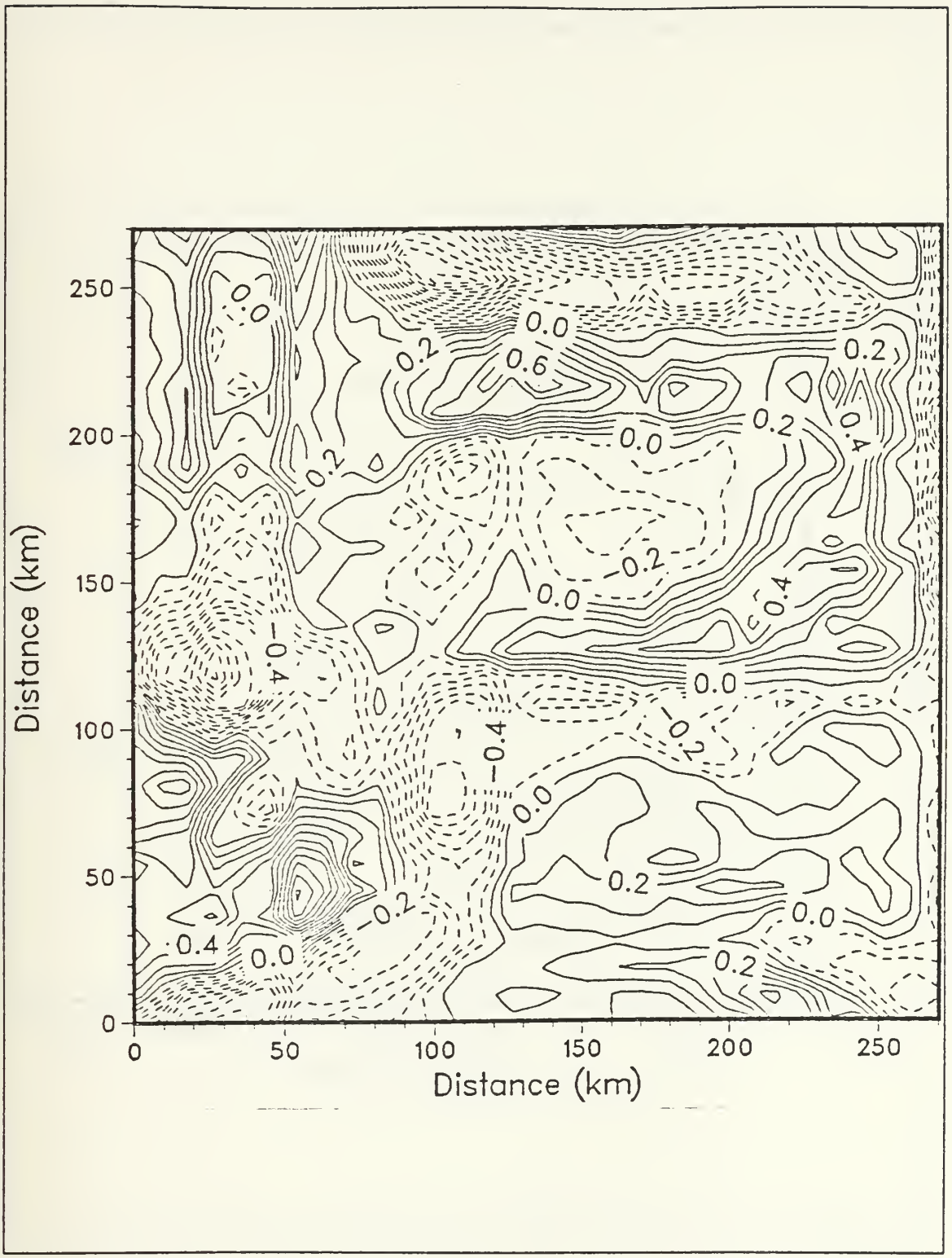

Figure 4.15 Same as Fig. 4.9 but at 200 m.

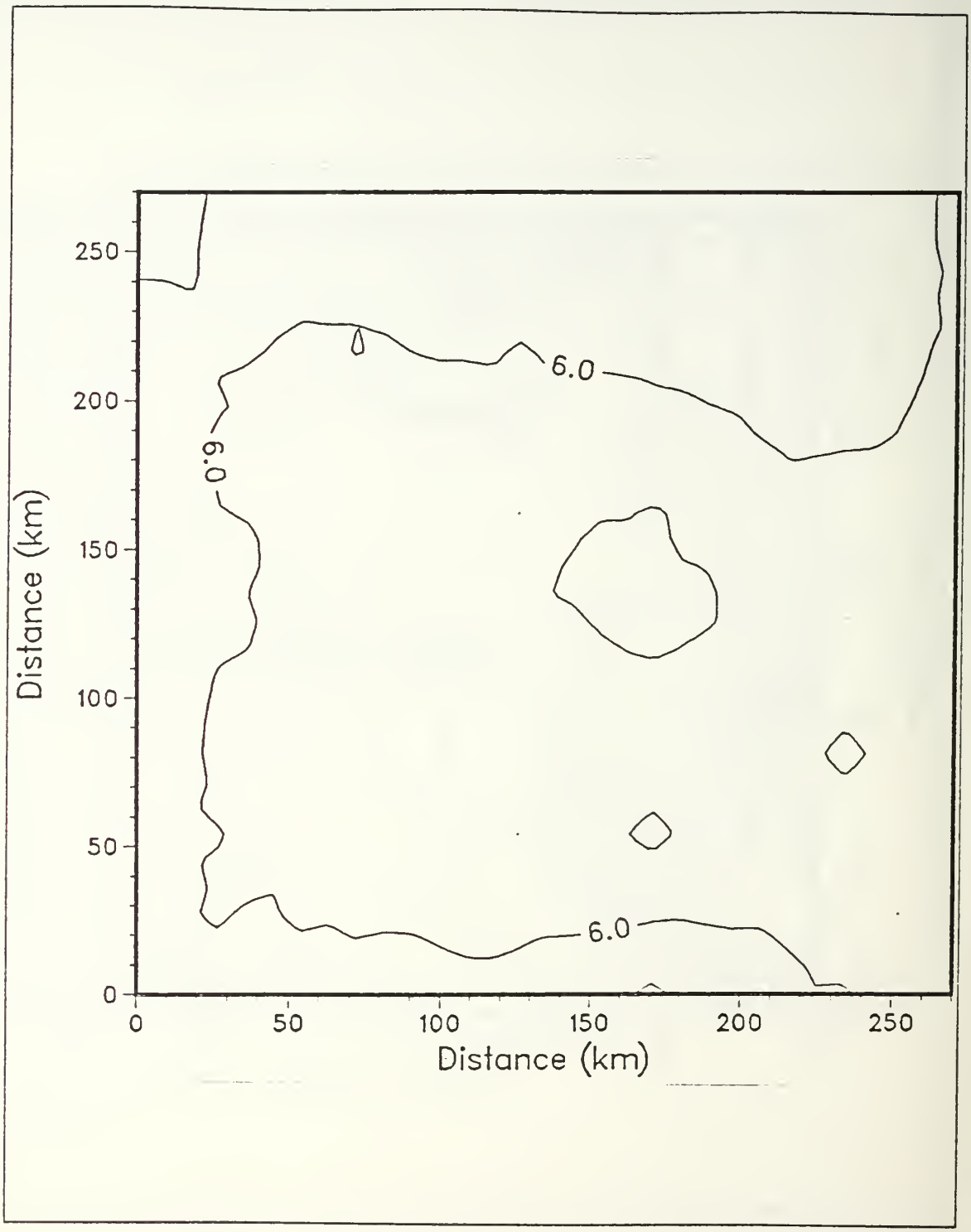

Figure 4.16 Same as Fig. 4.8 but at 550 m,
pattern correlation 0.84,
T range of 5.15 to 7.08 C.

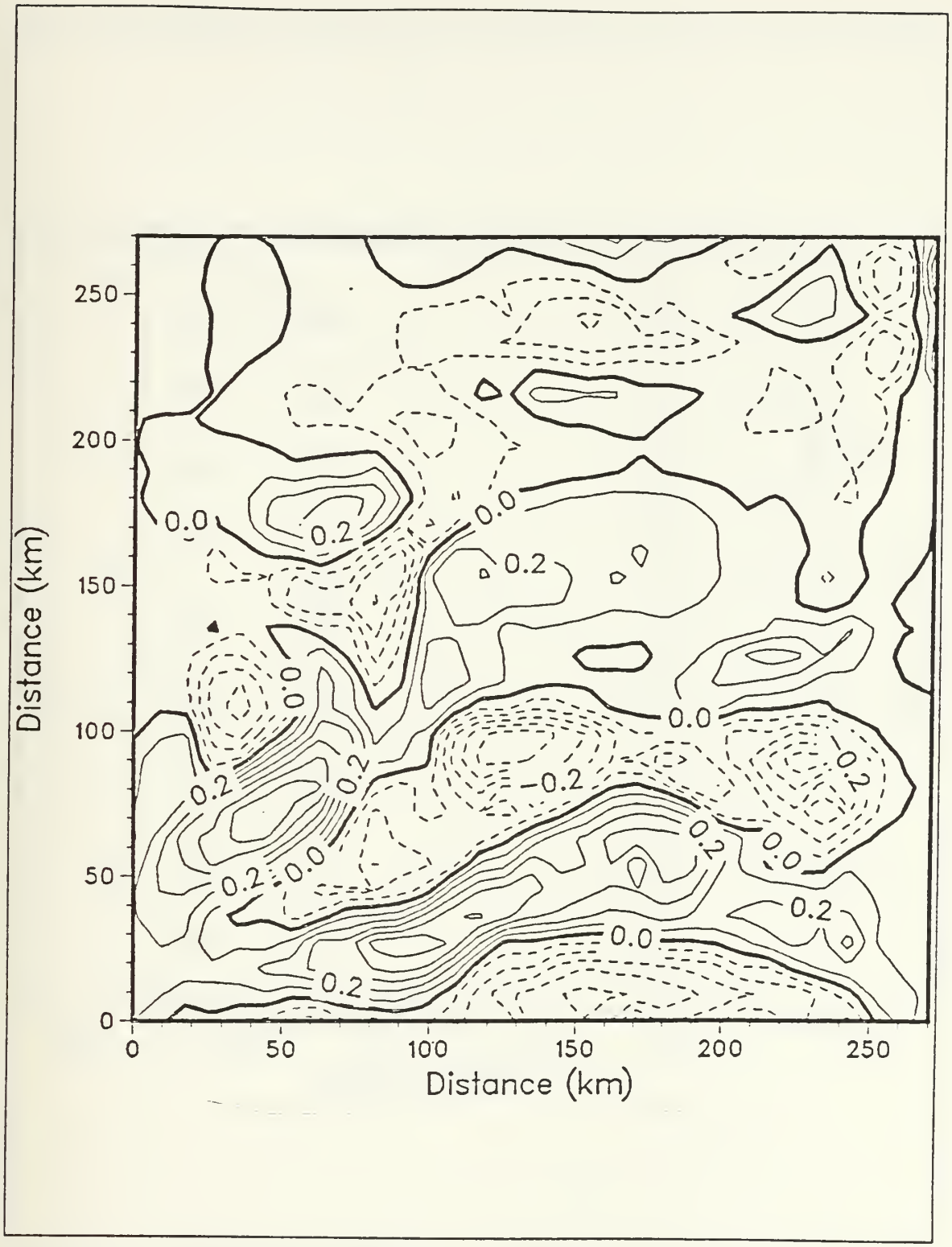

Figure 4.17 Same as Fig. 4.9 but at 550 m.

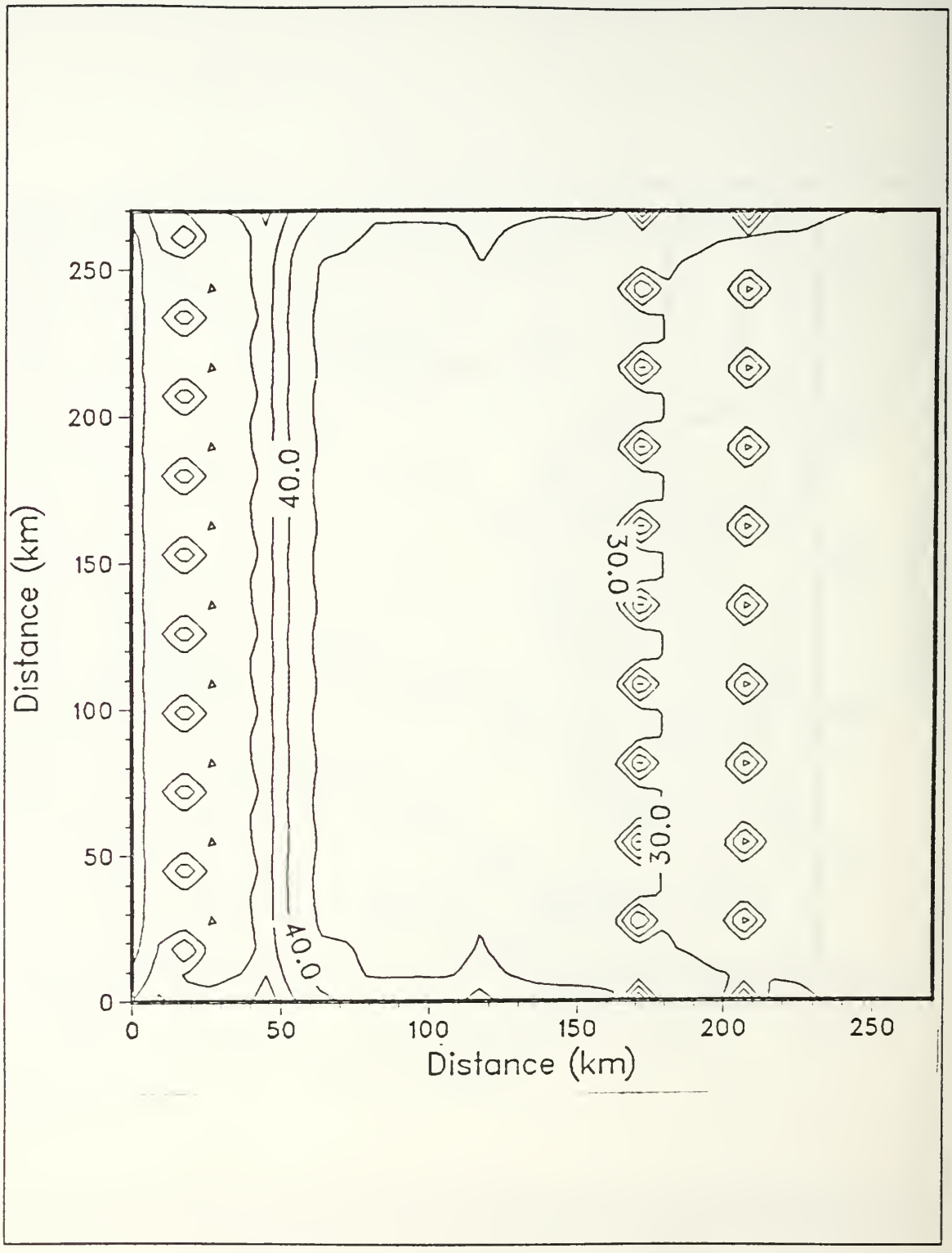

Figure 4.18 Same as Fig. 4.7 but for the advection case.

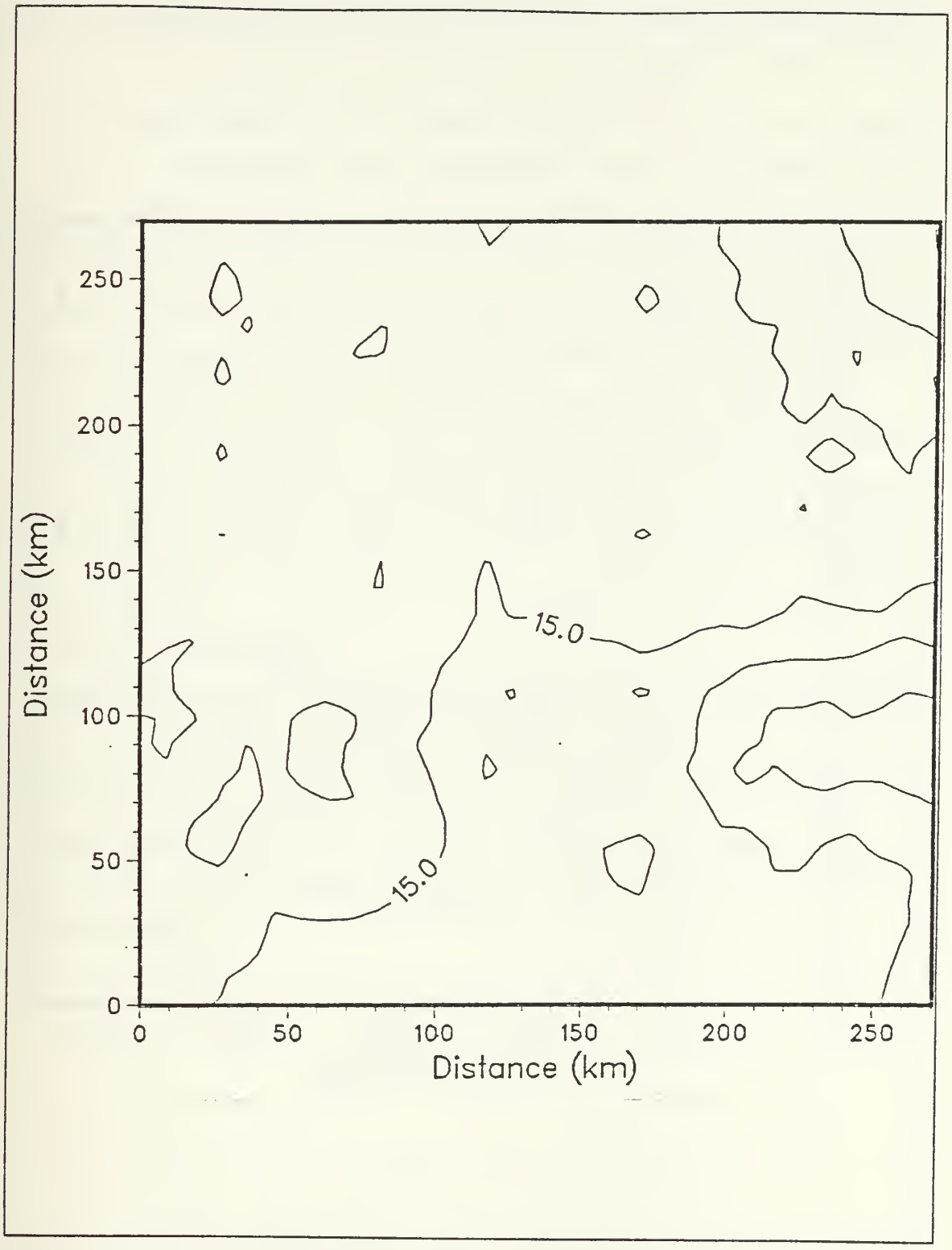

Figure 4.19 Same as Fig. 4.8 but for the advection case.

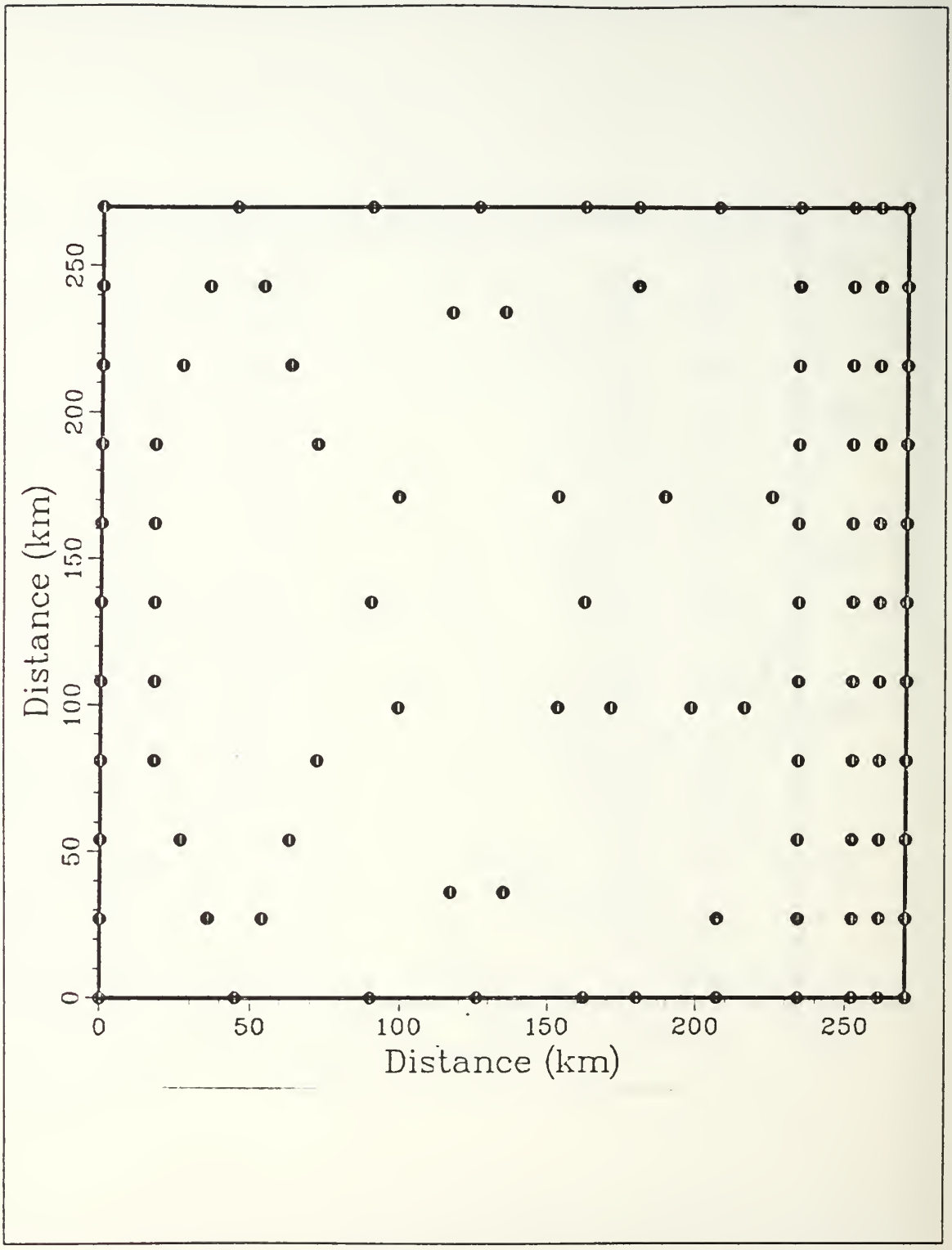

Figure 4.20 Survey III station positions.

respective error fields (Figs. 4.21 and 4.22) follows the same reasoning in that minimum errors coincide with XBT stations with maximum errors occurring in areas furthest from the observational positions in both distance and time scales.

No appreciable differences in the pattern correlation values are revealed between the two cases or with the other surveys. Examination of the OA temperature field at the surface for each case (Figs. 4.23 and 4.25) illustrates the improved portrayal of the mesoscale temperature features in the western domain as compared to those from the previous surveys. Greater resolution of the cool filament along the eastern boundary and of the cool and warm temperature anomalies in the western domain is achieved with the random sampling pattern. The temperature difference maps support this view, showing less temperature departures throughout the domain (Figs. 4.24 and 4.26).

Disparities between the two cases of Survey III are illustrated at the surface. Most noticable are the differences, although small, along the eastern boundary in association with the temperature front. Temperature differences are larger both in magnitude and area extent along this boundary in the second case due to erroneous advection parameters.

D. SURVEY COMPARISON

A statistical analysis was conducted in the same fashion as that which was done for the P-3 cruises. Similar results were produced. The pattern correlation values between each of the surveys were all above 90%, mean absolute errors were less than 2% at all depths and a majority of the root mean-square error was attributable to unsystematic errors. Through visual comparison, it is readily apparent that Survey III, which employed a random sampling pattern, was deemed to be the 'best' strategy among those tested.

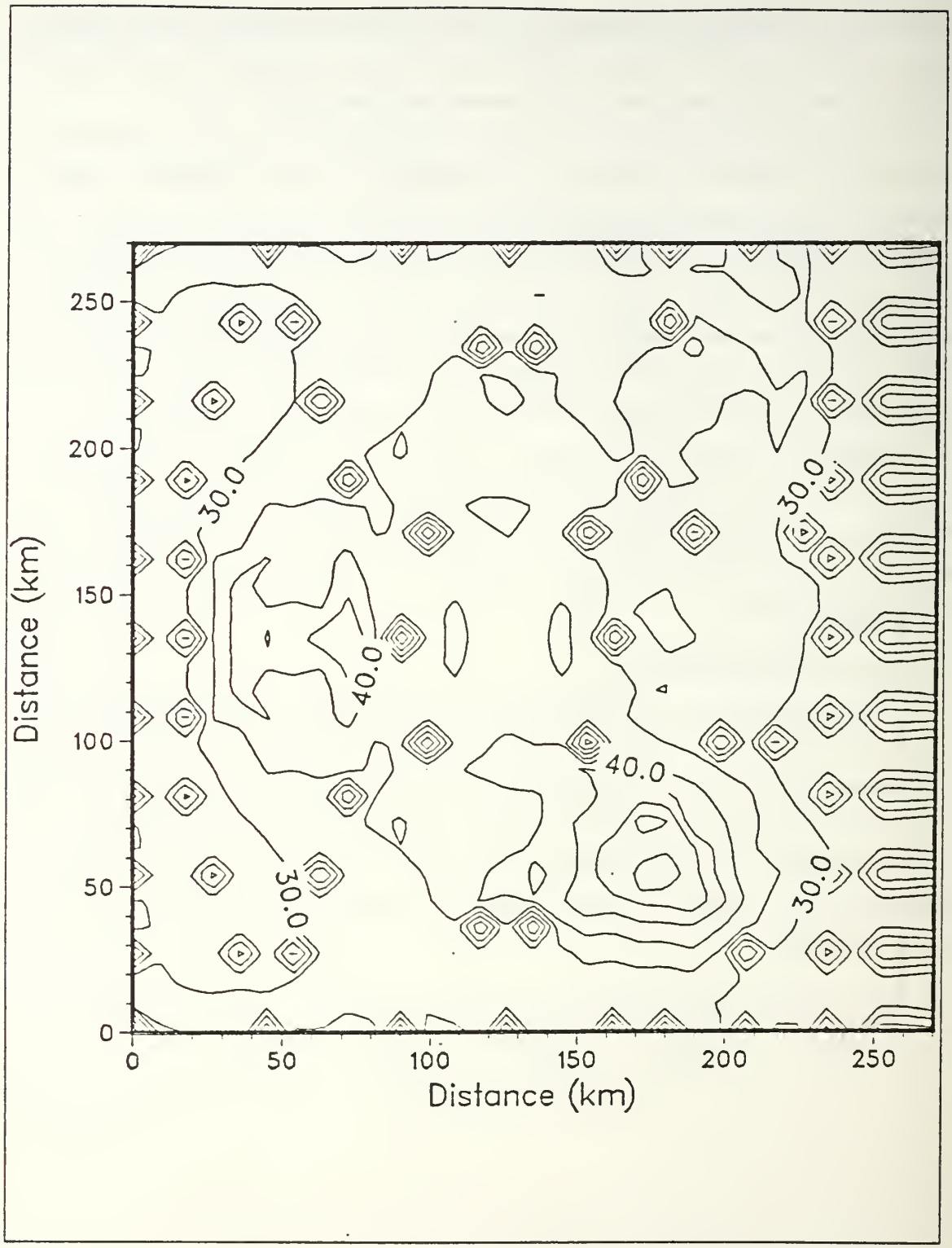

Figure 4.21 Survey III temperature error field.

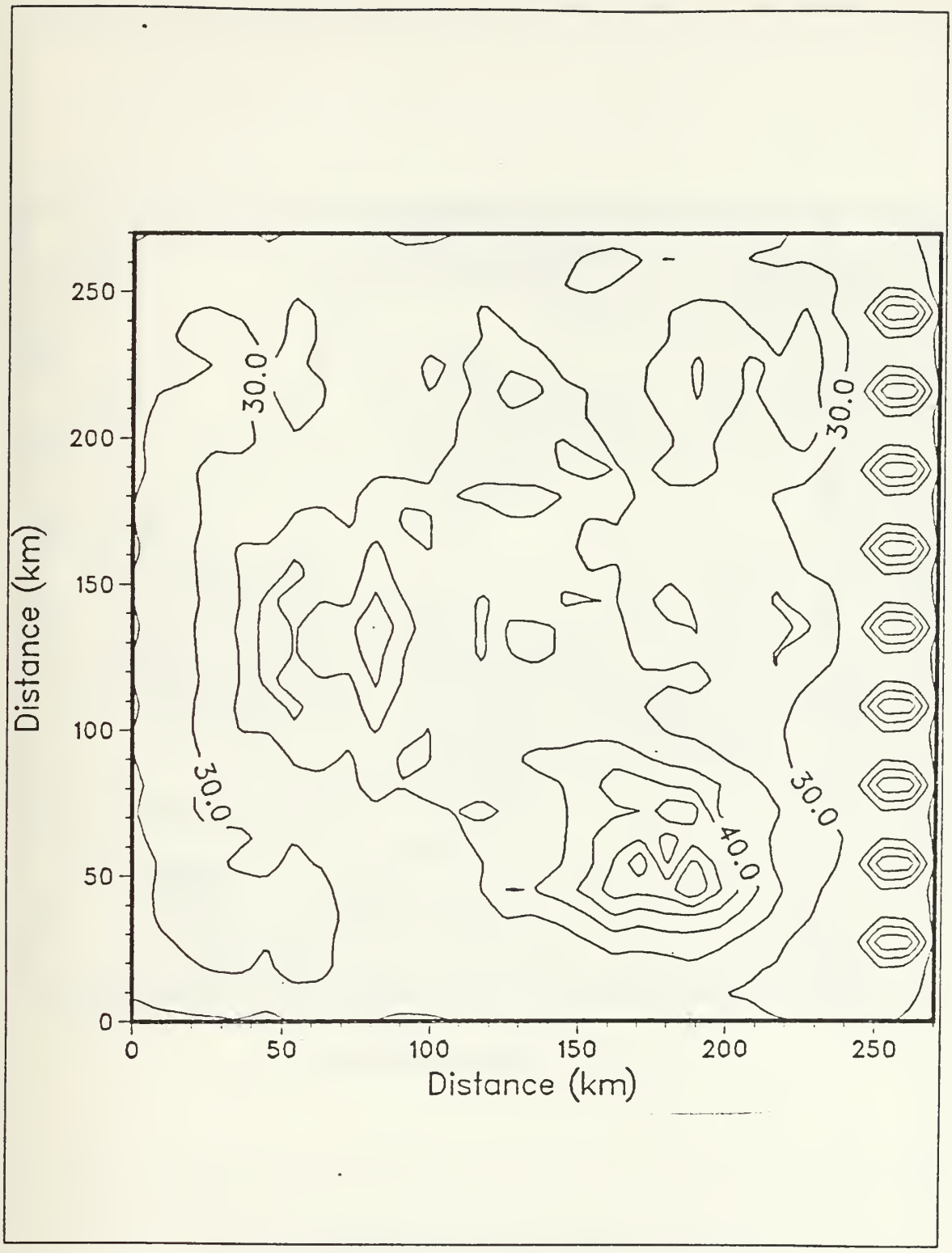

Figure 4.22 Same as Fig. 4.21 but for the advection case.

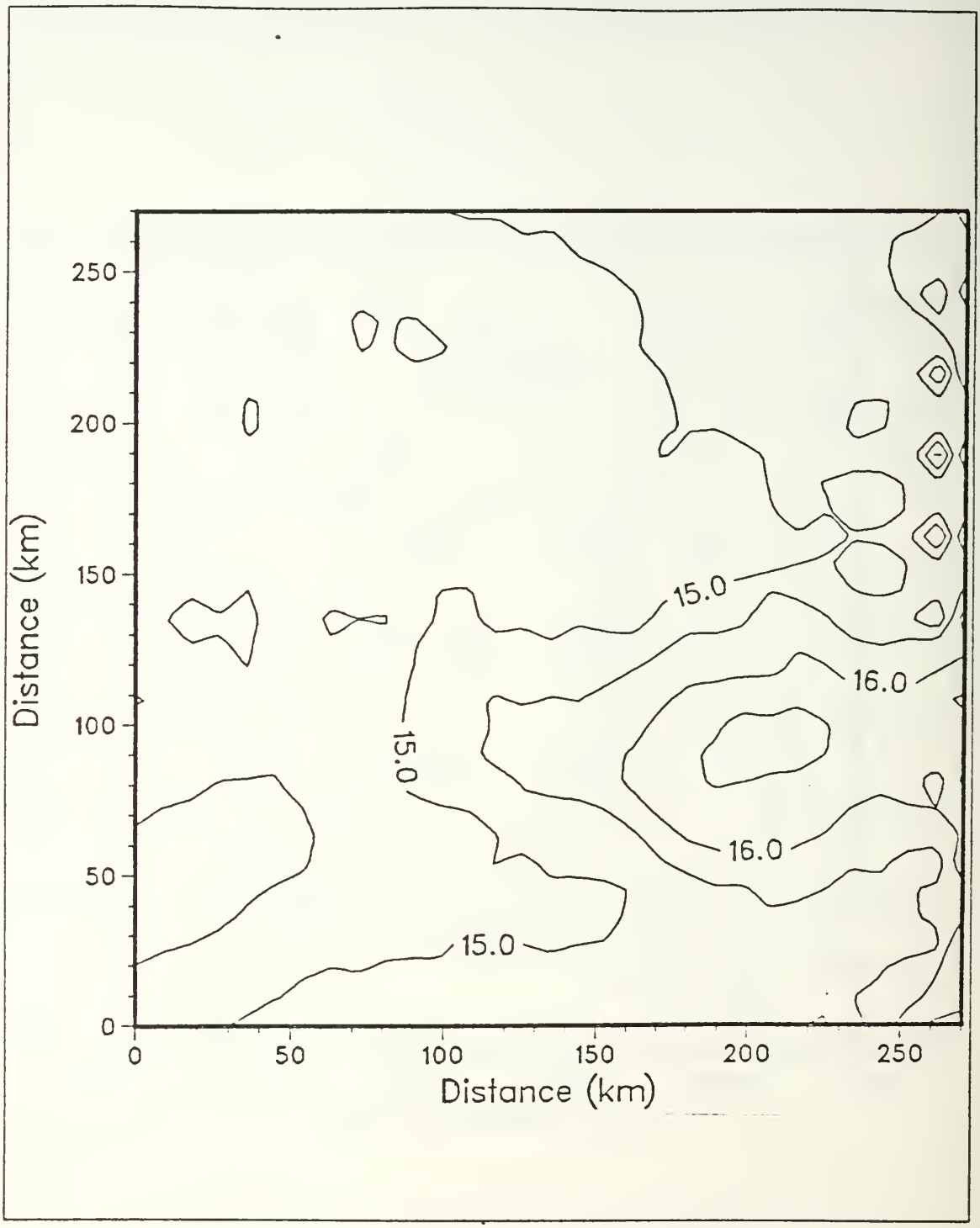

Figure 4.23 OA interpolated SST field on day 40,
Survey III, pattern correlation 0.66,
T range of 13.75 to 16.94 C.

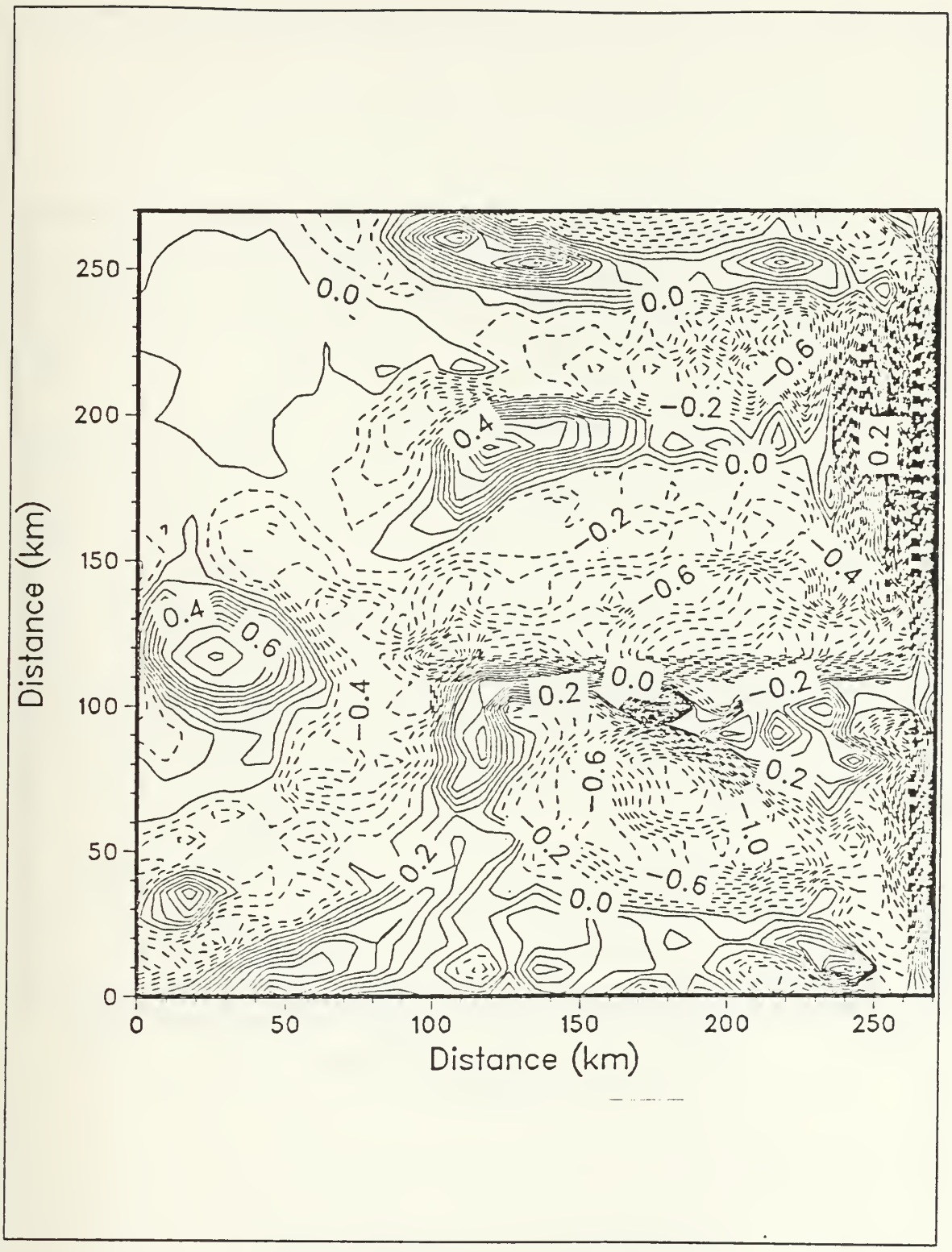

Figure 4.24 SST difference field on day 40, Survey III.

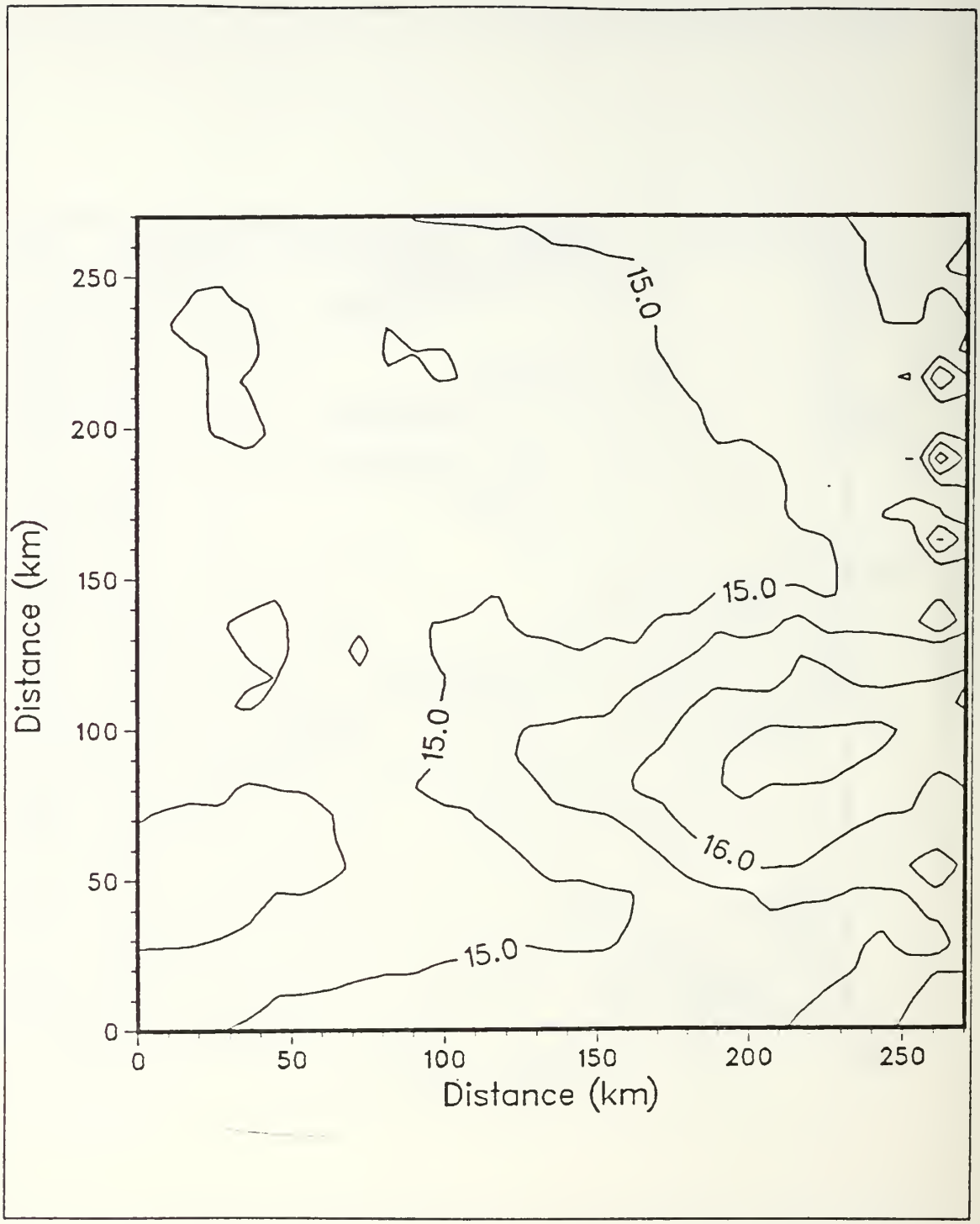

Figure 4.25 Same as Fig. 4.23 but for the advection case, pattern correlation of 0.69, T range of 13.77 to 16.93 C.

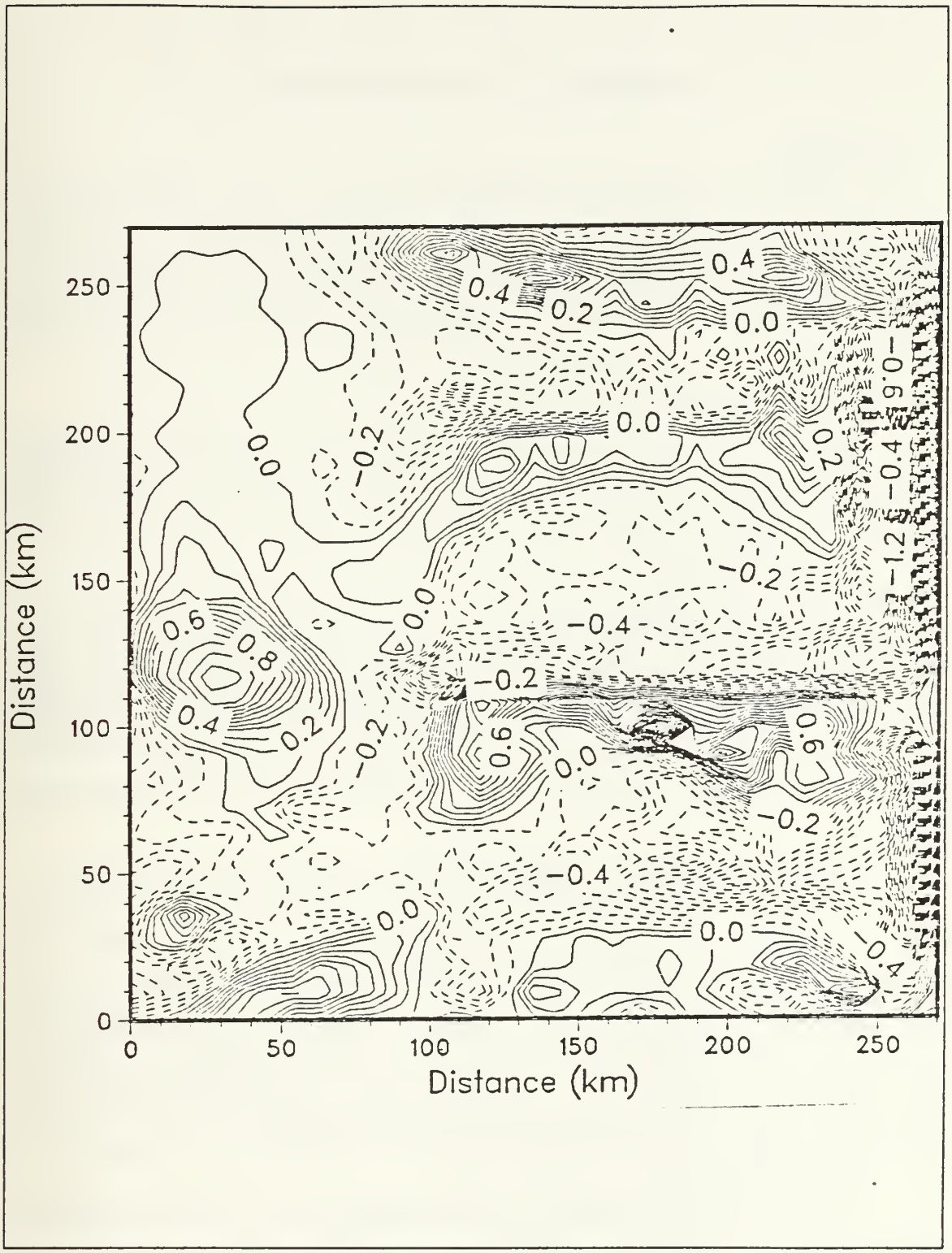

Figure 4.26 Same as Fig. 4.24 but for the advection case.

V. SUMMARY AND CONCLUSIONS

A. SUMMARY

This study has examined along-track spacing increments from model output to determine the largest separation of data sampling permissible to achieve a reasonable representation of ocean mesoscale features without serious aliasing. With this objective, three sampling strategies were tested and analyzed by conducting simulated aircraft and shipboard cruises.

1. Sampling Strategies

Previous experience and knowledge of the temperature field was useful in selecting the sampling schemes, which were all constrained to the use of ninety-nine observations. The patterns which were chosen and their corresponding results can be summarized as follows.

a. Uniform Pattern

The sampling strategy of distributing observational stations in a uniform or near uniform pattern is the typical P-3 flight deployment used for acquiring data. Due to the large size of the area investigated, a minimum spacing distance of 27 km was used. This proved to be inadequate, as in several instances both mesoscale and tight gradient features, with spatial scales less than the sampling distance, were inaccurrately depicted.

b. Non-Uniform Stratified Pattern

Because of a coastal bias in the temperature field, use of a finer sampling scheme was necessary to resolve the coastal temperature structure. This produced a much improved picture of the major temperature features along the eastern boundary of the studied domain. The concentration of heavier sampling along the coast resulted in fewer observations offshore with spacing distances between stations as far apart as 81 km in the east-west direction. As a consequence, many of the mesoscale features in the central and offshore regions of the domain were not resolved.

c. Random Pattern

Heavier sampling along the coast was maintained in view of the excellent results which were achieved by use of the non-uniform stratified sampling pattern in the eastern domain. In an attempt to better resolve the temperature structure in the

central and western regions, a random sampling scheme was employed offshore. The result was a higher quality depiction of the mesoscale features in these areas. The cool and warm temperature anomalies undetected or poorly represented by the uniform and non-uniform stratified sampling schemes were resolved to a greater extent with the random sampling pattern. Although this pattern was deemed as being the 'best' sampling strategy in space and time as compared to the previous two, more research is required to determine if this random sampling pattern or a different one is the 'optimal' scheme which can be employed elsewhere in oceanic regions with similar temperature characteristics as those observed in this study.

2. **P-3 Cruises versus Shipboard Hydrographic Surveys**

The pattern correlation values for each cruise and survey versus the assumed 'perfect' temperature field for the three sampling patterns conducted at the different depths showed no large deviations. When comparing the correlations computed between each cruise and corresponding survey, similar statistical results were obtained. Pattern similarities greater than 95% were shown to exist at each depth as represented by the comparison between the P-3 cruise and the hydrographic survey which used the random sampling scheme (Table 5). Mean absolute errors of 10% or less at each depth solidifies the conclusion that there is no desired preference between aircraft and hydrographic sampling if the time period of observations is 5 days or less.

TABLE 5

STATISTICAL MEASURES OF P-3 CRUISE III VS. HYDROGRAPHIC SURVEY III

	Surface	25 m	50 m	200 m	550 m
P-3 III Mean Temp	15.07	13.71	12.25	8.60	6.08
Hydro III Mean Temp	15.10	13.74	12.21	8.57	6.09
P-3 III Variance	0.28	0.18	1.36	0.88	0.05
Hydro III Variance	0.27	0.19	1.40	0.89	0.06
Pattern Correlation	0.96	0.98	1.00	0.99	0.97
MAE	0.10	0.07	0.08	0.09	0.07

3. Objective Analysis

Due to the limited number of observations, the use of an objective analysis technique was employed to analyze the data field. This technique served as an excellent method for the comparison of each sampling pattern with the assumed 'perfect' PE temperature fields. The basic temperature pattern was well represented in all cases examined. Major drawbacks of the technique were its underestimation of the temperature anomalies due, in large part, to the small number of samples; the misrepresentation of strong, tight gradient features and smaller mesoscale features, which were less than the station spacing distances; and the false representation of stationary features when the entire field was advected at the mean eddy propagation speed due to the use of an isotropic correlation function.

Caution must be exercised in the determination of the values which are supplied to the OA technique as this routine is very parameter dependent, that is, depending on the oceanic variable of interest, the individual sampling pattern selected and the geographic area of interest, different parameter values must be used. The most important of these to consider are the number of influential points to be used, the corresponding spatial and temporal radii of influence and the parameters which define the correlation function.

B. RECOMMENDATIONS

This study is a first step in determining an optimal ship or aircraft sampling pattern for the analysis of mesoscale processes in the California Current System. Future work should examine an ensemble of other possible sampling schemes. Analysis of hydrographic cruises conducted over longer time periods, e.g., two weeks, should be undertaken to better determine the degree of synopticity required of shipboard surveys for field representation of mesoscale features.

Field observations are known to contain both instrumental and aliasing errors. This study used clean observational data generated by a PE model. Experiments should be conducted in the future in which random noise is added to the PE model observations with the resulting values applied to the OA technique. This will produce results which are more realistic of the true ocean.

This study presents several avenues which have military applications. Research on optimal sampling strategies conducted through the use of simulated cruises would be useful in the planning stages of military operations. Of special importance are those

operations concerned with anti-submarine warfare. It is well known that mesoscale features, especially eddies, affects significantly all the characteristics of the acoustic field, in particular, at the receiver, the arrival sequence, the amplitude and the angular distribution of energy. If knowledge of the relevant oceanic conditions exist, their influences on sensors, systems, platforms and tactics will be advantageous and aid in the maintaining of superiority through the optimum use of acoustic and other detection devices. Hence, it is important, in the future, to quantify the impact of the quality of the ocean thermal structure maps on acoustic propagation calculations, including transmission loss, etc., and on ASW tactical decision-making. Then operational guidance can be developed for effective ocean sampling strategies.

APPENDIX A
OBJECTIVE ANALYSIS PARAMETER DETERMINATION

1. EFFECT OF DETRENDING AND FILTERING

Within the objective analysis technique, two functions exist which may be used to create a map of the smoothed field of interest from a collection of noisy observations. These routines, detrending and filtering, may be applied either separately or in combination.

The data consists of statistical fluctuations about a mean value with some bilinear X, Y trend. This bilinear trend field,

$$\psi_r = ax + by + c + [\varphi_r] + \varepsilon_r,$$

may be removed by using least squares estimates for a, b and c.

If small scale noise exists, the data can be filtered in both the X and Y directions. The filter employed is a second-order Shapiro filter which eliminates all wavelengths twice the size of the grid length as was described in greater detail in Chapter 1.

The question of whether to remove the trend and/or filter the data was examined. A multitude of cases were studied to determine this answer, only one of which will be presented below.

The first cruise consisted of 99 observations. Station spacing in the north-south and east-west directions were held constant at 30 km and 40 km, respectively (Fig. A.1a). This simulated case was examined at the surface on day 40. Figure A.1b shows the PE model output map of the temperature field for comparison. The radius of influence and the maximum number of influential points were fixed at 50 km and 8, respectively. Four maps were generated to illustrate the effects of detrending and filtering the data. The first map depicts the temperature field with the data observations neither detrended nor filtered (Fig. A.2a). Eddies are much less defined or even missing in some areas entirely and tight gradient features are seen as being broader. This result can be attributed to the sampling strategy used in this particular case. By removing the trend in the data and not applying the filter resulted in Figure A.2b, the basic structural pattern remains unchanged. The reduction in the standard deviation, when the bilinear trend was accounted for, was from 0.8°C to 0.6°C, not very large. Thus, the bilinear trend was found to be unimportant, as it doesn't

contribute much to explaining the data. When the filter alone was applied to the data (Fig. A.3a), one major structural change occurred. A cold-core eddy located 200 km offshore was closed off. This indicates that there are very little high frequency signals available in the data to be filtered out. A similar map results when the detrending and filtering techniques are applied in combination (Fig. A.3b).

Many other cases were examined at different depths and the results of removing the trend and filtering the data were similar to those descibed above. Since the bilinear trend was determined to be insignificant and filtering of little consequence other than for aesthetic reasons, these two operations will not be applied in conjunction with the objective analysis technique to map the desired fields.

2. EFFECT OF VARYING THE NUMBER OF INFLUENTIAL POINTS

As stated in Chapter 1 the highest correlated data points within the influential domain are chosen to form an estimate at the interpolation points. When there are numerous data observations within the radius of influence a sorting technique is used which not only sorts by correlation but also by the number of influential points dictated by the user. This latter parameter is a determining factor which affects the resolution of the field of interest.

Two separate cases were examined in order to find the most suitable number of influential points to be used. The first case studied comprised 99 observations. Station spacing in the north-south direction was held constant at 30 km. Spacing in the east-west direction varied from a maximum of 80 km offshore with steadily decreasing distances toward the coast to a minimum of 8 km (Fig. A.4a). This simulated test case was examined at the surface on day 40. The mean temperature was 15.15^{o}C with a variance of 0.96(°C)^{2}. Figure A.4b shows the PE model output of the temperature field on day 40 at the surface. The dominant feature depicted is the north-south oriented jet located adjacent to the coast. The following decisions were used in the analysis:

- data observations were not detrended;
- data observations were not filtered;
- a 50 km radius of influence was used; and
- the maximum number of influential points was varied from 8 to 4 to 2.

Figures A.5 through A.7 show the results of varying the number of influential points and their associated error fields. Concentrating our attention on the north-south oriented jet it is evident that as the number of points of influence decreases from 8 to

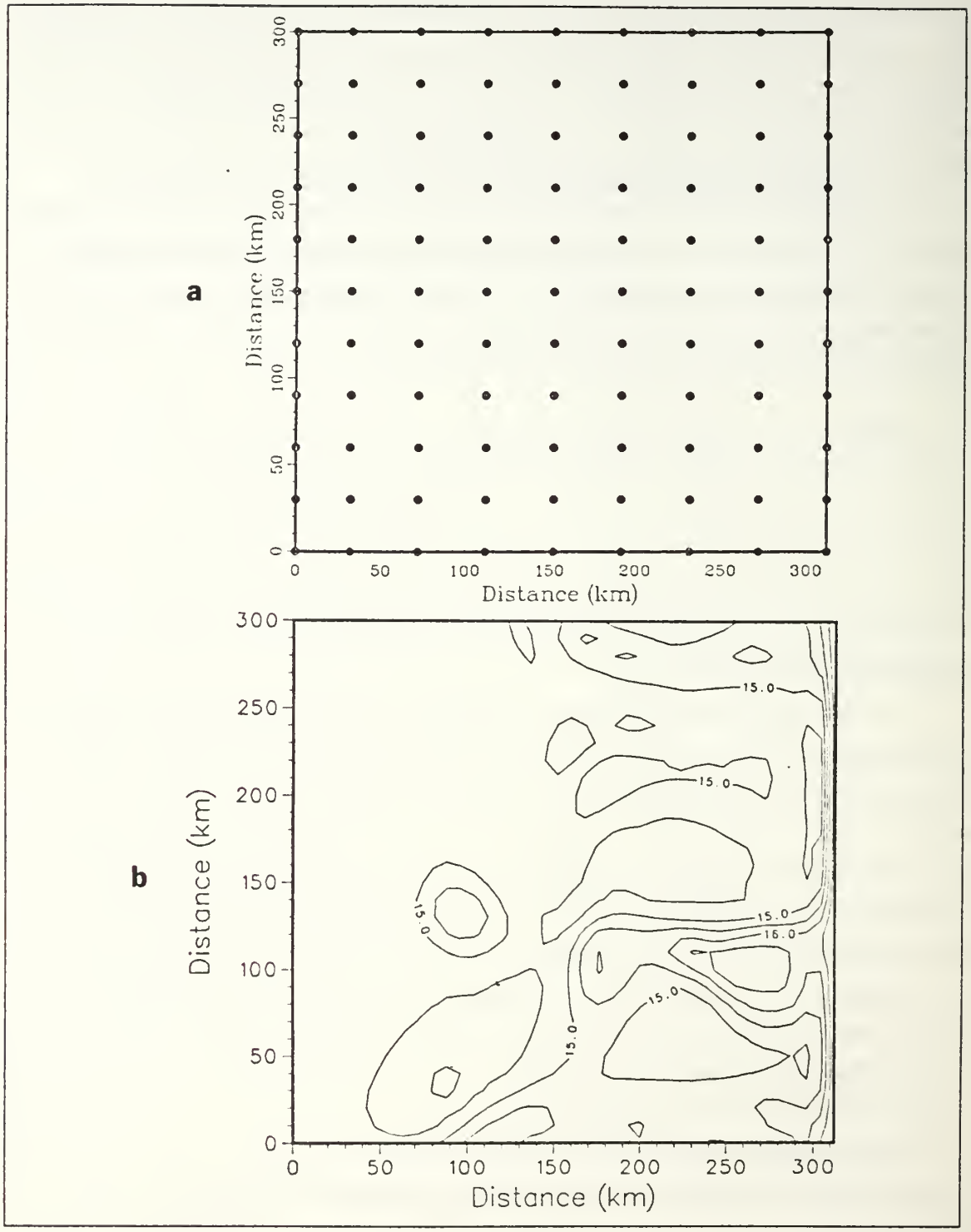

Figure A.1 (a) Station spacing of initial case,
(b) PE model SST field on day 40,
contour interval of 0.5 C.

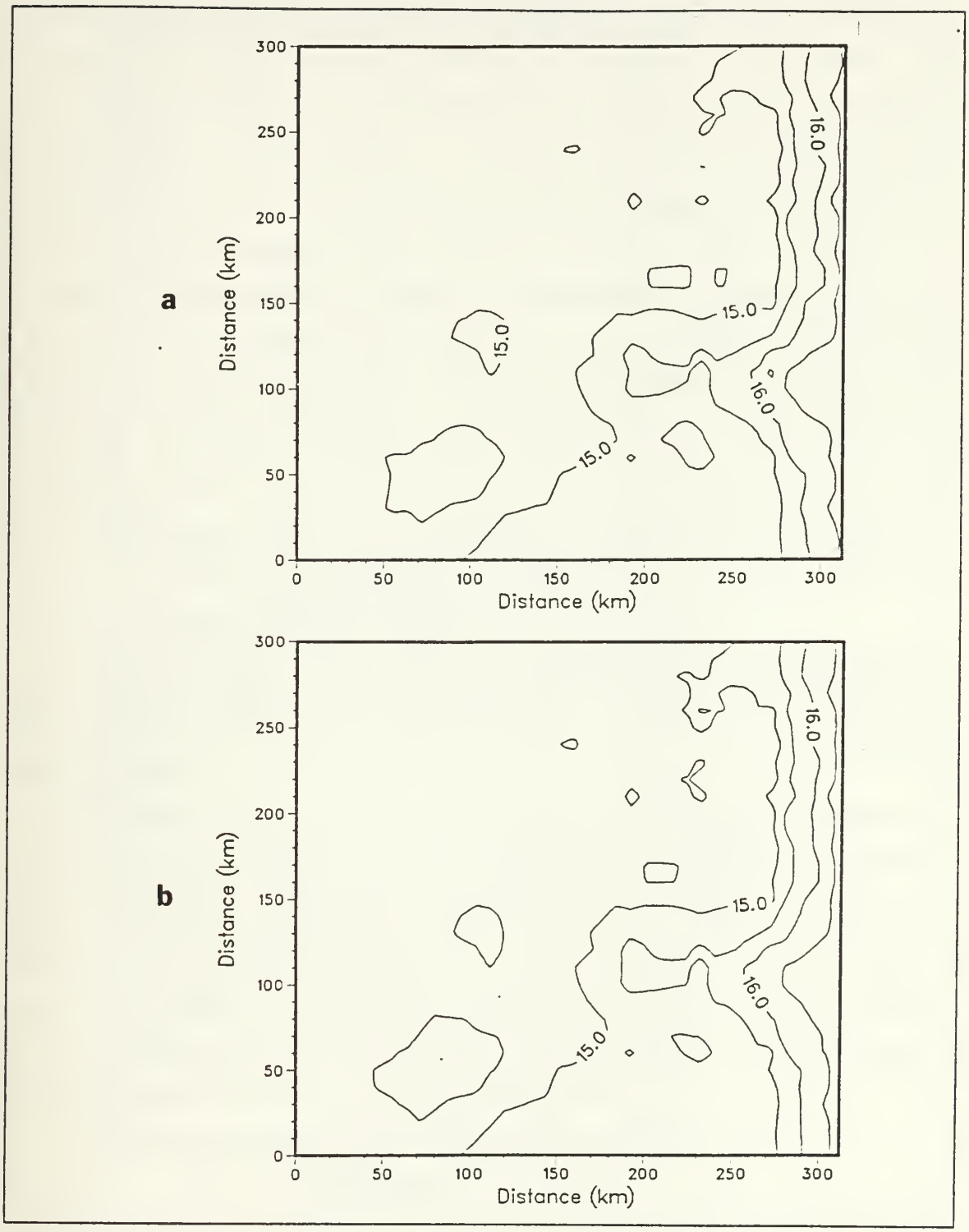

Figure A.2 OA SST field on day 40 with
(a) data neither detrended nor filtered,
(b) with trend removed.

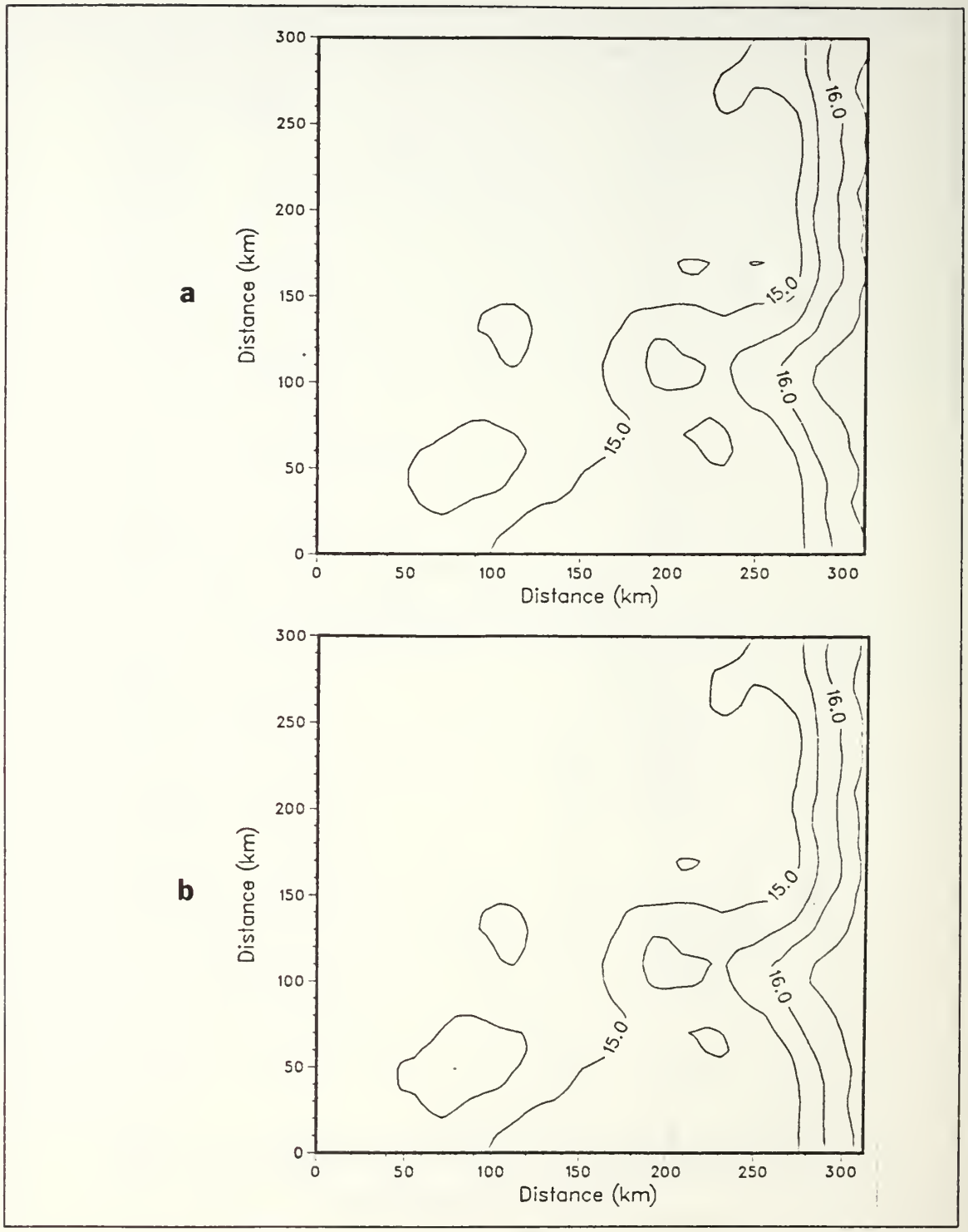

Figure A.3 OA SST field on day 40 with (a) data filtered, (b) with trend removed and data filtered.

2, the resolution of this feature increases. A drawback of decreasing the number of influential points is that the error in estimating the field increases. For example, the maximum error in the temperature field increases from 54% to 66% when the number of influential points is decreased from 8 to 2 (Figs. A.5b-A.7b). This increase in error is concentrated in the domain furthest from the coastline where the sampling is sparse and not near the coast where sampling is densest. The error remains relatively constant close inshore where the dominant features of the domain exist.

The second case which was examined is a modification of the first. Spacing in the east-west direction was further reduced close to the coast. The north-south spacing and the number of observation points remained unchanged (Fig. A.8a). This case was created in an attempt to achieve even better resolution of the north-south oriented jet by increasing the sampling along the coast. The second sampling strategy used the same objective analysis parameters as in the first case. The mean temperature was $15.21^{o}C$ with a variance of $0.92(^{\circ}C)^{2}$. By decreasing the number of points of influence from 8 to 2 the north-south oriented jet is better depicted (Figs. A.9 through A.10). As in the first case the error behaves as expected.

In conclusion, it appears that to achieve the required resolution of tight gradient features, one must employ closely sampled spacing strategies and the points of influence should be small in number. These criteria have been applied in the sampling cruises of this study.

Even though better resolution resulted from a decrease in the number of influential points, the north-south oriented jet still lacked the tight gradient aspect as illustrated from the PE model output temperature field. Depending on whether the feature is oriented in a north-south or east-west direction, the spacing of observations should be less in the orientation direction of the feature. Otherwise the feature will be biased. A basic solution to this problem is to ensure that the grid and sample spacing in the X, Y horizontal domain are equivalent. To achieve this the PE model output spacing was changed from an 8 x 10 to a 9 x 9 km grid cell.

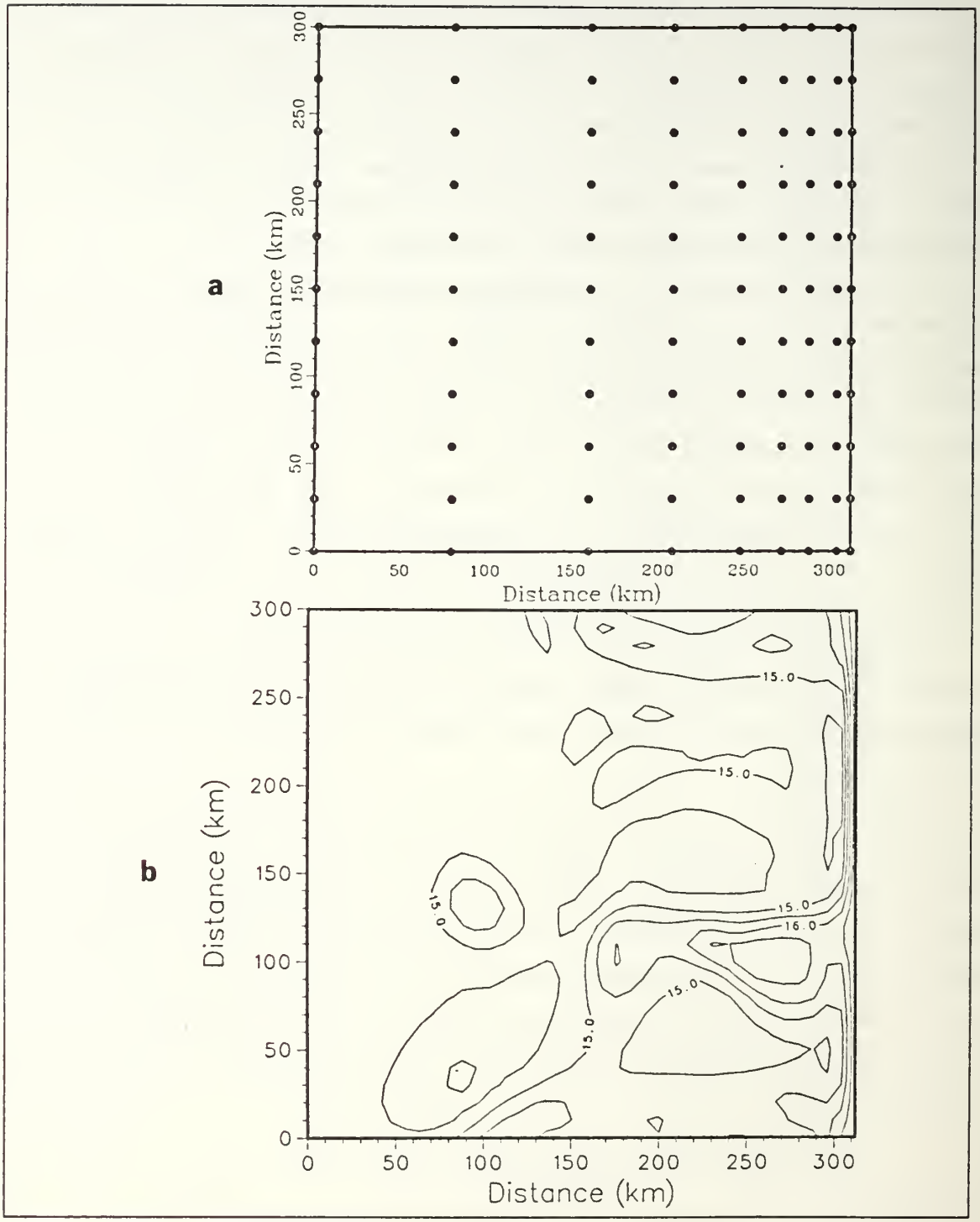

Figure A.4 (a) Case 1 station spacing,
(b) PE model SST field on day 40,
contour interval of 0.5 C.

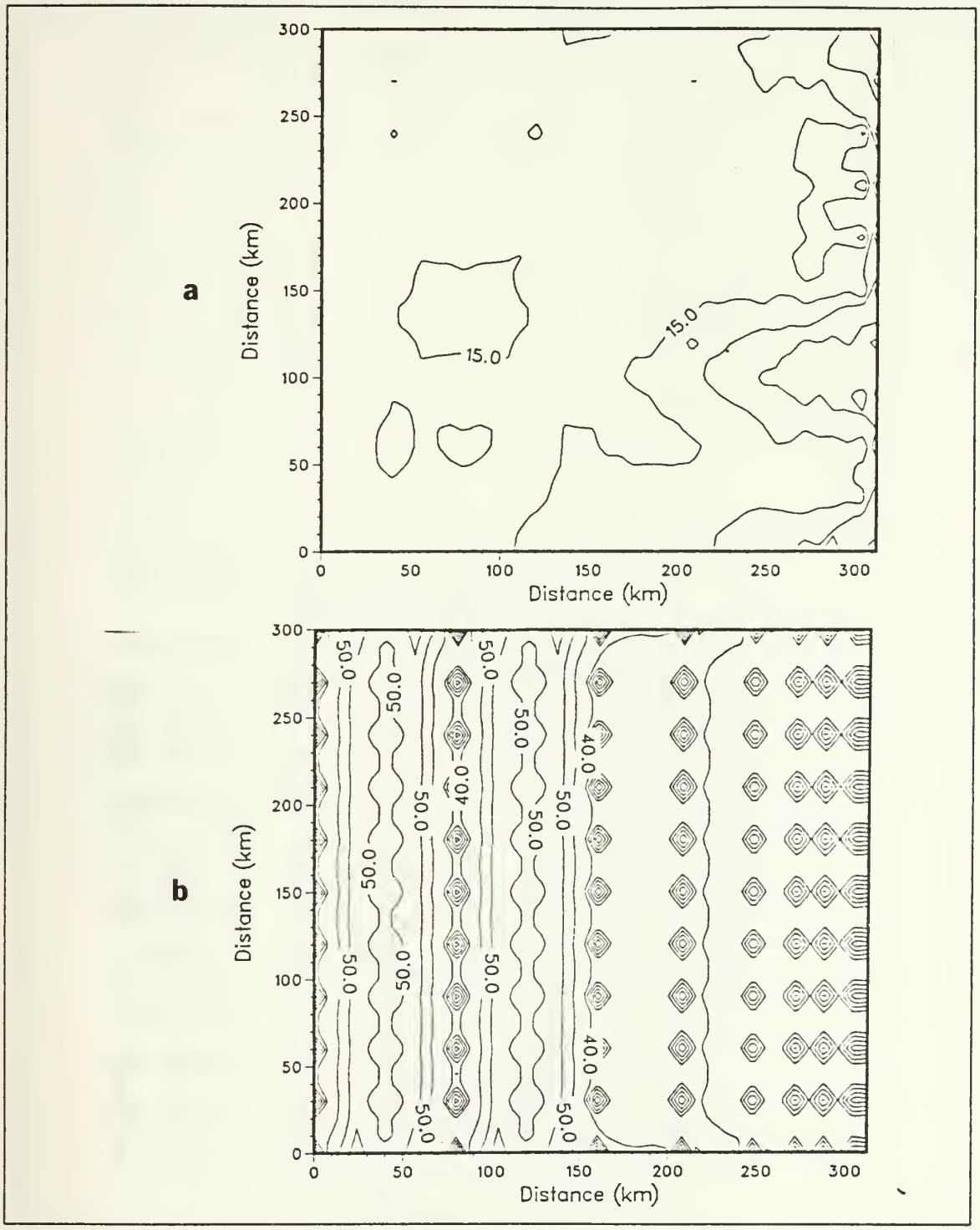

Figure A.5 Case 1 OA SST field using
(a) 8 points of influence with
(b) associated error field.

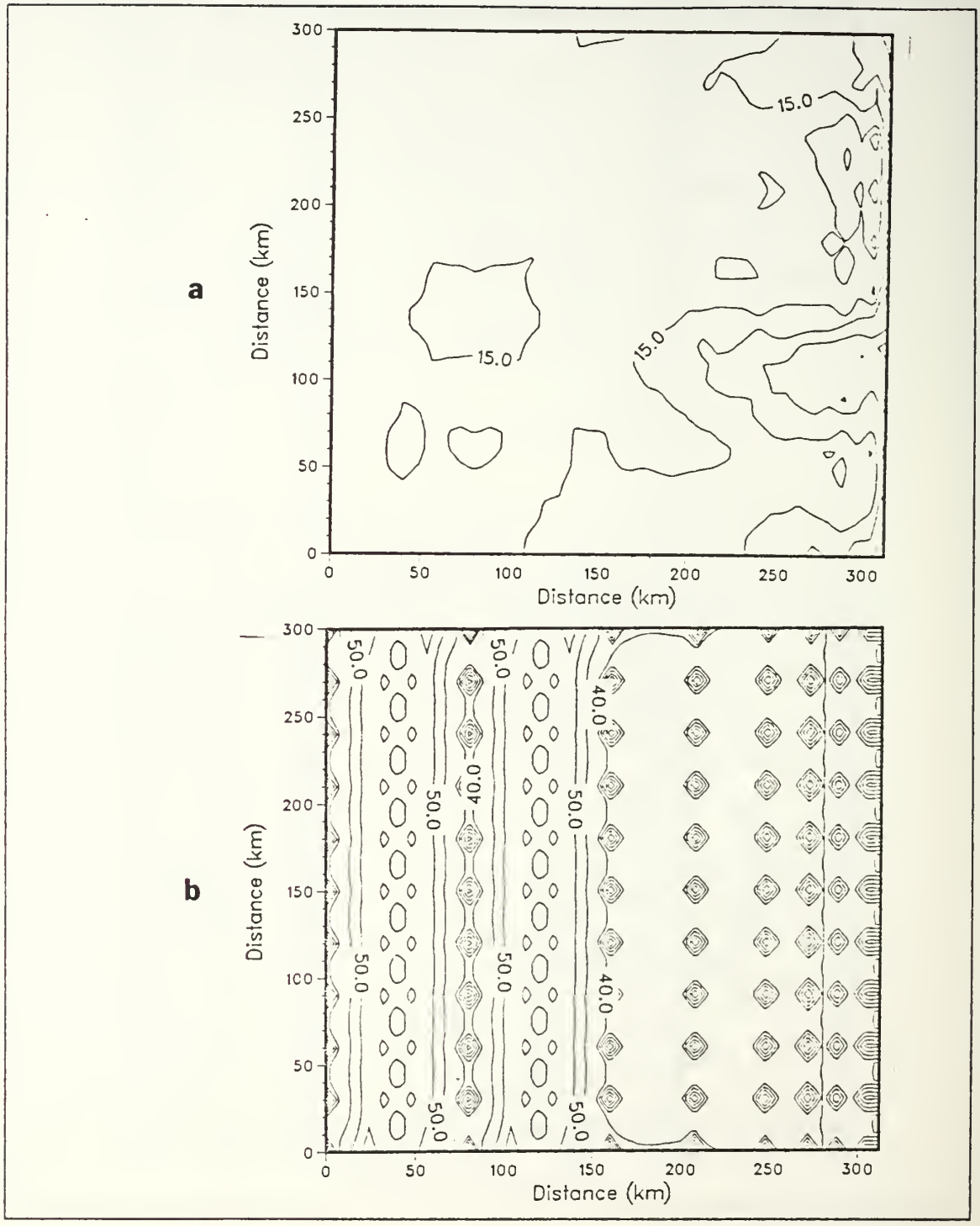

Figure A.6 Case 1 OA SST field using
(a) 4 points of influence with
(b) associated error field.

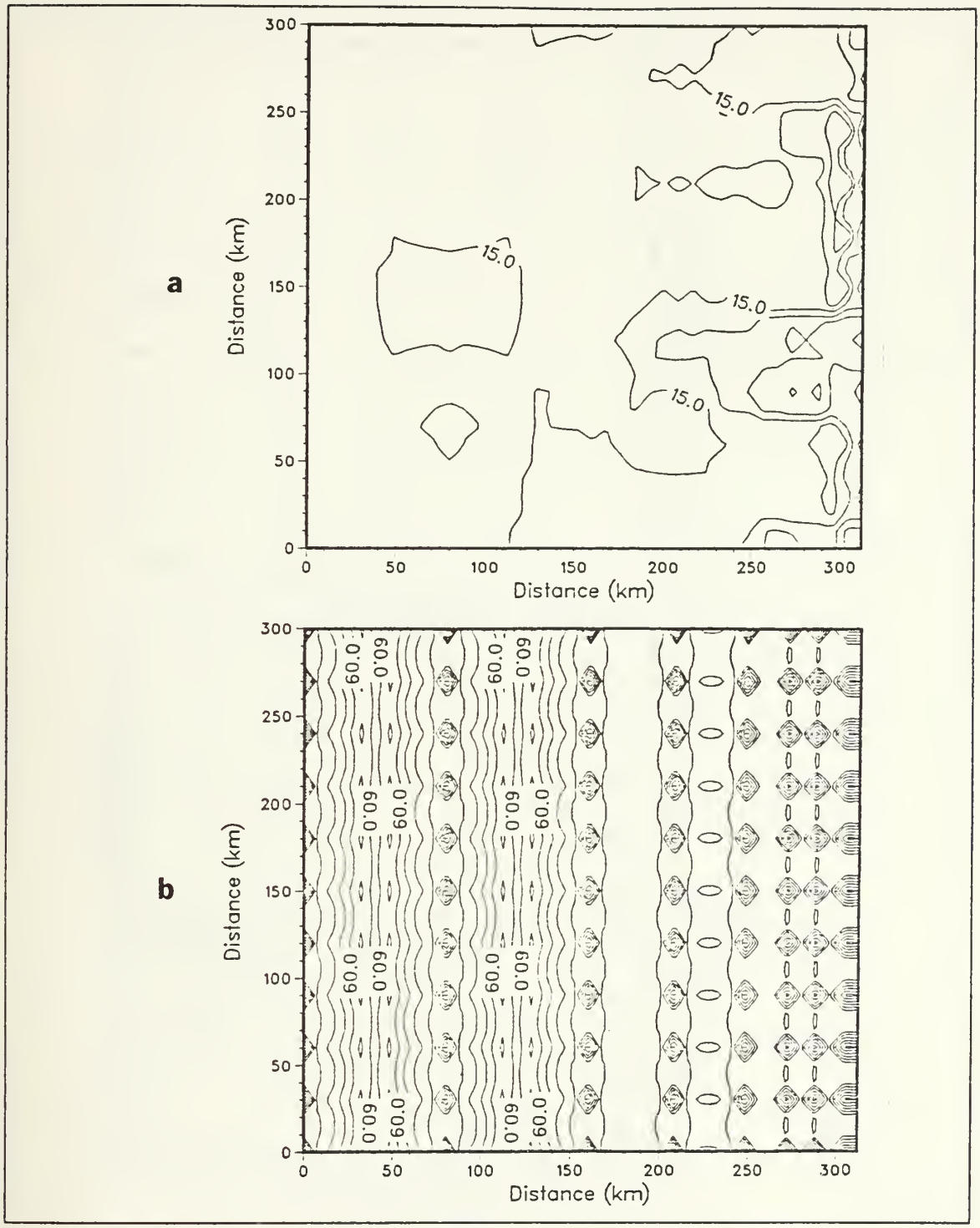

Figure A.7 Case 1 OA SST field using
(a) 2 points of influence with
(b) associated error field.

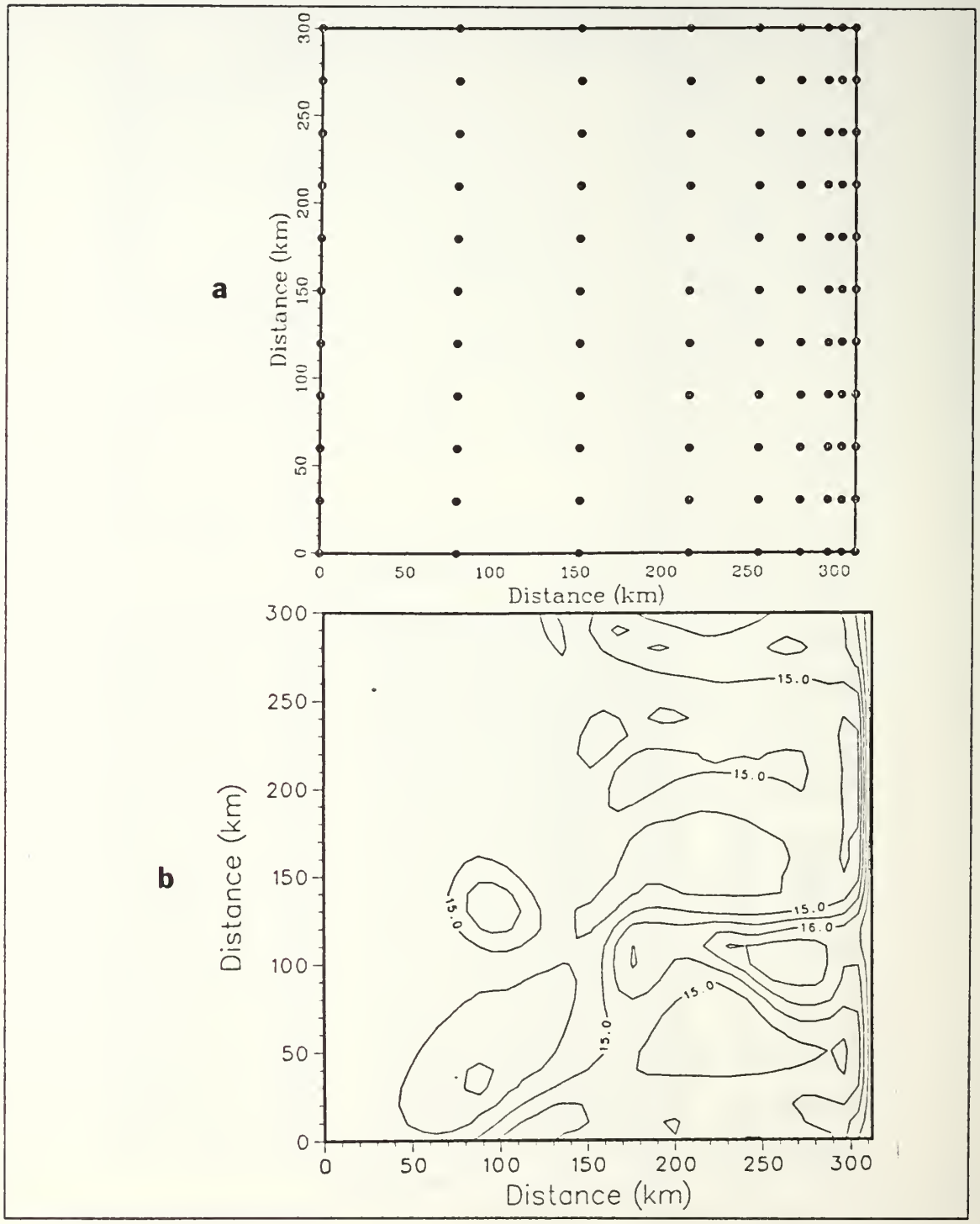

Figure A.8 (a) Case 2 station spacing,
(b) PE model SST field on day 40,
contour interval of 0.5 C.

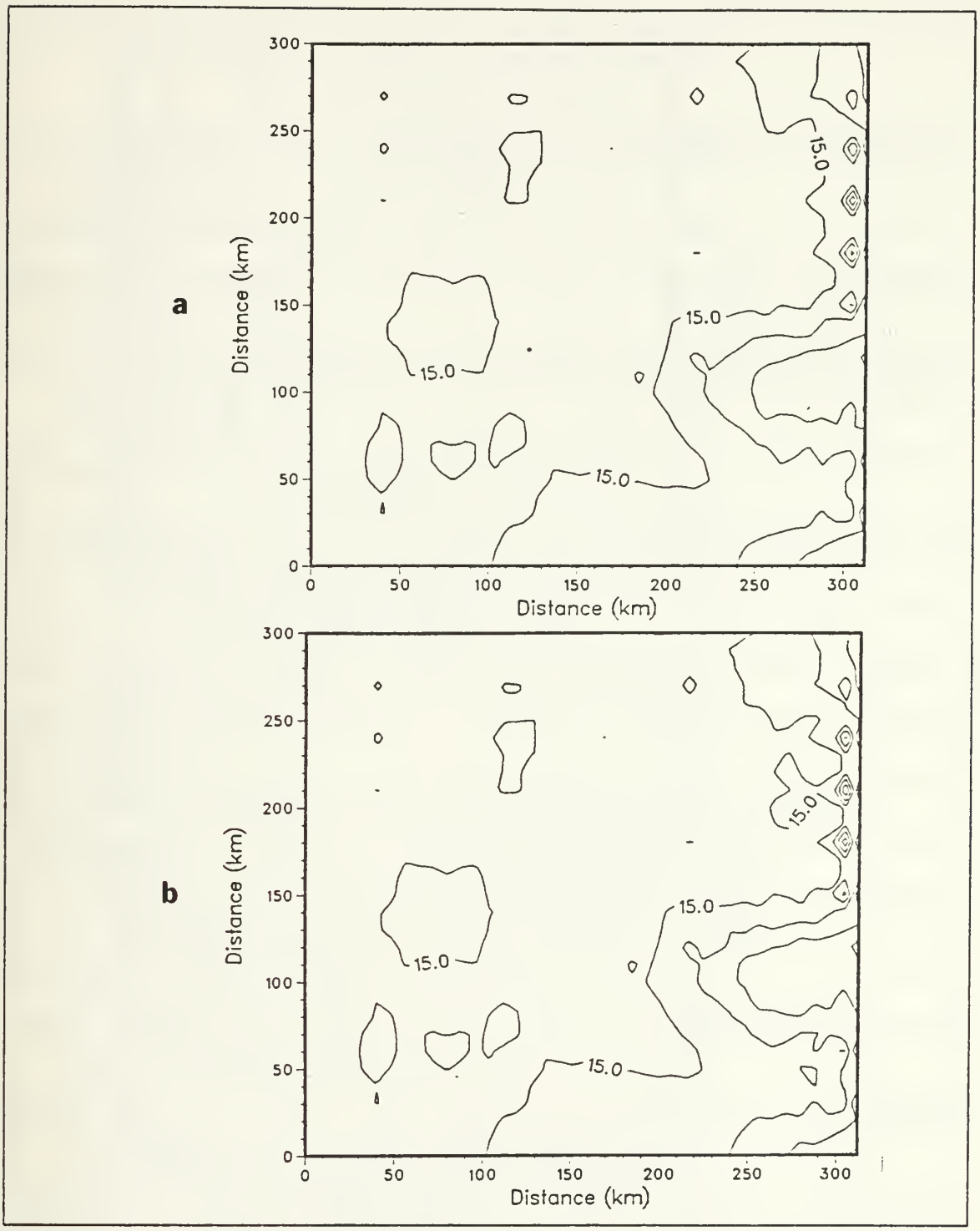

Figure A.9 Case 2 OA SST field using
(a) 8 points of influence,
(b) 6 points of influence.

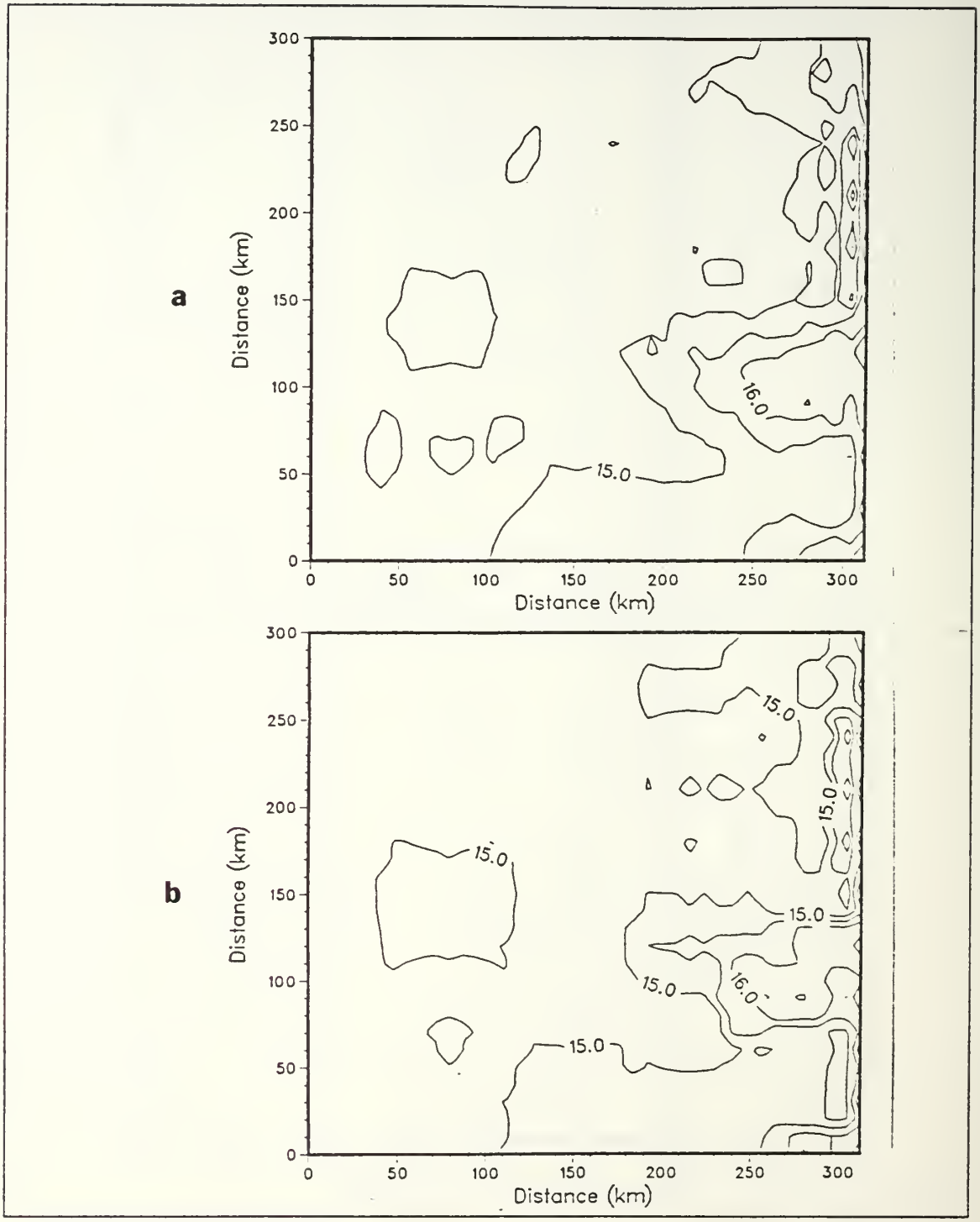

Figure A.10 Case 2 OA SST field using
(a) 4 points of influence,
(b) 2 points of influence.

LIST OF REFERENCES

Arakawa, A. and V.R. Lamb, 1977: Computational design of the basic dynamical processes of the UCLA general circulation model. *Methods in Computational Physics*, J. Chang. Ed., Academic Press, **17**, 173-265.

Bernstein, R.L., L. Breaker and R. Whritner, 1977: California Current eddy formation: Ship, air, and satellite results. *Science*, **195**, 353-359.

Bretherton, F.P., R.E. Davis and C.B Fandry, 1976: A technique for objective analysis and design of oceanographic experiments applied to MODE-73. *Deep-Sea Res.*, **23**, 559-582.

Carter, E.F. and A.R. Robinson, 1981: Time series of synoptic maps of the Western North Atlantic: A space-time objective analysis of Polymode AXBTs. *Division of Applied Sciences, Harvard Univ., Reports in Meteorology and Oceanography, Number 15*, 14 pp.

Chelton, D.B., 1984: Seasonal variability of alongshore geostrophic velocity off central California. *J. Goephys. Res.*, **89**, 3473-3486.

Colton, M.C. and C.N.K. Mooers, 1984: OPTOMA program interim report: The airborne ocean thermal structure mapping project. *NPS Technical Report No. NPS-68-85-008*, 98 pp.

Freeland, H.J. and W.J. Gould, 1976: Objective analysis of mesoscale ocean circulation features. *Deep-Sea Res.*, **23**, 915-923.

Gandin, L.S., 1963: *Objective Analysis of Meteorological Fields.* Leningrad, Gidrometeorizdat, 266 pp.

Hickey, B.M., 1979: The California Current System- hypothesis and facts. *Prog. in Oceanogr.*, **8**, 191-279.

Kosro, P.M. and A. Huyer, 1986: CTD and velocity surveys of seaward jets off Northern California, July 1981 and 1982. *J. Geophys. Res.*, **91**, 7680-7690.

McWilliams, J.C., 1976: Maps from the mid-ocean dynamics experiment: Part I. Geostrophic streamfunction. *J. Phys. Oceanogr.*, **6**, 810-827.

Mooers, C.N.K. and A.R. Robinson, 1984: Turbulent jets and eddies in the California Current and inferred cross-shore transfers. *Science*, **223**, 51-53.

Philander, S.G.H. and J.L. Yoon, 1982: Eastern boundary currents and coastal upwelling. *J. Phys. Oceanogr.*, **12**, 862-879.

Rienecker, M.M., C.N.K. Mooers, D.E. Hagan and A.R. Robinson, 1984: A cool anomaly off northern California: An investigation using IR imagery and *in situ* data. *J. Geophys. Res.*, **90**, 4807-4818.

Robinson, A.R., J.A. Carton, C.N.K. Mooers, L.T. Walstead, E.F. Carter, M.M. Rienecker, J.A. Smith and W.G. Leslie, 1984: A real time dynamical forecast of ocean synoptic/mesoscale eddies. *Nature*, **309**, 781-783.

Shapiro, R., 1971: The use of linear filtering as a parameterization of atmospheric diffusion. *J. Atm. Sci.*, **28**, 523-531.

White, W.B., 1977: Secular variability in the baroclinic structure of the interior North Pacific from 1950-1970. *J. Mar. Res.*, **4**, 587-607.

White, W.B. and R.L. Bernstein, 1979: Design of an oceanographic network in the midlatitude North Pacific. *J. Phys. Oceanogr.*, **9**, 592-606.

Willmott, C.J., S.G. Ackleson, R.E. Davis, J.J. Feddema, K.M. Klick, D.R. Legates, J. O'Donnell and C.M. Rowe, 1985: Statistics for the evaluation and comparison of models. *J. Geophys. Res.*, **90,** 8995-9005.

Wooster, W.S. and J.L. Reid, 1962: Eastern boundary currents. *The Sea*, **6,** 253-260.

INITIAL DISTRIBUTION LIST

		No. Copies
1.	Defense Technical Information Center Cameron Station Alexandria, VA 22304-6145	2
2.	Library, Code 0142 Naval Postgraduate School Monterey, CA 93943-5002	2
3.	Chairman (Code 68Tm) Department of Oceanography Naval Postgraduate School Monterey, CA 93943	1
4.	Chairman (Code 63Rd) Department of Meteorology Naval Postgraduate School Monterey, CA 93943	1
5.	Professor C.N.K. Mooers (Code 68Mr) Department of Oceanography Naval Postgraduate School Monterey, CA 93943	3
6.	Dr. M.L. Batteen (Code 68Bv) Department of Oceanography Naval Postgraduate School Monterey, CA 93943	1
7.	Professor R.L. Haney (Code 63Hy) Department of Meteorology Naval Postgraduate School Monterey, CA 93943	1
8.	Dr. M.M. Rienecker (Code 68Rr) Department of Oceanography Naval Postgraduate School Monterey, CA 93943	1
9.	Dr. W.J. Schmitz Woods Hole Oceanographic Institute Woods Hole, MA 02543	1
10.	Professor R.L. Smith College of Oceanography Oregon State University Corvallis, OR 97331	1
11.	Professor A.R. Robinson Division of Applied Sciences Pierce Hall Room 100D Harvard University Cambridge, MA 02543	1
12.	Dr. T.B. Curtin Code 1122 Office of Naval Research 800 North Quincy Street Arlington, VA 22217	1

13.	Dr. T.W. Spence Code 1122 Office of Naval Research 800 North Quincy Street Arlington, VA 22217	1
14.	LT John L. Heishman 504 Delaney Road Huntsville, AL 35806	2
15.	Director Naval Oceanography Division Naval Observatory 34th and Massachusetts Avenue NW Washington, DC 20390	1
16.	Commander Naval Oceanography Command NSTL Station Bay St. Louis, MS 39522	1
17.	Commanding Officer Naval Oceanographic Office NSTL Station Bay St. Louis, MS 39522	1
18.	Commanding Officer Fleet Numerical Oceanography Center Monterey, CA 93943	1
19.	Commanding Officer Naval Ocean Research and Development Activity NSTL Station Bay St. Louis, MS 39522	1
20.	Commanding Officer Naval Environmental Prediction Research Facility Monterey, CA 93943	1
21.	Chairman, Oceanography Department U.S. Naval Academy Annapolis, MD 21402	1
22.	Chief of Naval Research Naval Ocean Research and Development Activity 800 N. Quincy Street Arlington, VA 22217	1
23.	Office of Naval Research (Code 420) Naval Ocean Research and Development Activity 800 N. Quincy Street Arlington, VA 22217	1
24.	Scientific Liason Office Office of Naval Research Scripps Institution of Oceanography La Jolla, CA 92037	1
25.	Commander Oceanographic Systems Pacific Box 1390 Pearl Harbor, HI 96860	1

220247

Thesis
H42385 Heishman
c.1 Sampling strategies in space and time: effects on representation of mesoscale processes.